Precision Control of Continuous Microcontact Printing

by

Maia R. Bageant

B.S., Massachusetts Institute of Technology (2011)
M.S., Massachusetts Institute of Technology (2013)

Submitted to the Department of Mechanical Engineering
in partial fulfillment of the requirements for the degree of

Doctorate in Mechanical Engineering

at the

MASSACHUSETTS INSTITUTE OF TECHNOLOGY

February 2018

Author . Signature redacted .....
Department of Mechanical Engineering
December 20, 2017

Certified by .. Signature redacted .....
David Hardt
Ralph E. and Eloise F. Cross Professor of Mechanical Engineering
Thesis Supervisor

Signature redacted

Accepted by .....
Rohan Abeyaratne
Chairman, Committee on Graduate Students

Precision Control of Continuous Microcontact Printing

by

Maia R. Bageant

Submitted to the Department of Mechanical Engineering
on December 20, 2017, in partial fulfillment of the
requirements for the degree of
Doctorate in Mechanical Engineering

Abstract

This work focuses on the development of experimental equipment enabling the scale-up of microcontact printing for industrial use. An examination of existing experimental microcontact printing hardware and identification of its deficiencies are given, and the design and implementation of improvements are detailed. In particular, these improvements focus on the enabling of closed-loop force control of the printing process by the establishment of a deterministic computational platform and additional sensing.

An understanding and rationale for the overall control design of the microcontact printing process is developed. Though the goal is to control the compression of each individual microscale feature on the microcontact printing stamp, force control is shown to offer significant advantages over displacement control.

Analytical dynamic models of the system are developed, iterated, and verified experimentally. Initially, a simple model consisting of two separable single-input, single-output (SISO) systems was developed, but this model was shown to fail to capture relevant dynamics. A twelfth-order multi-input, multi-output (MIMO) model describing the system was then developed and verified experimentally using specially constructed frequency response measurement tools.

Controller design was then undertaken for both the simple and complex model. The simple model was accommodated with proportional-integral and pure integral designs. The complex model required an augmented full-state feedback controller with a Kalman state estimator, which was designed and implemented in discrete time. Nonideal properties inherent to the printhead system, including uncontrollability and unobservability, were quickly identified. Maximum potential control performance under these constraints was explored and demonstrated experimentally, and it was shown that the inherent limitations made satisfactory closed-loop performance impossible.

A conceptual printhead design for control is also presented. Mechanical design principles based on the lessons indicated by the system model and control design are laid out. A conceptual design is developed based on these principles, and basic geometry, packaging, and component selection is completed, allowing for a dynamic system model to be evaluated. The new printhead design is found to offer a significantly

improved dynamic response, making the force control problem very tractable, and additionally solves a number of other design flaws inherent to the original printhead. An example control design and resulting performance is presented.

Thesis Supervisor: David Hardt
Title: Ralph E. and Eloise F. Cross Professor of Mechanical Engineering

Acknowledgments

This work would not have been possible without a great deal of support from many different people.

Financially, I am grateful to the Clean Water and Clean Energy Project and KFUPM for generously funding the majority of this project.

My incredible peers and colleagues have been a great source of strength and knowledge for me throughout this work; in particular, I must thank Matthew Ashner, Lauren Chai, Marcel Thomas, Peter Ascoli, Chris Merian, Adam Libert, Scott Nill, and Larissa Nietner for their support, suggestions, kind ears, and encouragement over many years.

I must also thank the faculty who helped to guide me and teach me throughout the years, in particular my committee, whose skills and experience far exceeding my own helped give me vision that I otherwise would not have.

I am also infinitely grateful to my advisor, Professor Dave Hardt, who has not only been patient and supportive for a very long time and through what has been a difficult process, but who has also come to be a mentor and teacher to me in many ways, both on the books and off.

And finally, I would like to thank my family for their patience and support through all the years. They were supportive, patient, and loving throughout it all, a source of comfort in tough times, and of jubilation in successful ones. I could not have completed this project without their strength and love.

Contents

List of Figures

List of Tables

Chapter 1

Introduction

1.1 Project Motivation

Microscale and nanoscale manufacturing in the past few decades has supported some of the most important technological revolutions of the modern era. Most notably, the development of conventional photolithography has enabled the proliferation of computing technologies that are now ubiquitous, appearing in everything from smartphones to smart refrigerators.

Photolithography is a process in which a light-reacting chemical mask, called a photoresist, is applied to a silicon substrate and subsequently patterned using specialized optics. When the patterned substrate is developed and etched, the mask serves to block etching of the substrate, allowing a three-dimensional pattern to be etched into the silicon. These patterns create structures that serve as basic computing elements, transistors, and allow for complex integrated circuits and silicon logic to be implemented. Over the course of decades, the characteristic size of one of these transistors has shrunk from the micron scale down to the nanometer scale, and continues to decrease. Current state-of-the-art processes are targeting 7-11 nanometer transistor sizes. [16]

Though its capabilities are incredible, one of the major downsides of conventional lithography is its high cost. A single extended ultraviolet (EUV) photolithography machine capable of patterning 7 nanometer transistors sells in 2017 for approximately

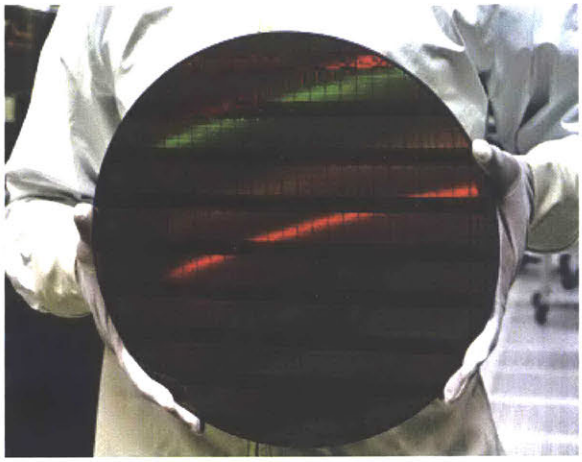

Figure 1-1: *Etched silicon wafer.* A single silicon wafer can contain hundreds of processors, each worth hundreds of dollars. [1]

$110 million. [17] But, a single 300-millimeter wafer produced by these machines can contain hundreds of processors, each worth hundreds of dollars—making a single wafer easily worth hundreds of thousands of dollars. [1] And, the chips produced from this wafer offer tremendous power, with processing speeds in the rate of gigahertz.

But consider the case of fabricating simple conductive circuits for RFID tags, or large-area flexible displays, or disposable conductive paper circuits. These are technologies that already exist and require conductive patterns with feature sizes on the order of tens to hundreds of microns, and for which market demand is already forecast—perhaps up to $73 billion by 2025. [18] Producing these potentially disposable products with conventional photolithography machines makes them prohibitively expensive, and applies high-capability technologies where low-capability ones are perfectly suitable. Clearly, then, it would be more economical to pursue manufacturing technologies that are a right-size fit for these applications: low-performance but low-cost, and capable of pattering large areas. [2]

Enter printed electronics technologies. The goal of printed electronics manufacturing technologies is to leverage existing printing technologies, which are capable of creating large areas of low-cost patterned surfaces such as newspapers or packaging, and apply those concepts to the production of electronics components. The cost per area of a printed electronic device is predicted to be 1% or 0.1% of the cost per area of

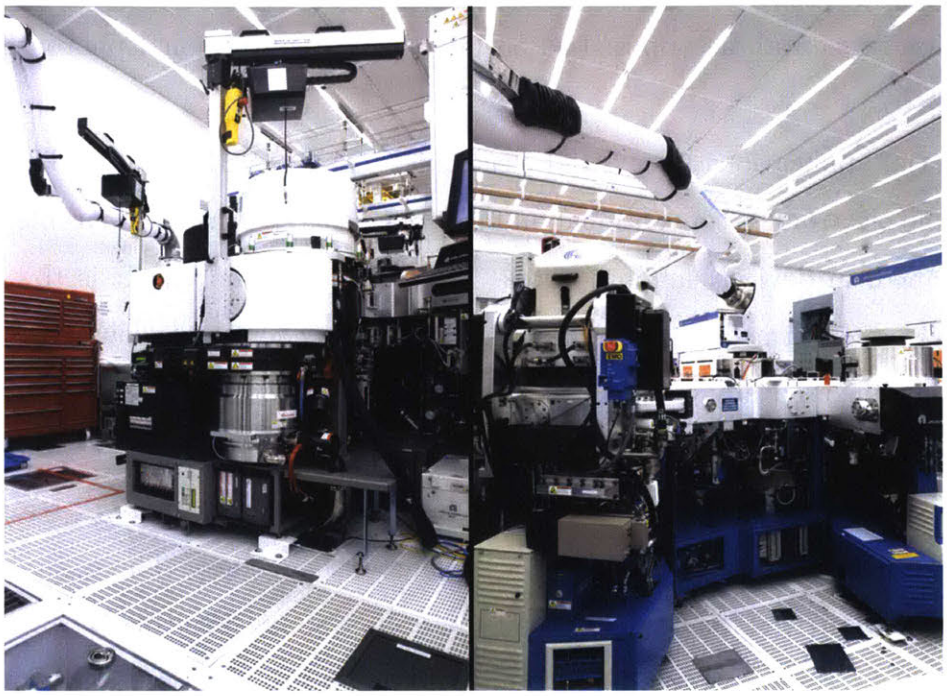

Figure 1-2: *Traditional photolithography equipment.* This Applied Materials facility in Santa Clara, CA contains machines such as the Applied Materials Endura machine, used to deposit metals onto a wafeer, and the Applied Materials Tetra machine, used to produce photolithographic masks. [1]

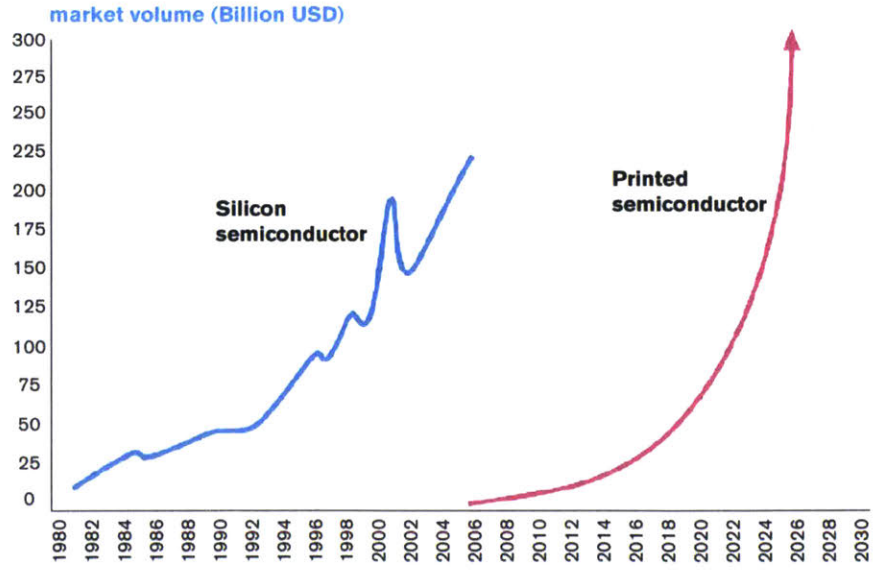

Figure 1-3: *Printed electronics market forecast.* Forecasted demand for the printed electronics market could be many billions in the coming years. [2]

a traditional silicon device; and to start up a printed electronics plant might require $30 million in capital, as opposed to $3 billion for a conventional photolithography plant. [2]

Potential applications for printed electronics include RFID or optical codes, low-cost simple electronics, conventional and flexible displays, sensors, wearable electronics, and medical devices, among others. [2, 18, 6]. The movement is toward what industry leaders term "ubiquity:" having sensors and devices so low-cost that they can be implemented anywhere and everywhere that electronic sensing, tracking, or communication could be useful.

The major hurdle in accessing this market, however, has proven to be transitioning print media technologies to printed electronics technologies. There are two chief technological barriers: feature size, and material system. Printing technologies are intended to produce patterns for human reading and recognition, and typically do not need to accurately replicate features below 100 microns in scale. (For example, a typical high-resolution printed document might be 600 ppi, which corresponds to about 40 microns per dot.) Second, printed electronics have additional demands they make on their material system: the ink must be conductive, and applied in a sufficiently thick layer to achieve conductivity. [2] Both of these challenges have been active areas of research in recent years.

Research efforts have tended to focus on a handful of printing technologies that have shown great promise: microscale gravure printing, microscale flexographic printing, inkjet printing, microscale screen printing, and microcontact printing (also known as soft lithography). A brief overview of the capability of existing efforts in these technologies is given in Chapter 2; but the focus of this work is on microcontact printing.

1.2 Microcontact Printing

Microcontact printing, also known as soft lithography, is a parallel manufacturing process in which a highly compliant polymer stamp with raised features is used to transfer a microscale or nanoscale two-dimensional pattern to a substrate.

In a typical implementation of microcontact printing, the stamp is made from polydimethylsiloxane (PDMS), a rubbery silicone polymer. PDMS is commercially available as a two-part self-crosslinking compound, such as Dow Corning Sylgard 184 [19]; when the two liquid components are mixed and cured (at room temperature or above), the compound will self-crosslink and form a durable, long-lasting, chemically resistant, elastomeric material that replicates the features of its container down to the nanoscale [20].

To create the features of the stamp, a mold with a negative of the desired stamp pattern is required. Molds can be fabricated by many different means, most commonly using conventional lithography machines to pattern a silicon wafer with a resist such as SU-8 [16]. The elasticity of the PDMS aids in mold removal, allowing the mold to remain undamaged for future casting of the same pattern [21].

The PDMS stamp then must be inked. Depending on the nature of the ink and the differing surface energies between the stamp, the ink, and the substrate, different inking methods are possible or favorable. Inks of interest have typically been liquid conductive inks such as PEDOT or silver nanoparticle suspensions [8]. However, microcontact printing is also capable of utilizing nonliquid chemical inks and films, such as thiols [21, 20, 13, 22], since the ink need not be carried in pits from which it must be transferred (as in gravure or flexographic printing, see Chapter 2).

There are several methods of applying inks to the stamp; the most suitable one will depend on the nature of the ink and the application. In one form, a liquid ink chemical may be spin coated onto another surface, an "inkpad," made of a material with less favorable surface energy than PDMS. The PDMS stamp can then be contacted to this inkpad, lifting a thin liquid or solid film [8]. It is also possible to coat the stamp in a liquid ink and then allow it to dry, coating it with a dry chemical such as a thiol [20]. Compatible chemical inks may also be diffused into the stamp's molecular matrix by soaking [23]. Finally, it is also possible to coat the stamp with a liquid ink and then transfer the liquid to a substrate, though controlling the amount of ink on each feature has proven a difficult research task [8].

Different types of substrates are typically used with each different type of ink.

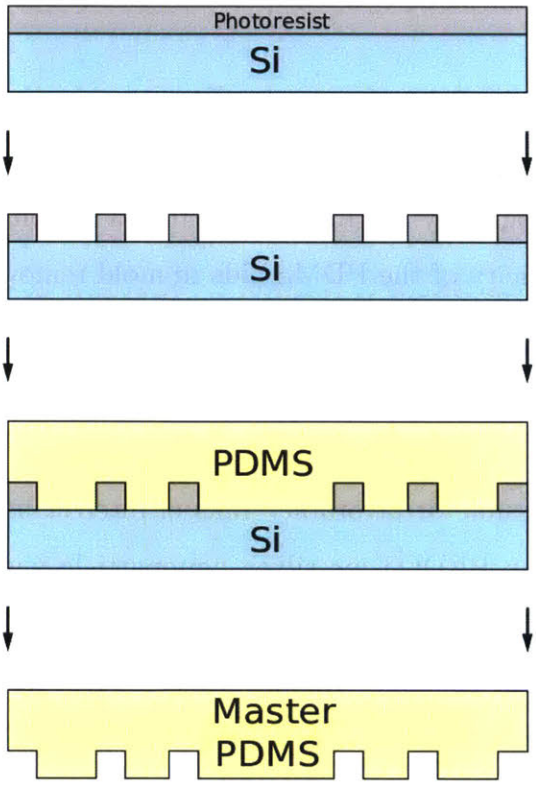

Figure 1-4: *PDMS stamp fabrication process.* To fabricate the stamp, a mold is typically created using conventional lithographic techniques to pattern photoresist onto a silicon wafer. However, the wafer is not etched; instead, liquid PDMS is cast onto the wafer and cured, taking on the negative of the pattern. The elasticity of the PDMS allows it to be easily peeled from the mold and for the mold to be reused multiple times. [3]

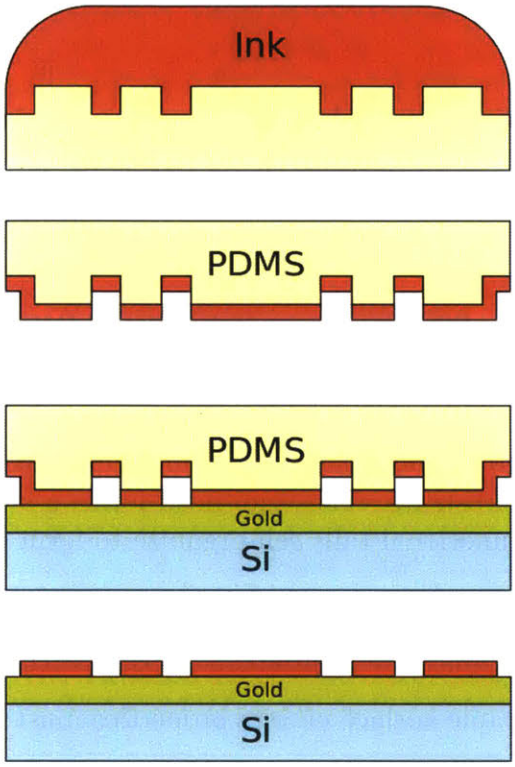

Figure 1-5: *Inking and printing process.* A common method of inking PDMS stamps involves coating the stamp with a liquid ink consisting of the ink chemical in a volatile solvent. The solvent may be allowed to evaporate, leaving a film of dry chemical, which may then be applied to a substrate. The chemical bonds to the substrate, forming a pattern with modified surface properties as compared to the base surface. [3]

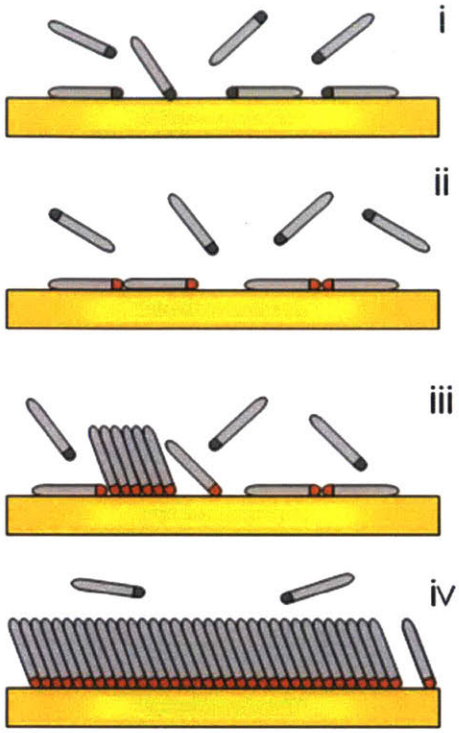

Figure 1-6: *Ink molecular self-assembly.* Thiol molecules undergo self-assembly when applied to a metalized substrate. The thiol head forms a strong covalent bond with the substrate, and the functional tails self-organize to form regular patterns. [4]

When conductive liquid inks are utilized, a substrate that meets the application needs but also has favorable surface energy properties must be chosen. For example, conductive silver nanoparticle suspensions may be successfully printed on glass and polyethylene film. [8] Thiol inks, however, are intended to be printed on pre-metallized substrates such as gold- or aluminum-coated polyethylene film. The thiol molecule has a head with a sulfur atom that bonds strongly to the metal, and a functional tail that can mask and change the surface properties of the substrate. Many of these thiol chemicals are used as etchant resists; after the metallized substrate is patterned, the non-printed metal is chemically removed, leaving a conductive pattern under the thiol molecules. However, using the thiol to change surface energy and control wetting or de-wetting of the substrate by another chemical is also an established technique. [13, 24, 25]

Microcontact printing has the fundamental capability to create any pattern that a

stamp can replicate, and PDMS has successfully been used to replicate features on the tens of nanometers scale [20]. It can also be expanded to a large area by making a large stamp; and it also can be extended to a continuous roll-to-roll process by wrapping the stamp around a cylinder. In this way, microcontact printing is capable of producing many square meters of patterns with features on the order of single microns, a unique combination of capability and speed compared to other printing-based processes [6]. The current limitations of microcontact printing are typically in the material system, especially when it comes to depositing thick layers of conductive inks [8]; and in the lack of industrial-scale equipment capable of successfully controlling the process.

1.3 Specific Implementation of Microcontact Printing

The specific implementation of microcontact printing in this work was developed chiefly by Merian and Hale based on a large body of established techniques from researchers such as Chris Love and George Whitesides [13, 8, 24, 21].

1.3.1 Tooling

Typical PDMS tooling is fabricated by casting PDMS into a silicon wafer patterned with developed SU-8 photoresist. However, when this type of stamp is used in a roll-to-roll process, wrapping it around a cylindrical roll creates an undesirable seam that interrupts continous printing. For this work, a seamless cylindrical stamp, fabricated using a technique developed by Petrzelka [5], is utilized. The seamless cylindrical mold is created using centrifugal casting; by directly exposing photoresist on the inside surface of a spinning drum, a seamless cylindrical analogue of the silicon wafer can be created. [22].

The cylindrical stamps are produced in a custom casting machine developed by Joe Petrzelka. The machine consists of an open-ended spinning drum, a heating element, a linear motion stage with an optical assembly, and a fixed laser source. [5]

To create a stamp, a layer of SU-8 polymer photoresist is first injected into the spinning drum and heat cured to create a planarizing layer, exactly concentric with the axis of spin of the drum. Once cured, the SU-8 is treated as a permanent layer and is chemically and thermally resistance to subsequent processing. [22]

To create the mold features, a layer of AZ 9260 photoresist, typically 15 μm in thickness, is then cast on top of the SU-8. This layer is softbaked to prepare for exposure. The AZ photoresist is a positive photoresist; the areas exposed to a particular wavelength dissolve when mixed with a liquid developer agent, leaving behind a three-dimensional structure. [22, 26]

The AZ photoresist is then exposed in a direct-write process. A 405nm laser source is redirected at a 90° angle using a stage-mounted optical assembly. As the drum rotates at a slow speed and the linear stage moves the optic, the laser may be cycled on and off to raster a pattern on the interior. This process is highly sensitive to focus and errors in the laser spot size, and any aberrations are passed on to the mold and thus to the tool. [22, 5, 27] Figure 1-7 shows a schematic of the stamp fabrication process; an example of a finished stamp is shown in 1-8.

Once the writing process is complete, a developer agent is inserted into the drum, dissolving the exposed AZ polymer, and leaving a 3-dimensional negative mold. By casting liquid PDMS precursor into this mold and thermally curing at high spin speed, a seamless cylindrical stamp can be created. Notably, sufficient PDMS must be added to close the inner diameter of the stamp to that of the printing roll, as inidcated in 1-9. More detailed procedures and process parameters for stamp creation can be found in Peter Ascoli's master's thesis document [22].

The seamless PDMS stamp must then be mounted onto the print roll. The stamp is intentionally constructed such that the inner diameter of the stamp is less than or equal to the 50mm outer diameter of the steel printing roll. Due to the high surface adhesion of PDMS, the stamp cannot be easily slipped onto the roll. An innovation by Petrzelka was to utilize a custom-made air collar to create a cushion of high pressure air between the stamp and the print roll, allowing it to be maneuvered to the center of the roll. The air may then be disabled, causing the PDMS stamp to contract onto

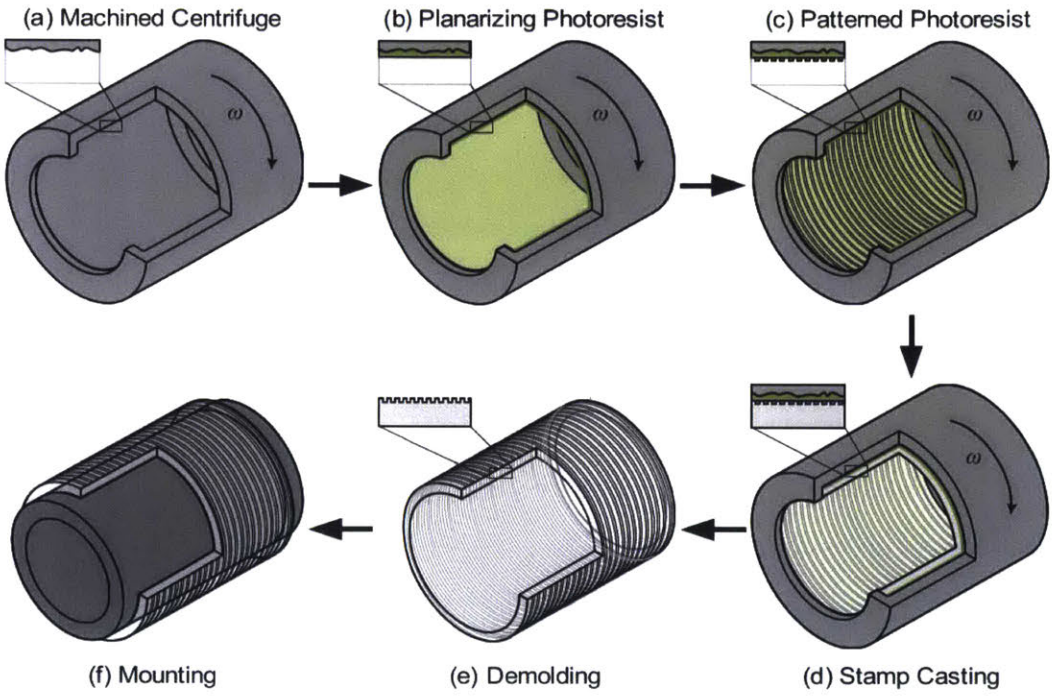

Figure 1-7: *Seamless cylindrical stamp fabrication process.* The steps to fabricating a seamless stamp involve creating a planarizing SU-8 layer (b); patterning a layer of AZ 9260 (c); and casting and curing PDMS (d). [5]

Figure 1-8: *Seamless cylindrical stamp.* A finished seamless cylindrical stamp. This stamp, produced by Ascoli, had a set of discontinuous patterns to investigate stamp production capability. [22]

the roll [5]. Further work to characterize and reduce stamp distortion resulting from this process is necessary.

1.3.2 Printing

The printing process utilized in this work is an evolution of established processes. In benchtop explorations of the capabilities of microcontact printing, stamps were typically applied either by allowing them to contact under their own weight, or by manually applying a controlled force on the benchtop, either with manual pressure or a calibrated weight. Initial machines developed by Stagnaro [23] and Petrzelka [9] focused on using mechanical or electromechanical actuators to apply consistent, constant forces across the printing area. The printing process utilized in this work directly builds off the work done by Petrzelka [9] and Libert [10], focusing on the utilization of machine repeatability to control the application of precise printing load across the area of the stamp.

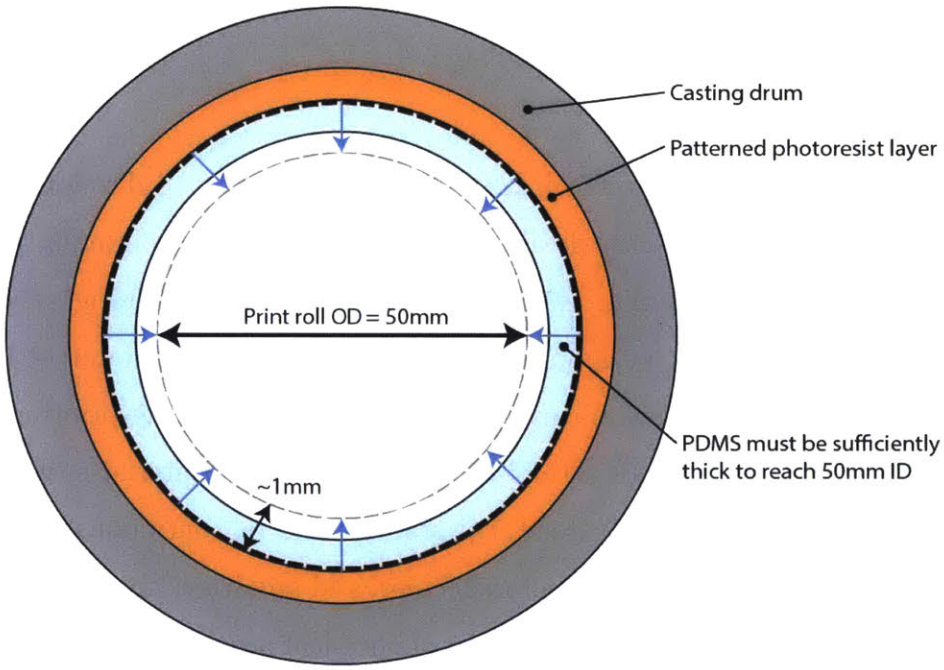

Figure 1-9: *Dimensional constraints on the cylindrical casting process.* A cross-section of the drum during the fabrication of a seamless cylindrical stamp is shown. The stamp is created by casting material into a featured mold, until it closes in to the proper diameter. For typical experimental stamps, the wall thickness is approximately 1mm.

1.3.3 Material System

Initial efforts by Hale [8] and Petrzelka [9] demonstrated successful outcomes using a silver nanoparticle ink and glass material system. However, for printed electronics applications, it is typically desirable to utilize low-cost substrates [2]; additionally, roll-to-roll printing requires the use of flexible substrates, as the material is spooled and unspooled to a finite minimum radius.

To that end, Libert [10] and Nill [28] made initial efforts to develop a material system compatible with low-cost flexible polymeric substrates, nominally polyethey-lene film. Hizir [29] and Merian [30] continued development. Through the work of Merian [13] and Hale [8] it became clear that controlling the amount of liquid ink applied to the raised features and carried onto the substrate during printing was very difficult. However, switching to a thiol-metalized substrate material system allowed a move away from liquid inks. Instead, the stamp could be continuously dipped into a bath of volatile solvent bearing thiol molecules, and an air stream could be utilized to evaporate the solvent, drying a solid film of chemical onto the stamp. Then, a dry thiol chemical could be applied to the metalized substrate, to which it would bond when brought into contact by the raised stamp features. [13] Though ODPA and aluminum were investigated as a low-cost thiol/metal combination, the slow rate of bond formation (on the order of 1 minute) required to form a self-assembled mono-layer made this material combination unattractive for high-speed printing [30]. In the end, the fast bond formation and strong bond of hexadecanethiol (HDT) to gold-coated PET film was determined to be the most attractive material system to study the physics of printing. The HDT molecules are suspended in a 15 millimolar con-centration solution in ethanol; they are deposited by the stamp onto a PET film with a 20 nm thick layer of gold. The HDT bonds nearly immediately and forms a mask resistant to gold etching chemicals, allowing post-printing patterns to be studied. [13]

1.4 Summary

In summary, microcontact printing is an attractive alternative to conventional lithography for the production of low-cost, low-performance printed electronics. By leveraging technologies from the printed media industry such as roll-to-roll material handling and patterned master printing rolls, high-throughput printing can be achieved. Achieving pattern sizes smaller than the capability of conventional printing techniques is a major technological challenge. Further, material systems that are economically feasible for and compatible with any specific application must also be developed.

To study the microcontact printing process, a printing process in which a seamless cylindrical stamp is fabricated, mounted on a machine, coated with a thiol-based ink, and brought in contact with a gold-coated substrate has been developed. Further development of this printing process has focused on using the same material system, but scaling up speed and scaling down feature size while maintaining process robustness. Pursuit of this goal required the development of an experimental printing platform, which is the focus of the next chapter.

Chapter 2

Experimental Platform

2.1 Prior Art

In industry, high-speed two dimensional printing technologies have been in development since the 19th century, and indeed even back to the original printing press. Printing technologies can be divided into two categories: technologies based on a master patterned plate, termed "conventional printing," and technologies that do not require a master, termed "non-impact printing." Among these techniques, flexography, gravure, screen, and inkjet have all been investigated for their potential to produce microscale patterns at high-speed. [7]

In gravure printing, a printing roll made from a hard, durable material, typically metal, is patterned with a series of engraved pits. Ink is transferred to the gravure roll typically through a bath, and then excess ink is removed using a doctor blade, which skims close to the surface of the rigid gravure roll, leaving ink only in the pits. When an ink-filled cell contacts a substrate, some of the ink in the cell transfers to the substrate. Recent efforts have utilized silicon etching technologies to produce rolls that are capable of printing 5μm patterns. [6] However, the transfer of ink in gravure printing is dependent on fluid physics of the ink exiting the cell, and further decreases in size and increases in speed begin to encounter physical limits. [29]

Flexographic printing, on the other hand, utilizes raised features instead of pits to transfer the actual pattern to the substrate. A "soft" master printing roll, typically

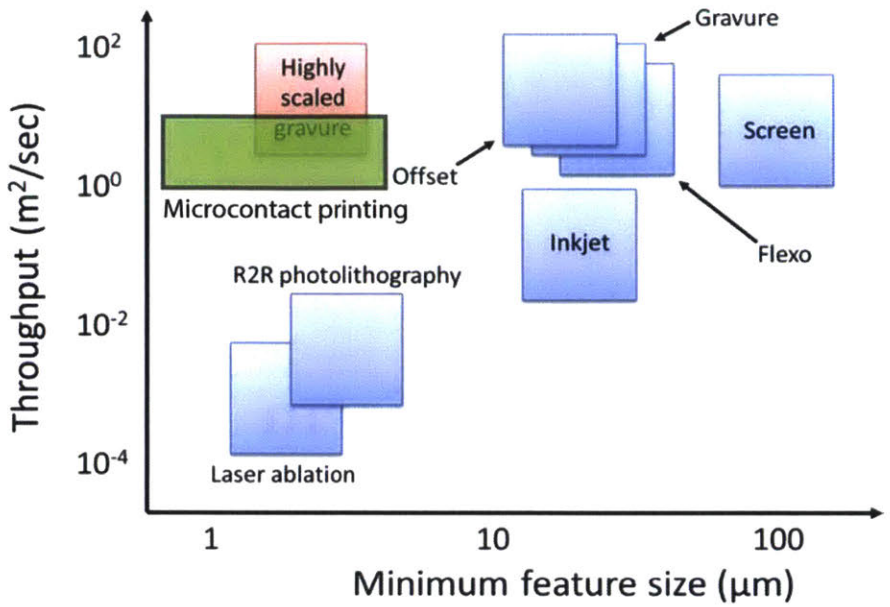

Figure 2-1: *Microcontact printing throughput/feature size capability, compared to other printing processes.* Microcontact printing is physically capable of throughputs on the order of 1-10 m/s, and feature sizes down to 1μm and below. It offers similar throughput capability as microscale gravure printing, but allows for finer patterns. Note that the target capabilities of microcontact printing have been added to the original figure. [6]

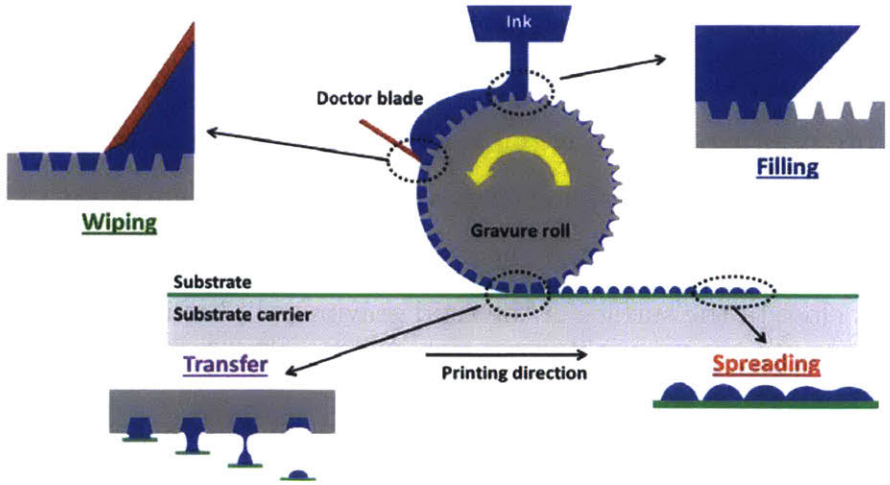

Figure 2-2: *Schematic showing the operation of gravure printing.* Liquid ink is deposited directly from the pits on the gravure roll onto the substrate. At very small scales, the ink transfer and spreading fluid phenomena can create undesirable "smearing" effects. [6]

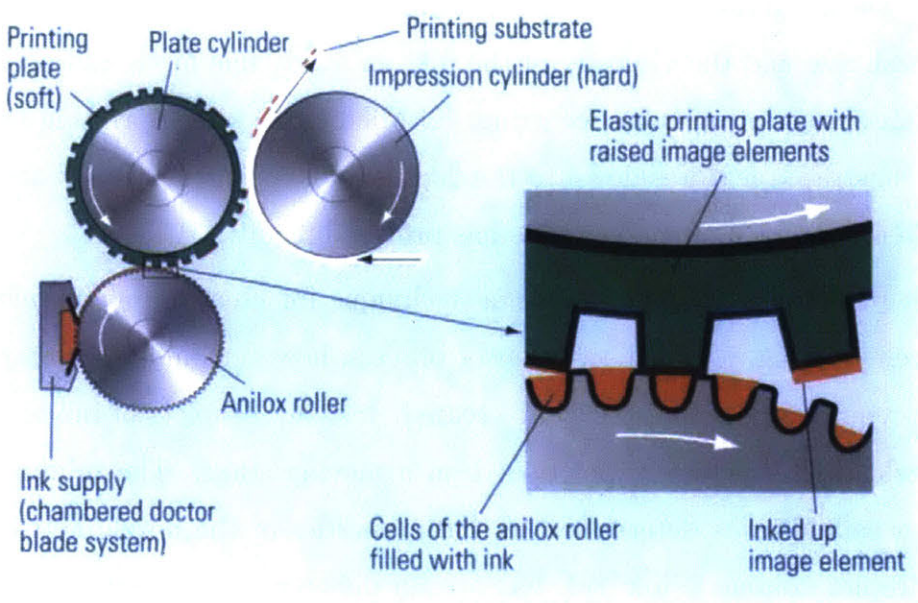

Figure 2-3: *Schematic showing the operation of flexographic printing.* In flexographic printing, ink is transferred from the pit array on the anilox roll to the raised features on the print roll. The patterned print roll then transfers ink to the substrate. The minimum print roll feature size that can be inked is determined by the minimum possible size and spacing of the pits on the anilox roller. [7]

a hard rubber, is patterned with raised features. A roll covered with cells that are smaller than the typical feature size of the printing roll, called the anilox roll, is inked in much the same way a gravure roll is inked. However, instead of directly printing onto a substrate from the anilox cells, the ink is transferred to the flexographic roll's raised features; these features then transfer the ink to the substrate. In this way, flexographic printing removes the direct dependence of feature fidelity on transfer from the ink cells; but patterns are still limited by the speed of ink transfer from and the size of the anilox cells, which must be smaller than the flexographic printing roll features. [6, 7, 29]

Gravure printing and flexographic printing are both continuous, roll-to-roll printing technologies. Another technology being applied to microscale patterning is screen printing. Screen printing is another conventional printing technique, requiring a master, but instead of a continuous roll-to-roll process, it is a discrete sheet-to-sheet process. A stencil is supported by a fine screen mesh, and a viscous ink is pushed through the mesh, depositing onto the substrate sheet where the stencil has an open-

ing. The feature resolution of screen printing is limited by the combination of the screen mesh size and the viscosity of the ink; an overly fine mesh and overly viscous ink will prevent printing from occurring. [6] Micro-scale screen printing has successfully demonstrated features down to the 20μm range, but decreasing feature sizes to the single micron or nanometer range has proven difficult. [31, 32]

Inkjet printing is another promising technique for creating microscale patterns. Like screen printing, it is a sheet-to-sheet process; however, unlike screen printing, it does not require a fixed master to be created. Instead, droplets of ink are deposited by a nozzle that is typically positioned on a moving stage. The minimum feature resolution capability is determined by the properties of the nozzle and the ink; reducing droplet volume below 1pL has proven difficult, but features on the order of 1μm have been achieved. [33, 34] However, the serial nature of this design limits the potential throughput of this process, as there are physical limitations on the speed of the nozzle movement and the placement of each ink drop. [6]

Microcontact printing, introduced notably by the Whitesides group [21], avoids a number of the issues encountered by the aforementioned techniques. First, liquid inks are not necessary to print, as raised features can transfer solid chemical inks or films, removing the fluidic limitations on feature size; in inkjet, screen, and gravure printing, liquid ink is mandatory. (In cases in which liquid inks are desirable, microcontact printing is subject to many of the same challenges that of microscale flexography.)

Flexographic stamps, like PDMS microcontact printing stamps, are a compliant polymeric material; however, PDMS is capable of replicating features down to the 10nm scale, opening the potential to create patterns an order of magnitude smaller than typical flexographic limits. [20] Additionally, the high natural compliance of the PDMS stamp reduces surface accuracy tolerances, as the polymer will deform to achieve conformal contact at nanometer scales. Unfortunately, this also means that the stamp features are sensitive to deformation and distortion, and that efforts to control the printing contact process were necessary. To demonstrate that microcontact printing could be scaled up for industry use, efforts were undertaken to develop experimental equipment that could solve the underlying technological problems and

serve as a proof of concept for industry.

One relevant group is the Center for Hierarchical Manufacturing at the University of Massachusetts, Amherst. This center has a number of large, industry-standard printing platforms to study the process limits and industry scale-up of of nanoimprint lithography and micro-gravure printing. [35, 36] Though both of these processes are parallel micromanufacturing processes, they differ in implementation from microcontact printing. Nanoimprint lithography may use a similar PDMS stamp, but it is intended to create three-dimensional surface texture instead of two-dimensional patterns. Micro-scale gravure printing, like microcontact printing, creates two-dimensional microscale patterns, but does so using a pitted gravure roll, where ink is transfered from the gravure wells to the substrate by fluid dynamics. The speed and size of micro-scale gravure is physically limited by the fluid dynamics of the ink. [37, 38, 29] Microcontact printing, in contrast, is not constrained by the fluid dynamics of ink transfer out of gravure wells, and provides an attractive alternative for specific pattern geometries at high speeds.

Several generations of equipment have been developed by prior researchers in the author's group at MIT. Initial efforts focused on developing equipment that used passive compliance to print patterns in the 10 to 100 micron scale at high speeds. Some early conceptual efforts produced by Goel et. al. [39] were capable of printing roll-to-roll patterns on the order of tens of microns at up to 100 feet per second. Their conceptual machine lacked any web handling capability beyond a basic impression roll, and had no sensing; yet pattern replication was still achieved. Subsequent efforts developed in conjunction with NanoTerra Inc., a start-up based in Cambridge, Massachusetts, were continued in the same vein. Stagnaro [23] engaged in a more in-depth study, establishing design parameters for web handling concepts such as wrap angle, and for a compliance-backed stamp printing roll. Stagnaro's design incorporated a drive roll, a torque brake, and tension sensing; inking was performed by pre-soaking the stamp in the inking chemical, which would then diffuse out of the PDMS molecular matrix. This machine could replicate patterns at 400 feet per minute but started to encounter physics problems such as air trapping at 200 feet per

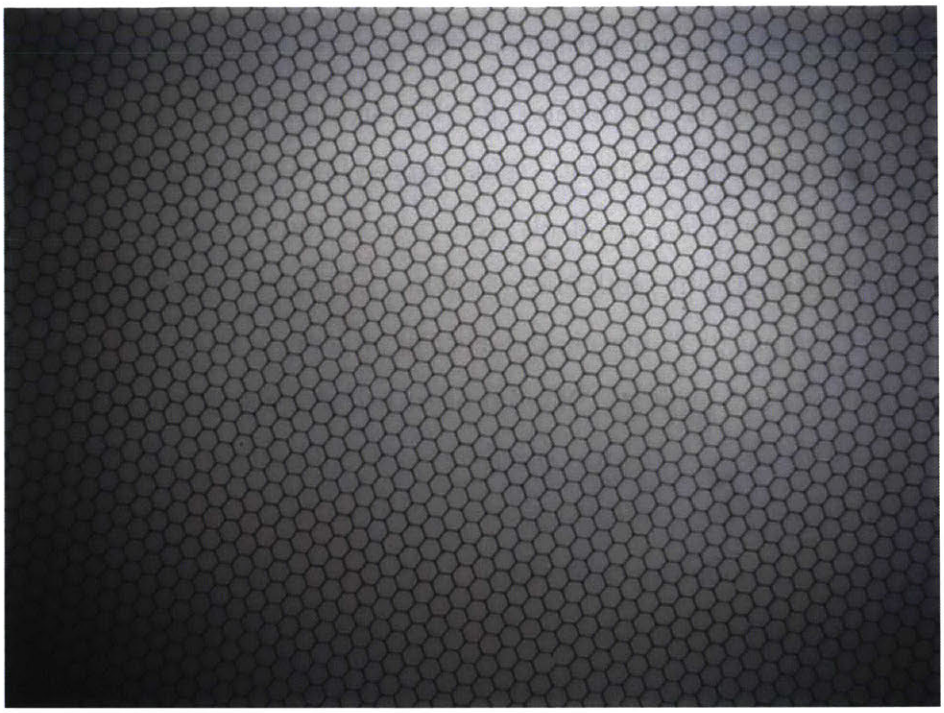

Figure 2-4: *Sparse hexagonal pattern generated using microcontact printing.* This sparse, highly-sensitive pattern was printed using silver nanoparticle inks on glass, using techniques developed by Hale and equipment developed by Petrzelka. Line thickness is 5μm and hexagon pitch is 100μm. [8, 9]

minute. The patterns produced by the Stagnaro machine were measured offline using a microscope and digitally processed in order to analyze their fidelity to the intended original pattern. [40]

Later efforts by Petrzelka produced a machine that focused on precise control of the contact process. This machine consisted of a single degree-of-freedom stage on which a plate substrate could be mounted, and a two degree-of-freedom printing roll. Petrzelka implemented a precise controller that utilized in-process sensing and a hybrid state-space/classical feedback controller to demonstrate via printed substrates and contact imaging that precise control of the contact process could result in perfect print fidelity for very fine patterns. The sample pattern was a sparse hexagonal grid with 5μm wide lines on 100μm wide hexagons; this pattern was highly sensitive to collapse due to overpressure, but the controller developed by Petrzelka could successfully maintain contact conditions in the narrow process window. [8, 9]

Though Petrzelka's machine served as an excellent demonstration that more so-

phisticated closed-loop contact control could accommodate more difficult patterns, it was only capable of discrete printed areas limited to a few square inches, typically microscope slides or four inch silicon wafers, and offered no method for continuous inking. Innovations in these areas would be necessary to scale up efforts for industrial application.

Another research group at the Chinese University of Hong Kong developed a similar approach. Like Petrzelka's machine, this group used flexures to support their printing roll, and developed a sophisticated controller capable of dealing with coupling between degrees of freedom. This machine also incorporates web handling for the study of continuous printing, and successfully printed features down to the submicron size at a speed of approximately 0.4 in/s. [25, 41] Though this effort produced impressive results, industrial printing occurs at much higher speeds, and avoiding the coupled flexural design of the print roll can significantly reduce cost and complexity and potentially increase robustness.

Notably, no experimental or industrial platform yet in development could (1) provide for precise control of the microcontact printing process, (2) allow for high-speed printing of up to 1m/s, and (3) allow for in-process sensing of stamp contact or substrate patterning. To that end, design and fabrication of hardware meeting these needs was undertaken.

2.2 Hardware

The experimental hardware consists of several related modules. Overall, there is a structural frame with a breadboard backing that allows mounting of components. On this frame is mounted (1) a web handling system that manages the unprocessed and processed substrate; and (2) a platform on which the printhead assembly is mounted.

2.2.1 History

Most of this hardware was designed and assembled in a joint effort between Scott Nill [28], Adam Libert [10], and Larissa Nietner [27] during the course of their individual

master's work. The project had two central goals: (1) to solve the problems associated with transforming a roll-to-plate benchtop demonstration to an industry-ready roll-to-roll microcontact printing process; and (2) to demonstrate closed-loop contact control.

The concept of contact control centered around an extension of work by Petrzelka in which it was shown that total internal reflection can be used to visualize the contact pattern of PDMS on glass. [9] It was deemed desirable to use this visualization method on-line to control the process variable that most directly impacted quality: the fidelity of the contact region to the desired pattern. To this end, Nill designed a camera system that could view the printing contact area through a glass impression roll, and from that image could compute two measurements, one indicating the total area of contact, and the other indicating the difference between the left and right sides of the contact region ("balance"). [28]

However, data presented in the master's theses of Nill [28] and Libert [10] show that the effectiveness of contact control was disappointing. The contact control relied on image processing in order to derive its two measurements. Even when the imaged area was reduced to a minimum, the rate at which the image could be processed imposed a severe limit on the maximum loop rate of the controller. Even if this limitation were rectified by improving the image processing algorithm and hardware, the optical limitations of viewing through a 6in diameter glass cylinder placed physical limits on the amount of information that could be gathered in a single image. [28]

This work undertook the completion of both goals, with a focus on establishing superior sensing and control of the printing hardware and contact interface, and demonstrating closed-loop printing. To these ends, an initial survey of hardware limitations revealed that operation of both the printing and web handling modules were poorly characterized, insufficient for the desired research tasks, or both. Shortcomings included:

- Uncharacterized, asymmetrical behavior of web handling motors
- No measurement of web tension

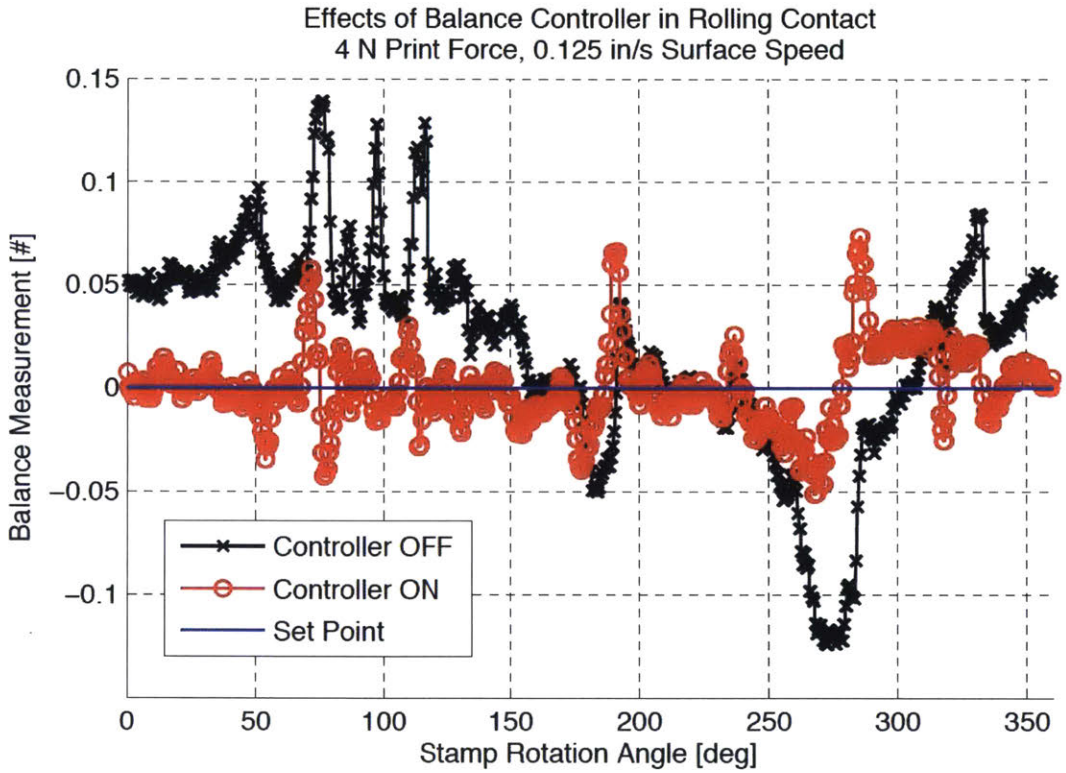

Figure 2-5: *Poor control of the printing process under contact control.* This plot from Adam Libert's thesis document shows the poor performance of the legacy closed-loop contact control design. The controller was capable of maintaining the commanded mean value, but could not reject disturbances under even very slow printing speeds (0.125in/s). The control loop operated at a non-deterministic 10Hz rate. [10]

- No measurement of printing force
- Only indirect measurement of stamp angular position, which proved incompatible with web tension measurement
- No deterministic timing sources for control
- Poor performance of contact controller [10]

In support of achieving measurable, high-performance closed-loop printing control, this thesis undertook various tasks related to characterizing and (where possible) improving the various components as related to their performance during the microcontact printing process.

2.3 Web Handling

The web handling system consists of an active unwind roll, an active rewind roll, two idler rolls, and an impression roll-print roll assembly. The unwind roll contains unprocessed substrate, which is fed into the system. The rewind roll takes up processed substrate. A schematic of the system is shown in 2-6.

Idler rolls were chosen for this design in order to keep the angle of the web approaching the impression roll constant. As material is transferred from the unwind roll to the rewind roll, the effective diameter of those rolls changes, and thus the angle of the span coming from those rolls change. Inserting constant-diameter idler rolls into this span breaks it into two spans, one of which remains at a constant angle no matter the amount of material on the wind or unwind rolls. This constant span can be utilized to make measurements or apply other processing steps to the web. More information on how this design was selected can be found in Adam Libert's master's thesis document [10].

The active rolls consist of studded self-expanding shafts (Double E Company model CLEV12-TBA) mounted in a cantilevered configuration [10]. Each shaft is driven by a SureServo SVL-204 low inertia AC brushless servo motor. A SureServo

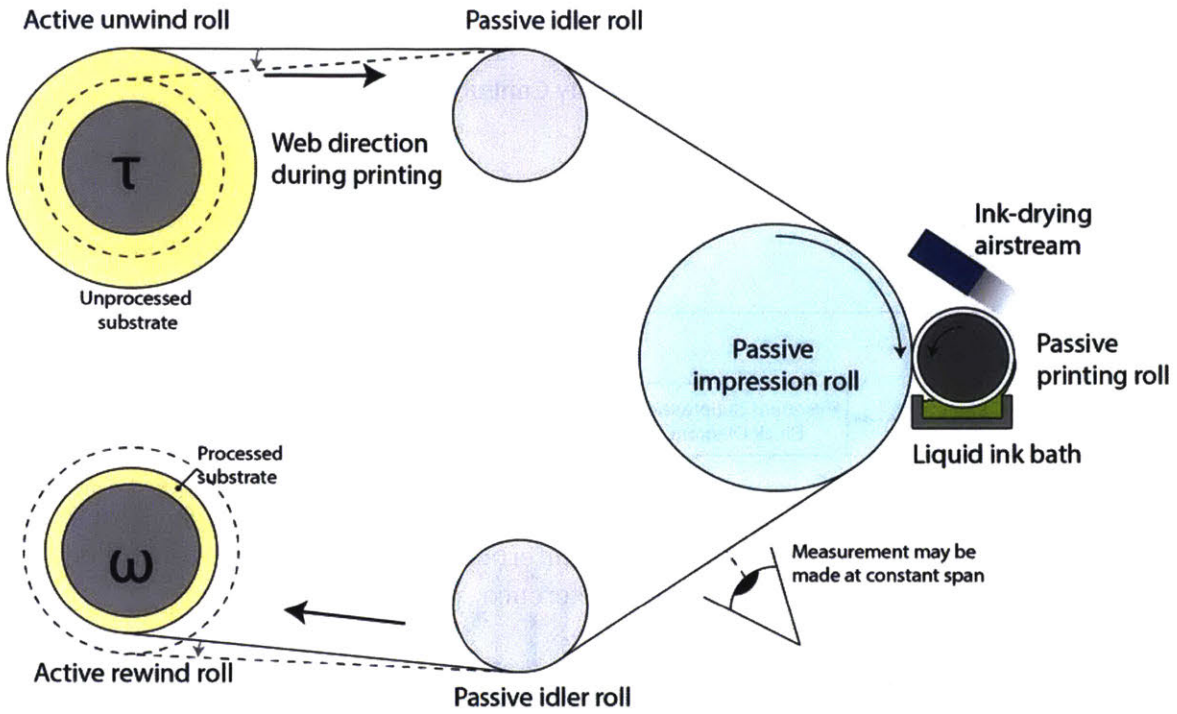

Figure 2-6: *Schematic of the experimental printing machine web handling system.* An active unwind roll acts as a torque brake against an active rewind roll, which acts as a speed source. Two passive idler rolls measure tension and create a constant span suitable for measurement. As the web is processed, the diameter of the unwind and rewind rolls changes (indicated by dotted line), changing the angle of the web span.

SVA-2040 servo driver controls each motor. Using the proprietary SureServo software, these rollers were programmed over USB to operate either in torque mode or velocity mode.

During printing, it is ideal for one motor to serve as a torque source and for one to serve as a velocity source. The torque source is driven backwards and serves as a brake, maintaining the desired tension in the web. The velocity source is driven forward, overwhelming and backdriving the torque brake, and maintains the desired speed of the web. If both motors are driven as velocity sources, the torque is not directly controlled and could potentially increase to the point of web breakage. If both motors are driven as torque sources, likewise, the speed is not directly controlled and may increase beyond desirable limits to the motor's allowed maximum.

The SureServo controller is designed to meet web handling applications, in which this combined torque-velocity combination is frequency encountered, and may be

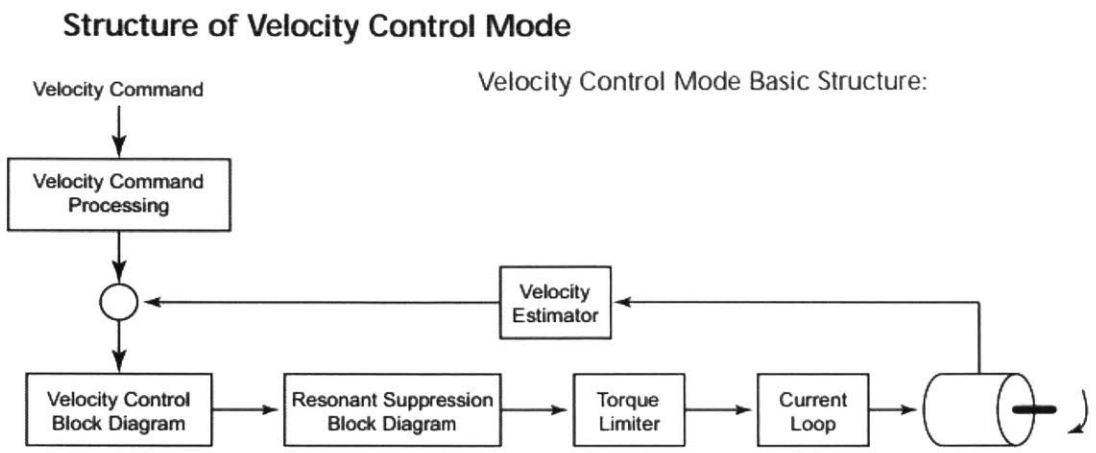

Figure 2-7: *Block diagram showing operation of SureServo velocity control mode.* Velocity is controlled by a feedback loop internal to the SureServo controller unit that receives an external command as a reference. [11]

programmed to control the servo in either torque mode or velocity mode. In velocity control mode, an internal estimator in the SureServo controller performs closed-loop feedback control on the motor current in order to match a velocity command given by an analog voltage input. This mode offers some limited control over the system response via user-set parameters that affect the velocity control and that can apply filters to, for example, suppress resonances present in the physical system. For the scope of this work, these features were left as default. A block diagram of the velocity control mode operation is replicated in 2-7.

The torque control mode likewise uses an internal feedback loop to maintain the torque output to the commanded setpoint, which also is set using an analog voltage input. The torque control mode is notably simpler and offers no method for user modification of the control loop behavior, but does also offer filtering features again for physical resonance suppression. A block diagram showing the torque control mode operation is replicated in 2-8.

During the course of this project, it was found that it was important to the printing process (1) to establish sensing and improve accuracy of the web tension and speed during printing, and (2) to be able to control these aspects in both "printing" and "anti-printing" directions of web travel. To achieve this functionality, the SureServo

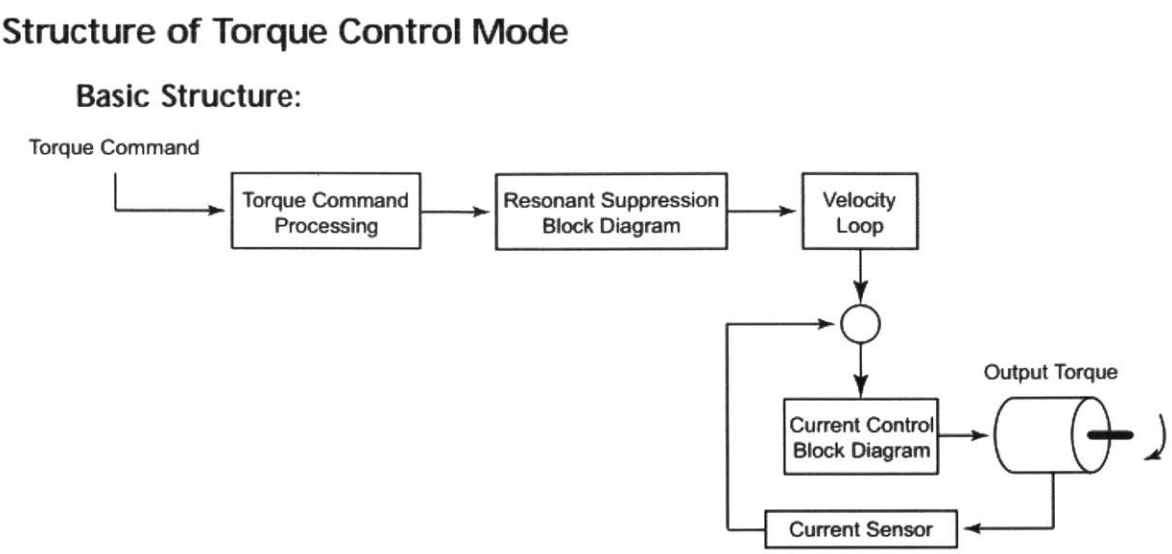

Figure 2-8: *Block diagram showing operation of SureServo torque control mode.* Torque is also indirectly controlled by an internal feedback loop in the SureServo control unit. [11]

controllers were programmed into Dual torque-velocity mode. In this mode, a digital signal would determine whether the SureServo controller operated in torque or velocity mode, and could be changed on the fly.

By interfacing this feature with a LabVIEW program, the web could be commanded into any combination of direction, torque, and speed, and"inverse" mounting of the web, which required a signal to be inverted, could be accommodated for specific experiments. Speed and torque references were set using two analog voltage commands which were sent to the appropriate controller depending on configuration. A reproduction of the user interface showing these options is given in 2-9.

2.3.1 Sensing Tension

One important measurement to make while studying the dynamics of the moving web is the tension maintained in the web. In industry, this is conventionally done by instrumenting idler rolls as close to the process being studied as possible, as changes in tension are affected by dynamics such as rotational inertia of the rollers and elastic tension of the web.

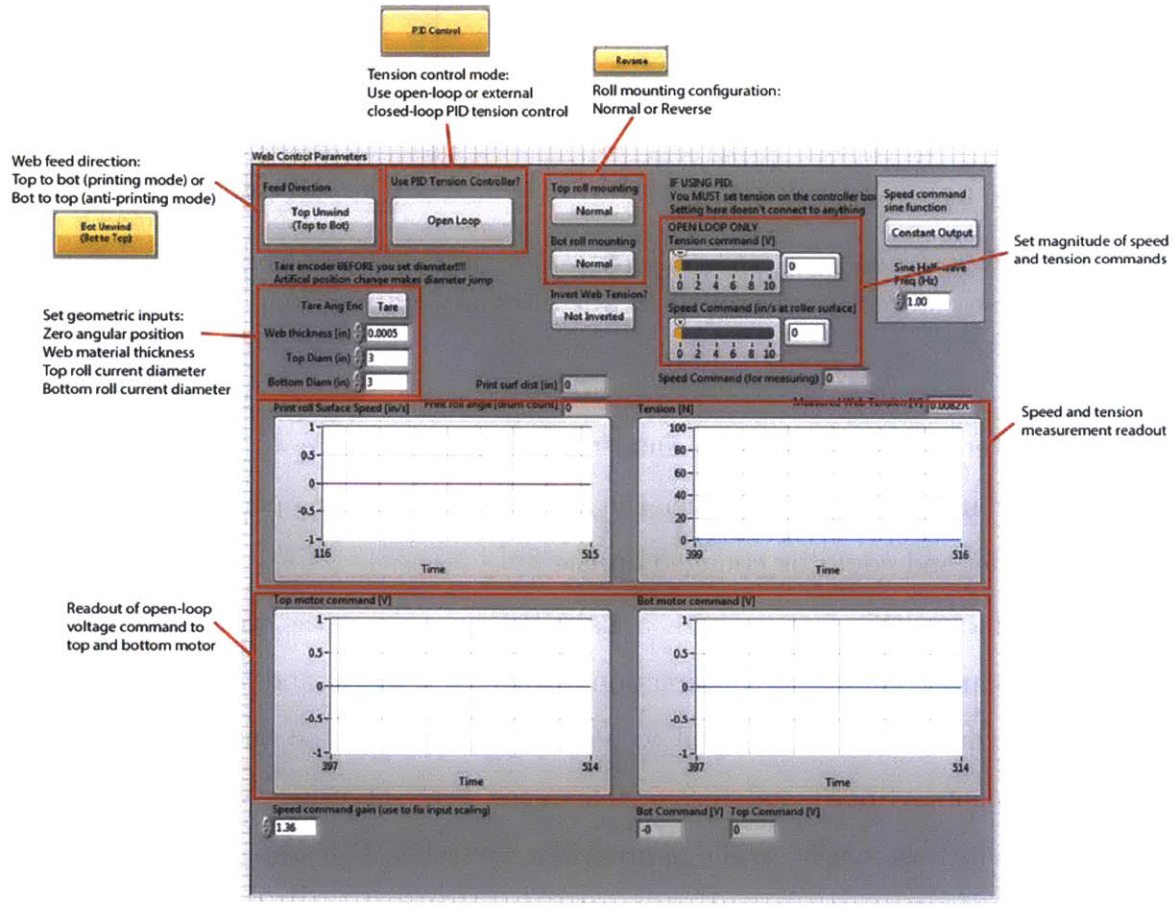

Figure 2-9: *Custom printing software user interface.* Settings, inputs, and outputs are indicated in the diagram.

When measurement and closed-loop control of the web tension became desirable for complementary experiments, tension-sensing rolls were installed. These rolls operate under the principle that a web in tension will apply a radial load to a cantilevered roll, causing a moment to be transferred to its fixed base. This moment can be measured by mounting the roll on a load cell or other force transducer. FMS RMGZ900 force-measuring idler rollers operating on this principle were obtained from our collaborators and were installed on the experimental equipment.

These rollers interface with the FMS CMGZ309 Digital Tension Controller unit. This unit is capable of accepting input from one tension-sensing roll; two tension-sensing rolls were installed, and a physical switch was spliced in to select either the upper or lower idler roller as the measurement source. For proper measurement, after using the switch to change measurement target, the "Calibration" routine on the CMGZ309 controller must be run to set the proper zero-load offset.

The CMGZ309 unit also internally computes a feedback-controlled tension command that it outputs as an analog voltage. The controller parameters may be set by the user on the front panel of the unit; when configured for the speed-torque setup utilized here, the derivative component of the PID control is disabled. [42]

This tension command must be sent to whichever motor is in torque control, and whether it must be inverted or not depends on the particular configuration of the substrate rolls and the printing direction. Thus, the output voltage from the CMGZ309 controller must be passed through the master LabVIEW program, which is responsible for conditioning the output command and assigning it to the proper drive roll. The user may then select whether this feedback signal or an open-loop signal generated by LabVIEW software should be sent out to whichever motor is currently in torque mode. A schematic of the entire system showing the path these signals take is shown in 2-10, and the user interface selections to set up the proper configuration are shown in 2-9.

It should be noted that empirically, it has been observed that different sets of controller parameters are optimal for different web feed configurations. It is believed that this is due to mechanical asymmetries between the printing (top to bottom)

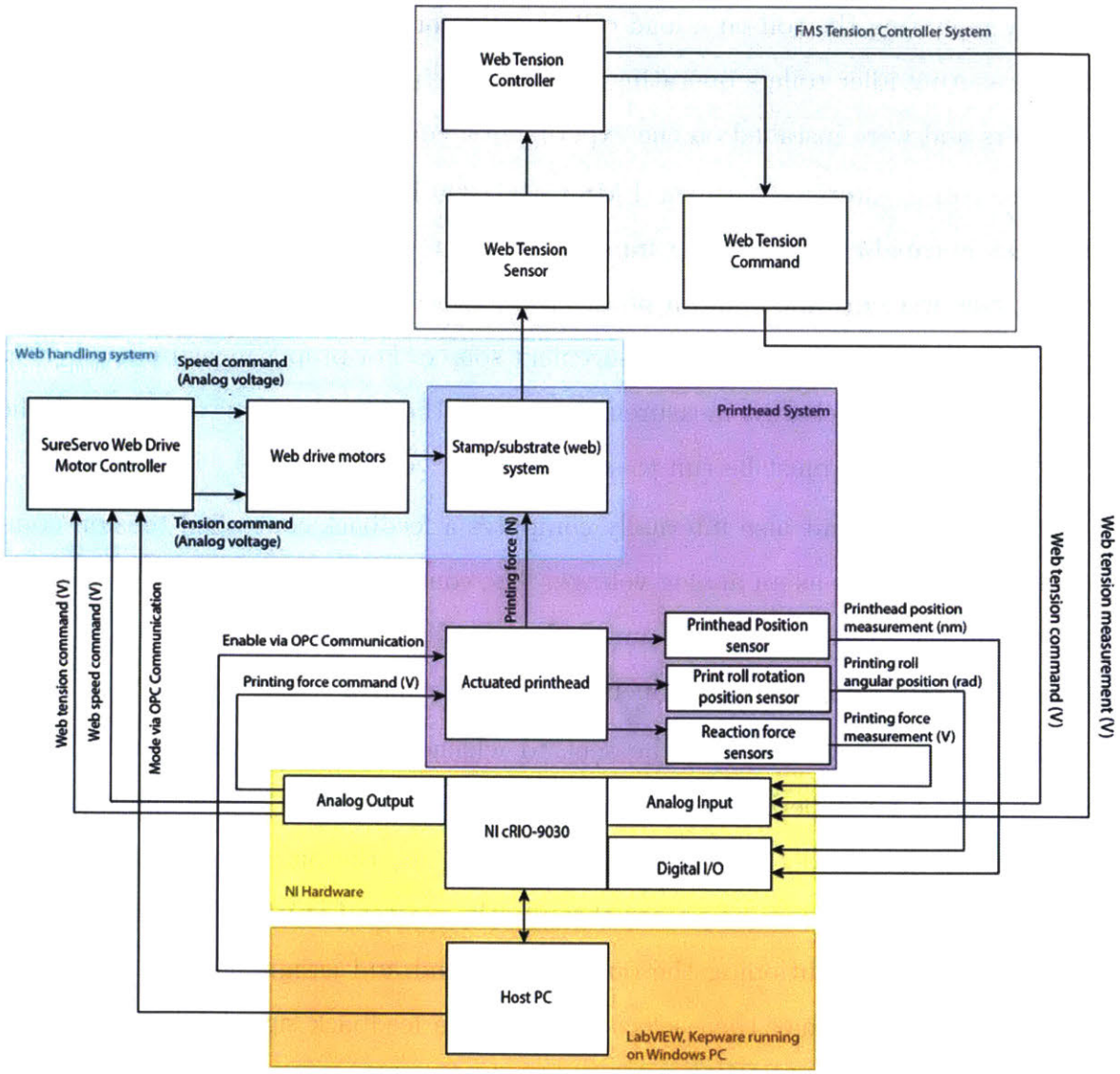

Figure 2-10: *Complete diagram of experimental printing system signal flow.* Colors indicate individual subsystems.

and anti-printing (bottom to top) web feed directions, as well as physical differences between the two tension measurement rolls. Care should be taken to re-tune this controller for specific experimental conditions if its performance is critical.

2.3.2 Measuring Speed

Another parameter of interest when studying web dynamics is the web velocity. This is also important to the printing process, both as a measure of output capacity, but also as a factor that can influence the printing quality.

Originally, web speed was measured using an optical encoder disk mounted to a passive idler roller, which was read by a stationary readhead mounted to the dead shaft protruding from the idler [10]. This method was incompatible with the tension sensing roller, however, as the tension sensing idlers do not have a dead shaft, and the instrumentation located at the base of the cantilevered roller makes adding a rotation encoder difficult.

To restore the capability of measuring web speed during printing, a magnetic ring encoder was installed on the print roll. Under no-slip conditions, the angular measurement of the encoder is directly proportional to the surface travel of the web. It also has the added benefit of providing a direct (rather than indirect), high-resolution measurement of stamp angular position.

The encoder is a magnetic ring encoder manufactured by RLS, model MR075E-060-A-048-B-00. It is 75mm in diameter and has 48 magnetic poles around its circumference. When paired with the RLS LM15-IB-1D0-C-B-10-A-00 readhead, each pole can be interpolated to 1000 points at a clock speed of 1 MHz, giving an encoder resolution of 48,000 counts per revolution. For a typical stamp with an approximately 52 mm outer diameter, that means surface position can be measured to 3.4 μm and maximum speed is approximately 686 mm/s, or 27 in/s. This maximum speed could be increased by up to fifteen times by replacing the readhead with the LM15-IB-1D0-K-B-10-A-00 variant, which has a 15 MHz clock speed.

In order to mount and unmount stamps, the roll must be removed from the printhead assembly, and a collar with a 50mm internal diameter must be able to slip over

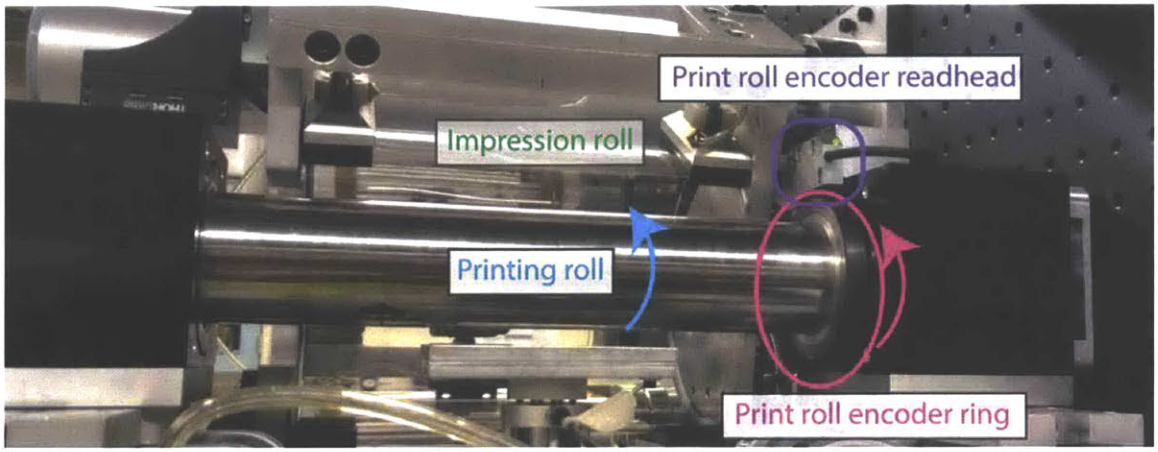

Figure 2-11: *Print roll encoder, installed on machine.* The print roll rotation encoder is indicated in the pink circle, matching the rotation of the print roll. The encoder readhead is visible immediately above the ring, indicated in the purple oval. The encoder readhead detects the magnetic field entering the area where the pink and purple indicators intersect.

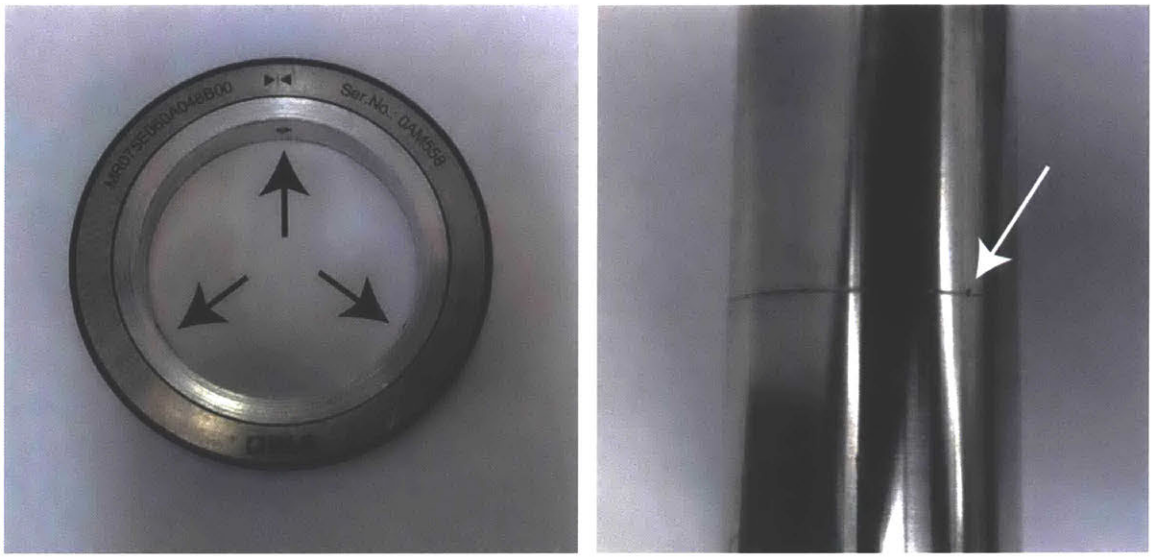

(a) Magnetic encoder mounted on adapter. (b) Groove and conical detent on print roll.

Figure 2-12: *Rotational encoder ring/print roll interface.* The removable encoder ring (a) uses three spring-loaded ball contacts (indicated by arrows) to sit in a groove on the print roll (b). To prevent slippage during printing, one of the ball contacts also sits in a conical pocket (indicated by arrow) on the groove.

either end. (This collar is attached to a pressurized air source, and inflates a cushion of air between the PDMS stamp and the roll in order to slide it on or off the printing roll. [9])

To avoid an extensive redesign of the printhead and stamp mounting procedure, the encoder ring was designed to work around this need. The encoder ring is mounted on an aluminum adapter. This adapter has three spring-loaded ball contacts inset into it. These ball contacts fall into a groove that, when the printhead is reassembled, is located directly under the LM15 readhead. A single conical pocket located on the groove serves to catch one of the three ball contacts and prevent circumferential slippage during printing. Any of the three ball contacts may be located into this pocket because the encoder is only used incrementally. This groove-ball contact system allows the encoder ring to removed easily and without tools from the roll during disassembly, and easily replaced within tolerance to the proper location under the readhead.

The print roll surface velocity measurement is merely used as a readout, though it could be used for closed-loop control of the web speed. The system already has the capability to send an arbitrary speed profile out to the motor in velocity mode, so implementing the control law in the LabVIEW master VI would be the only necessary step. However, due to nontrivial dynamics of the web, rollers, and motors, modeling the web system and developing a suitable control law was outside the scope of this work and was a task undertaken by collaborators.

2.3.3 Known Issues

Through empirical experience with the web handling system, a number of performance issues that will impact future users of the system came to light. The observed behavior of these issues and, where possible, recommendations for improvement are detailed here.

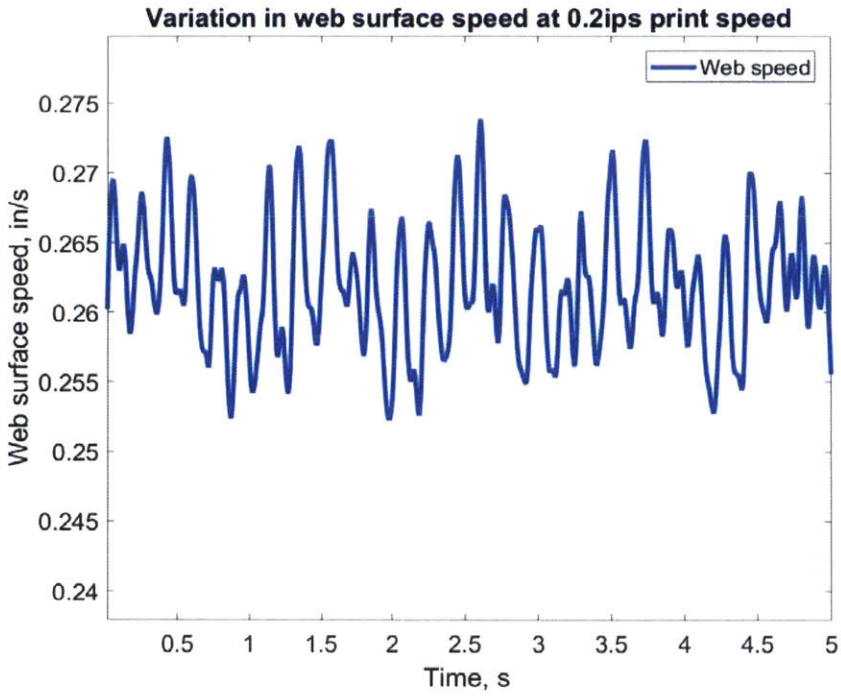

Figure 2-13: *Experimental data showing web handling motor "cogging" behavior at 0.2in/ss printing speed.* At a low printing speed of 0.2in/s, the "cogging" effect is visibly perceptible, and excursions from the mean speed are on the order of 5%. Note that a 0.2in/s print speed is commanded, but a scalar offset is present that makes the otuput mean speed approximately 0.26ips. This scalar is constant for a given roll mounting and printing direction, but varies between configurations.

Cogging

At low speeds ($\leq$ 0.5 in/s), both motors will display "cogging" behavior; that is, instead of turning smoothly and continuously, the motor will turn in short discrete steps, like the second hand of a clock ticking. This behavior becomes less noticeable as the speed increases, and is not visibly observable for speeds greater than about 1 in/s. Figures 2-13, 2-14, and 2-15 show web speed profiles at 0.2, 1.0, and 4.0 in/s printing speed commands.

It is hypothesized that this problem results from a combination of the properties of a brushless AC motor and the control capabilities of the SureServo controller; that is, it appears that the SureServo controller is not optimized for smooth performance of brushless AC motors at very low speeds. The original design specification for this web handling system was a top speed of 1m/s (approximately 40 in/s). The motors

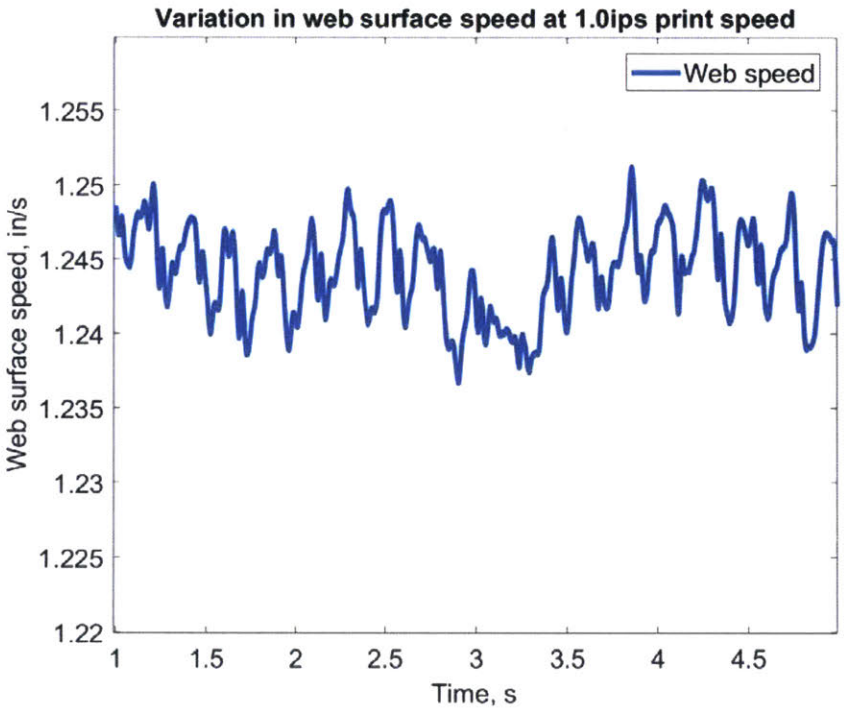

Figure 2-14: *Experimental data showing web handling motor "cogging" behavior at 1in/s printing speed.* At 1 in/s printing speed, cogging is less apparent. Though the magnitude of the cogging is approximately constant, it is now only about 1% of the average web speed. Note that the timescale is compressed by 1s in this plot as compared to 2-13, but the vertical axis is approximately the same scale.

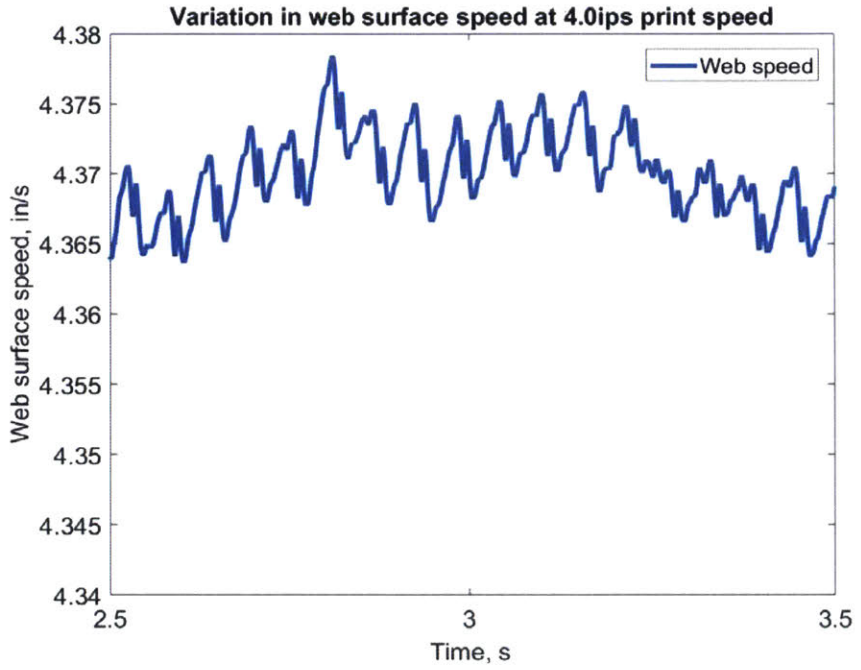

Figure 2-15: *Experimental data showing web handling motor "cogging" behavior at 4ips printing speed.* The cogging effect's approximately 0.01in/s magnitude is now <1% of the mean printing speed. Note again that only 1s of data is displayed here, for clarity, but the vertical axis scaling is comparable to 2-13 and 2-14.

themselves have a maximum continuous speed of 3000 rpm, which corresponds to a web surface speed of over 450 in/s. The cogging behavior is most observable when operating in the bottom 0.1% of the motor's service range. [12]

If smooth and accurate motion at low speeds is experimentally critical, it is recommended that industrial combinations of motors and motor controllers optimized for low web speeds be substituted for the SVL-204 motors and SureServo SVA-2040 controllers.

Control of web speed

Though the web handling motor's velocity is closed-loop controlled, the web feed speed is open-loop. The user enters a speed command, which is scaled by a fixed factor and inverted as necessary in the LabVIEW software to match the web feed configuration. It is then sent as a reference to the motor's velocity controller.

The actual surface speed of the web as measured by the print roll encoder differs from the command by a scaling factor dependent on the web configuration (roll mounting and print direction), magnitude of the web speed command, and the web tension command. (2-13, 2-14, and 2-15 above show a mean speed differing from their commanded setpoint.)

Also, the surface speed of the web will change as the printed material is spooled out from a full to empty roll; for a constant angular velocity command to the web handling motor, the actual surface speed of the web varies according to

$$v_{surf}(t) = \pi D(t)\omega(t), \tag{2.1}$$

where $D(t)$ represents the instantaneous diameter of the rewind roll at time t, and $\omega(t)$ is the angular velocity in units of revolutions at time t. As the web is processed and transferred from the unwind roll to the rewind roll, $D(t)$ changes, and the $\omega(t)$ reference command must also be adjusted to keep $v_{surf}(t)$ constant.

In summary, if accurate control of web speed is necessary, direct closed-loop feedback control of web speed should be implemented. No hardware modifications are

necessary to accomplish this, but a study of the dynamics of the web system and the digital implementation of a suitable control law in the LabVIEW master VI would be required.

Control of web tension

Web tension may be controlled via an open-loop command, or by the FMS CMGZ309 web tension controller. To manually specify an open-loop command, the user interface shown in 2-9 shold be set to "Open Loop." Again, here, the reference command should be scaled by a gain to achieve the desired effect in the physical system, but this factor is dependent on the web feed direction, commanded speed, and commanded tension. Like speed, the conversion between the torque command on the torque control mode motor to the actual tension felt by the web is dependent on the diameter; that is,

$$T_{surf}(t) = \tau(t)r(t) \tag{2.2}$$

where the tension force $T_{surf}(t)$ experienced by the web depends on the instantaneous radius of the unwind roll $r(t)$ and the torque command $\tau(t)$; to keep $T_{surf}(t)$ constant during printing, $\tau(t)$ must be adjusted to account for changes in $r(t)$. These problems make a strong case for implementing closed-loop tension control.

Closed-loop control may be enabled by setting the user interface shown in 2-9 to "Closed Loop." This changes the reference signal from an open-loop voltage generated by the LabVIEW master VI to a voltage signal generated internally by the FMS CMGZ309 controller, using PID. This controller can only generate a positive output voltage, which corresponds to only one direction of torque. To change direction, the polarity must be inverted either physically or through external software. Thus, to close the feedback loop, this reference signal is fed through the LabVIEW master VI and may be recorded and inverted as necessary to match the web configuration; the path of the signal is shown in 2-10.

When set to control an active brake acting as the tension source, the CMGZ309 controller only allows for PI control, and disables derivative control. It can store two

different sets of PI parameters, which must be selected using the CMGZ309 interface. These parameters must be determined by the user by following a standard tuning procedure outlined in the instruction manual [42].

Unfortunately, after extensive empirical tuning, it was found that the CMGZ309's internal control could not follow a constant tension reference with good performance, especially at low speeds when the aforementioned cogging effect was observed. The cogging effect tended to induce oscillation in the tension, which is not unexpected considering the complex dynamics of the web system. It is also possible to induce oscillation if the reference is passed through too slowly compared to the closed-loop dynamics of the web-tension controller system; at the time of this writing the reference is passed through at a rate of 1 kHz. Additionally, the dynamics of the web system were observed to be influenced by printing direction, magnitude of speed reference, and magnitude of tension reference, which made no single set of PI parameters ideal.

If precise web tension is critical to future work on this system, it is recommended that the CMGZ309 not be used to generate a control signal. Instead, study of the web dynamics could be undertaken to generate an appropriate control law, and this law can be implemented digitally in the LabVIEW master VI with no hardware changes necessary.

Ideal operating regime

One final known issue observed with the system is the fact that it is possible to stray outside an ideal operating regime. When the system is operated in torque-speed mode, the ideal situation is that the motor acting as a speed source can exert infinite torque to maintain speed regardless of load; and that the motor operating as a torque brake can maintain the commanded torque at any speed.

However, no motor is capable of infinite torque or infinite speed, so it is possible when operating at the edges of the motor's capabilities to violate these assumptions. The consequence is that the speed and torque sources can no longer be considered ideal and independent, and now are a function of the magnitude of the other's command. From the datasheet for the SVL-204 motor, referenced in 2-16, the ideal operating

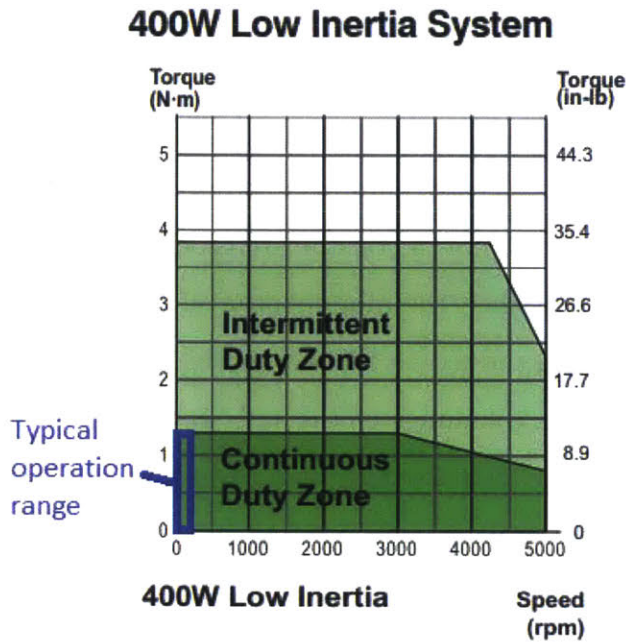

Figure 2-16: *Torque-speed curve for the SureServo SVL-204 motor.* Typical experimental printing speeds fall below 1% of the motor's velocity capability, but printing torques up to the continuous duty limit of 1.4Nm are commonly used. [12]

regime should occur for speed commands less than 3000 rpm (approximately 450 in/s surface speed at minimum rewind diameter) and torque commands less than 1.4 Nm (approximately 20 lb of tension at minimum unwind diameter).

It is recommended for any experiments with web dynamics that an analysis be undertaken to ensure that, if the motors are to be treated as ideal sources, they are sufficiently within this operating regime.

2.4 Printhead-Impression Assembly

The second major component in the microcontact printing machine, after the web handling system, is the printhead-impression assembly. As the web is passed through this assembly, the stamp dips into a bath of liquid ink; the liquid ink is dried by evaporating the volatile solvent; and the remaining dry chemical ink is used to pattern the substrate. A schematic and photograph of the complete printhead-impression assembly is shown in 2-17.

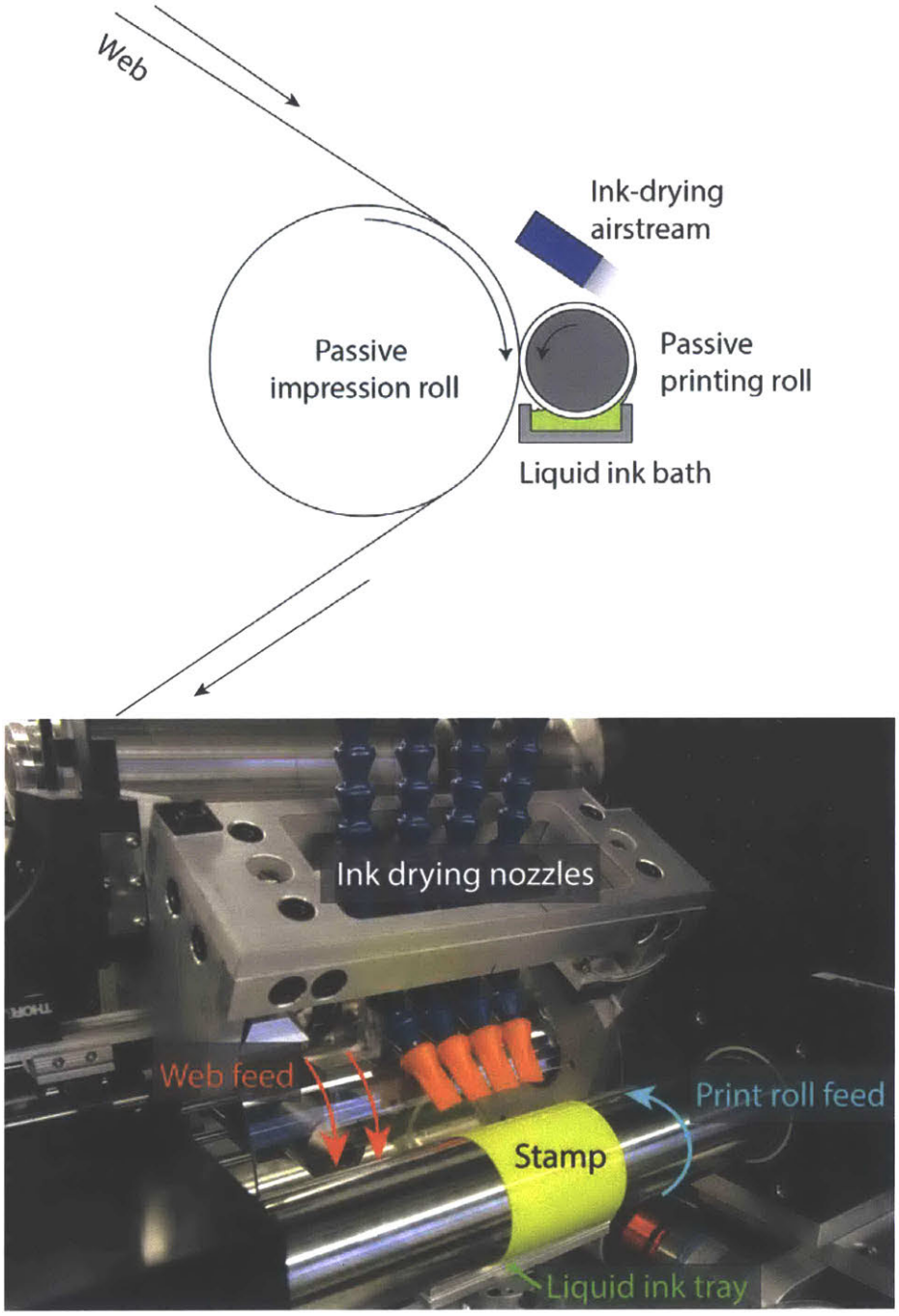

Figure 2-17: *Schematic and close-up view of the printhead-impression assembly.* (Top) In this schematic view, the web feeds from top left to bottom left. (Bottom) A yellow dyed stamp is currently mounted on the printing roll. The blue and orange nozzles direct the ink-drying airstream onto the stamp. The substrate feeds downward as the print roll rotates upward.

2.4.1 Impression Cylinder

Mechanical Design

The impression cylinder consists of a glass cylinder with a diameter of 6 in, which accommodates a web width of 5in. It is supported radially at three points on New Way curved air bearings, in a 30mm x 60mm concave L-profile shape, with a 3in radius curve; and axially on New Way 40mm diameter flat round puck-style air bearings. These air bearings have a porous media surface that creates a uniform, high-pressure, low-friction cushion of air between the bearing and and an immediate surface. Each air bearing is mounted on a ball-headed joint to allow it to self-center when airflow is enabled. [10]

A typical airgap between the radial bearings and the impression cylinder is 3 to 5 μm. [43] This means that the impression cylinder must be subject to very little runout in order to avoid closing the air gap and contacting the bearing surfaces.

Design for Contact Imaging

Additionally, the impression cylinder was designed to be transparent in order to allow for optical inspection of the contact regime by aiming a camera through the cylinder. However, the 6in diameter of the cylinder forces a minimum standoff distance of 6in between any camera and the contact area; because of the tradeoffs between resolution and area incurred by this standoff, the desired combination of wide-area and high-resolution imagery could not be obtained. [28]

Subsequent efforts to reduce the standoff were undertaken by utilizing a hollow extruded quartz cylinder with a 6in diameter and a 3mm wall thickness instead of the solid glass impression roll. A camera could then be inserted inside the hollow roll, reducing the standoff distance to 3mm, and greatly mitigating the problem. Unfortunately, the hollow glass cylinder exhibited runout on the order of 600μm and thus was not within the 10μm diameter tolerance necessitated by the air bearings; during printing this caused a tendency for the hollow roll to spontaneously jam in the radial bearings and shatter. At the time of this writing the solid roll is being used for

on-machine printing. A non-precision, passive, off-machine duplicate of the hollow roll-camera system was constructed by Peter Ascoli in order to reestablish contact area imaging capability. [22]

Web Handling Dynamics

The glass impression roll is driven passively by the friction of the tensioned web running over its surface. The low friction of the air bearing constraints enable a no-slip condition to persist throughout printing. However, because the solid glass impression roll has a large mass, it is a significant rotational inertial in the web dynamic system.

2.4.2 Continuous Inking

The continuous inking system was developed by Chris Merian. [13] The ink is sourced from a shallow tray mounted on a pneumatic solenoid valve that may be lowered or raised. When raised into position, the stamp dips into the ink tray and is coated with liquid. Typical stamp thickness is 1mm, so the maximum depth that the stamp may be submerged before the tray contacts the printing roll is also 1mm. Because the current ink tray is constrained to fit in an approximately 1in wide by 4in long area, only a 1mm deep by 1in wide by 4in long volume of ink is available to the stamp during printing. Without replenishment, this volume is quickly consumed, limiting maximum autonomous printing duration. Future work could extend this duration by increasing the volume of ink available to the stamp, or by creating a means of automatically controlling and replenishing the level of ink in the tray. The diagram in 2-18 shows the design of the ink tray.

The ethanol solvent carrying the thiol ink is then evaporated off the stamp using jets of clean, dry air as the stamp rolls toward the substrate. By the time the stamp contacts the substrate, there should be no liquid ethanol present. The recommended dryer nozzle volumetric flow rate for a particular web feed speed is given in Chris Merian's thesis document [13].

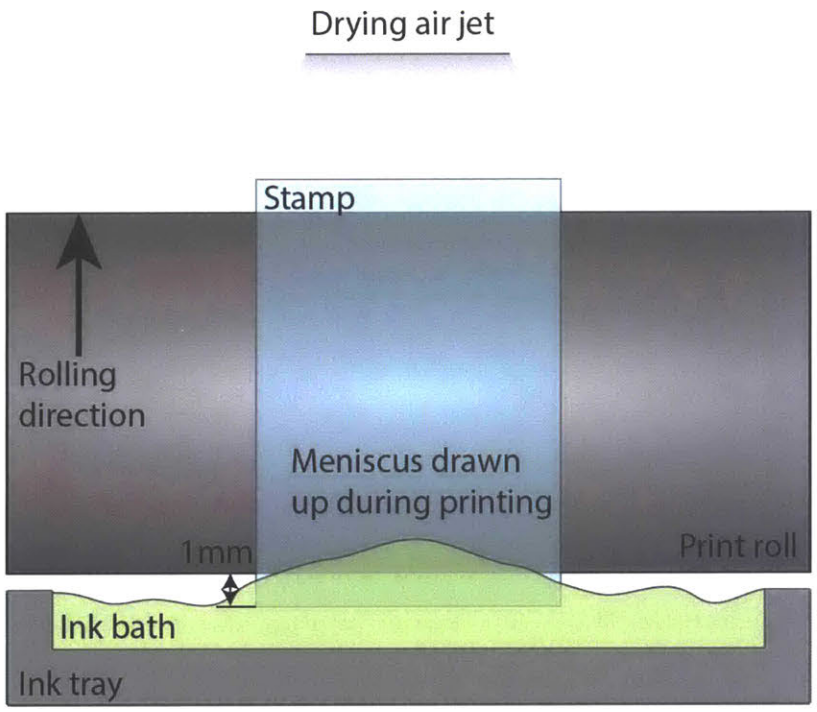

Figure 2-18: *A schematic of the continuous inking bath.* As the stamp rolls through the liquid ink bath, a meniscus of wet ink is drawn up. A drying air jet evaporates the ink solvent. The maximum that the stamp may submerge before the tray impacts the print roll is the stamp thickness, nominally 1mm.

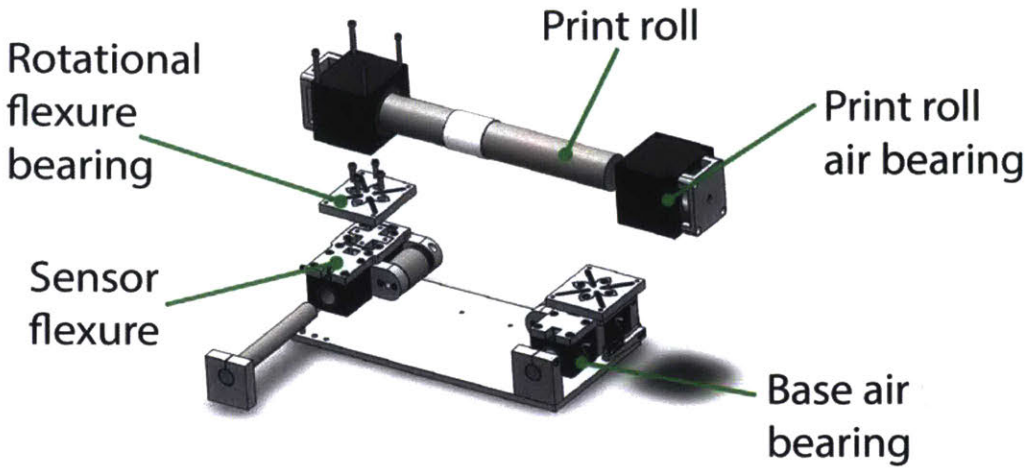

Figure 2-19: *Exploded view of the printhead assembly.* Major components of the printhead assembly are labeled.

2.4.3 Precision Actuated Printhead

The final major component of the microcontact printing system is the precision actuated printhead, originally constructed by Adam Libert [10]. The printhead consists of a solid 2in diameter print roll supported in New Way Air Bearings 2in air bushings on either end, with a 50mm diameter round New Way air bearing as a thrust constraint on either end. This assembly is mounted onto a pair of rotational flexure bearings set atop 1in diameter New Way air bushings that allow for in-plane rotation of the print roll. Labeled components of the print roll are shown in 2-19.

This print roll is capable of moving in two degrees of freedom in-plane, so that it can achieve arbitrary axis-to-axis distances from the impression roll, as well as arbitrary axis-to-axis angles. Two H2W voice coil actuators, one located on each base air bearing, control this motion. As will be discussed in the next chapter, this in-plane motion gives the print roll the ability to absorb major errors in stamp mounting and stamp and impression roll diametric runout, and to control the force or displacement applied to the stamp during printing.

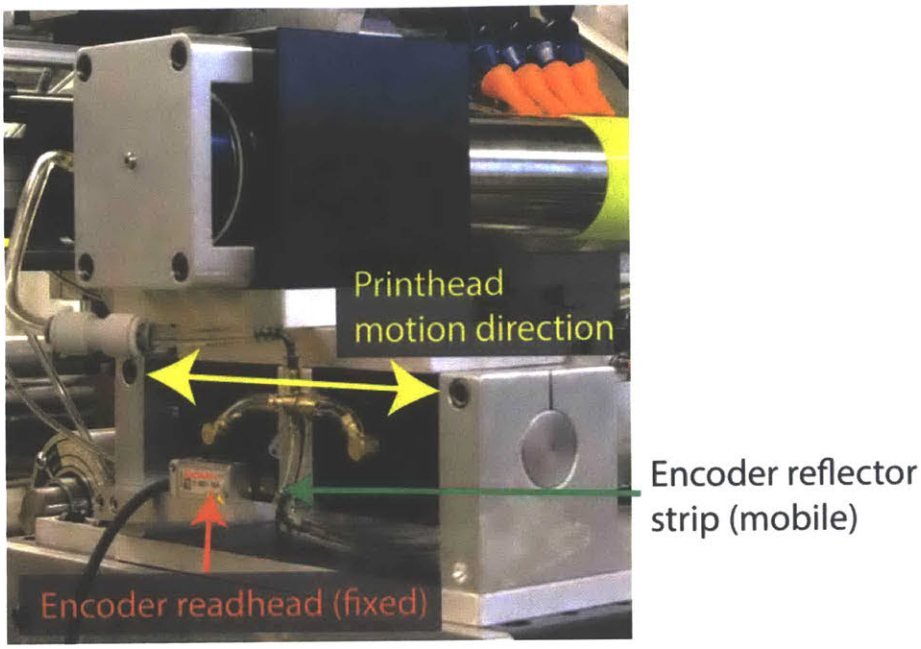

Figure 2-20: *Location of Renishaw linear encoders on the printhead.* The readhead is fixed to the baseplate on a cantilevered mount, and the reflector strip is mounted to the mobile base air bearing.

Linear Encoder Sensors

The precision actuated printhead is also fitted with two Renishaw linear encoders with 20nm resolution. These encoders are located on the base air bearing and measure relative displacement between the base air bearing and the fixed printhead platform.

The encoders require a 5V power supply, and output a standard A/B/Z encoder signal. Both encoder signals are routed through a breakout board and into a National Instruments digital I/O cable, which then connects to a National Instruments digital I/O C-series module. The data from this module is then input into LabVIEW, where the encoder pulses are counted at 40MHz to determine position. The clock rate of the encoders is 10MHz, which establishes the minimum counting rate to avoid missing pulses.

2.4.4 Reaction Force Sensors

The printhead is also equipped with with two reaction force sensors. These sensors were retrofit the existing printhead geometry after it was determined that a force

measurement needed to be undertaken. The design, fabrication, and verification of these sensors are an original contribution of this work.

The principle of operation of the sensors is a full-bridge silicon strain gauge mounted on a flexural bearing. These two sensors are then directly in the load path from the voice coils through the stamp to structural ground, and measure the exact force transmitted through the stamp in static conditions (and a sufficiently close approximation in dynamic conditions). This bearing was designed to be an order of magnitude stiffer than the stiffest theoretical stamp in order to appear rigid in the scope of stamp dynamics, but still allow for measurable strain to occur under typical printing forces (2 - 6N).

Flexural bearing design

The chief challenges in selecting the flexure design were: to fit into the existing geometry without major modifications of the printhead assembly; to be insensitive to forces not in the printing direction; and to avoid contributing dynamics to the printing system in the desired printing bandwidth of up to 100Hz.

To meet these needs, a flat plate with two pairs of parallel blade flexures was chosen. The printhead assembly would mount to a center platform, and reaction forces from the printing process would be transmitted through the flexural blades, causing deformation and strain. The strain could then be measured using an off-the-shelf strain gauge, and an empirical force-strain curve established to calibrate the sensor.

The final design is shown in 2-21.

To establish the desired stiffness of the flexures, the first task was to estimate the stiffness range of the stamp.

Per Petrzelka [9], a featured polymer stamp may be modeled as an elastic bilayer consisting of a soft "feature" layer on top, and a stiff bulk "backing" layer behind it. In this model, a "stiff" stamp arises when the features are small compared to the overall stamp, and the backing layer dominates; and a "soft" stamp arises when the fatures are large compared to the overall stamp, and dominate.

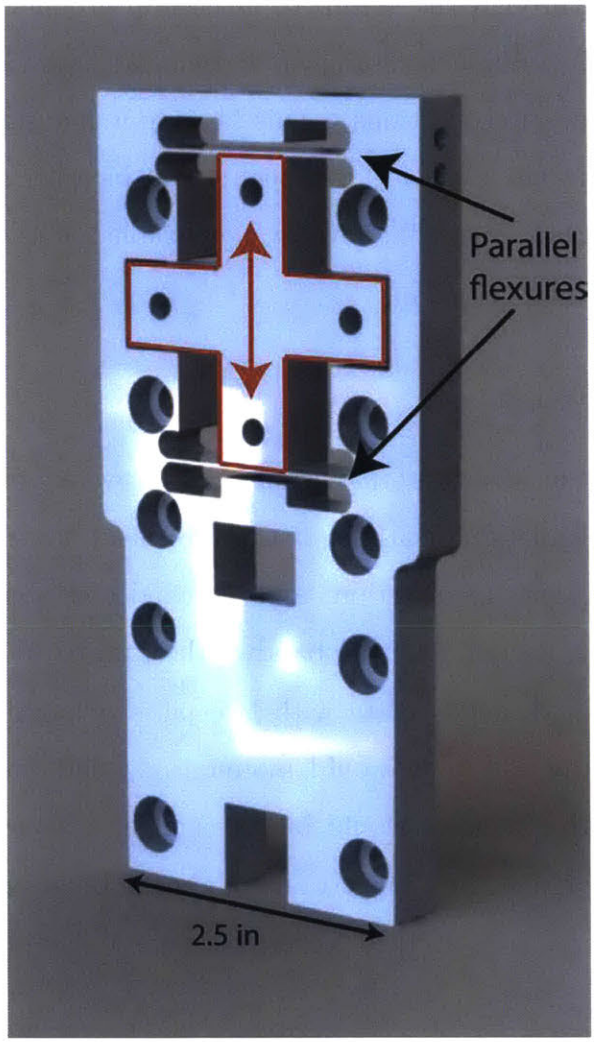

Figure 2-21: *Flexural sensor final design.* The cross-shaped platform (red outline) moves under printing forces (red arrow). The sensor is constructed out of 6061-T6 aluminum.

Petrzelka establishes the bulk deformation of an elastic cylinder pressing against a rigid plane as

$$f = \int_{-l}^{l} p(x)dx = \frac{32\sqrt{6}}{6}\frac{\delta^{5/2}r^{*3/2}}{t^3}E_0, \tag{2.3}$$

where $r*$ is the equivalent mapped radius of a cylinder pressing against a flat plane, derived from two cylinders in contact:

$$r^* = \frac{r_1 r_2}{r_1 + r_2} \tag{2.4}$$

Thus, the nonlinear force-displacement curve for the stiffest possible stamp would be given by

$$f = \left(\frac{32\sqrt{6}}{6}\frac{r^{*3/2}}{t^3}E_0\right)\delta^{5/2} = (K_{bulk})\delta^{5/2}, \tag{2.5}$$

where K_{bulk} will be a stiffness per length determined by the material properties and geometry of the thick stamp.

On the other hand, the softest possible stamp, in which the features dominate the stamp, is derived by Petrzelka as

$$f = \frac{4}{3}k\sqrt{2r^*}\delta^{3/2}, \tag{2.6}$$

where k represents sheet stiffness in units of Pa/ m:

$$k = \frac{E_0(a+w)}{ha}K. \tag{2.7}$$

K is a geometric factor that depends on the dimensionless quantities Petrzelka terms feature aspect ratio $A = h/a$ and pattern ratio $P = w/a$, where h is the feature

height, w the feature width, and a the interfeature spacing. K is then expressed as

$$K = \frac{1}{K_I^{-1} + K_{II}^{-1}} \frac{(A+P)+0.6}{(A+P)}, \tag{2.8}$$

$$K_I = \frac{2\pi}{3} \frac{AP}{(P+1)^2} \left[-\log\cos\left(\frac{\pi}{2} \frac{P}{P+1} \right) \right]^{-1} \tag{2.9}$$

$$K_{II} = \frac{4}{3} \frac{P}{(P+1)^2} \tag{2.10}$$

Similarly to the above expression, we can then write

$$f = \left(\frac{4}{3} k \sqrt{2r^*} \right) \delta^{3/2} = (K_{feature}) \delta^{3/2}, \tag{2.11}$$

where similarly $K_{feature}$ is a stiffness per length for the soft, feature-dominated stamp.

A print roll with a 2in diameter and an impression roll with a 6in diameter yield

$$r^* = \frac{50 * 150}{50 + 150} = 37.5\text{mm} \tag{2.12}$$

The stiffness of interest for designing the flexural sensor is the stiffest possible stamp. Within the geometric limitations of the existing hardware, this is a 1mm thick featureless stamp. The curve describing the force-displacement profile for this exact geometry is given as

$$F = (f)(l_{contact}) = (9.5 * 10^7)(E_0)(50mm)(\delta^{5/2}) \approx (3 * 10^{12})(\delta^{5/2}) \tag{2.13}$$

A typical Young's modulus for PDMS is 360-870 kPa [44]; the above equation simplifies using the middle value, 620kPa. (The actual elastic modulus will depend on the particular formulation of PDMS used as well as the exact ratio of the mixing of the two components.)

This nonlinear curve displays cylindrical Hertzian stiffening with large displacements, but the region of small displacements on the order of 10μm is of interest. Linearizing the stiffness in this region, we find the analytically predicted stiffness to be in the range of 0.02N/μmto 0.05N/μm (again, depending on exact material

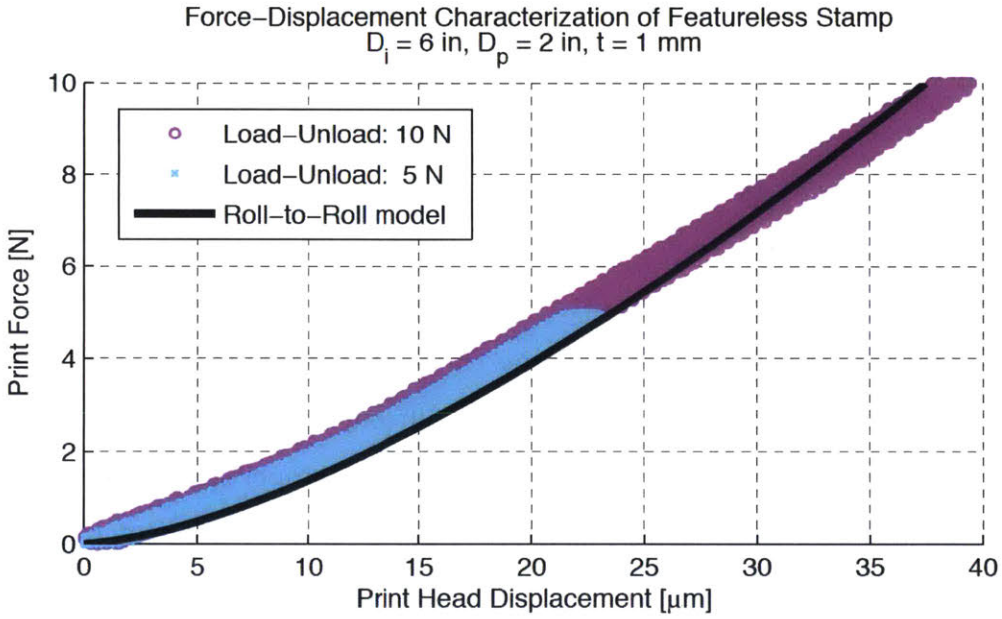

Figure 2-22: *Featureless stamp stiffness curve.* Force-displacement curves for loading and unloading of featureless 1mm thick stamp, as measured empirically by Libert [10]. In this test, the force was ramped up to a maximum and then returned to zero over a 75-second timescale. The black curve indicates the stiffnes curve predicted by Petrzelka's work [9].

properties).

Empirical tests completed by Adam Libert, as shown in 2-22, indicate that the higher range of stiffness is applicable here, with estimated stiffnesses in the 0.05N/μm to 0.1N/μm range for displacements on the order of 5μm.

Thus, for the construction of the flexure sensor, 1N/μm was chosen as a design target for the stiffness in the direction of interest. By iterating on the length of the flexural blades as well as the thickness, a design was reached in which the as-built stiffness, accounting for taper from waterjet kerf, was 0.97N/μm. This stiffnes was computed using finite element analysis to apply combined printing loads and printhead static weight.

At a maximum displacement of about 4μm, the stress state in the flexural blade had a factor of safety of 1.4 over yielding. To prevent excessive displacements resulting from dynamic loads that could trigger yielding, steel spherical hard stops were installed. These hard stops consist of fine thread precision inserts with ball-ended stainless steel set screws. The inserts are threaded and set with permanent adhesive into the body of the flexure structure. The ball contact set screws are then threaded into the inserts and, using precision shims, set to the proper spacing to prevent yeild. The ball contact set screws are then also set with a semi-permanent Loctite thread-locking adhesive.

Another design element of the sensor was consideration of the strain state. As strain would be the variable to be measured, sufficient strain per unit force needed to be generated to be measurable; but, conversely, too much strain would be equivalent to lower stiffness, and would violate the design goal of 1N/μm minimum stiffness. Finite element analysis predicted a range of 20-30$\mu\epsilon$ strain occurring near the fixed base of the flexure during 30N printing loads, as shown in 2-23. This resulted in an expectation for 0.5-1$\mu\epsilon$/N which established the requirement for the sensitivity of the strain gauge.

A strain gauge is an ideal sensor here as a permanent installation to measure strain. The underlying functionality of a strain gauge is derived from the fact that inducing strain in a conductive material changes its geometry, thus changing its conductive

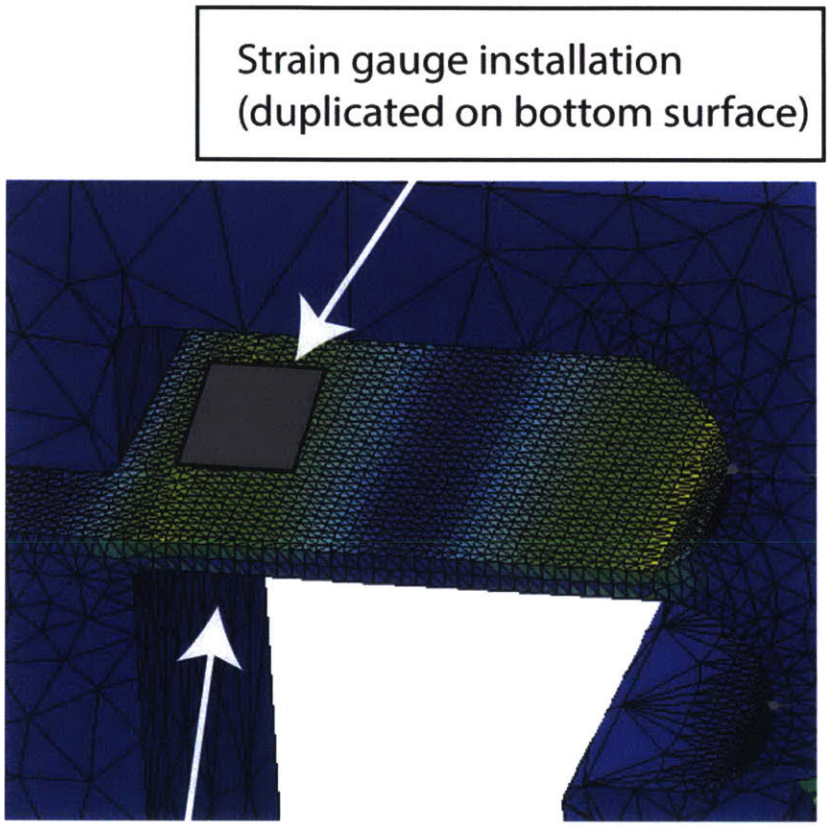

Figure 2-23: *FEA predicting strain state at strain gauge location.* Strain state under a 50N normal force, representing the printhead static weight, and a 30N maximum printing force is 20-30$\mu\epsilon$ where the strain gauge is applied.

cross section, and thus changing its resistance. The design of strain gauges are such that strain along a single axis is amplified, while off-axis strain effects are minimized. [45]

Gauge factor is a measurement of how sensitive the strain gauge is as a sensor [45]. Output voltage is related to strain by the equation

$$\frac{V_O}{V_{EX}} = -(GF)(\epsilon), \tag{2.14}$$

where GF represents the gauge factor, V_{EX} the excitation voltage being passed into the strain gauge, and V_O the output voltage.

A large gauge factor is indicative of high sensitivity, which is desirable, as voltage outputs per microstrain are typically very small and require a large amplification factor. However, large gauge factor also makes the gauge sensitive to unwanted strain, such as thermal expansion.

Typical metal strain gauges have gauge factors on the order of 10, which, at a 10V excitation signal, would produce an unamplified voltage output of

$$V_O = -(10\text{V})(10)(30 * 10^{-6}\text{m/m}) = 0.003\text{V} \tag{2.15}$$

over the entire range of printing, or an unamplified resolution of about 0.1mV/N. A 7-bit resolution on a 1N signal would then yield an unamplified output change of 0.8μV. Trying to amplify and remove noise from such small signals was deemed undesirable.

Instead, a high gauge factor silicon strain gauge was selected. These gauges are manufactured by Micron Instruments and have a gauge factor of 175±10 [46]. This increases the equivalent output signal from 0.8μV to 14μV, greatly helping signal-to-noise ratio.

Unfortunately these high factor gauges are also extremely sensitive to changes in ambient temperature, with nominal resistance changing by 42% per degree Fahrenheit change, and gauge factor changing by 23% per degree Fahrenheit change. To accommodate this issue, the gauges, which are sold in a half-bridge configuration

(two per backing), were mounted in a full-bridge configuration (one backing on either side of the flexure blade). This configuration proved insensitive to the typical ambient temperature fluctuations found in the lab, as characterized further in the next section.

The flexure design is already insensitive to torsion transmitted from the much-softer rotational bearing flexures due to the minimized length of the flexure blades, but this effect was additionally mitigated by mirroring the strain gauge installation on both the inboard and outboard sensor. On both sensors, the strain gauges were installed on the "outside" edge, away from the stamp. Pure moment loads would then induce strains of equal magnitude but opposite sign in each sensor, and would not appear in total force (i.e. the sum of inboard and outboard force).

The strain gauge sensors were powered by and amplified by a pair of Mantracourt SGA units. These units offer many options, controlled by DIP switches, and for this application are set to excite at 10V; output in a 0 to 10V range; and amplify at a 5.72mV/V amplification factor. Overall, this correlates to a gain of 87 on the output voltage from the strain gauge.

The outputs from the strain gauges were extremely linear, as shown in Figure 2-27, and differed in gain by less than 2%.

Sensor Characteristics

The performance of the strain gauges were amplified to establish their capabilities and accuracy in the realms of thermal stability, linearity, sensitivity/noise, and resolution.

Thermal stability was measured empirically. Upon turn-on, the strain gauges exhibit self-heating behavior, in which thermal strain created by self-heating dissipation effects creates a strain offset. This effect was observed to stabilize within a matter of minutes. It is recommended that upon turn-on, the strain gauges be allowed to come to thermal equilibrium over about five minutes. A graph showing measured voltage over time at the point of turn-on is shown in 2-24.

Long term thermal stability is also important for the operation of this sensor. As this machine is intended to be used for continuous microcontact printing over

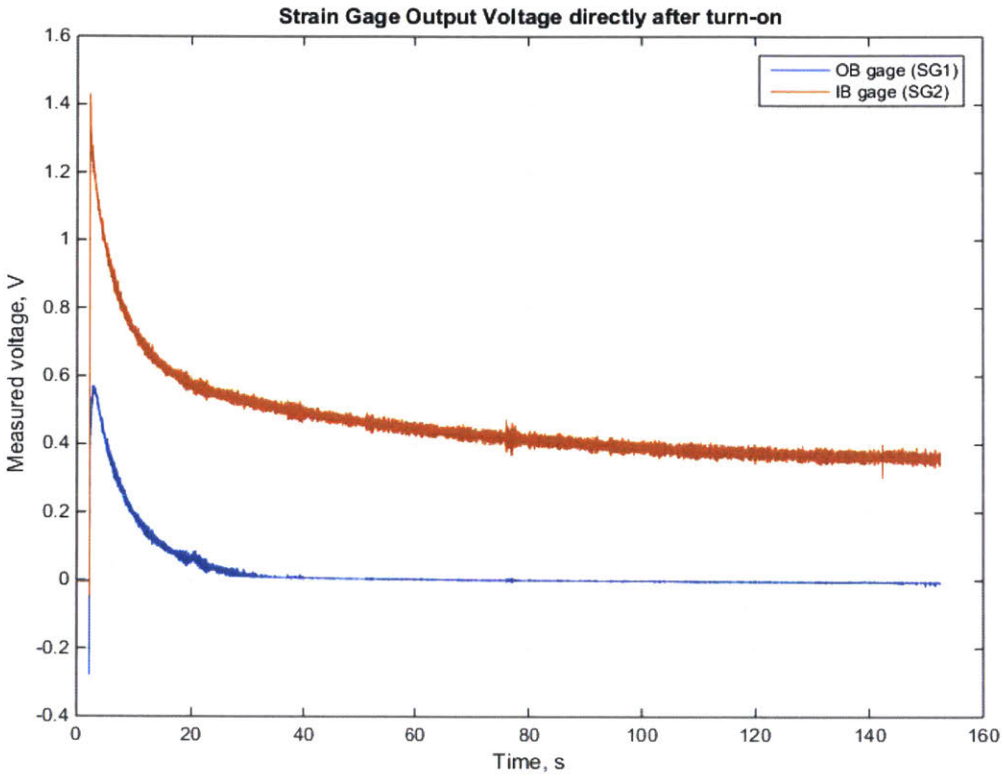

Figure 2-24: *Strain gauge sensor power-on transient.* When powered on, the strain gauges undergo resistive self-heating and some thermal strain, giving them a transient period of several minutes before they reach equilibrium.

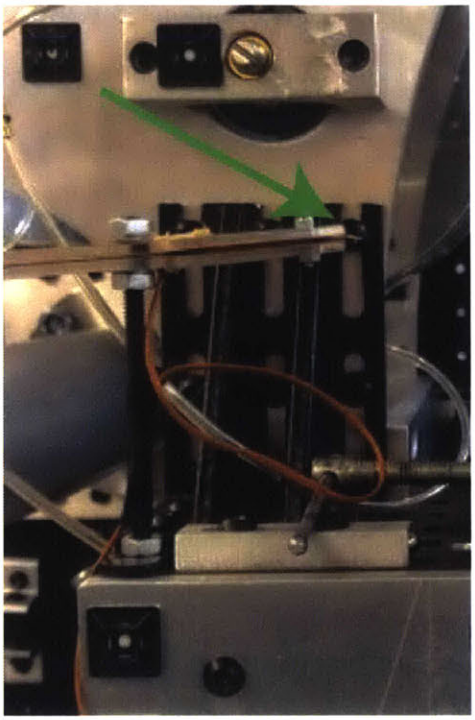

Figure 2-25: *Thermocouple sensor for strain gauge characterization.* A small thermocouple sensor on a boom was constructed. The boom allows the sensor to be placed very close to the strain gauges in order to accurately sense the local ambient temperature. The arrow in the figure indicates the thermocouple junction tip.

potentially long periods, thermal drift in the sensor could cause an output drift in the force applied to printing. To examine thermal stability, a temperature sensor was constructed using a K-type thermocouple, a small support structure, and a National Instruments NI-9211 C-series module. A LabVIEW VI was constructed that took a temperature measurement and then recorded strain gauge voltage for 10 seconds once every prescribed measurement period.

For a dataset in which the measurements were conducted every 15 minutes over the course of 12 hours, no correlation between the ambient lab temperature, which ranged from 22.7°C to 23.3°C, and the voltage drift of the sensor. Output measurements from this test are shown in 2-26. Thus, it was determined that ambient temperature fluctuations were not a significant contributor to sensor drift; however, that sensor drift was indeed present, but on the scale of an hour, it was deemed to be at a level that was acceptable. To allow for accurate continuous operation of the machine over

durations that exceed one hour, an autonomous calibration routine was included in the LabVIEW software, which is capable of zeroing the sensor against a fixed hard stop in order to remove offsets.

The linearity and gain of the sensors were established using two methods. The first method was an off-machine calibration and linearity check using calibrated weights; the sensors were both found to be nearly perfectly linear within their designed regime of operation, and to differ by only 1.8%.

However, when the sensors were installed on the machine, they were subject to residual forces and torques created by absorption of assembly errors and by fastener friction. These forces and torques enforced a non-neutral strain condition on the sensors, necessitating an on-machine, in-place calibration.

To accomplish this, an external handheld tension/compression force sensor with a 50N capacity and a 0.05N resolution was utilized. In the case that the outboard side was being measured, the measurement procedure would be the following: place sensor into custom measurement fixture and attach measurement fixture to outboard side, away from print roll; apply large bias force to the inboard side to press it against a mechanical stop; and finally apply a staircase of forces to the outboard side using the voice coil actuator and record the measured force output. This measurement simultaneously benchmarked both the actuator output and the sensor measurement against an external, calibrated reference, and showed excellent linearity and stability for both. Nonlinearities in the force sensor behavior are chiefly caused by parasitic friction occurring in the system, typically between the voice coil core and shell. (Removing the print roll removes the mechanical constraint that enforces the gap between the core and shell, introducing assembly errors here.)

Because the strain gauge sensors are analog devices passed through an analog amplifier, resolution becomes limited by either noise or the digital-to-analog conversion.

The digital-to-analog conversion is performed on the National Instruments NI-9215 C-series module, which has a 16-bit ADC. On its input range of $\pm$10V, this equates to 0.3mV resolution. The peak-to-peak noise on this device is given as 7 times the least significant bit (LSB) [47], which is equal to 2.1mV.

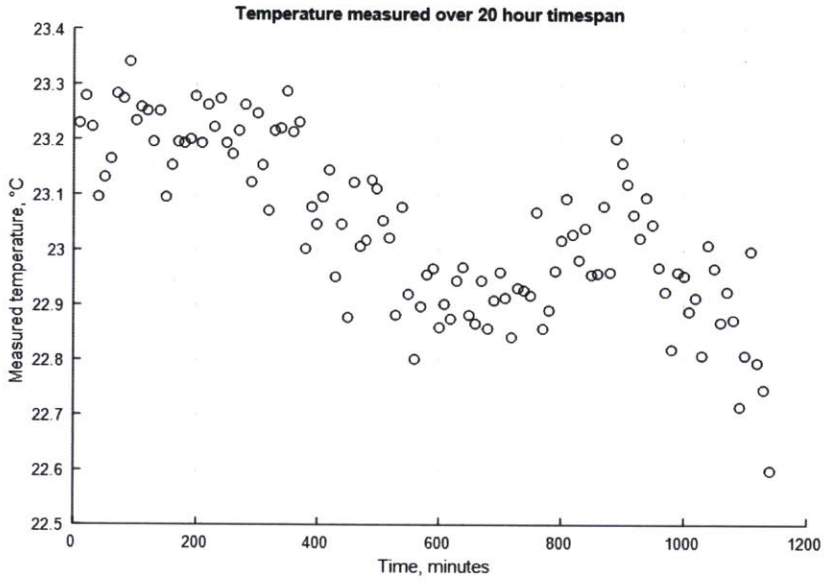

(a) Thermocouple measurements over long period.

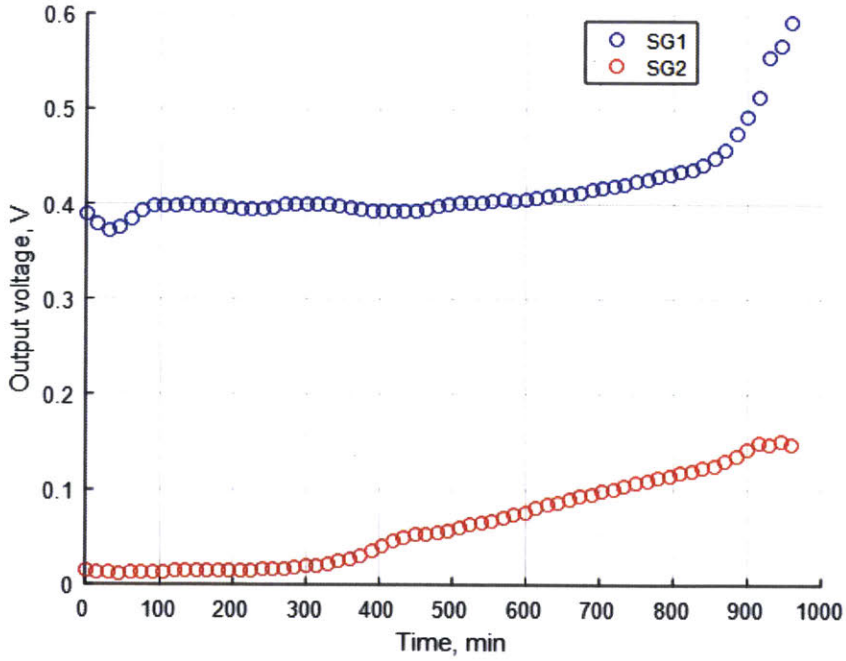

(b) Long term thermal behavior of strain gauges. The behavior has no statistically significant correlation with the temperature curve.

Figure 2-26: *Strain gauge sensor thermal stability.* Though the strain gauges show a tendency to drift in their DC value, the drift was slow enough to be mitigated with periodic re-zeroing.

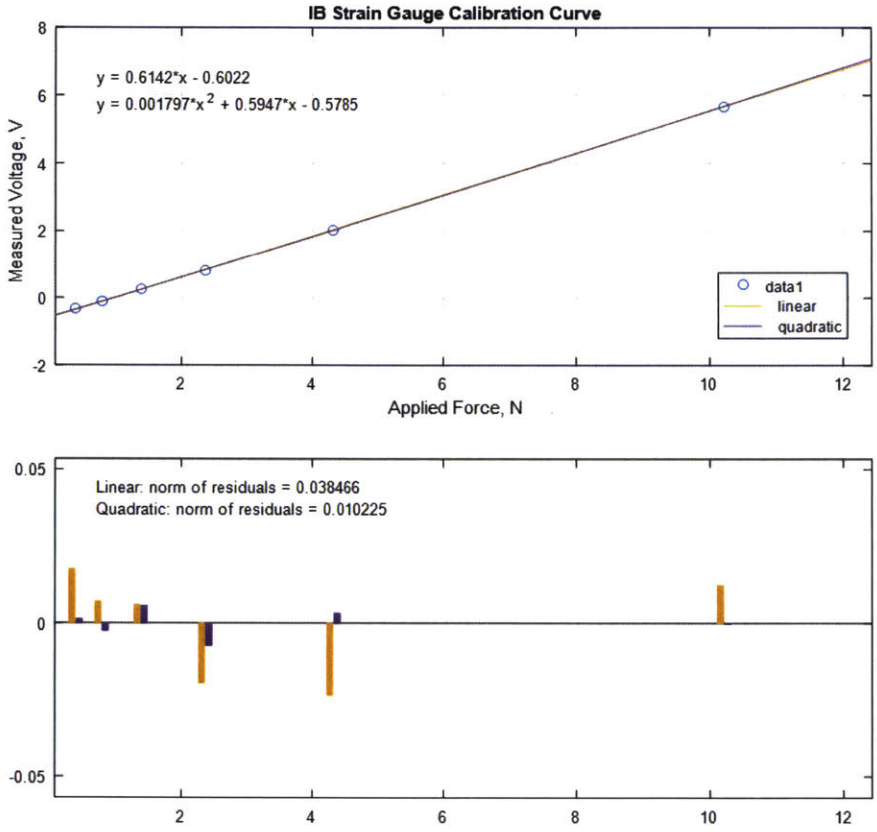

Figure 2-27: *Linear calibration curve of flexure sensor.* A weight-based calibration of the sensor confirmed that it was extremely linear. This calibration is for the inboard sensor, and differs from the outboard sensor in slope by only 1.8%.

This must be compared to noise created by electromagnetic interference and other effects. In practice, it is very difficult to measure the level of noise created by only electromagnetic interference, as the sensor will always be actively picking up any vibrational or force disturbances imparted to it, unless the sensor flexure platform is fixed to the body. Since the goal of this measurement is to establish the capabilities and real-world performance of the sensor on-machine, the lumped noise was characterized in two situations: printing-like conditions, in which the air bearings were active and the stamp was preloaded against the impression roll; and "fixed" conditions, in which the air bearing was not active. In the latter conditions, noise RMS values were measured at a maximum of 0.0663N = 40mV; in the former conditions, noise RMS values were measured at a maximum of 0.0425N = 25.4mV.

All told, the resolution can be considered to be noise-limited to 0.07N. Determining the exact value of the sensor noise independent of disturbances is possible, but is not necessary for real-world use of the sensor.

2.4.5 Electronics

The experimental platform relies on an electrical system designed and constructed by Nill [28], plus several external modules.

This system consists of a high-power two-phase AC circuit, a low-power 24V DC circuit, and low-voltage precision sensor modules.

The high-power AC circuit and low-power DC circuit were both unchanged from Nill's work. To summarize its design very briefly, the two-phase power is routed through a series of buses, fuses, and magnetic contact relays (controlled by 24V signals) to the web handling motor control units. The 24V circuit generally provides powered relay signals to components such as solenoids controlling air shutoff and actuated circuit breakers; it also serves as a power source for components such as the National Instruments input-output hardware. Signals to turn the relays on or off are received via ethernet from a computer running LabVIEW and KepWare OPC software.

Changes were made to the low-voltage precision sensor modules. The first change

is that the initial design, which consisted of National Instruments NI-9215 C-series analog input and National Instruments NI-9401 C-series digital output modules in a passive Compact RIO chassis, was replaced. The passive chassis provided the capability to record high-speed data samples to a buffer and read it into LabVIEW, but otherwise provided no deterministic timing capability. Instead, the timing source for control was the PC's software clock, which in the Windows operating system consists of a 1ms software timer subject to jitter based on process priority.

This lack of a suitable deterministic timing made implementation of control unfeasible. The first order of business was to install a previously purchased National Instruments NI-9146 ethernet expansion chassis into the machine. This is an upgrade over the passive chassis in that it has an integrated FPGA chip which may be programmed to take on computational tasks in addition to interfacing with the C-series modules. The FPGA chip provided a deterministic hardware-timed clock at 40MHz.

FPGA stands for Field-Programmable Gate Array, and is a chip that is a reconfigurable application-specific integrated circuit (ASIC). Without going into excessive detail, the FPGA chips integrated into National Instruments products offer a number of types of logic structures on each chip: flip-flops (bit storage between cycles), look-up tables (LUTs, combinatorial implementation of logic in RAM), DSP multipliers (multiplication-specific circuitry to offload resource-intensive multiplication from LUTs), and block RAM (memory). These structures physically operate in parallel, making them excellent for applications requiring deterministic timing, as independent loops will not delay or slow other independent loops, and timing can be regulated precisely. (On conventional serial processors, parallelism is achieved by slowing down the effective clock rate so that all sequential instructions necessary for one time step may be executed within one effective clock step. One process failing to complete in a timely manner can thus impact all subsequent processes in the timestep.) The other key advantage of the FPGA is that it has a fast deterministic hardware-timed clock. For control applications, this is highly desirable, because the stability and performance of discrete-time control designs depend on the rate, jitter, and delay of the sampled input and output signals. [48]

Initial efforts to develop control based on the NI-9146 unit alone were unsuccessful. Though the FPGA was ideal for tasks such as counting pulses from the 10MHz clock rate encoder readheads, as the control design complexity increased from SISO to MIMO designs, the chip's resources were completely consumed by computationally intensive tasks, such as matrix multiplication. As it became clear that the ability to implement MIMO controllers requiring matrix multiplication was a necessary next step in the project, it also became clear that the expansion chassis's Xilinx Spartan-6 LX 45 did not offer sufficient computational resources to support these techniques without significant loss of numerical precision.

It was determined then that additional computational resources in the form of a National Instrument Compact RIO with built-in real-time controller would benefit the project by offering greater freedom and sophistication in control design by removing resource constraints. A National Instruments Compact RIO NI-9030 chassis with integrated real-time processor and FPGA chip was then installed into the machine.

The real-time processor differs from the FPGA fundamentally, offering complementary capabilities. A real-time processor is built on the same kind of chip that generalized computer processors are, but runs on an operating system platform that prioritizes timing, increasing the effective clock rate and decreasing jitter. Though instructions do not physically run in parallel and parallelism must be virtualized, real-time controllers offer support for floating-point data types and matrix multiplication, as well as expanded library support. Real-time controllers are an attractive solution to developing complex deterministic controllers, as loops performing floating-point matrix multiplication can be optimized to run on the order of kilohertz, which improves timing over a generalized PC chip, but improves flexibility and numerical accuracy over an FPGA.

The National Instruments cRIO-9030 unit offers both a dual-core Intel Atom E3825 chip running the 64-bit NI Linux Real-Time operating system and a Xilinx Kintex-7 FPGA chip integrated into the device. The Kintex-7 chip also offered considerable performance gains over the Spartan-6, most notably an increase in DSP multiplier blocks from 58 to 240. Like the NI-9146, the cRIO-9030 is ethernet-controlled,

can be powered by a 24V DC signal, and seamlessly integrates with LabVIEW.

With access to both the real-time and the FPGA processing platforms, as well as the host PC, the logical path was to optimize which platform would be assigned which computing task.

2.5 Software

When the capability of the real-time controller was added to the system, the software platform was completely redeveloped in order to restructure the computational tasks.

Computational tasks included:

- Acquisition of hardware inputs via the analog input and digital input C-series modules
- Transmission of hardware outputs
- Counting of pulses generated by encoders on the printhead and web handling systems
- Computation of control outputs based on control law
- Recording of data
- Communication with OPC software controlling relays

A diagram illustrating the distribution of these tasks is shown in 2-28.

An additional complication came from the limitations on functionality in how the FPGA processor, the real-time processor, and the host PC were able to interact. First, the C-series module inputs are physically routed through the FPGA in the NI-9030, which means that all external inputs and outputs will pass through the FPGA at some point. The FPGA could also be configured to be "folded" into the real-time controller and abstracted, in scan mode, or to be directly programmed as an independent processing platform, in direct mode.

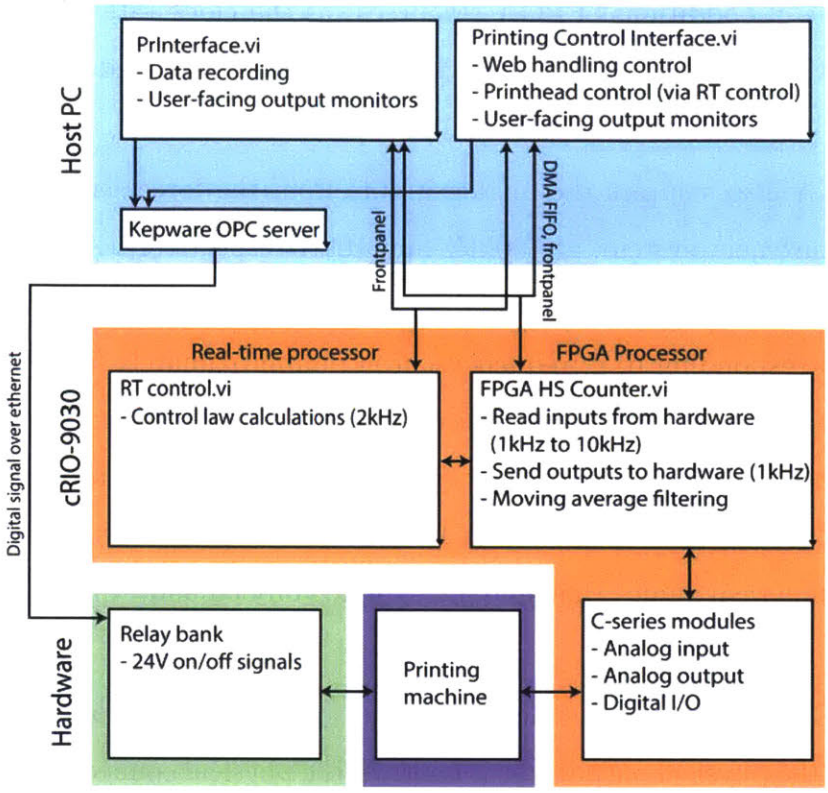

Figure 2-28: *Distribution of computing tasks among real-time, FPGA, and PC platforms.* Relevant LabVIEW VI program names are also included. VIs in the orange section should always be running in the background, and one of the VIs in the blue section should be selected as the user-facing frontend.

For this work, the necessity of counting encoder pulses at very fast clock rates meant that the FPGA must be programmed in direct mode. The benefits of direct mode are that the FPGA's capabilities are not masked by the real-time controller's limitations; the chief disadvantage is that data must be passed manually from any one platform to another using LabVIEW data types.

2.5.1 FPGA Tasks

The FPGA chiefly deals with acquiring and conditioning inputs, and sending out outputs. Independent loops, both operating at the base clock rate of 40MHz, count quadrature pulses from the Renishaw linear encoders (10MHz clock rate) and the RLS magnetic ring encoder on the print roll (1MHz clock rate). Though the encoder readheads could be counted at their clock rates, overclocking the quadrature counting

loop consumes no additional FPGA resources (as the clock rate must be decreased using a "wait" command) and ensures that pulses are not missed.

The FPGA also samples the analog inputs from the force sensors and from the tension measurement system, at 100kHz and 10kHzrespectively. A filtered version of the force sensor input is also generated using a moving average filter with a window size of 14, corresponding to a frequency cutoff of approximately 500Hz. Because the FPGA is able to compute these measurements at 10-30 times the control loop clock rate, the signals may be abstracted as continuous in the eyes of the other processing platforms. These signals are passed as LabVIEW frontpanel elements, as they are a handful of numerical values that may be sampled on-demand.

The FPGA is also responsible for passing output values from other loops and platforms to the physical outputs, as it controls the physical connection to the C-series modules. This is accomplished with simple pass-throughs, implemented as LabVIEW frontpanel elements, that allow the FPGA loop to sample the value on-demand and pass it through to the outputs.

Finally, because the FPGA is the nexus through which all inputs and outputs pass, it is responsible for recording data. A parallel loop on the FPGA may be activated to sample the input and output values at 10kHz to a FIFO (First In, First Out) memory element. This memory element is a LabVIEW datatype that uses DMA (Direct Memory Access) to stream large quantities of data between a host processor and a target processor by allowing them to concurrently access memory elements. On the NI-9030, DMA may be configured in Target-scoped (FPGA only, inter-loop), Target-to-host (FPGA to host PC), or Host-to-target (host PC to FPGA). To record data to the PC's hard drive for later analysis, the Target-to-host FIFO was employed; the PC acquires the oldest values from the queue, maintaining time history, and stores sampled data in RAM in order to prevent slow file-writing operations from causing overflow of the FIFO buffer. The data is saved to file when the host PC VI is stopped.

2.5.2 Real-Time Tasks

With the FPGA providing inputs and sending outputs at a high clock rate, the real-time controller becomes responsible for control tasks.

Over the course of this project, the control strategy varied from simple PID control strategies to full-order state estimation and full state feedback. Though the former strategies could be implemented on the FPGA due to their simplicity, later control strategies, which required matrix multiplication and numerical precision, could only be implemented on the real-time controller.

The core functionality of the real-time controller involved reading front panel elements from the FPGA, computing control variables, and outputting front panel elements to the FPGA, implemented in one deterministic loop. Within this functionality, different control strategies, selected inputs, and integration with other VIs is available; for example, the printing force command may be directly selected via the real-time controller VI, or it may be selected through the Printing Control VI, using the real-time controller VI as a backend. The main loop on the real-time VI was optimized to run at 4kHz.

2.5.3 Host Computer Tasks

The host computer is used to record large amounts of data from the FPGA via the Target-to-host FIFO data structure. Because this data is read from a FIFO buffer, the non-deterministic timing of the host computer loop is acceptable, as long as enough elements are read from the buffer each loop to ensure delayed reads do not overflow the buffer.

Additionally, the VI used to control web handling is run from the host computer. This design was chosen because (1) the web-handling operations are all open loop, or (in the case of torque control) the feedback loop is closed externally and independently to the host computer, so deterministic timing is not crucial; and (2) the web handling equipment is controlled using a software program installed on the host PC that served as an OPC server, sending flags via ethernet to relays that switched on and off 24V

signals. This means that any signals intended for the web handling system would need to be passed back to the host computer regardless of origin.

2.6 Summary

The contributions listed in this chapter served to correct the fundamental gaps in capability required to achieve the desired objectives. The equipment was upgraded with additional purpose-built force sensors, allowing for force sensing and control. Additionally, the inadequate computational platform was upgraded, and a new software platform distributed across three computational targets was developed to properly exploit the new platform's capabilities. Finally, modifications and additions to the web handling assembly were completed, including web torque measurement and closed-loop control; replacement of the web speed measurement; and characterization of the performance and limitations of the web-handling system as a whole. Overall, these improvements were necessary in order to complete the experimental objective of precise control of the printhead.

Chapter 3

Analytical Modeling of Printhead Dynamics

3.1 uCP Process Dynamics

In order to establish an accurate analytical model of the microcontact printing process, it is necessary to understand the physics that control this process, and to establish the physically relevant inputs and outputs.

3.1.1 Defining Quality Printing

A high-quality print produced by the microcontact printing process is defined by several characteristics: first, it has no point defects, either of excess or inadequate printing; second, it has maintained good contact throughout the entire print region, avoiding collapse defects or falling out of contact; and third, it replicates the desired print pattern to an acceptable degree of exactness.

Point defects are generally caused by contaminants, isolated stamp defects, or pre-existing substrate defects. PDMS has a high surface affinity and tends to retain any dust it encounters in unclean environments [20]. The dust particles can cause either voids in printed features, if they reach the stamp post-inking and block the inked stamp from coming in contact with the substrate; or stray marks bleeding off of

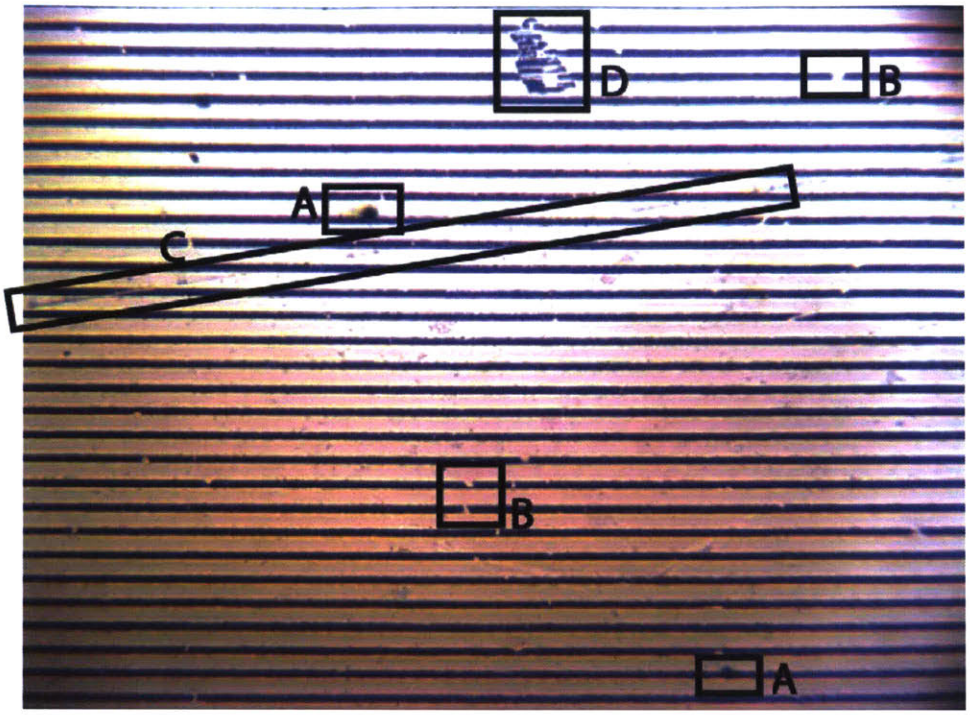

Figure 3-1: *Examples of point defects that may appear on an etched print.* (A) shows an excess printing point defect; (B) a void point defect; (C) a pre-existing substrate defect; (D) a point defect of unknown origin. Un-annotated original generated by Chris Merian. [13]

features, if they contact the stamp pre-inking and are also inked alongside the stamp features.

Other empirically observed point defects include droplets of liquid thiol ink that have been aspirated and come in contact with the substrate; and pre-existing defects in the gold-coated PET substrate such as scratches, pits, or foreign materials. [13] To reduce these defects, careful manufacturing environment hygiene, high-quality substrate, and careful handling of the substrate is required. A cleanroom type manufacturing environment is recommended for defect-free production.

The second characteristic of quality printing depends on the pressure applied to the stamp during printing. When insufficient pressure is applied, the stamp may fail to make contact with the substrate, leaving unprinted voids. When excessive pressure is applied, the stamp experiences a failure mode that previous work has termed "roof collapse;" in this mode, the between-feature regions of the stamp, which are not intended to make contact with the substrate during printing, are pressed into

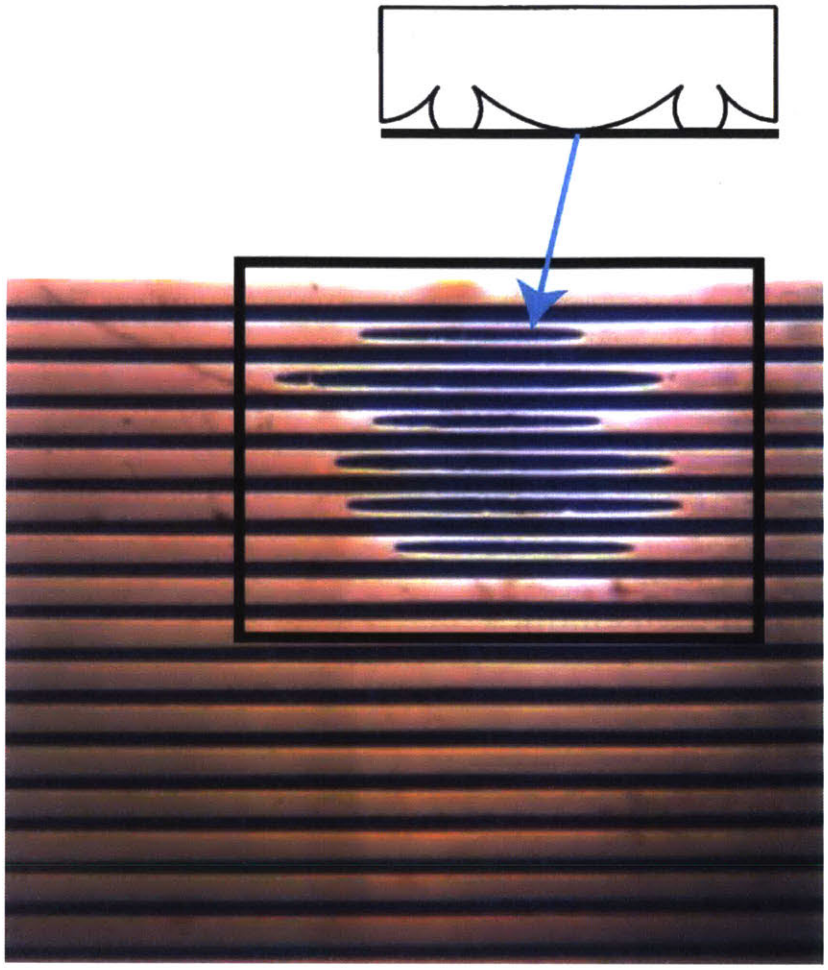

Figure 3-2: *Etched print showing roof collapse failure mode.* The roof collapse failure occurs when excessive pressure causes the "roof" between features to touch down onto the substrate. Base image generated by Chris Merian. [13]

contact, creating stray printing marks. [9, 8] Increasing pressure beyond the roof collapse point pushes the stamp into a total collapse failure mode, in which the features and roof expand sufficiently under Poisson effects to blanket print a surface. To achieve printing free of under-pressure and over-pressure defects, printing pressure at each feature should be kept within a range of acceptable pressures.

The third measure of quality is the degree to which a pattern is dimensionally replicated. For example, if the contact area of a line feature on a stamp is 10 μm wide, then it is desirable for the width of the printed line pattern to be 10 μm wide. The actual printed width, however, may exhibit some mean shift and some variance, as the features will widen under pressure, and stamp surface or contaminant defects

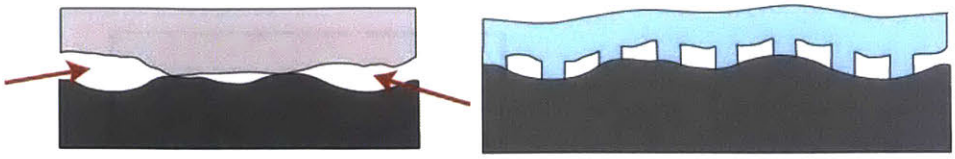

(a) Rigid contact (b) Conformal contact

Figure 3-3: *Comparson of rigid and conformal contact modes.* Micro- and nanoscale surface variations prevent rigid surfaces from making full contact, resulting in voids between the surfaces (examples indicated by arrows). Compliant surfaces exhibiting conformal contact eliminate these voids.

create width variation. [13, 22] The levels of acceptable dimensional deviation from a nominal pattern are expected to depend on the demands of any specific application.

3.1.2 Printing Mechanics

While contaminants can be controlled by maintaining a cleanroom manufacturing environment, under-pressure and over-pressure defects must be controlled by modulating stamp pressure during the printing process.

Any two surfaces will have surface variations and asperities on the micro- and nanoscale. When brought into contact, two rigid surfaces with variations will inevitably have some microscale gaps, and will not contact across the entire region, as illustrated in 3-3. A compliant, conformally contacting surface, however, is able to distort to accommodate surface variations in a mating surface, reducing or eliminating gaps in the contact area.

For microcontact printing, with characteristic features heights in the 10 μm to 50 μm range, it is critical that microscale voids between the printing tooling and the substrate be eliminated. One strategy to accomplish this would be to ensure that both a rigid tooling surface and a rigid impression surface are an exact match, but fabricating these surfaces to ensure gaps below the scale of 1 to 10 μm is difficult and expensive, and even if achieved, does not account for the thickness variation found in low-cost substrates such as a PET web. A better strategy, then, is to induce some compliance in the printing contact region; a compliant material can deform, conforming itself to an arbitrary rigid surface on the fly.

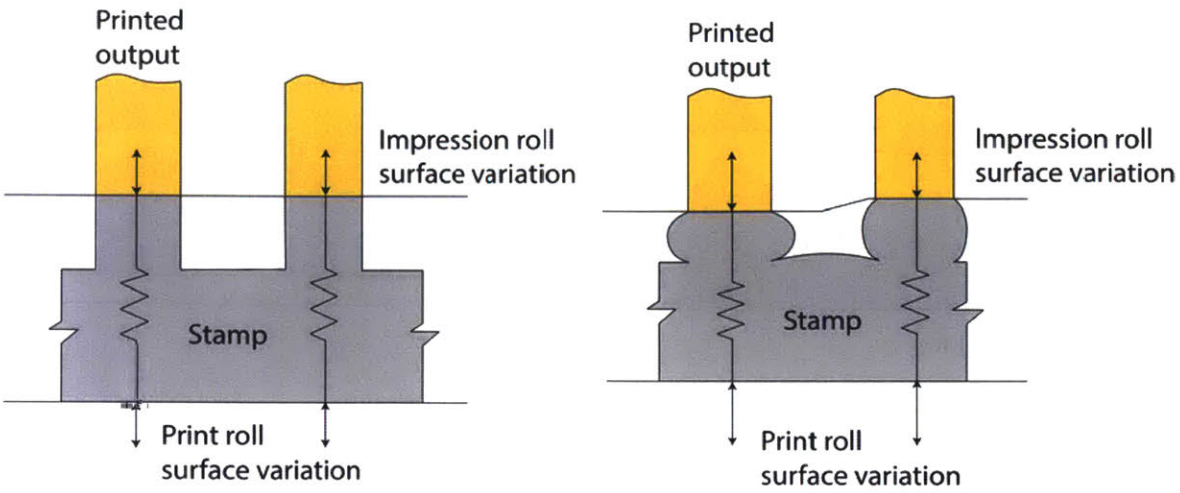

Figure 3-4: *Individual feature behavior during compression.* (Left) Under ideal printing conditions, all features (gray) are compressed the same amount, producing identical printed outputs (yellow). (Right) When nonideal surface variation is encountered, the compliant features are compressed by different amounts; but, their compliance allows them to absorb a range of surface variations without significant dimensional change to the printed output.

Consider a compliant elastic layer with raised features, bounded between two rigid surfaces, as shown in 3-4. Any surface variation of the print roll and impression roll appear to the compliant layer as displacement disturbances of its bounding surfaces, inducing compression of the elastic feature. This compression causes variation in pressure at the surface interfaces, as well as Poisson effects that cause deformation of the feature and compliant material; but, if disturbances are kept within an allowable range, the printing pattern remains largely unchanged. This property allows the compliant features of PDMS microcontact printing stamp to passively accommodate surface variation and maintain contact across a region.

To enforce contact across an entire region, it is necessary to apply some minimum pressure to create contact on each feature and close all voids. Moderate pressure or surface variation beyond this point will cause little change in the stamp's contact pattern; a schematic of this effect is shown in 3-4. This is true until the collapse threshold is exceeded; at this point the areas with the highest local pressure (corresponding to the "high spots" of the irregular surfaces) will begin to experience the collapse failure detailed above. An exaggerated illustration of these contact states is

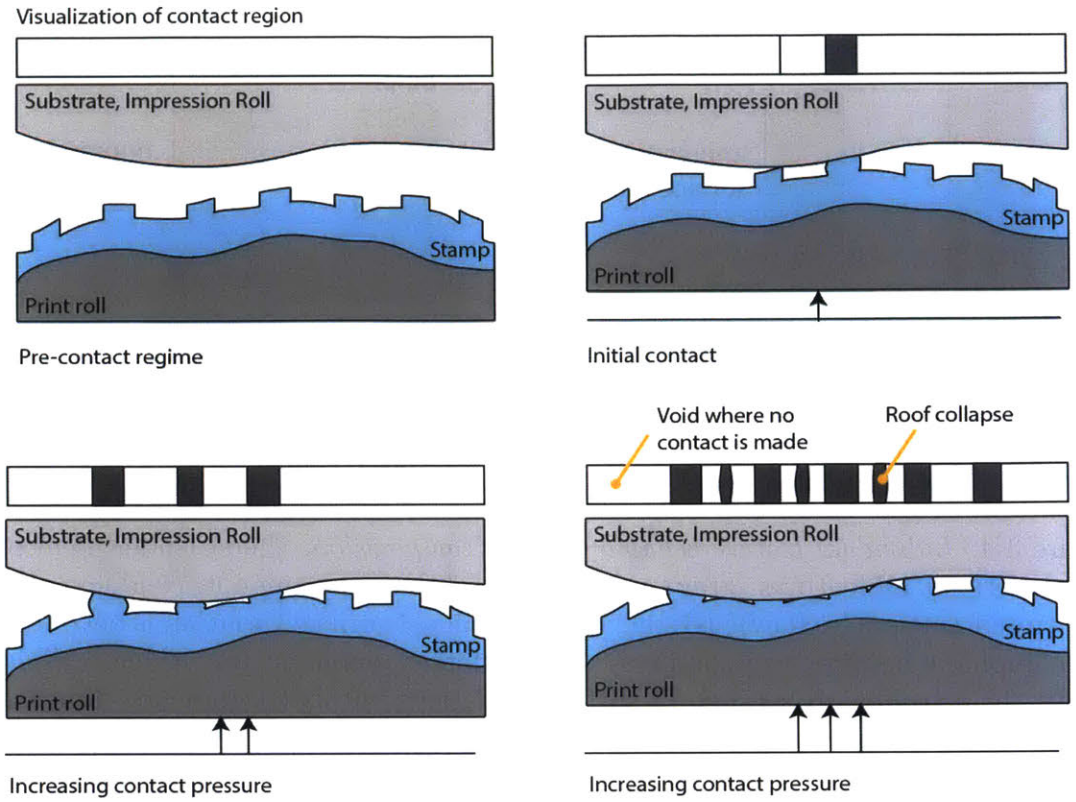

Figure 3-5: *An exaggerated visualization of the effect of pressure on the contact region of the stamp.* As pressure is initially increased, the features on the "high points" come in contact. Increasing pressure compresses these features, allowing lower features to contact. Further increasing the pressure exceeds the collapse threshold, causing roof collapse first in the high region. The stamp in the figure is shown with exaggerated surface variation, causing a no-contact void simultaneously with a roof collapse region.

shown in 3-5.

Using knowledge of this threshold, the ideal printing state may then be described. In the ideal case, in which all bounding surfaces have perfect regularity, applying some minimum contact pressure, $P_{contact}$, would compress all features equally, and create equal pressure on each feature. As long as this pressure was less than the collapse pressure, $P_{collapse}$, perfect contact would be achieved; i.e., $P_{contact} < P_{print} < P_{collapse}$.

In the nonideal case, in which the bounding surfaces or the stamp itself have significant irregularity, there will be variations in local pressure from feature to feature depending on the degree of compression enforced by the irregular surfaces. The minimum pressure to ensure contact increases, as features located on "high spots" must be compressed until features located in "low spots" can contact. However, the

features located at high spots will approach the collapse pressure sooner, decreasing the maximum allowable pressure. Thus, the acceptable range of pressures is decreased to the range $P_{contact} + \Delta P_{low} < P_{print} < P_{collapse} - \Delta P_{high}$. If surface variation of the print roll, impression roll, substrate, and stamp are low, ΔP_{high} and ΔP_{low} are minimized, maximizing the region of acceptable pressures.

Ideally, all features across the stamp will be subject to pressures within this range, ensuring that all features are in contact, but no features are collapsing.

3.1.3 Adaptation to the Roll-to-roll case

In the above analysis, contact is abstracted as being between two one-dimensional boundaries, represented by arbitrary lines. On a roll-to-roll platform, the contact region occurs between two cylindrical rolls. This introduces several new concerns that need to be adequately addressed in order to establish an accurate model.

The first concern is that contact between two cylinders, one of which has a compliant outer surface, appears as a two-dimensional rectangular region instead of a one-dimensional line, as shown in 3-6. This introduces the possibility of both axial and circumferential variations in printing pressure, and raises the question of whether modeling contact as a line is sufficient to capture any necessary effects. If the contact region can be modeled as a line, then only pressure adjustments in the plane containing the axes of both rolls are needed–i.e., the optimization problem is two-dimensional. If the contact region must be modeled as a rectangle, then out-of-plane adjustments may also be required, increasing the optimization problem to three dimensions.

For the experimental apparatus described in Chapter 2, the contact region has an axial width of 50 mm. The circumferential height of the rectangular contact region is dependent on the stamp's elastic properties and the applied pressure.

Hertzian mechanics give the contact area for the case of two axially-parallel cylinders in contact. [49, 9] However, the classic Hertzian solution assumes that both cylinders are homogenous and have homogenous elastic properties throughout; in this case, as noted by Petrzelka, the cylinder has a finite elastic layer wrapped around a much stiffer, essentially rigid, core. The question becomes whether the print roll must

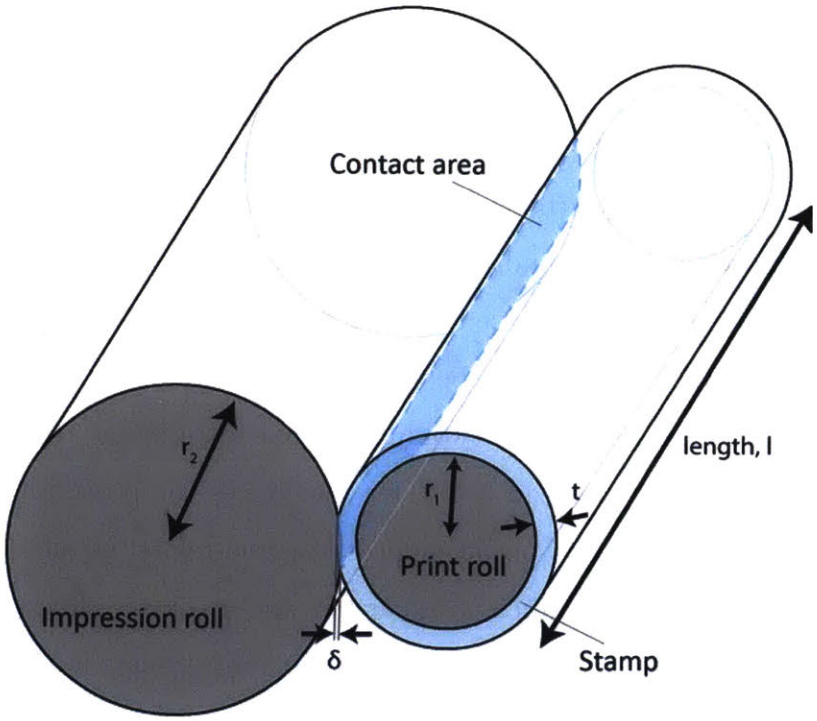

Figure 3-6: *Hertzian contact between two cylinders.* When at least one of the cylinders is elastic, a rectangular contact region results. Dimensional annotations corresponds to equations (3.1) to (3.3).

be represented as a nonhomogenous roll, or if the deformation may only be considered local to the PDMS. [9]

This question is also considered in work done by Bentall and Johnson [50] and Meijers [51], and covered by Johnson's text [49]. Meijers derives an exact solution; but the edge cases, contact width $l >>$ stamp thickness t and $l << t$, both converge to simpler models. In the case that $l << t$, the Meijers model converges to the Hertzian solution; and in the case that $l >> t$, the contact width converges to $l = \sqrt{6r^*\delta}$. In this expression, r^* is an equivalent radius that maps contact between cylinders with radii r_1 and r_2 to an equivalent roll with radius r^* contacting a plate:

$$r^* = \frac{r_1 r_2}{r_1 + r_2} = \frac{50\text{mm} * 152\text{mm}}{50\text{mm} + 152\text{mm}} = 37.6\text{mm}; \tag{3.1}$$

and δ is the radial compression depth, as shown in Figure 3-6.

Unfortunately, this means that there is not a simple expression that gives contact width for a given impression depth and stamp geometry. However, for the nominal experimental stamp (30μm lines on a 100μm pitch), when applying 4-5 N total printing force, the width of the contact region has been measured to be between 1 and 2 mm. Additionally, the ratio of length l to height h of the rectangular contact region for this particular stamp is then

$$\frac{l}{h} \geq \frac{50\text{mm}}{2\text{mm}} = 25, \tag{3.2}$$

which is quite large. But perhaps most notably, under ideal operating conditions, a constant force is maintained on the printing region, which corresponds to also maintaining a constant contact area. Small variations in force application result in even smaller variations in contact width, as the bounding contact width models both relate contact width l to indentation depth δ by:

$$(\sqrt{2r^*\delta})_{Hertzian, l<<t} < l < (\sqrt{6r^*\delta})_{Bentall, l>>t} \tag{3.3}$$

Thus, for a particular nominal stamp with a single ideal printing force, there is a single ideal contact width that will occur. Empirically, this contact width will

not vary significantly from 1.5mm, meaning $\frac{l}{h} > 25$ will remain true, and that the contact region will exhibit a relatively constant stiffness as it undergoes relatively small indentation and relaxation.

These observations have been taken as sufficient evidence to model the contact region as a one-dimensional line. Then, the pressure need be modulated only in-plane, and may be considered as a force per unit length along the line of contact, instead of a force per unit area in a contact region.

Consider, then, a print roll with a single degree of freedom, contacting a fixed, rigid impression roll in-plane. In this case, the printing roll may be translated radially closer to or farther from the impression cylinder in order to increase or decrease compression throughout the contact region, but both cylinders remain axially parallel in plane. Adjustments to the print roll can accommodates only zeroeth order variation; that is, an offset—any higher order surface variation must be accommodated by the passive compliance of the stamp. If surface variation in any segment of the contact line requires excessive deformation, causing local pressure to exceed the collapse pressure, print quality will start to degrade.

Adding a second degree of freedom to this in-plane abstraction allows the printing roll to both translate radially relative to the impression roll and to tilt in-plane, creating an angle between the axes of each cylinder. Adding this degree of freedom means that first order surface variation can now be accommodated by tilting the print roll instead of by compression of the stamp; that is, a slope in addition to an offset. Stamp compliance need only accommodate second order and higher surface variation. This concept is illustrated in 3-7.

To add a third degree of freedom to the in-plane abstraction, one could consider a method to shape the stamp along a curve, or a method to bisect the stamp into two regions and apply different pressure profiles along those regions. It is also possible to carry this idea to the Nth order for a stamp with N features, ideally imagining that the pressure on each individual feature could be controlled. However, a typical stamp used in the pursuit of this work might have features on a 100 μm pitch across a 25 to 50 mm wide area, meaning $250 < N < 500$. Designing a mechanism to independently

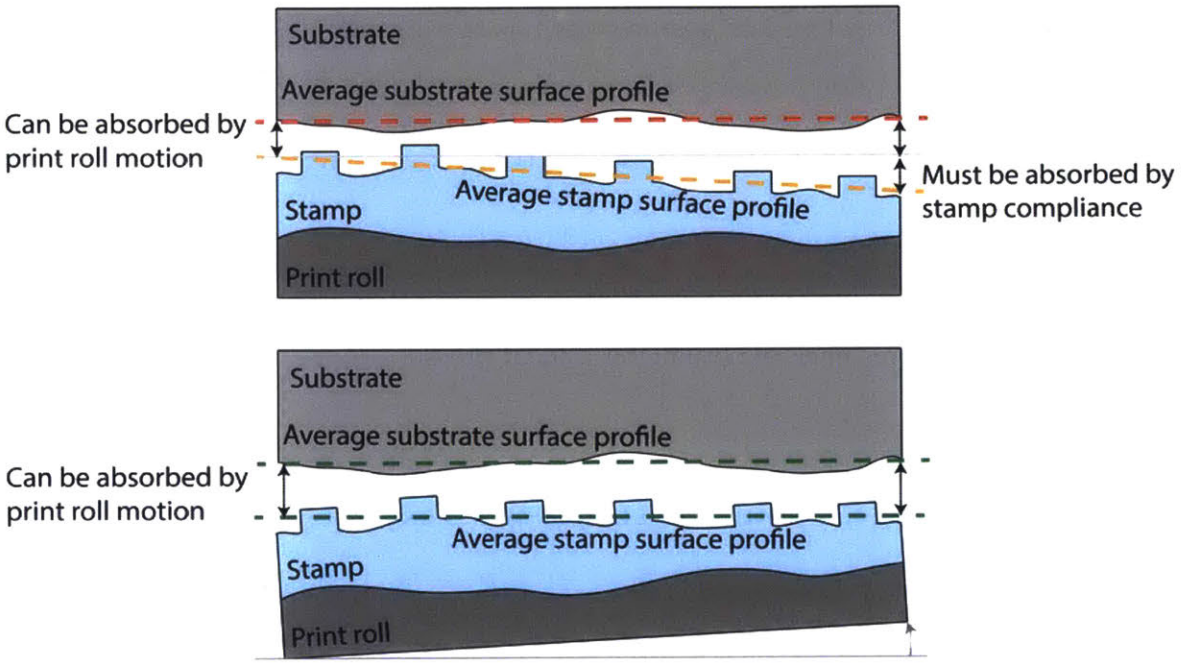

Figure 3-7: *Schematic showing how deliberate print roll rotation reduces effective surface variation.* Allowing a second degree of freedom in the rigid print roll allows the largest source of variation, a first-order taper, to be absorbed by the motion of the printhead itself instead of by the compliance of the stamp. The ideal situation occurs when the average surface of the stamp is aligned with the average surface of the substrate; in this case, the surface variation that must be absorbed by the stamp's compliance is minimized.

control the pressure of five hundred 100 μm-wide regions is difficult and impractical. To even achieve a third degree of freedom requires either a nonrigid print roll, or a mechanism by which the stamp may be compressed independent of the print roll movement. Additionally, each additional degree of freedom accounts for a smaller and smaller fraction of the error absorption budget, exhibiting diminishing returns for the increasing technological complexity. And, limiting the degrees of freedom to two allows the leveraging of conventional technologies and existing study. To that end, two degrees of freedom has been selected as the optimal design. [10]

3.1.4 Selection of Control Variable

A stamp with ideal compliance presents a large $P_{contact} < P_{print} < P_{collapse}$ window, accommodating large local variations; that is, for a printing pressure P_{print} within the window, for n features each experiencing a local pressure P_i,

$$\begin{aligned} P_1 \neq P_2 \neq ... \neq P_i \neq ...P_n; \\ P_{contact} < P_1, P_2, ..., P_i, ...P_n < P_{collapse} \end{aligned} \tag{3.4}$$

Given perfect knowledge of contact line topography, P_{mean} could be computed as a weighted average. If feature i has an acceptable pressure window expressed by $P_{contact} + (\Delta P_{low})_i < P_i < P_{collapse} - (\Delta P_{high})_i$, then the expression

$$P_{mean} = \frac{P_{contact} + (1/n)\sum(\Delta P_{low})_i + (1/n)\sum(\Delta P_{high})_i + P_{collapse}}{2} \tag{3.5}$$

describes the most robust possible average printing pressure. Local variation occurring throughout the stamp, impression roll, and print roll make this difficult to compute analytically, but it is easy to establish empirically for a given stamp using only a handful of test prints.

Each individual feature may be considered to be an elastic element; and the stamp

as a whole is an elastic element with some compound stiffness deriving from the feature geometry. The contact process can be thought of as applying a pressure or force to each feature, resulting in a deformation; or, applying a deformation, resulting in a force. Physically, the goal is to achieve a targeted nonzero compression for each feature, regardless of geometry; this corresponds to the case of applying a "just right" force to induce contact without collapse, customized to each feature. Thus, it is desirable to be able to control the deformation or strain applied to each feature, and by extension to the entire stamp.

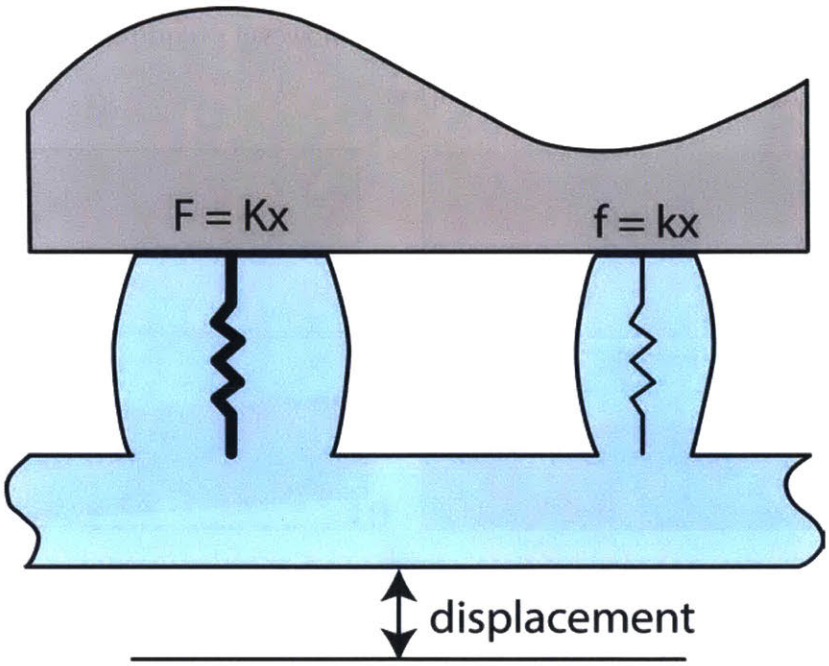

Figure 3-8: *The ideal printing state: equal compression of each feature.* In the ideal printing state, the exact amount of force required to compress each feature the same amount is applied. In this diagram, $F > f$ as the large feature's effective stiffness K is larger than the small feature's effective stiffness k.

To apply the same enforced displacement to each feature, clearly each feature must be moved toward the impression roll the same distance. The issue with this simple concept arises from the fact that due to spatial errors from many sources, each feature starts at an unknown distance from the impression roll. Further, even if the print roll and impression roll are perfectly flat surfaces, the stamp itself may have some variation; in this case, even if the print roll is advanced perfectly parallel to the

impression roll, different features will see different levels of compression.

The simplest example of this idea is the concept that the average surface of the stamp is tapered. (Assume that there are local variations in the stamp thickness, but that they are small compared to the overall taper of the stamp.) In this situation, it would be ideal to angle the print roll such that the average surface of the stamp comes parallel to the impression roll, as shown in 3-9, and then to compress the features. (Each feature may experience varying compression due to local spatial variation, but the assumption that local variation is small relative to taper means that locally variations in compression will also be small.) To be able to accomplish the alignment of the stamp surface and the impression roll, however, requires prior knowledge or measurement of the stamp's inherent taper.

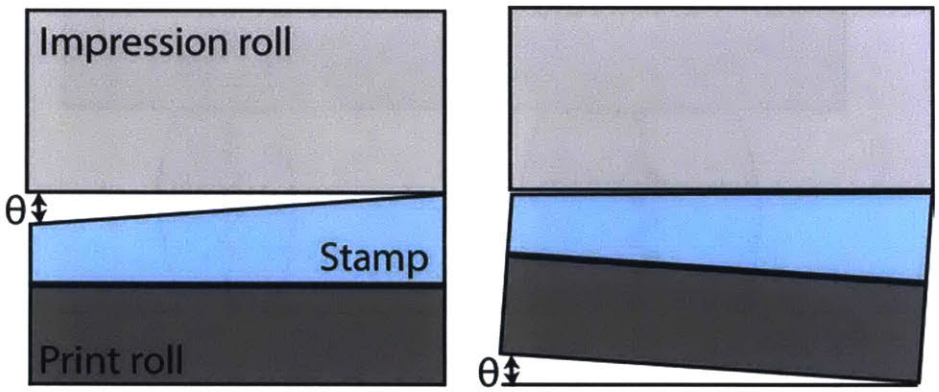

Figure 3-9: *Elimination of a known stamp taper using print roll rotation.* In the simple example of stamp taper, equal contact and compression across the entire stamp can be achieved by tilting the printing roll relative to the impression roll, but only if the taper angle θ is known or can be measured.

Though it may be simple to measure taper in this example, consider the case in which taper varies around the stamp's circumference; now a complete mapping of taper to stamp angle is required to achieve the same result. And, further complexity could be easily envisioned; the print roll and the impression roll may also have some runout, and as the impression roll has a different diameter than the stamp, now a mapping of taper to stamp-impression roll relative angular position is necessary. Plus, this mapping would need to be repeated for any particular stamp, and would likely need to be repeated for each mounting and unmounting of the stamp, given the

imprecision inherent in that process; and measures would need to be taken to ensure that the print roll and the impression roll are always brought into contact at a known angular position. Even worse, even if all displacement variations of the machine can be measured or eliminated—the low-cost PET substrate itself has thickness variations!

Thus, though it would be ideal to control the displacement of the stamp's line of contact, in practice this is very difficult to achieve due to inherent variation stackups that become large at the microscale.

If displacement is one side of the compliance coin, the other side is force. By applying the correct force per feature, the desired displacement per feature can also be achieved. Technically this is an indirect way of controlling contact; but the advantage of using force to control contact is that prior knowledge of stamp and machine errors becomes unnecessary.

Again, considering each feature as an elastic element, the goal would be to induce the same displacement in each feature by applying the correct force for its individual stiffness. To do this exactly would require a degree of freedom for every single feature, which may number in the hundreds or thousands on a single stamp. But, to do this approximately is relatively simple.

If we consider all of the elastic features acting in parallel to create some overall equivalent elasticity, K_{tot}; and if the compression desired per feature is δ_0; then the force that should be applied overall is simply $F_{tot} = K_{tot}\delta_0$. Because the features are all in parallel, the load transfer through each feature will be proportional to its individual stiffness, and (in the absence of dimensional errors) will be exactly the right force to compress the feature to δ_0. (Additionally, measurement of the total stamp elasticity K_{tot} is much more straightforward than mapping the surface offset of all components in the printing interface. In the most complex case in which a stamp had significantly varying feature geometry, it could be measured per angular position region.)

Realistically, spatial variation in the machine and the stamp will induce some offset error δ_{offset} in the compression, so that the actual compression experienced by each feature will be $\delta_0 + \delta_{offset}$; and the stiffness of each feature will depend both on the

geometry of the pattern but also on the bulk PDMS material behind it. But, if these variations are kept sufficiently small (but not negligible) by good design, applying an average force across the entire stamp should result in a sufficiently accurate recreation of the desired per-feature compression state.

As discussed in Chapter 2 and above in Section 3.1.3, this work utilizes a two degree-of-freedom rigid printing roll. The two degrees of freedom allow for the average tilt resulting from errors in the stamp, impression roll, and print roll surface to be offset out, and for varying compression to be applied to the stamp. Then, to apply some printing force F_{tot}, chosen to achieve the desired compression δ_0, the force state that should be induced in this printhead, by inspection, should satisfy $F_1 + F_2 = F_{tot}$, and the moment $T = -lF_1 + lF_2 = 0$, where F_1 and F_2 are force applied at each end of the print roll, and $2l$ is the length of the print roll.

In order to maintain this force state in the face of disturbances generated by machine errors, substrate errors, and vibration, it is desirable to establish closed-loop force control of the system. The ideal closed-loop controller should be able to maintain the force to such a level that no feature is over-compressed to failure or falls out of contact. To set a quantitative goal, for a stamp with 15μm tall features, a 5% compression is equivalent to 0.75μm. At an approximate average stiffness of 0.1N/μm, that means total printing force should be controlled to better than 0.075N. This force can be considered "small" in that it is easy to induce this amount of force in the printhead even by creating vibrational noise in the printing machine system, so disturbance rejection was another key goal.

To achieve closed-loop control of the printhead, the first step was to develop and verify a dynamic model. This proved more difficult than expected, as detailed in the remainder of this chapter.

3.2 Printhead Dynamics

The physical printhead system has two force inputs, F_1 and F_2, located at the inboard (F_2) and outboard (F_1) sides of the printing roll. The positions of each translational

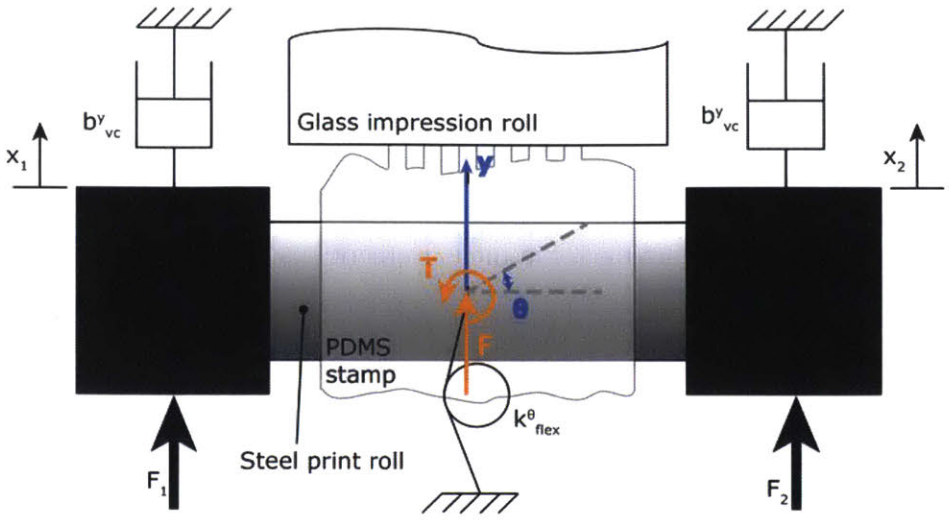

Figure 3-10: *Simple schematic of the separated roll model.* Though the input forces are actually F_1 and F_2, located on either end of the print roll, in this model they may be abstracted as total force F and total torque T (indicated in orange). The two degrees of freedom are then y, translation of the print roll center of mass, and θ, rotation about the center of mass.

bushing relative to the printhead base are denoted x_1 and x_2, and the actual angle about and translational position of the printhead's center of mass are denoted θ and y. The output variables considered are total reaction force onto the center of mass of the print roll, F, and pure moment exerted on the center of mass of the printroll, T. The width of the print roll from translational rail to rail is $2l$. Figure 3-10 shows the basic geometry of the print roll.

3.2.1 Separable System

Notation for this section is explained in a table below. Figure 3-11 shows the configuration of the physical parameters.

Variable	Physical meaning
F_1	Outboard voice coil force input
F_2	Inboard voice coil force input
F_1^{out}	Outboard reaction force measurement
F_2^{out}	Inboard reaction force measurement
F	Total force exerted on print roll COM (center of mass)
T	Total torque exerted about print roll COM
x_1	Displacement of outboard end
x_2	Displacement of inboard end
y	Displacement of print roll COM
θ	Angle of print roll about COM
J_p	Print roll rotational inertia
M_p	Print roll mass
k_s^y	Stamp translational spring constant
b_s^y	Stamp translational damping coefficient
k_s^θ	Stamp rotational spring constant
b_s^θ	Stamp rotational damping coefficient
b_p^y	Voice coil combined translational damping coefficient
k_p^θ	Spring-return rotational flexure spring constant
b_p^θ	Voice coil combined rotational damping coefficient

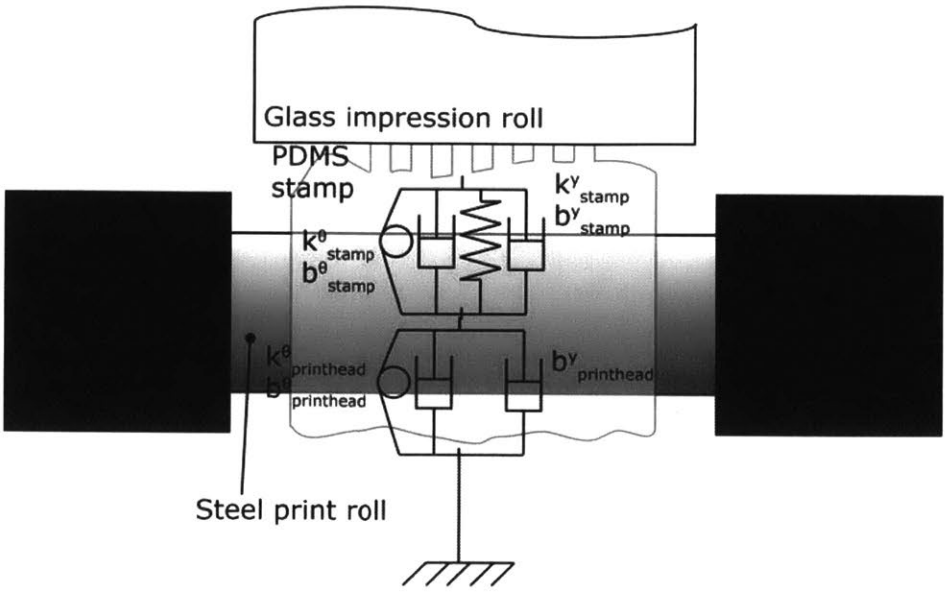

Figure 3-11: *Simple roll model with all lumped parameter elements diagrammed.* If the force-sensing and rotational flexures are assumed to be rigid, the system may be modeled as a fourth-order separable system. The printhead itself has zero translational stiffness in this model, and the F_1 and F_2 inputs may be transformed to the F_{in} and T_{in} coordinates.

The initial approach to modeling the printhead dynamics was to make the simplifying assumption that the force sensor flexures and the rotational flexures are sufficiently stiff compared to the stamp as to be rigid in the translational direction. In this case, the inputs F_1 and F_2 can be modeled as being directly input into either end of the rigid print roll, and can be transformed to

$$F_{in} = F_1 + F_2, \tag{3.6}$$

$$T_{in} = -lF_1 + lF_2. \tag{3.7}$$

The reaction forces measured on either end by the flexural force sensors, F_1^{out} and F_2^{out}, can likewise be transformed into total force and total torque:

$$F = F_1^{out} + F_2^{out} \tag{3.8}$$

$$T = -lF_1^{out} + lF_2^{out} \tag{3.9}$$

The position coordinates may also likewise be transformed, as x_1 and x_2 in this model correspond directly to the locations of the ends of the rigid print roll:

$$x_1 = y - l\theta \tag{3.10}$$

$$x_2 = y + l\theta \tag{3.11}$$

$$\theta = \frac{1}{2l}(x_2 - x_1) \tag{3.12}$$

$$y = \frac{1}{2}(x_1 + x_2) \tag{3.13}$$

Furthermore, F and T are completely independent variables, as are F_{in} and T_{in}. This means that any inputs into F_{in} merely translate the center of mass, causing no change to T, and vice versa. It also means that the spring, mass, and damper elements of the system can be cleanly separated into rotational and translational components.

Then, only two equations of motion are required to describe this fourth-order system:

$$J_p\ddot{\theta} = T_{in} - \left(k_s^\theta + k_p^\theta\right)\theta - \left(b_s^\theta + b_p^\theta\right)\dot{\theta} \tag{3.14}$$

$$M_p\ddot{y} = F_{in} - \left(k_s^y\right)y - \left(b_s^y + b_p^y\right)\dot{y} \tag{3.15}$$

For the system in which θ and y are the outputs, the state dynamics are then represented by

$$\begin{bmatrix} \ddot{y} \\ \dot{y} \\ \ddot{\theta} \\ \dot{\theta} \end{bmatrix} = \begin{bmatrix} -\frac{b_s^y + b_p^y}{M_p} & -\frac{k_s^y}{M_p} & 0 & 0 \\ 1 & 0 & 0 & 0 \\ 0 & 0 & -\frac{b_s^\theta + b_p^\theta}{J_p} & -\frac{k_s^\theta + k_p^\theta}{J_p} \\ 0 & 0 & 1 & 0 \end{bmatrix} \begin{bmatrix} \dot{y} \\ y \\ \dot{\theta} \\ \theta \end{bmatrix} + \begin{bmatrix} \frac{1}{M_p} & 0 \\ 0 & 0 \\ 0 & \frac{1}{J_p} \\ 0 & 0 \end{bmatrix} \begin{bmatrix} F_{in} \\ T_{in} \end{bmatrix} \tag{3.16}$$

$$\begin{bmatrix} \theta \\ y \end{bmatrix} = \begin{bmatrix} 0 & 1 & 0 & 0 \\ 0 & 0 & 0 & 1 \end{bmatrix} \begin{bmatrix} \dot{y} \\ y \\ \dot{\theta} \\ \theta \end{bmatrix} + 0 \tag{3.17}$$

This two-input, two-output representation is block diagonal, as expected for a separable system. It is then much more convenient to work with this system as a pair of separate single-input, single-output systems. The force-displacement transfer functions for these systems, computed directly from the equations of motion, are given by

$$J_p \ddot{\theta} = T_{in} - \left(k_s^\theta + k_p^\theta\right) \theta - \left(b_s^\theta + b_p^\theta\right) \dot{\theta} \tag{3.18}$$

$$\frac{\theta}{T_{in}} = \frac{1}{J_p s^2 + \left(b_s^\theta + b_p^\theta\right) s + \left(k_s^\theta + k_p^\theta\right)} \tag{3.19}$$

$$M_p \ddot{y} = F_{in} - \left(k_s^y\right) y - \left(b_s^y + b_p^y\right) \dot{y} \tag{3.20}$$

$$\frac{y}{F_{in}} = \frac{1}{M_p s^2 + \left(b_s^y + b_p^y\right) s + \left(k_s^y\right)} \tag{3.21}$$

However, as discussed in earlier sections, it is necessary to control force instead of position due to the unknown profile of the stamp at any given instant. The forces on the stamp in the translational and rotational directions are given by

$$F = F_k + F_b = (k_s^y) y + (b_s^y + b_p^y) \dot{y} \tag{3.22}$$

$$T = T_k + T_b = (k_s^\theta + k_p^\theta) \theta + (b_s^\theta + b_p^\theta) \dot{\theta} \tag{3.23}$$

$$\tag{3.24}$$

Combining 3.21 and 3.24, and choosing the direction of F to be in the printing direction and T to be counterclockwise, we can write down

$$\frac{F}{F_{in}} = \frac{(b_p^y + b_s^y)s + k_s^y}{M_p s^2 + (b_p^y + b_s^y)s + k_s^y} \tag{3.25}$$

$$\frac{T}{T_{in}} = \frac{(b_p^\theta + b_s^\theta)s + (k_p^\theta + k_s^\theta)}{J_p s^2 + (b_p^\theta + b_s^\theta)s + (k_p^\theta + k_s^\theta)} \tag{3.26}$$

Qualitatively, this model consists of a complex pole and a real zero. The zero arises because there is some generalized frequency, conceptually $s = -k/b$, at which $M\ddot{y}(t) = -F_{in}(t)$, perfectly canceling the input force; and no force is transmitted to the stamp.

An empirical fit to the measured separable systems was performed. Because the second-order structure of both systems was known, the second-order parameters ζ and ω_n were derived from the experimental step response; the logarithmic decrement formula was used to estimate the parameter ζ, and peak-peak timing was used to estimate ω. The fitted transfer function was then compared to the experimental data to confirm a match, resulting in the transfer functions:

$$\frac{F}{F_{in}} = \frac{35.6s + 300000}{s^2 + 35.6s + 300000} \tag{3.27}$$

$$\frac{T}{T_{in}} = \frac{4.71s + 61.69}{s^2 + 4.71s + 61.69} \tag{3.28}$$

Frequency responses and step responses for these transfer functions are shown in 3-12 and 3-13.

This simple model depends on (1) the assumption that the two systems may be decoupled, and (2) the assumption that the points at which the input forces are applied may be abstracted to be either end of the roll, even though physically there are several components separating the voice coil actuators from the print roll. To determine how realistic this model is, the next step was to evaluate the validity of the decoupling assumption using empirical measurements.

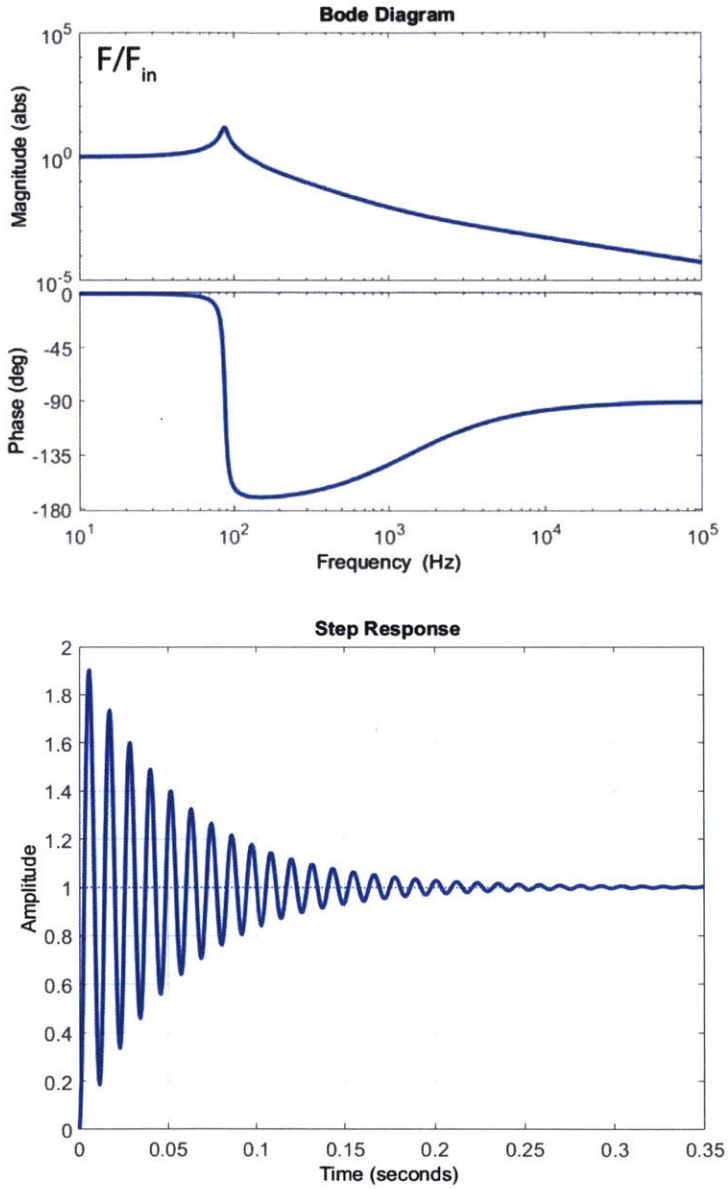

Figure 3-12: *Bode plot and step response for the F/F_{in} transfer function.* The stamp's compliance, with relatively low damping, dominates this response.

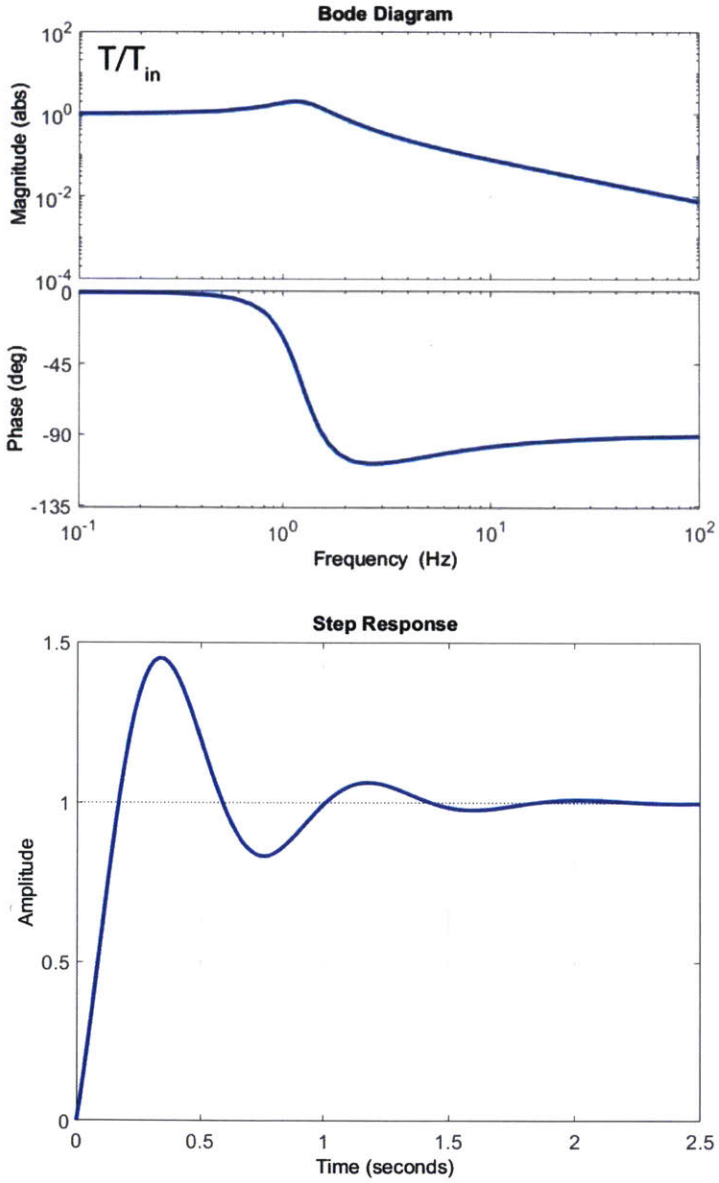

Figure 3-13: *Bode plot and step response for the T/T_{in} transfer function.* The damping inherent in the voice coils improves this open-loop step response over that of the translational direction.

Validity of Decoupling Assumption

The validity of this decoupling assumption depends on the assumption that the stiffnesses k_1^f and k_2^f, representing the flexures that transfer the input forces F_1 and F_2 to the print roll, are infinite. In practice, several possible criteria could be measured to establish this assumption:

1. k_1^f and k_2^f are sufficiently stiff that any dynamics resulting from their compliance is at frequencies well above the 1 to 100Hz frequency range of interest; by rule of thumb, $\geq$ 1000Hz; or

2. Any dynamics introduced by k_1^f or k_2^f are of sufficiently small amplitude in the frequency range of interest that they may be neglected; arbitrarily, 5% of the reference value; or

3. If the cross-term transfer functions F/T_{in} and T/F_{in} are of an insignificant magnitude compared to the matched-term transfer functions F/F_{in} and T/T_{in}; arbitrarily, less than 10% of the matched-term transfer functions over the frequency range 1 to 100Hz.

Experimentally, these criteria may be evaluated by measuring the frequency response of all four transfer functions F/F_{in}, T/T_{in}, F/T_{in}, and T/F_{in}, and comparing their magnitudes at each frequency. The results of these measurements found that the magnitude of the cross-terms F/T_{in} and T/F_{in} was typically about 20% of the magnitude of the normal terms F/F_{in} and T/T_{in}; a demonstrative dataset is shown in Figure 3-14. Additionally, the cross-term exhibited significant dynamic activity in the 1 to 100Hz range. This was taken as a violation of the separation criteria, and evidence that the assumptions that (1) the dynamics were separable, and (2) that the components intervening between the voice coil and the print roll were not sufficiently stiff to be neglected.

As detailed in Chapter 4, controller design for this decoupled model was still explored, as it was expected that the coupling would decrease performance capability, but that it might still yield a stable system with acceptable performance. However, to

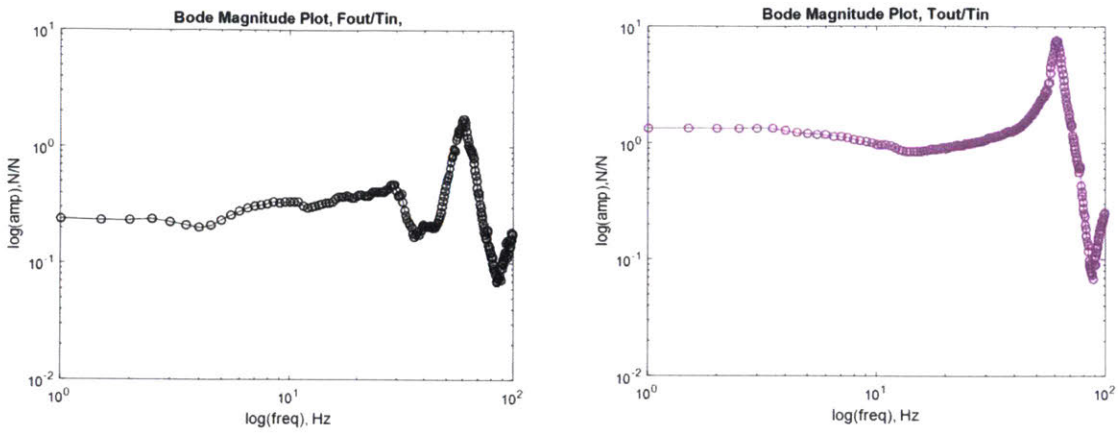

Figure 3-14: *Comparison of normal- and cross-term transfer function experimental frequency responses.* Comparing the cross-term magnitude (left) to the normal-term magnitude (right); all torques have been normalized using roll half-length l in order to be equivalent to force applied at the end of the roll. The typical magnitude of the cross term is approximately 20% of the typical magnitude of the normal term, and the cross term clearly contributes non-negligible dynamics in the frequency range of interest (1 to 100Hz).

achieve maximum performance, it was determined that a more detailed model would need to be undertaken.

3.2.2 Fully coupled system

If the assumption that the system can be modeled as two separable second-order systems is violated, the system must be considered as a full-order coupled model and treated as a multi-input, multi-output (MIMO) system.

Additionally, if the flexures cannot be modeled as rigid, their dynamics contribute to the system. Not only does this add energy storage elements to the system, but it also renders the assumptions $F_{in} = F_1 + F_2$ and $T_{in} = -lF_1 + lF_2$ invalid, as the input forces are now being applied to the roll through dynamic elements instead of directly, and sensors and actuators have become non-colocated. The system must then be modeled with the two physical inputs F_1 and F_2.

A further consequence of this increased separation between the sensors and the stamp is the fact that the sensors are now measuring a dynamic force that is not equal to the dynamic force applied to the stamp; for example, forces caused by the inertia

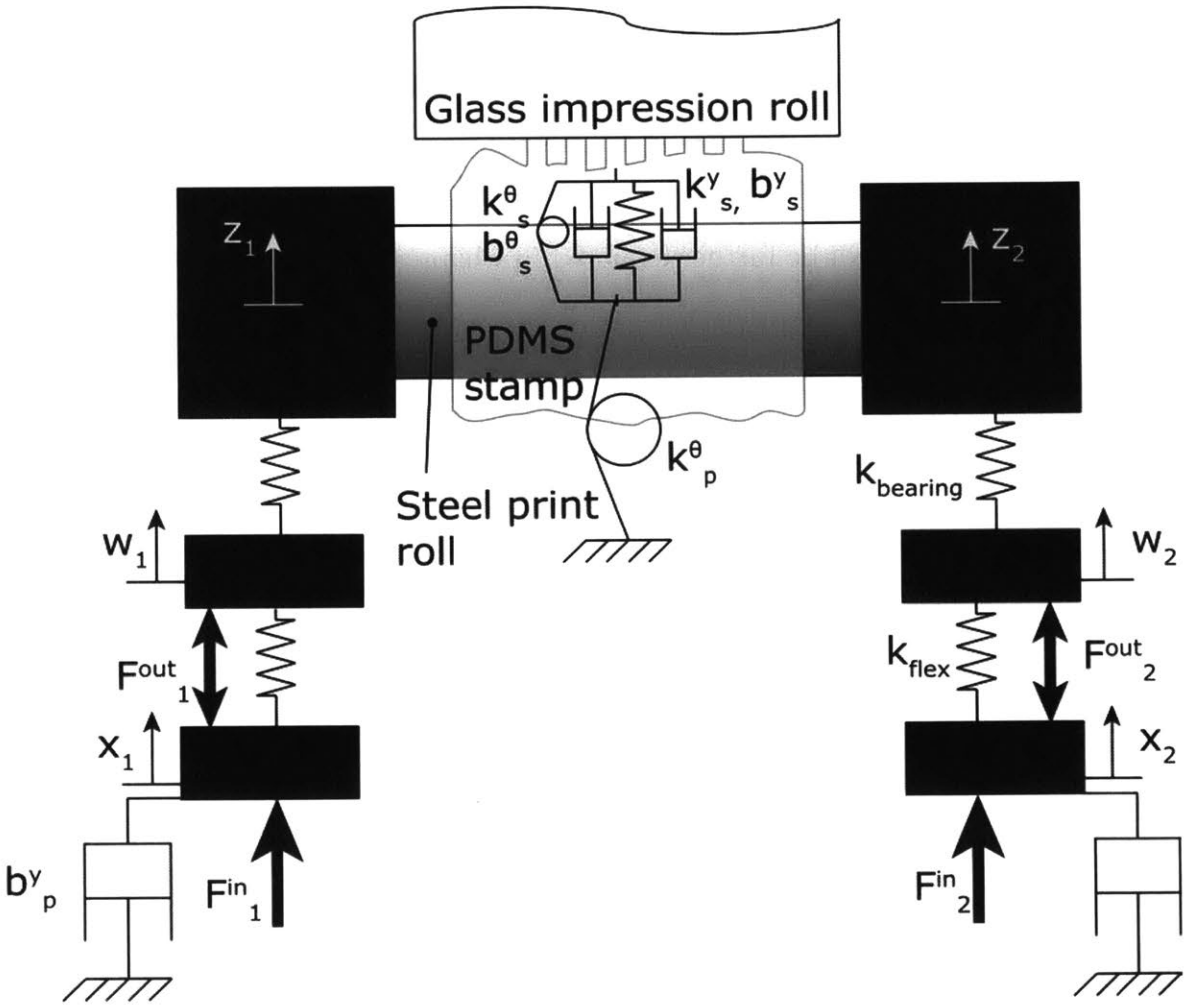

Figure 3-15: *Schematic of the full twelfth-order roll and stamp system.* With the bushing o-ring compliance included, the system order increases to 12th. Elements shown in this diagram represent their physical source, but some are dependent (such as the printhead rotational stiffness k_p^{θ} and stamp rotational stiffness k_s^{θ}).

of the mass associated with the displacement w_1 in Figure 3-15 will be reflected in force measurement F_1^{out}, but will not necessarily be directly applied to the stamp. A simulated frequency response to the input F_1 using the displacements w_1 and z_1 is shown in 3-16. Below 10Hz, the two displacements track well except for a 180 degree phase offset. Above that frequency, the tracking grows more and more approximate; since the force sensor is considered to measure stamp reaction forces under the assumption that $w_1 \approx z_1$, and this assumption is now violated, the sensor does not even accurately measure higher-frequency dynamic stamp reaction forces. This could be corrected if the flexure sensor measured between w_1 and z_1 instead of x_1 and w_1; this idea will be further explored in Chapter 5.

A key question was as to the nature of the compliant components between the actuators and the print roll. Initially, it was known that compliance had been inserted between the actuator and the print roll by installing the force measurement flexures, though efforts were made to keep these sensors sufficiently stiff that they could be abstracted as rigid; adding these dynamics to the system model created an 8th-order coupled MIMO system. However, as will be shown in section 3.3, physical measurements of the system indicated that its order was still greater than 8th, which implied that there was an additional compliance somewhere in the system. This compliance was discovered to derived from the installation method of the print roll air bushings; the cylindrical air bushing units have rubber o-rings wrapped around their outer diameter, which allow them to be pressed and elastically centered within a specialized pillow block. (Figure 3-17 shows the o-rings and the location of the compliance.) Per manufacturer application guidelines, the bushings should then be potted in the pillow blocks by injecting epoxy into a port in the block. Unbeknownst to the author, this step was never performed; and on the scale of the microcontacting printing process, where 10μm features are being compressed by only a few microns, the resulting additional compliance from the rubber o-rings had a significant effect, increasing the system order. Derivation of the intermediate 8th order system is omitted here in favor of the empirically verified 12th order system.

The configuration of the system is shown in 3-15. Due to dependent elements, the

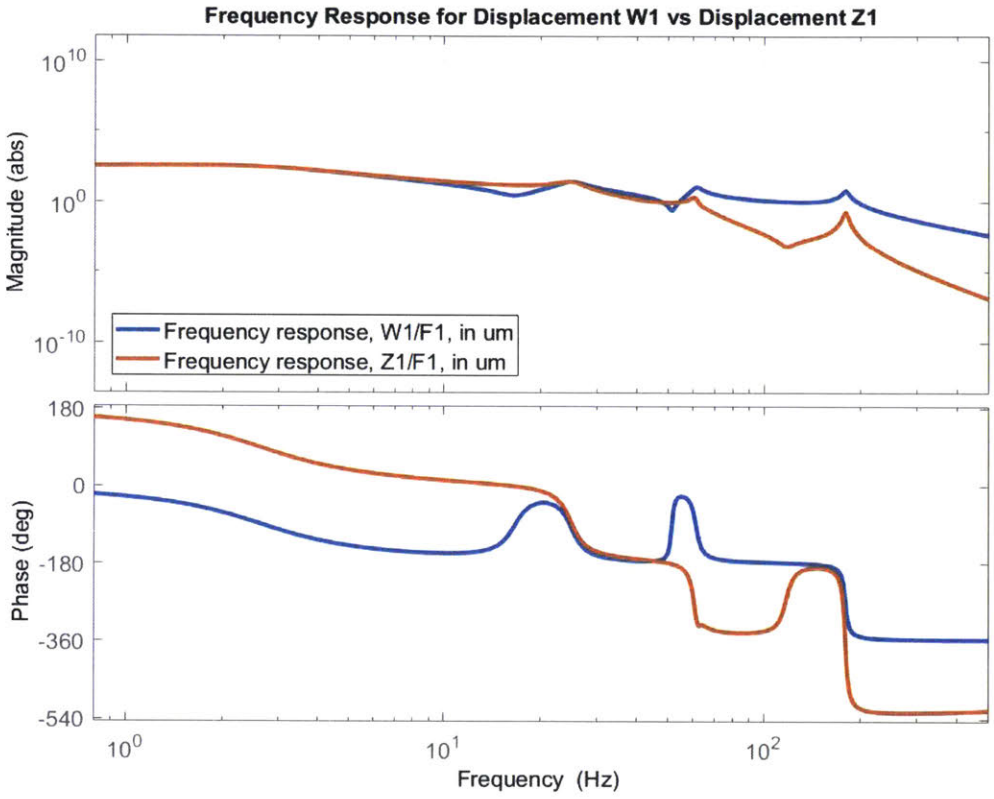

Figure 3-16: *Simulated frequency response for displacements w_1 and z_1 to input F_1.* Below 10Hz, the assumption $|z_1| \approx |w_1|$ is true. Between 10Hz and 60Hz, w_1 approximately tracks z_1, but differs by up to 10μm. Above 60Hz (the resonance frequency of the o-ring compliance), z_1 (above the compliance) is no longer accurately tracked by w_1 (below the compliance). Also notable is that at frequencies below 10Hz, w_1 and z_1 are offset in phase by 180 degrees.

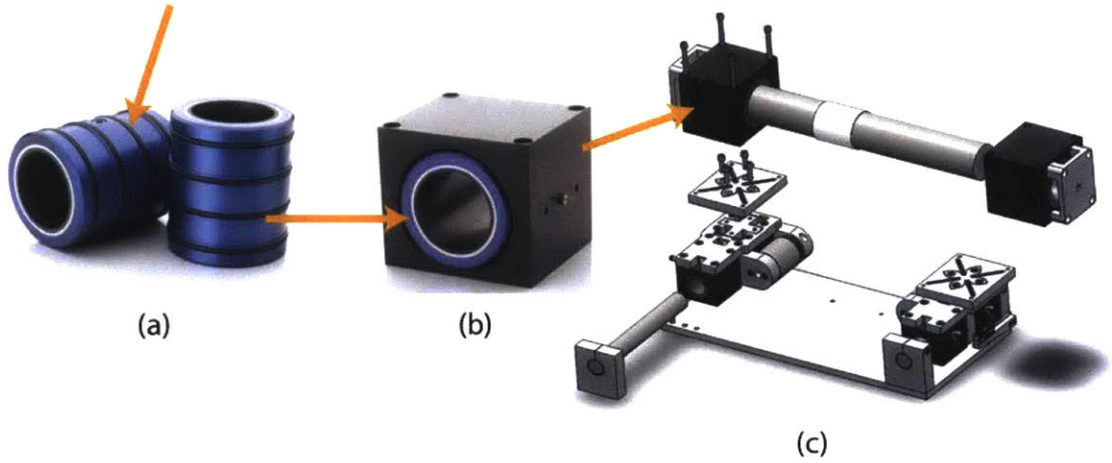

Figure 3-17: *Location of additional compliance created by air bushing o-ring mounts.* Note that a metric air bushing (anodized blue by the manufacturer) is shown for clarity; the air bushing on the printhead is a standard size (anodized black). The o-rings are the black bands indicated by an arrow in (a). This air bushing is inserted axially into a pillow block in (b), centered by the o-rings. The pillow block was then integrated into the printhead, (c).

total system order is 12.

Notation for this section is given in the table below.

Variable	**Physical meaning**
$2l$	Roll width from rail to rail
F_1	Outboard voice coil force input
F_2	Inboard voice coil force input
F_1^{out}	Outboard flexural force measurement
F_2^{out}	Inboard flexural force measurement
F	Total force exerted on print roll COM
T	Total torque exerted about print roll COM
x_1	Position of the outboard translational base
x_2	Position of the inboard translational base
w_1	Position of the outboard printhead pillow block
w_2	Position of the inboard printhead pillow block
z_1	Position of the outboard end of the print roll
z_2	Position of the inboard end of the print roll

Variable	Physical meaning
J_p	Print roll rotational inertia
M_p	Print roll mass
k_{lf1}	Outboard flexure stiffness
k_{lf2}	Inboard flexure stiffness
b_{lf1}	Outboard flexure damping
b_{lf2}	Inboard flexure damping
k_{uf1}	Outboard upper (bearing) compliance
k_{uf2}	Inboard upper (bearing) compliance
b_{uf1}	Outboard upper (bearing) damping
b_{uf2}	Inboard upper (bearing) damping
b_{vc1}	Outboard voice coil damping coefficient
b_{vc2}	Inboard voice coil damping coefficient
M_u	Upper (bearing) mass
M_{vc}	Mass of the translational base
k_t	Rotational flexure stiffness
k_{sy}	Stamp translational stiffness
b_{sy}	Stamp translational damping coefficient
$k_{s\theta}$	Stamp rotational stiffness
$b_{s\theta}$	Stamp rotational damping coefficient

The four equations of motion for the translational masses are given by:

$$M_{vc}\ddot{x}_i = F - b_{vc,i}\dot{x}_i - b_{lf,i}\left(\dot{x}_i - \dot{w}_i\right) - k_{lf,i}\left(x_i - w_i\right) \tag{3.29}$$

$$M_f\ddot{w}_i = -k_{lf,i}\left(w_i - x_i\right) - b_{lf,i}\left(\dot{w}_i - \dot{x}_i\right) - k_{uf,i}\left(w_i - z_i\right) - b_{uf,i}\left(w_i - z_i\right) \tag{3.30}$$

Two additional equations of motion for the printhead, given in the variables θ and y, are given by:

$$J_p\ddot{\theta} = -k_{st}\theta - b_{st}\dot{\theta} - k_t\theta - k_{uf1}(w_1 - z_1) - b_{uf1}(\dot{w}_1 - \dot{z}_1) - k_{uf2}(z_2 - w_2) - b_{uf2}(\dot{z}_2 - \dot{w}_2) \tag{3.31}$$

$$M_p\ddot{y} = -k_{sy}y - k_{uf1}(z_1 - w_1) - b_{uf1}(\dot{z}_1 - \dot{w}_1) - k_{uf2}(z_2 - w_2) - b_{uf2}(\dot{z}_2 - \dot{w}_2) \tag{3.32}$$

y and θ are no longer our chosen state variables, so we must change variables using the fact that

$$2l\theta = z_2 - z_1 \tag{3.33}$$

$$y = \frac{1}{2}(z_1 + z_2) \tag{3.34}$$

Changing variables and solving the two printhead equations of motion for z_1 and z_2 provide the two additional equations of motion. Sparing the reader the algebra, the final result is a state space representation of the form:

$$\begin{bmatrix} \ddot{x}_1 \\ \dot{x}_1 \\ \ddot{x}_2 \\ \dot{x}_2 \\ \ddot{w}_1 \\ \dot{w}_1 \\ \ddot{w}_2 \\ \dot{w}_2 \\ \ddot{z}_1 \\ \dot{z}_1 \\ \ddot{z}_2 \\ \dot{z}_2 \end{bmatrix} = A \begin{bmatrix} \dot{x}_1 \\ x_1 \\ \dot{x}_2 \\ x_2 \\ \dot{w}_1 \\ w_1 \\ \dot{w}_2 \\ w_2 \\ \dot{z}_1 \\ z_1 \\ \dot{z}_2 \\ z_2 \end{bmatrix} + \begin{bmatrix} \frac{1}{M_{vc}} & 0 \\ 0 & 0 \\ 0 & \frac{1}{M_{vc}} \\ 0 & 0 \\ 0 & 0 \\ 0 & 0 \\ 0 & 0 \\ 0 & 0 \\ 0 & 0 \\ 0 & 0 \\ 0 & 0 \\ 0 & 0 \end{bmatrix} \begin{bmatrix} F_1 \\ F_2 \end{bmatrix} \tag{3.35}$$

where the matrix A is given by (3.36).

$$A = \begin{bmatrix}
-\frac{b_{vc1}+b_{lf1}}{M_{vc}} & -\frac{k_{lf1}}{M_{vc}} & 0 & 0 & \frac{b_{lf1}}{M_{vc}} & \frac{k_1^f}{M_{vc}} & 0 & 0 & 0 & 0 & 0 & 0 \\
1 & 0 & 0 & 0 & 0 & 0 & 0 & 0 & 0 & 0 & 0 & 0 \\
0 & 0 & -\frac{b_{vc2}+b_{lf2}}{M_{vc}} & -\frac{k_{lf2}}{M_{vc}} & 0 & 0 & \frac{b_{lf2}}{M_{vc}} & \frac{k_{lf2}}{M_{vc}} & 0 & 0 & 0 & 0 \\
0 & 0 & 1 & 0 & 0 & 0 & 0 & 0 & 0 & 0 & 0 & 0 \\
\frac{b_{lf1}}{M_u} & \frac{k_{lf1}}{M_u} & 0 & 0 & -\frac{b_{lf1}+b_{uf1}}{M_u} & -\frac{k_{lf1}+k_{uf1}}{M_u} & 0 & 0 & \frac{b_{uf1}}{M_u} & \frac{k_{uf1}}{M_u} & 0 & 0 \\
0 & 0 & 0 & 0 & 1 & 0 & 0 & 0 & 0 & 0 & 0 & 0 \\
0 & 0 & \frac{b_{lf2}}{M_u} & \frac{k_{lf2}}{M_u} & 0 & 0 & -\frac{b_{lf2}+b_{uf2}}{M_u} & -\frac{k_{lf2}-k_{uf2}}{M_u} & 0 & 0 & \frac{b_{uf2}}{M_u} & \frac{k_{uf2}}{M_u} \\
0 & 0 & 0 & 0 & 0 & 0 & 1 & 0 & 0 & 0 & 0 & 0 \\
0 & 0 & 0 & 0 & 0.5(ii-aa) & 0.5(jj-bb) & 0.5(kk-cc) & 0.5(ll-dd) & 0.5(mm-ee) & 0.5(nn-ff) & 0.5(oo-gg) & 0.5(pp-hh) \\
0 & 0 & 0 & 0 & 0 & 0 & 0 & 0 & 1 & 0 & 0 & 0 \\
0 & 0 & 0 & 0 & 0.5(ii+aa) & 0.5(jj+bb) & 0.5(kk+cc) & 0.5(ll+dd) & 0.5(mm+ee) & 0.5(nn+ff) & 0.5(oo+gg) & 0.5(pp+hh) \\
0 & 0 & 0 & 0 & 0 & 0 & 0 & 0 & 0 & 0 & 1 & 0
\end{bmatrix} \tag{3.36}$$

(3.37)

$$aa = \frac{2l}{J_p}(-lb_{uf1}); \quad bb = \frac{2l}{J_p}(-lk_{uf1}); \; cc = \frac{2l}{J_p}(lb_{uf2}); \; dd = \frac{2l}{J_p}(lk_{uf2});$$

$$ee = \frac{2l}{J_p}(lb_{uf1} + b_{st}/(2l)); \; ff = \frac{2l}{J_p}(lk_{uf1} + k_{st}/(2l) + k_t/(2l));$$

$$gg = \frac{2l}{J_p}(-lb_{uf2} - b_{st}/(2l)); hh = \frac{2l}{J_p}(-lk_{uf2} - k_{st}/(2l) - k_t/(2l));$$

$$ii = \frac{2}{M_p}(b_{uf1}); \; jj = \frac{2}{M_p}(k_{uf1}); \; kk = \frac{2}{M_p}(b_{uf2}); \; ll = \frac{2}{M_p}(k_{uf2});$$

$$mm = \frac{2}{M_p}(-b_{sy}/2 - b_{uf1}); \; nn = \frac{2}{M_p}(-k_{sy}/2 - k_{uf1});$$

$$oo = \frac{2}{M_p}(-b_{sy}/2 - b_{uf2}); \; pp = \frac{2}{M_p}(= k_{sy}/2 - k_{uf2})$$

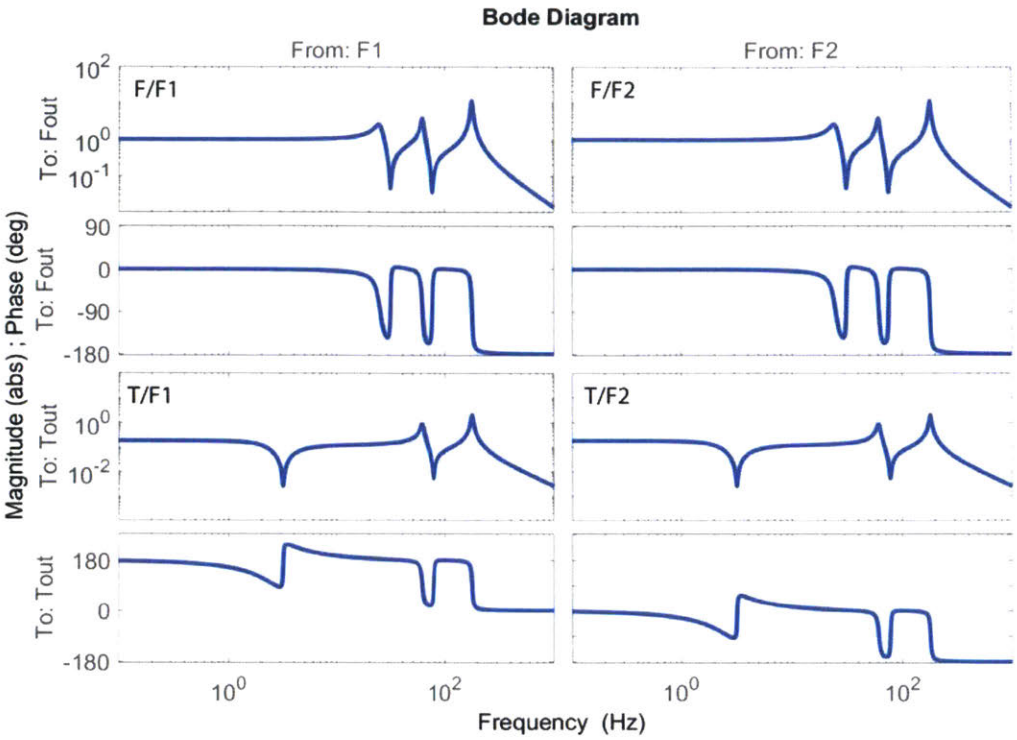

Figure 3-18: *Frequency response for all four transfer functions of the 12th order MIMO system.* As expected for the roughly symmetric system, for a chosen output, either the $F1$ or $F2$ input gives approximately the same response. Numerical parameters to generate this model are given in Appendix B.

The output measurements F and T are then given by

$$\begin{bmatrix} F \\ T \end{bmatrix} = \begin{bmatrix} 0 & k_{lf1} & 0 & k_{lf2} & 0 & -k_{lf1} & 0 & -k_{lf2} & 0 & 0 & 0 & 0 \\ 0 & -lk_{lf1} & 0 & lk_{lf2} & 0 & lk_{lf1} & 0 & -lk_{lf2} & 0 & 0 & 0 & 0 \end{bmatrix} x + 0u \tag{3.38}$$

The full parameters and Matlab code that replicates this model is given in Appendix B.

The frequency response of this model, with empirically determined constants, is shown in 3-18. (Methods used to identify these cosntants will be detailed in the next section.) The first thing an observer might note is that this frequency response shows a classic "stacked compliance" behavior; that is, pairs of complex poles grouped with associated complex zeros that create a "peak-trough" pair. This is expected from the system diagrammed in 3-15, which clearly has stacked compliances in the load transmission path. Overall, any input-to-output pairing has 12 poles and 10 zeros.

This system is both uncontrollable and unobservable. The rank of both the controllability matrix and the observability matrix is 6 instead of the full 12. This means that there are some system modes that cannot be affected by the inputs, or cannot be measured by the outputs. In general, this is not always a problem; if the uncontrollable modes are high frequency or small in amplitude (e.g. well-damped), controlling or observing them may not be necessary to achieving desirable performance, and they can be left untouched in control system design efforts.

In a canonical stacked compliance response as in 3-18, transmission zeros (appearing as anti-resonances in the frequency response) also arise. While resonances and DC gains can be manipulated using pole placement, these open-loop zeros cannot be modified using control, and will retain their frequency and magnitude. This could be acceptable if F were the only output of interest, as the transmission zeros occur at frequencies greater than 20Hz; this could make a 10Hz bandwidth achievable. But, unfortunately for this system, there is a slow, uncontrollable, poorly damped mode in the T output system that falls around 1-3Hz in frequency. Physically, this mode corresponds to the slewing (rotating) mode of the heavy print roll rolling back and force on the stamp; qualitatively, the pole placement controller cannot remove this mode's associated zero from the closed-loop response, and thus cannot reject disturbances or enforce following for frequency content in that range. More detail on these concepts will be presented in Chapter 4.

3.3 Printhead System Identification

The model presented in the prior chapter was identified after a great deal of effort. When the development of a controller for the system began, the simple decoupled model was assumed based on prior knowledge of the system, but initial experimental results differed significantly from expected behavior. The flexural stiffness was then incorporated into the model, changing its structure from two SISO second-order systems to one MIMO eighth-order system. A full-state feedback controller with a state estimator was developed and implemented for this system as well, but again

experimental results did not match expected behavior. Again, the conclusion was that something about the model must be incorrect, and extensive efforts to identify the system configuration, order, and parameters were undertaken. After these efforts, the system was determined to have a twelfth-order MIMO structure, and a model was successfully fit.

A multi-pronged approach was taken to identifying the correct system model. This approach included development of a swept sine frequency response measurement; Fourier transform measurements of impulse and white noise responses; system modification and isolation; and direct component measurements.

3.3.1 System Identification Tools

To enable direct measurement of the system's response, a set of tools and methods was developed to enable a measurement of output magnitude versus frequency.

Frequency Content Measurements

One of the first techniques developed was a frequency content measurement. A data sample of the variable of interest was recorded using the LabVIEW software, and this data sample was passed through a simple Matlab script that produced a plot of the frequency content of the signal. This measurement was able to identify both mechanical and electrical frequency content. (While mehcanical frequency content typically appears as a broad, "messy" peak, electrical frequency content appears as a very sharp, narrow peak. Electrical noise at 30Hz and 60Hz was observed and mitigated through the elimination of ground loops and improved shielding.) An example output of this plot is shown in 3-19.

This tool was most useful to identify the range of dynamics present and their relative magnitudes. Initially, it was used to identify a structural vibration issue; the support structure for the printing machine has a natural frequency of 4.5Hz, which was being activated by ambient vibrations such as nearby air handling equipment and street traffic, and caused disturbance displacements in the printhead of 6-10μm. By

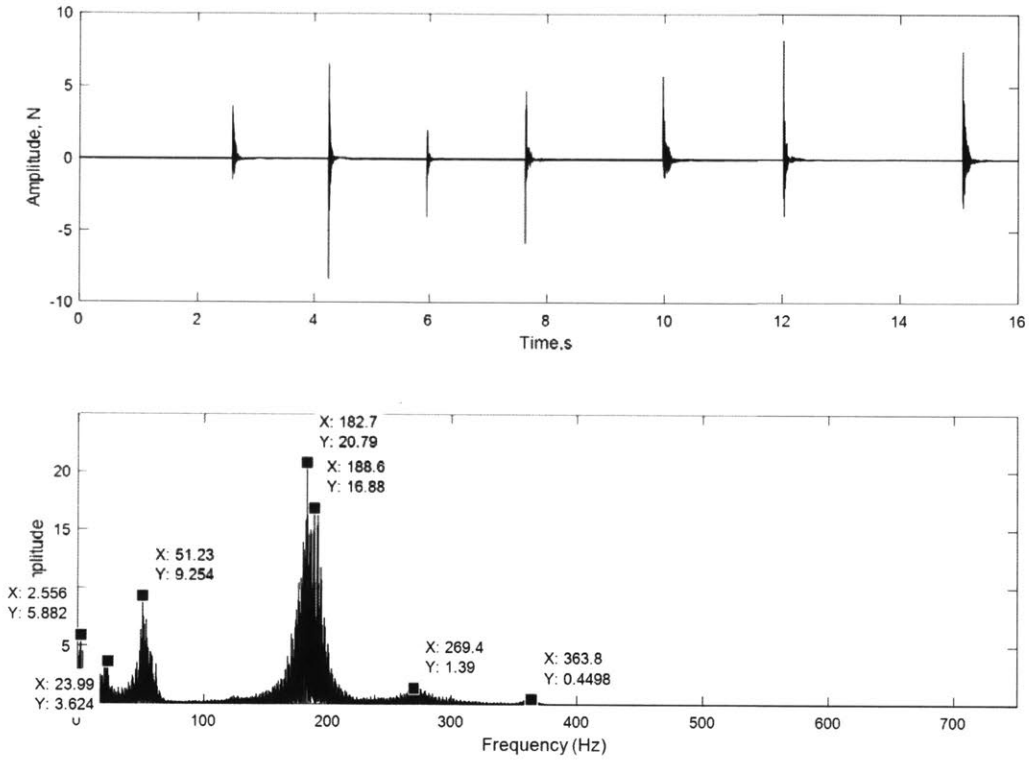

Figure 3-19: *Frequency response of manual impulse testing.* Annotated experimental measurement of frequency content in F created with manual impulse testing, in which hand tools were used to impart sharp forces to the center of the print roll. Double peaks are overlaid at the 180Hz range, as suggested by the broad spread there. High frequency behavior not included in the model also appears at 269Hz and 364Hz. Also notable here is that frequency content from the T response, such as the 2.5Hz mode, is "cross-contaminating" due to nonidealities of the test: the force impulse will also generate a torque input if applied off-center.

adding mass to the structure and inserting vibration-dampening polymer pads where it contacted the floor, the 4.5Hz vibration was increased in frequency and reduced in amplitude to the point where it was no longer measurable at the printhead. Similarly, 60Hz electrical noise in the analog flexure sensors was detected and traced back to the unshielded cooling fan installed in the electronics cabinet.

However, this tool was not very useful for system identification, for several reasons: first, it gave no indication of anti-resonances; second, though it could identify the frequency location of resonances, it was prone to cross-contamination from imperfect testing; and third, peaks occurring at the same frequency (due to, for example, mirrored system components) could mask each other. (In terms of imperfect testing, an example is that real-world imperfections such as the stamp being mounted off-center could create a signal in the output T even if $F_1 = F_2$ was true.) A more informative tool would be necessary in order to identify a system model.

Frequency Response Measurement

A far more useful tool was an experimental frequency response measurement tool. This custom tool was integrated into the LabVIEW control VI as a feature, and a Matlab script to post-process the measured data was also constructed. The tool operated on a very simple principle: a pre-generated swept sine signal was passed to one or both actuators on top of an existing preload, and the resulting force and displacement was measured. Using knowledge of the pre-generated swept sine signal (which typically was set to measure 10 cycles at each 1.0 or 0.5 Hertz step), the output magnitude at a given frequency could be directly computed. (Attempts to directly compute the phase were unsuccessful due mainly to degradation of the pre-generated sine signal as the swept sine frequency approached the Nyquest frequency. It was never deemed necessary to reconstruct the input sine wave to compute phase when magnitude was readily available, though in retrospect a reliable phase measurement would have been very enlightening.) Sample results of this measurement are shown in 3-20, and the corresponding time series and frequency content in shown in 3-21.

These measurements were the first certain indicators that the second-order de-

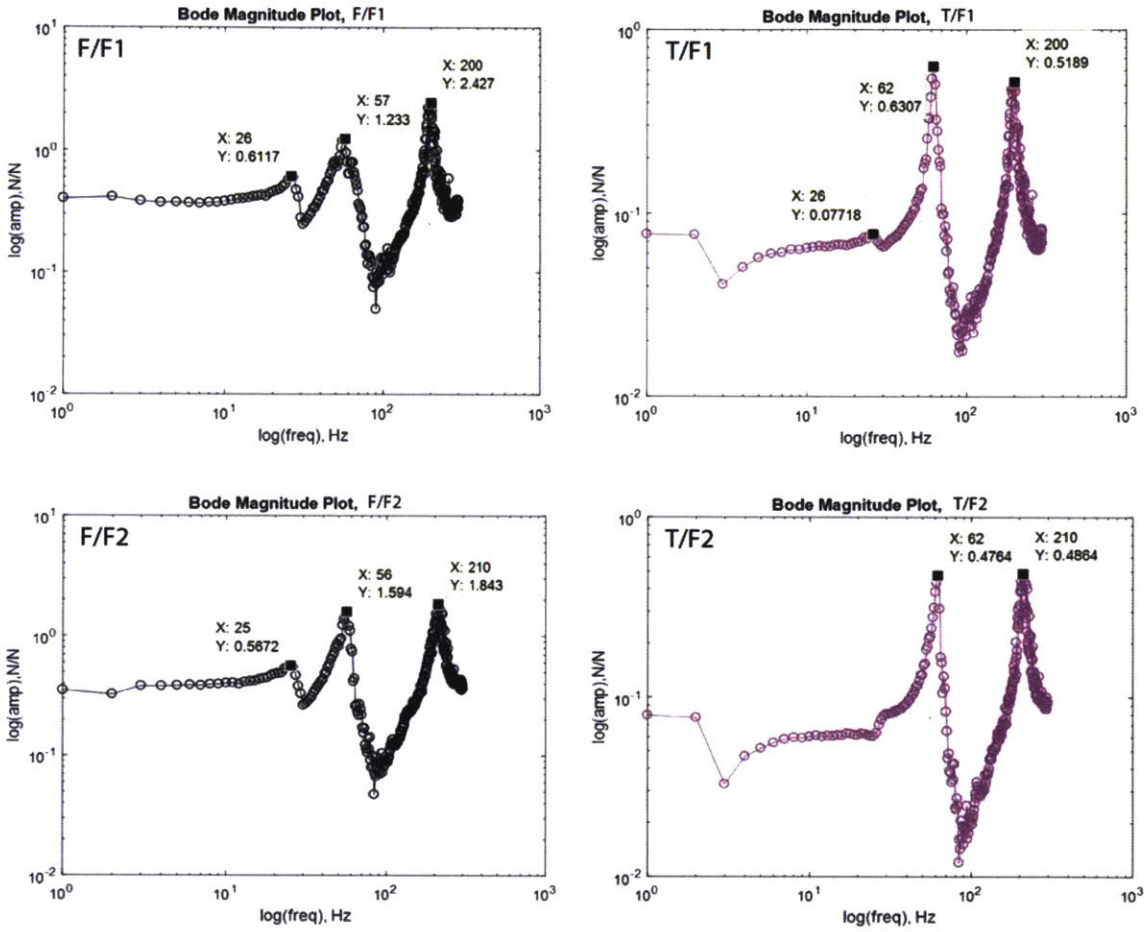

Figure 3-20: *Experimental measurements of printhead frequency response magnitude.* F_1 (top) and F_2 (bottom) versus F (black) and T (magenta) are shown. Peak frequencies and magnitudes are labeled; in the data labels, X indicates the frequency, and Y indicates amplitude normalized by the input signal. Exact peak locations were sensitive to parasitic friction induced in the system by removal and replacement of the print roll.

coupled model was incorrect. Two obvious resonant peaks at 60Hz and 180Hz and a suggestion of a third peak around 25-30Hz are visible, as well as the complex zeros resulting from the stacked compliances. What is not immediately clear from this plot is that the peaks at 50-60Hz and 180-190Hz are actually both double, overlaid peaks. This was deduced by measuring the slope on either side of the resonant peak and by comparing the peak's shape to a single pole pair versus a double pole pair. Additionally, the two peaks at 180-190Hz could be forced to separate if additional friction was induced in either b_{vc1} or b_{vc2}, such as if a component was rubbing or dragging due to an assembly error. It turns out that, very sensibly, the nearly-identical masses and stiffnesses associated with the two flexure sensors create frequency peaks that overlay; and the same phenomenon is associated with $k_{uf,i}$, the bearing stiffnesses.

This realization led to a revision of the model from 8th order to 12th order, but did not grant much insight into the actual lumped parameters that made up the model. Part of the underlying reason for this is that the frequency location of each peak and zero depends in a complex and coupled way on the many lumped parameters describing the system, most of which were unknown.

Parameter Estimation

To attempt to identify the model parameters for a given structure, a number of techniques were employed. These techniques included SISO and MIMO system fit finders included in Matlab system toolboxes and an adaptive convergence fit estimator implementing techniques developed by Annaswamy.

The first attempts were to use the Matlab `tfest()` tool to construct a single-input, single-output estimation for a particular combination of inputs and outputs. `tfest()` has several underlying methods that it may use to find a fit; in this case, a continuous-time transfer function was estimated using time-domain data, so the method underling `tfest()` was a nonlinear least-squares search, based on a set of initial parameter guesses. [52] The search aimed to minimize the weighted prediction error between the timeseries data input and a model, and successfully found fairly accurate numerical transfer function fits for the measured data for each SISO transfer

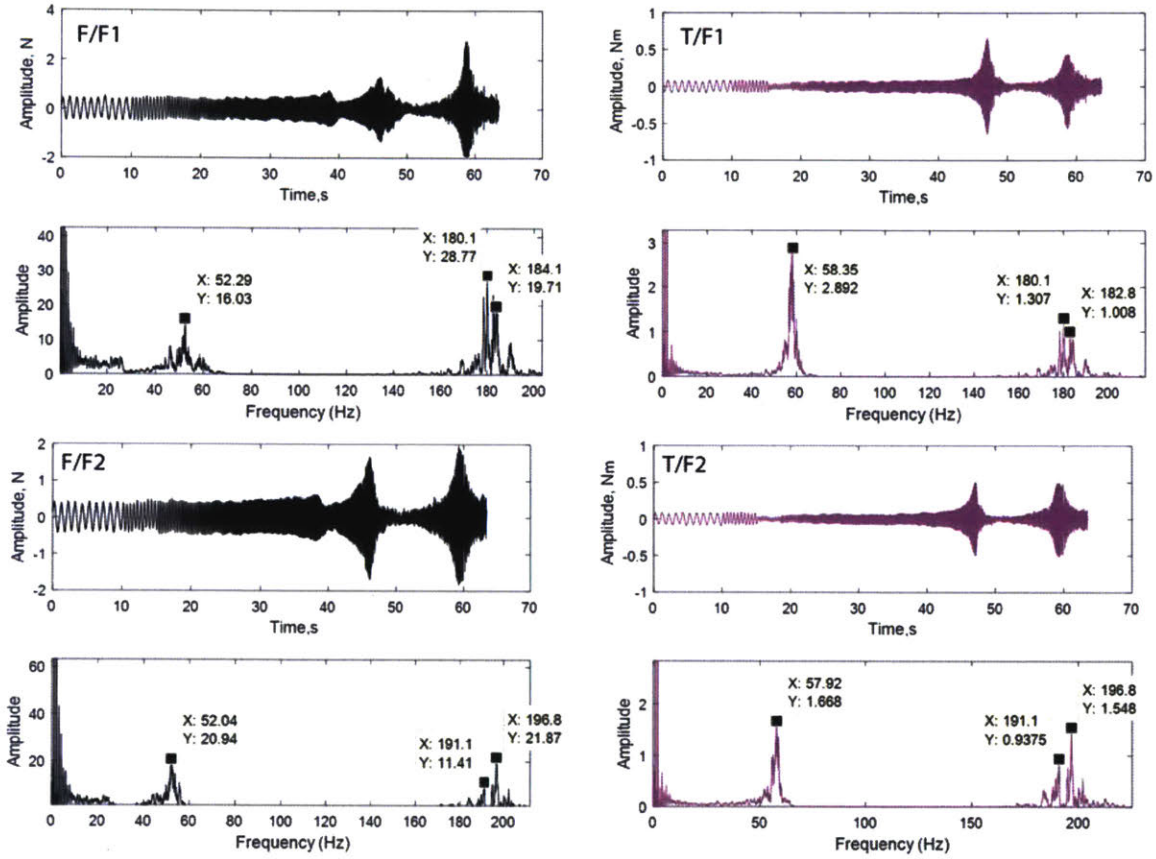

Figure 3-21: *Time series and frequency content for the measurements corresponding to the Bode magnitude plots in 3-20.* In the time series, the presence of resonances and anti-resonances can clearly be visually identified. In the data labels in these plots, X again corresponds to frequency, and Y to a dimensionless amplitude related to force for F and torque for T.

function, e.g. F/F_1.

The next step was then to use an optimization function (`lsqnonlin()`) to attempt to match an analytical transfer function with some unknown parameters, derived from the MIMO model, to this numerical fit. The numerical fit computed by `tfest()` and experimental data were taken as "truth;" the analytical transfer function, given proper values for all unknown parameters, should become numerically equivalent to the fit. `lsqnonlin()` was thus used to fit a least-squares set of bounded numerical values to the unknown parameters (e.g. the stiffness of the flexure sensors should be between 0.8 N/μm and 1.2 N/μm). `lsqnonlin()` starts at an initial guess and uses a nonlinear optimization to iteratively move the guess along a gradient to minimize a specified error function. [53] Two different functions were used; one computed error between a given model's frequency response magnitude and the numerical "truth" model's frequency response magnitude, and the other computed the error between the numerical "truth" and analytical guess transfer function characteristic polynomials.

This strategy did not yield success because the transfer function was very insensitive to the values of k_{st}, k_{sy}, b_{st} and b_{sy}—that is, the unknown and variable stamp stiffness and damping parameters. When given the same dataset and known set of dummy parameters but a varying starting point, the optimization algorithm would find significantly varying values for these parameters, as shown in 3-22.

The second attempts focused on using the Matlab `ssest()` and `greyest()` tools. Both of these tools were used to fit two-input, two-output experimental time data, in which a filtered white noise input was given to both F_1 and F_2, and the resulting outputs F and T measured.

`ssest()` uses input data (including, in this case, system order) and a prediction error minimization algorithm to fit a state-space form system. [54, 55] This method is detailed well in Ljung's text [56], but in essence minimizes a cost function, which is a weighted norm of the prediction error for a particular model.

Conceptually (for the scalar case), the cost function is defined as $V_N(G, H) = \sum_{t=1}^{N} e^2(t)$, where, for a linear model, $e(t)$ is the difference between the measured and predicted model output; i.e. $e(t) = H^{-1}(q)\,[y(t) - G(q)u(t)]$. [55]

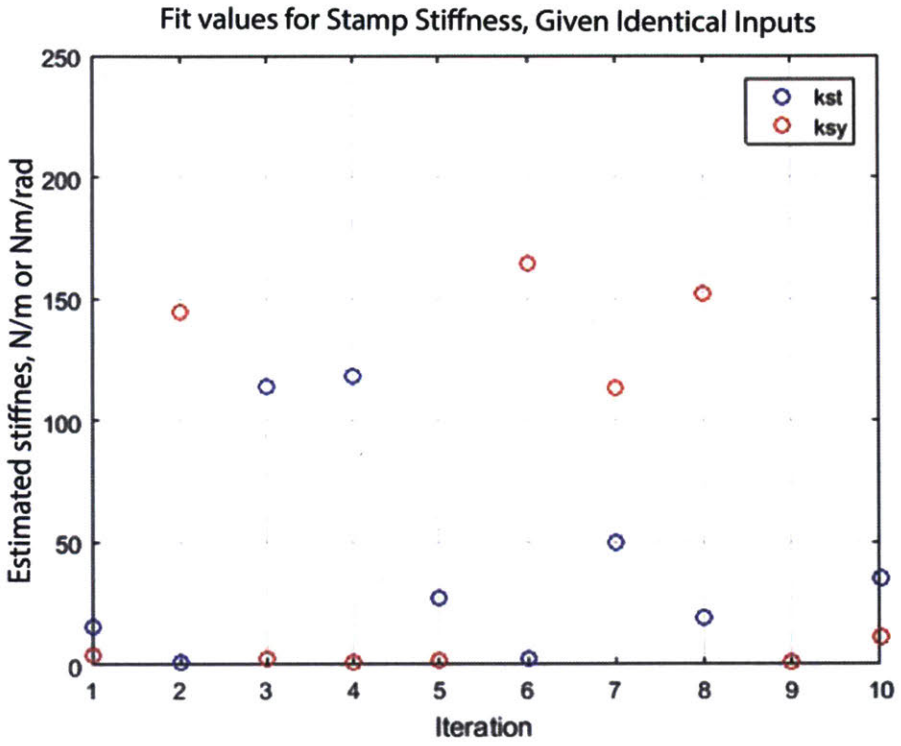

Figure 3-22: *Varying parameter fit results with identical search inputs.* The SISO search method found different results for the stamp rotational stiffness k_{st} and stamp translational stiffness k_{sy}, even though the same system data and dummy parameters were passed to the search on each iteration, and only the initial starting point was varied.

For any set of experimental data, `ssest()` was consistently unable to find a good fit; only a small fraction of the measured output was accounted for by the fit model. It is hypothesized that a variety of factors contributed to the failure, including the overlaying of the 60Hz and 180Hz modes; the unobservability of the system; and the "cross-contamination" between the F and T measurements due to imperfect testing.

The next effort was to reduce the number of free parameters that any estimator had to attempt to fit in order to better bound the problem. Because parameters like the roll mass were known or easy to measure, they did not need to be fit during the estimation process. The Matlab `greyest()` tool is a"grey box" estimator tool that fits state-space systems with some known and some unknown parameters. It uses the same underlying prediction error minimization algorithm as `ssest()`, but provides an easier input structure to specify which parameters and known and unknown. [55, 57] Unfortunately the greybox tool also did not produce successful results, stymied by the same issues as `ssest()`.

One final parameter fitting effort was attempted using adaptive techniques developed by Annaswamy [58] and extended by Limoge [59]. These techniques conceptually rely on the choice of a simple adaptive law that will converge the error in a set of parameters to zero, given sufficient information in the form of a time series of system states.

Given a MIMO LTI system with unknown parameters:

$$\dot{x_p}(t) = A_p x_p(t) + B_p u(t), \tag{3.39}$$

one may choose an estimator of the form

$$\dot{\hat{x}}_p(t) = A_m \hat{x}_p(t) + \left[\hat{A}_p(t) - A_m\right] x_p(t) + \hat{B}_p(t) u(t), \tag{3.40}$$

where A_m is an asymptotically stable matrix chosen as an initial estimate, and $\hat{A}_p$ and $\hat{B}_p$ are both estimated parameter matrices. The error between the estimated

states and parameters and the actual states and parameters may be defined as

$$e(t) = \hat{x}_p(t) - x_p(t) \tag{3.41}$$

$$\Phi(t) = \hat{A}_p(t) - A_p \tag{3.42}$$

$$\Psi(t) = \hat{B}_p(t) - B_p, \tag{3.43}$$

and the error dynamics described by the equation

$$\dot{e}(t) = A_m e(t) + \Phi(t)x_p(t) + \Psi(t)u(t). \tag{3.44}$$

Annaswamy shows in [58] that if the adaptive laws are chosen to be

$$\dot{\hat{A}}_p(t) = \dot{\Phi}(t) = -Pe(t)x_p^T(t) \tag{3.45}$$

$$\dot{\hat{B}}_p(t) = \dot{\Psi}(t) = -Pe(t)u^T(t), \tag{3.46}$$

where P is a symmetric positive-definite matrix derived from A_m, the error will asymptotically approach zero as $t \to \infty$. The relationship between P and A_m is given by

$$A_P^T + PA_p = -Q_0, \tag{3.47}$$

where Q_0 is an arbitrary symmetric positive-definite matrix. Implementation of this method requires two pieces of information: first, a canny choice of Q_0 (often, the identiy matrix will do); and second, full state knowledge of $x_p(t)$ over some time period, in order to compute error.

Though the algorithm could correctly converge to a known model when given data generated from that model, it could not be applied to identifying the unknown experimental model because the algorithm required complete state information in order to converge. Even by utilizing both the force and displacement measurements—assuming they are independent and their time derivatives can be accurately calculated—only eight of the twelve states can be represented. (Initially,

when the system was thought to be eighth order, this technique seemed promising.) Four of them still remain unknown, and an observer to compute them would require a system model, which (circularly) is unknown.

Work by Limoge [59] extends the above technique to be able to estimate higher-order systems using reduced order observations. The significant effort required to apply this work to the experimental system was not undertaken, given a low perceived chance of success.

System Isolation and Measurement Techniques

At this point, efforts using estimation tools were ceased, and efforts to measure as many potential system components as possible were undertaken. The rationale was that if enough known parameters could be established, and the unknown parameters could be bounded, either a manual adjustment of the system parameters or a simple search algorithm could be applied to establish the true system model. These efforts took two forms: measuring each component of the system's inherent properties in isolation (where possible), and using restraints to remove dynamics from the system in order to study the behavior of a simplified "partial" system; an example of one of these "partial system" experiments is shown in Figure 3-23.

Measuring each component consisted of disassembling the machine and weighing each mass component individually; and measuring the stiffnesses via force-displacement of the flexure sensors and the rotational bearing flexures. An estimate of the stamp stiffness had been measured by Libert [10]. This left the free parameters as the upper o-ring compliances, $k_{uf,i}$ (which were assumed to be very similar if not identical due to symmetry), and all damping coefficients.

The partial system was constructed by restraining pieces of the system using C-clamps and slider clamps. Measurements of this restrained system did offer useful information, such as confirmation that the 180Hz mode was coming from the flexures, and the 60Hz mode was coming from elements between the translational base and the print roll. However, the measurements were not unequivocal, because the finite stiffness of the clamps (given the inherent sensitivity of the precision printhead) was

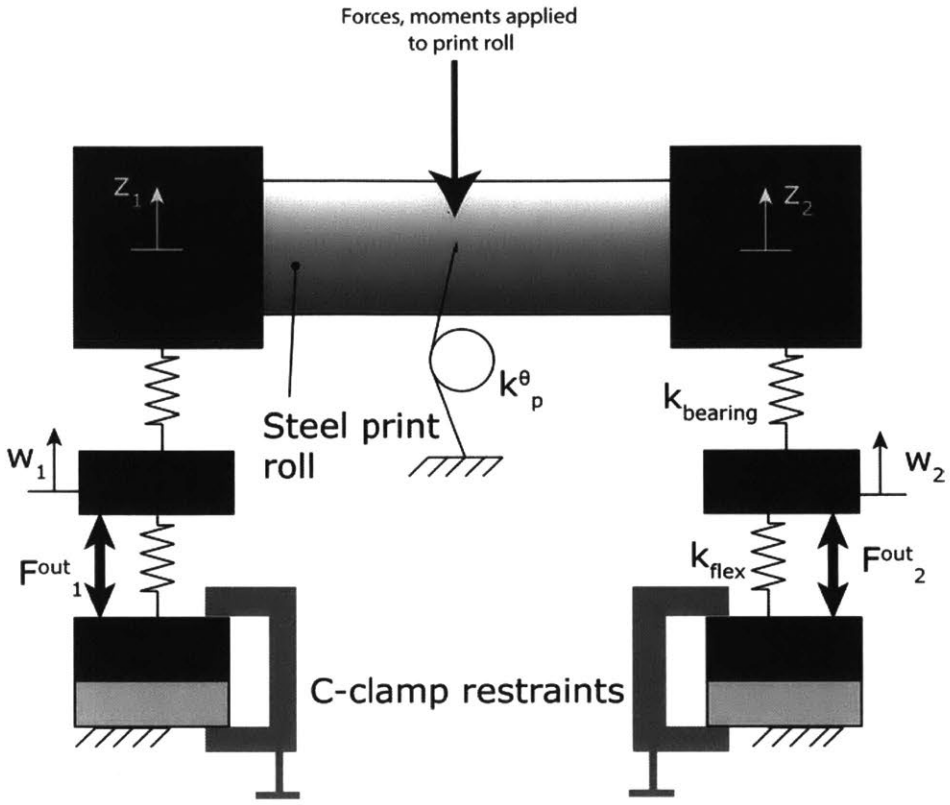

Figure 3-23: *Schematic of restrained system, used to isolate dynamics.* The system was brought out of contact with the impression roll and restrained using C-clamps; this simplified the system dynamics by removing the unknown stamp stiffness. Impulses applied to the print roll could be analyzed to determine frequency content and gain information about the system.

low enough to introduce new modes into the system response; these modes needed to be identified and removed in order to leave modes associated with the printhead elements.

Additional impulse tests were measured with the system in various configurations, including partially clamped, pulled out of contact with the stamp, and with the translational air bearings disabled. By combining information from all of these sources, the system structure and physical parameters could be confirmed. Figure 3-19 from earlier in the chapter shows a sample frequency content measurement resulting from one of these sets of impulse tests.

The location of the frequency peaks, which could be clearly identified from both Fourier frequency content measurements and swept sine measurements, was controlled

by the masses and stiffnesses (while the magnitudes of the peaks were controlled by damping). Even with most of the damping coefficients unknown, the fact that only one stiffness was now unknown allowed for a very simple parameter fit to match the peak frequencies of the model with known experimentally measured peak frequencies. Damping could then be adjusted to match peak magnitudes to measured magnitudes.

3.3.2 Empirical verification of dynamic model

The dynamic model was verified by comparing pole and zero frequencies to those measured experimentally using the above techniques. Though the exact frequency response depended on the quality of the measurement and any influencing factors like friction, the agreement is very satisfactory.

In sum, the response is qualitatively described by:

- A well-damped mode dominated by the stamp compliance, at about 25Hz;
- Two poorly-damped modes at 60Hz, dominated by the bushing compliance;
- Two poorly-damped modes at 180Hz, domianted by the flexure sensor compliance;
- And a low-frequency mode at approximately 1Hz, dominated by the combined torsional stiffness of the stamp and the slewing flexures.

Each mode resonance except one is paired with a following antiresonance. These antiresonances are generated by the combination of the stacked compliance structure of the system and the location of the sensors and actuators within this stack. This behavior is easily recognizable from applications such as stacked piezoactuators, as shown in Figure 3-25. Unfortunately, this stacked compliance structure creates a very uncontrollable system, the consequences of which will be detailed in the following chapter.

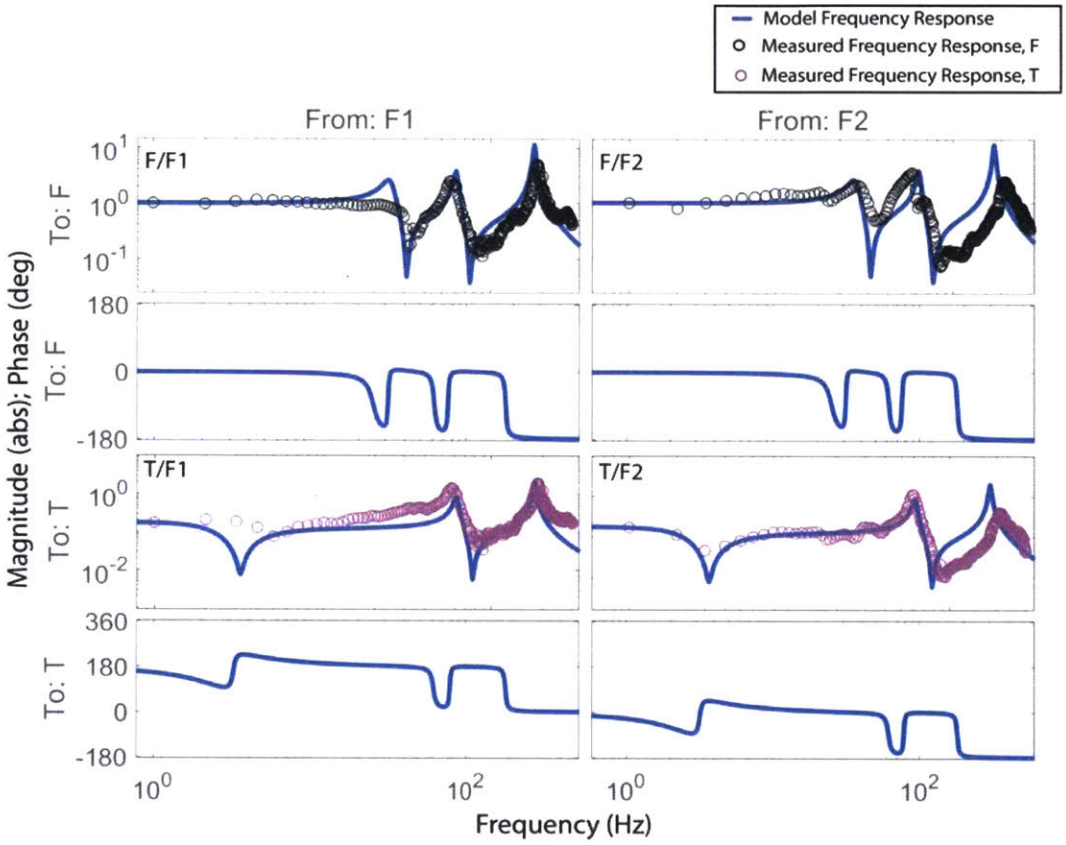

Figure 3-24: *Experimental confirmation of the analytical model.* Experimental magnitude data is well-represented by the model, even given imperfections in the measurement and inherent system variability. Resonances and antiresonances generally match up in frequency, though not necessarily in magnitude (a result of the difficulty of accurately measuring damping coefficients). Notably, components on the side corresponding to the F_2 input were more susceptible to system nonidealities (such as nonlinear friction effects) induced by disassembly and reassembly of the printhead during stamp mounting; the noisier frequency response reflects this.

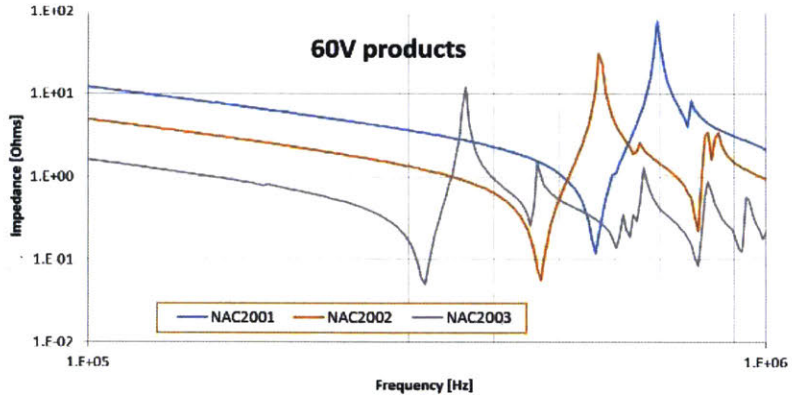

Figure 3-25: *Stacked compliance frequency response behavior, as demonstrated in commercial piezoactuators.* Frequency response for stacked piezoactuators, for several products manufactured by Noliac. [14] The same trough-peak pattern visible in the system identification of the printhead is clearly visible in each of the blue, orange, and gray traces.

Chapter 4

Controller Design

4.1 Introduction

With a system model established, the next task is to design a control algorithm that is capable of achieving a set of performance goals; namely, (1) zero steady-state error, and (2) rejection of disturbances created during the printing process. The end goal, however, is that the printed output shows satisfactorily low variation across the width of the stamp (i.e. is "balanced") and that pattern fidelity is satisfactory. These quantities cannot be measured in-process, but reaction force as measured by the flexure sensors is a direct substitute: zero steady-state error ensures that the features are balanced and compressed to the desired amount, and rejection of disturbances protects the output from transient local over-pressurization that could result in roof collapse or loss of contact defects.

Quantitatively, the bounds on these performance goals will depend on the sensitivity of the stamp. Empirically, for the nominal experimental stamp with 30μm wide lines on a 100μm wide pitch, a printing force of 4N and torque of 0N has been selected as optimal. Also, variations in as-fabricated stamp feature widths on the order of 1-5 μm have been observed [22]; and an increase in printing force of about 1N can increase the feature contact width of the nominal stamp by about 8μm [22]. Thus, to prevent vibrational printing disturbances from exceeding the natural variation in the stamp, an approximate bound of ±5μm about nominal may be selected for the

variation, which corresponds to about ±0.5N on a 6N command. Translating this into a simple rule of thumb, the bound for acceptable disturbances in total printing force was placed at ±10% of the F command; and disturbances in printing torque at $(l)(\pm 10\%)$ of the F command, where l is the print roll half-width, as the T command is set to zero.

Further, it was selected that impulse disturbances should be damped out within about 0.5s. At a 1 in/s printing speed, this would result in 0.5 in of web surface distance passed, which is about 4% of one revolution of the print roll. (If this transient occurs once per print roll revolution, 96% of the printed output would be unaffected.) At higher speeds, a faster disturbance rejection rate may be desirable.

Controller designs that aim to meet these control objectives for both the simplified separable model and the full-order state space model are presented in this chapter, along with experimental results for both approaches. Performance comparisons between the resulting designs may be drawn to establish whether the simplified model captures sufficient dynamics to permit satisfactory control, and whether the increased complexity required to include the full system's dynamics results in improved control performance.

4.2 Control of Separable System

As detailed in Chapter 3, if the system can be assumed to be rigid between the voice coil actuators and the printhead, a representative model is two decoupled second-order systems, one in the translational direction (F and y), and one in the rotational direction (T and θ).

The force control transfer functions, as derived in chapter 3, are given by

$$\frac{F}{F_{in}} = \frac{35.6s + 300000}{s^2 + 35.6s + 300000} \tag{4.1}$$

$$\frac{T}{T_{in}} = \frac{4.71s + 61.69}{s^2 + 4.71s + 61.69} \tag{4.2}$$

As detailed in the introduction, the stated control goals are to enable disturbance

rejection in steady-state so that typical printing disturbances are not visible in the output; and to minimize steady-state error.

4.2.1 SISO Design

To achieve both of these goals, the chief problems that needed to be addressed were (1) model errors and non-ideal properties that led to steady-state error; and (2) a poorly damped resonant peak inside the 1-100Hz desired bandwidth. (The peak appearing in the torsional system was much better damped but appeared at a much lower frequency, presenting a slightly different challenge.)

For both of these systems, a PI controller, or a low-frequency lag controller, can meet the stated goals, by boosting DC gain, and creating creating a phase bump before crossover to allow a high loop gain over the bandwidth.

In the following text, the designs presented in Figures 4-1, 4-2, 4-3, and 4-4 all do not meet the performance criteria that disturbances be rejected in less than 0.5s; i.e., that $T_{settle} < 0.5$s. Designs for both F and T that do meet this criteria are possible with both P and PI control, but empirically these higher-performance designs were found to cause instability in the experimental system, resulting in de-tuning of the controller to achieve robustness. Under these de-tuned conditions, both the P and the PI controller had more or less identical design performance. The designs presented represent the controller as-implemented for the experimental results shown in Section 4.2.3.

A satisfactory controller for the translational F system was:

$$C_{F,PI} = \frac{0.0205(s+98)}{s} \tag{4.3}$$

A pure integral controller offers almost identical performance:

$$C_{F,I} = \frac{2}{s}, \tag{4.4}$$

but because the resonance causes phase to drop below -180 degrees with no rem-

edy, the maximum gain is limited. Even so, designs for this controller are offered alongside the PI controller design because the pure integral controller is very simple to implement, and because (as will become clear later) the limitation on gain increase due to phase is not the driving factor blocking the successful control performance of these designs. Design outputs for the translational system are shown in 4-1 and 4-2.

For the rotational system, pure proportional control could actually serve to increase the performance, but could not remove the steady state error. Like the translational system, both a PI and a pure integral controller could meet the design needs. Satisfactory designs are given by:

$$C_{T,PI} = \frac{0.09(s+23)}{s} \tag{4.5}$$

$$C_{T,I} = \frac{2.5}{s} \tag{4.6}$$

and the design results are shown in 4-3 and 4-4.

Digital implementation of these controllers at a 4kHz loop frequency offered sufficient similarity to the continuous time that they are not replicated here.

Design Discussion

In the translational F-system design, the chief challenge to achieving good following across the 1-100Hz bandwidth is the presence of the resonant peak at approximately 80Hz. In a loop shaping approach, this frequency must be attenuated or notched out so that it will not cross unity as the gain is increased. (In the rotational T-system design, because the system was already well-damped, the undesirable resonance at approximately 1Hz did not make a large magnitude contribution, and control design was more tractable.)

Unfortunately, because the damping and frequency of this peak in the separable system model depends on the stamp's properties, it is uncertain and can vary significantly, as demonstrated in figure 4-5. This makes it difficult to remove the resonance using a loop shaping approach, because robust designs tend to sacrifice performance.

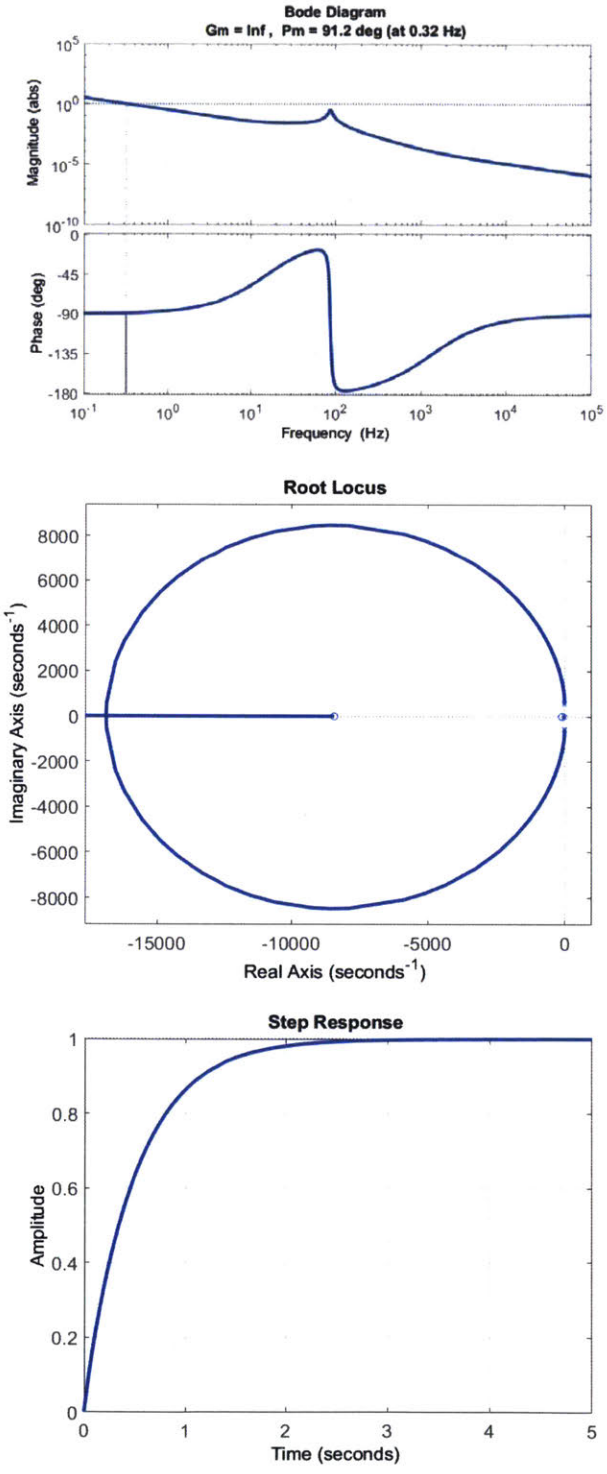

Figure 4-1: *Design results for F/F_{in} system with PI control.* PI control on the translational SISO system results in a well-damped response with no steady-state error. However, the desired disturbance rejection time of $T_{settle} < 0.5$s cannot not be met because the resonance at approximately 100Hz will cross unity.

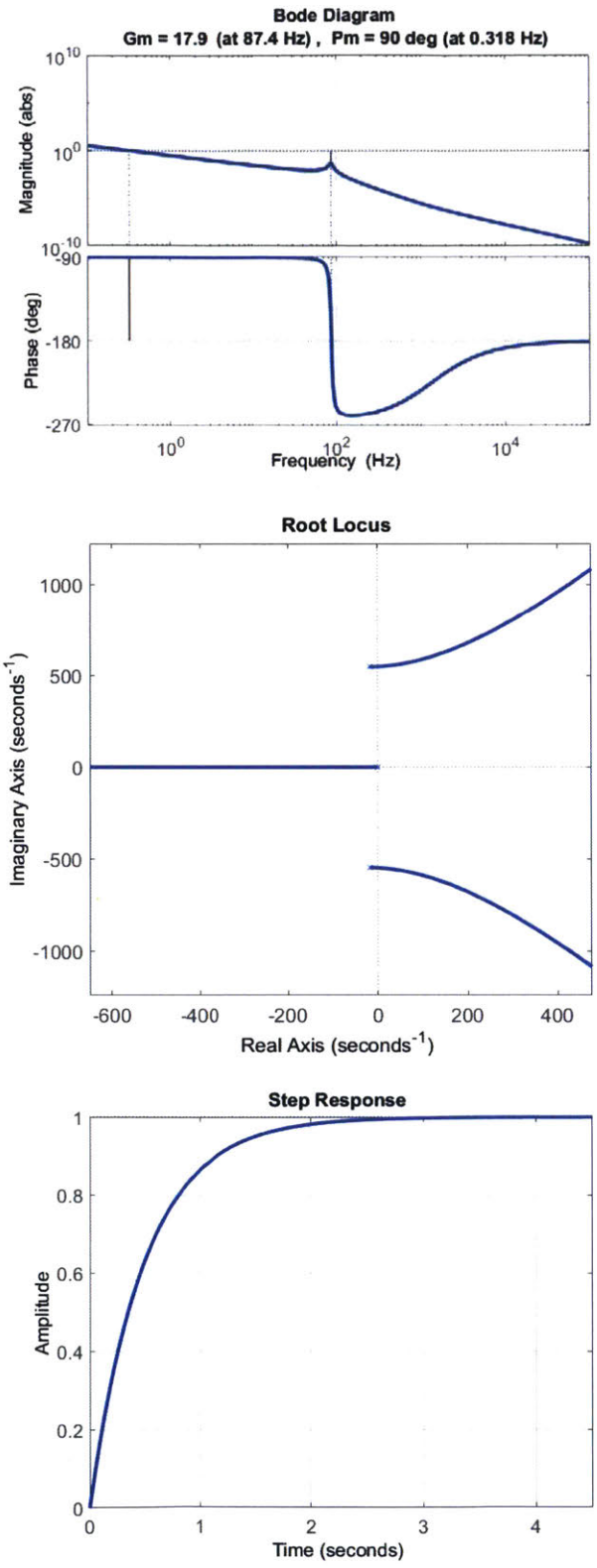

Figure 4-2: *Design results for F/F_{in} system with pure integral control.* A high frequency real zero is not shown on the root locus due to zoom. Here, integral gain has been selected to give nearly identical time-domain performance to the PI design in 4-1; but, unlike in the PI system, increasing the gain arbitrarily will cause system instability.

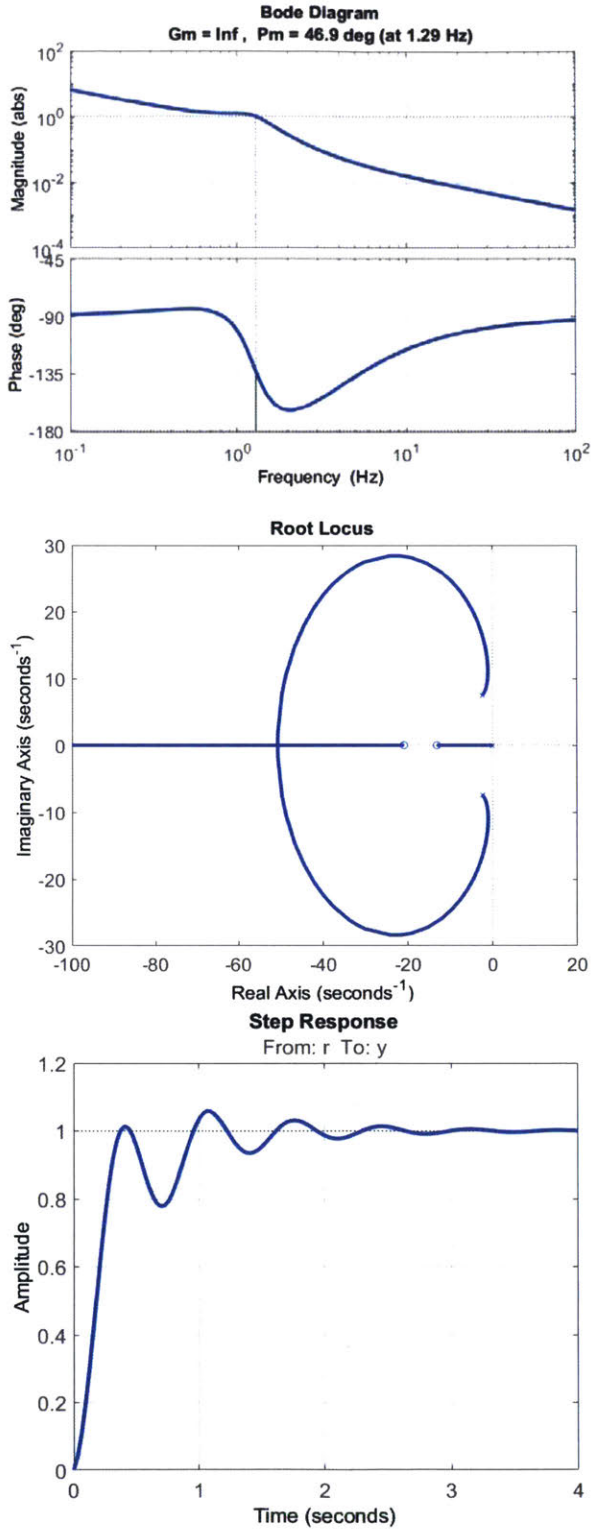

Figure 4-3: *Design results for T/T_{in} system with PI control.* The rotational system is inherently slow, with a natural pole at about 1Hz, so a PI design was chosen to decrease rise time in the time domain response.

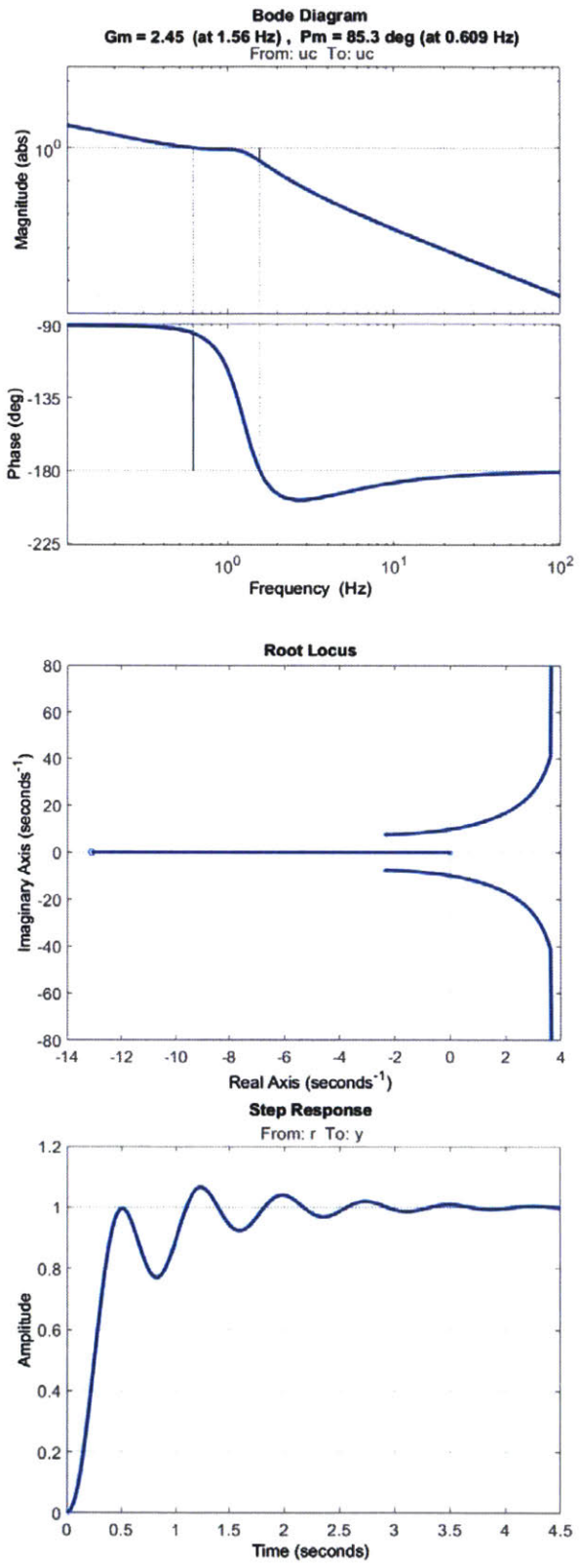

Figure 4-4: *Design results for T/T_{in} system with pure integral control.* As in 4-2, the integral gain has been chosen to achieve the same time domain behavior. Also as in 4-2, arbitrary increase of the integral gain will result in an unstable system.

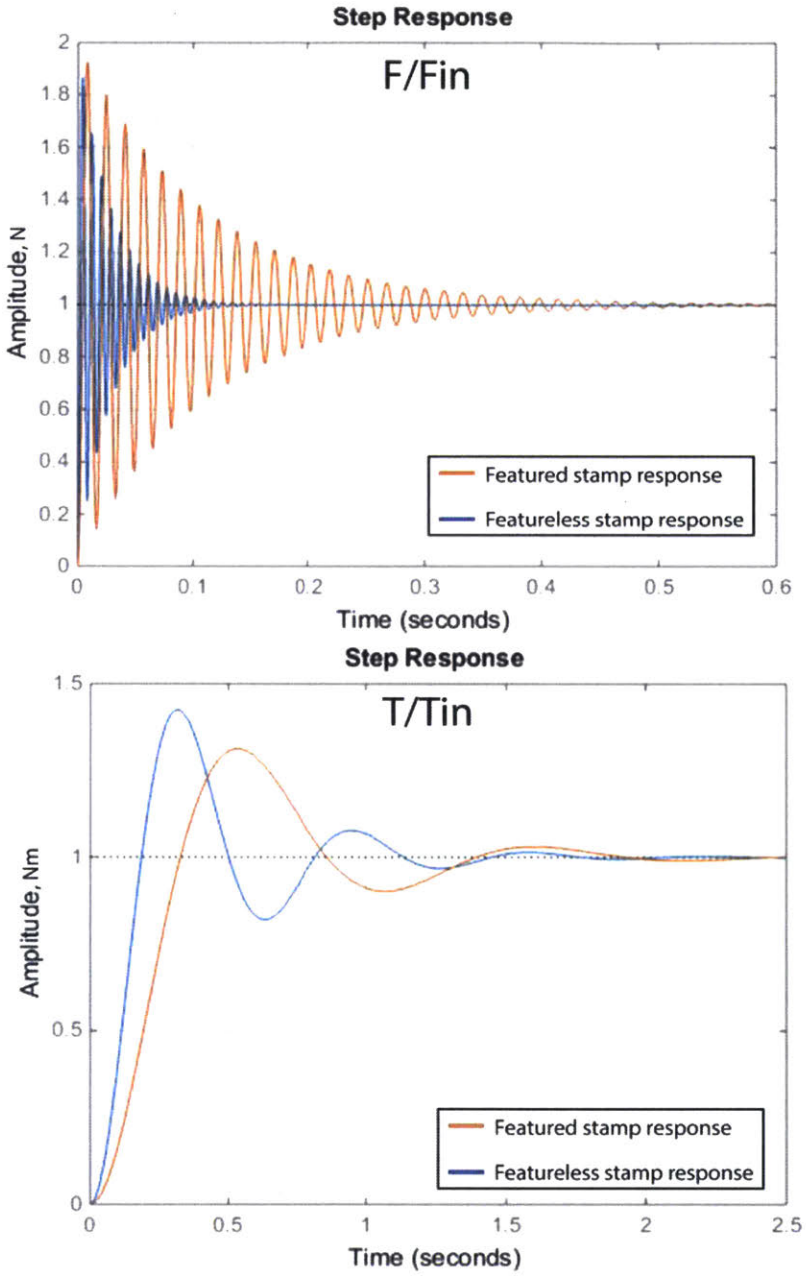

Figure 4-5: *Comparison of featureless and featured stamp effects on system response.* Because the system's response is dominated by the stamp's properties, there is significant variation. Shown are the step responses for the estimated maximum (blue) and minimum (red) stamp stiffness for the translational (top) and rotational (bottom) systems. Minimum stamp stiffness for this plot is determined by the capabilities of the stamp casting machine; maximum stamp stiffness occurs when the stamp is featureless.

To this end, the robust approach was pursued: for simplicity, pure integral control was implemented for the separable SISO systems, and the results were evaluated under experimental conditions. This gave the additional benefit that there would be a clear upper bound on gain, past which the system would be unstable; but at low gains, the system stability should not be affected. (For the PI design, the translational system was expected to have a range of gains for which instability was expected.)

4.2.2 Implementation

Implementation of the separated SISO controller was very straightforward. It is implemented digitally in LabVIEW on the real-time controller at a sample rate of 4kHz, with the following control law:

$$(F_{ref}[k] - F[k])(T_s) + e_F[k-1] = e_F[k]; \tag{4.7}$$

$$u_F[k] = K_{i,F} e_F[k] \tag{4.8}$$

$$(T_{ref}[k] - T[k])(T_s) + e_T[k-1] = e_T[k]; \tag{4.9}$$

$$u_T[k] = K_{i,T} e_T[k] \tag{4.10}$$

where T_s is sample time; F_{ref} and T_{ref} are reference force and torque commands, respectively; F and T are measured force and torque; e_F and e_T are force and torque error; u_F and u_T are plant inputs for force and torque; and K_i, F and $K_{i,T}$ are controller gains. Reference feedforward control was also made an option in order to reduced the transient response of the integral controller:

$$u_F[k] = F_{ref}[k] + K_{i,F} e_F[k] \tag{4.11}$$

$$u_T[k] = T_{ref}[k] + K_{i,T} e_T[k] \tag{4.12}$$

The feedforward gain was unity because the expected open-loop DC gain for both systems was unity.

$K_i = 1$ was a conservative gain choice, though gains up to $K_i = 4$ could be successfully used before instability under ideal conditions.

4.2.3 Results

Results were collected both during on-machine printing, and on the off-machine contact imaging machine. Experiments were:

1. Contact measurement of manually rolling the undriven imaging system over a piece of tape placed under the stamp, to simulate a disturbance in sample thickness or assembly;

2. Contact measurement and on-machine measurement of disturbance rejection to manual disturbances created by imparting impulses with hand tools;

3. Contact measurement of step response, sent as a command to the actuators;

4. And on-machine printing at speeds of 0.2, 0.5, 1, and 4 in/s. Printing was conducted without ink onto a PET substrate due to the scarcity of the necessary gold substrate.

All of the tests were conducted with a reference of $F = 4$ and $T = 0$. The printing tests were conducted under open loop web tension of 30N.

Each of these results was compared to the open-loop system to evaluate if the controller was successful in achieving the stated control objectives of zero steady-state error, and improved disturbance rejection.

The contact machine functions using episcopic microscopy, in which the beam path of the light source is co-linear to the beam return path to the lens. The contact imaging system has a hollow glass roll (analogous to the impression roll on the machine) that the stamp may contact; inside the roll, looking through the glass wall, is an episcopic imaging system, constructed by Nill and iterated upon by Ascoli. [28, 22] When a stamp is brought in contact with the roll, areas where the PDMS has adhered to the glass appear dark (an effect that is accentuated by dying the stamp black), and

areas where there is still an air gap remain light. This allows for both a qualitative and a quantitative measure of contact under printing conditions. An annotated photograph of the contact imaging system and a schematic showing its basic function are included in 4-6. More information on this technique is in Ascoli's thesis document. [22]

Quantitatively, the contact measurements are difficult to interpret; a great deal of optical noise is present due to the surface texture on the stamp, particulate contaminants, optical and surface variation on the impression roll, and underlying surface texture on the print roll. An example of the type of image produced on the contact imaging system is shown in 4-7.

Qualitatively, the observable differences between the pure integral and the open-loop system are scant, at least in the very small region of the stamp visible to the camera. The pure integral control does a marginally better job preventing loss of contact as the stamp encounters disturbances through rolling. Roof collapse is not significantly encountered in either regime. This would seem to imply that either the small area available to the contact imaging system does not contain enough data to detect any performance improvements under control; or that integral force control does not induce an observable improvement over open-loop control when facing a step disturbance in stamp thickness.

More quantitative conclusions can be drawn from the sensor outputs for F and T during these experiments. During the printing experiments, pure integral control keeps the mean steady-state force error to within 2% of the setpoint, achieving one stated control objective; but the open-loop system alone is capable is maintaining a 4% steady-state error. In terms of torque, the closed-loop system and the open-loop system both exhibit a steady-state offset of about 0.05 Nm, on a reference command of 0 Nm. In terms of RMS noise, the pure integral control actually does approximately the same or slightly worse (typical values 0.10N or 0.015Nm); though based on the design we expect high-frequency noise to be attenuated, clearly that is not happening in the experimental results.

Overall, these experimental results are most indicative of the fact that the separa-

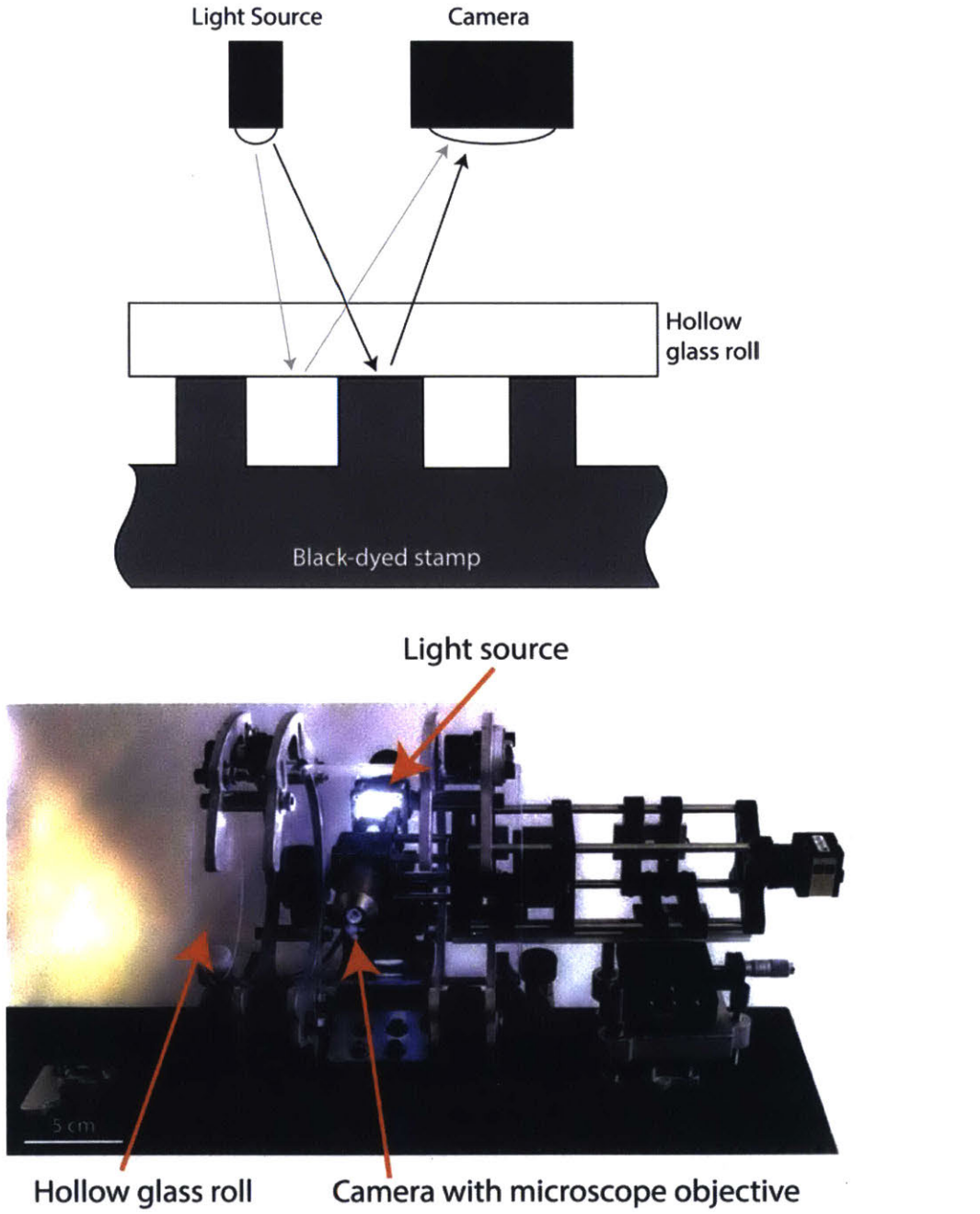

Figure 4-6: *Contact imaging system.* The contact imaging system uses an episcopic microscopy setup to examine the stamp's contact of a hollow glass roll. (Top) Light that bounces off air gaps appears light to the camera (gray arrow), while light that bounces off stamp contact regions appears dark (black arrow). Dying the stamp black accentuates this effect. (Bottom) The contact imaging system consisted of a hollow roll mimicking the printing impression roll with an episcopic microscopy system inside. The printhead system (not pictured here) may be placed on bench and brought into contact with the hollow glass roll in the same manner that it contacts the solid impression roll on-machine.

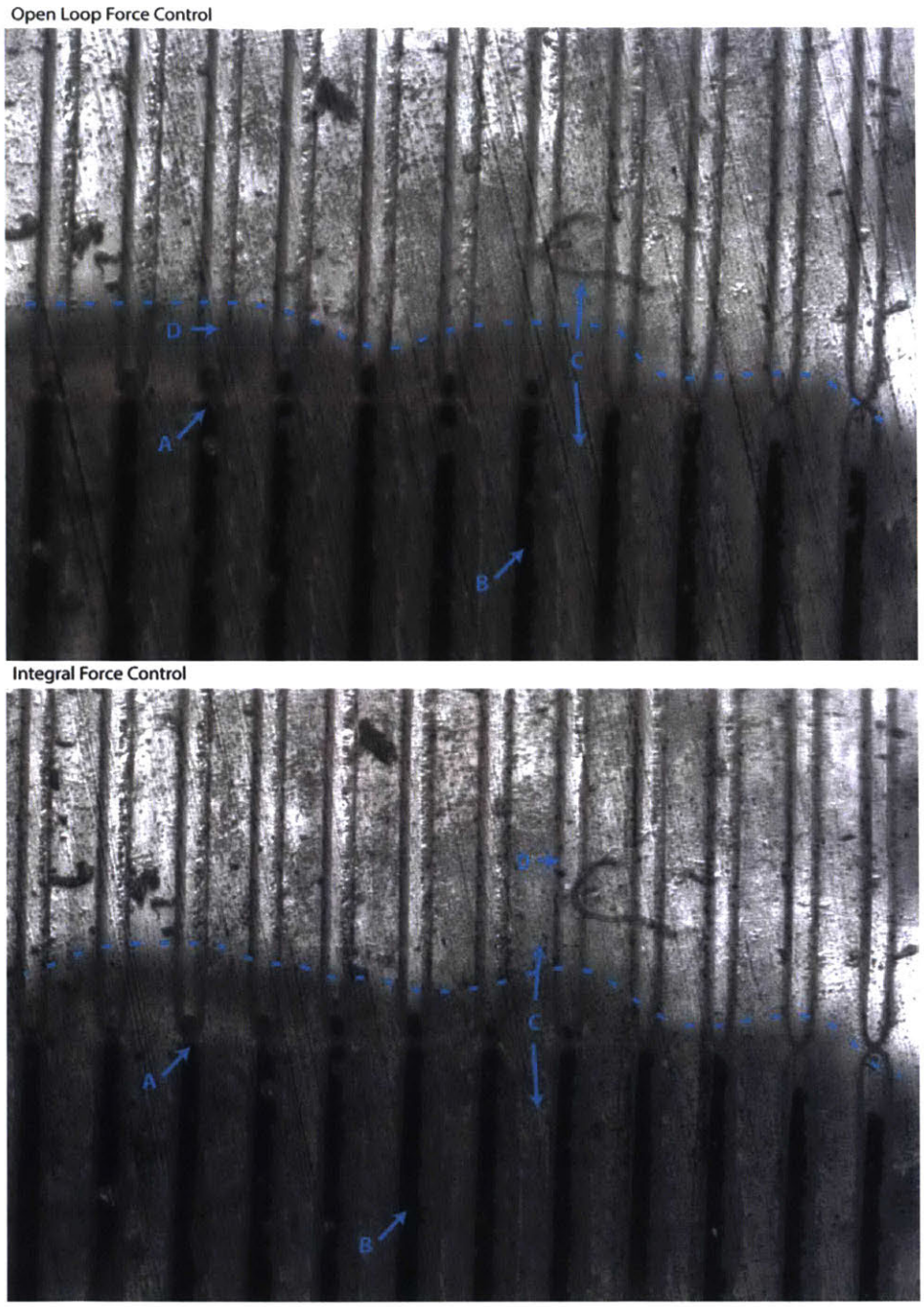

Figure 4-7: *Contact imaging system measurements of printing under open loop and integral control.* Two images of the same region were acquired on the contact imaging system, one (top) using open loop force control; the other (bottom) using integral control. Both images have been contrast enhanced for clarity. A strip of opaque tape placed under the stamp to induce surface variation is visible in the lower half of each image, with the tape edge highlighted by the dotted line. (A) is a gap in the continuous line features that marks the 0 degree position on this stamp. The dark region at (B) is a feature in contact with the glass roll; the light regions at (C) and (D) respectively are the stamp roof and a stamp feature, neither of which are contacting the roll. No significant differences between the two images can be observed.

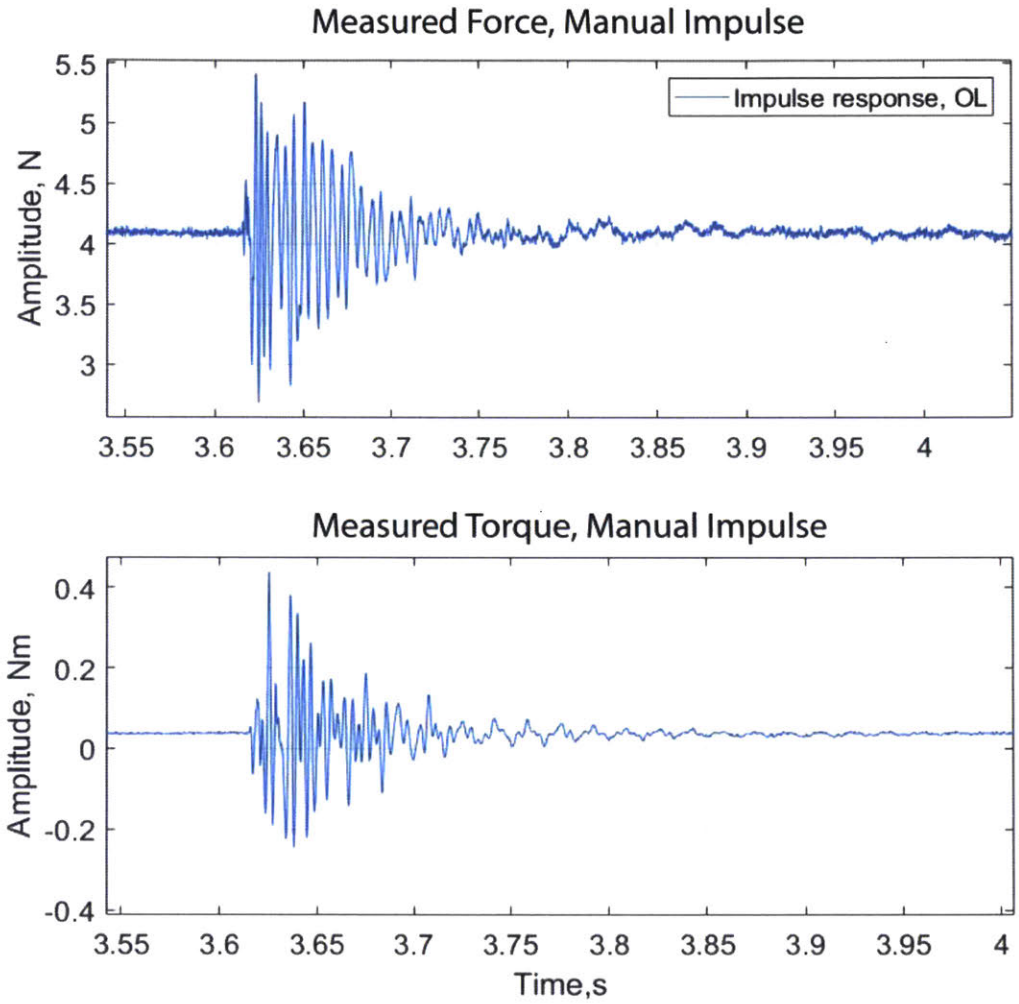

Figure 4-8: *Disturbance rejection of a manual impulse to the open-loop system.* A manual impulse was imparted by sharply tapping the print roll near the stamp with a hand tool, and the frequency and duration of the resulting response in the open-loop system was measured to establish a baseline. The open loop response persists for about 200ms, especially in the torque T output (bottom).

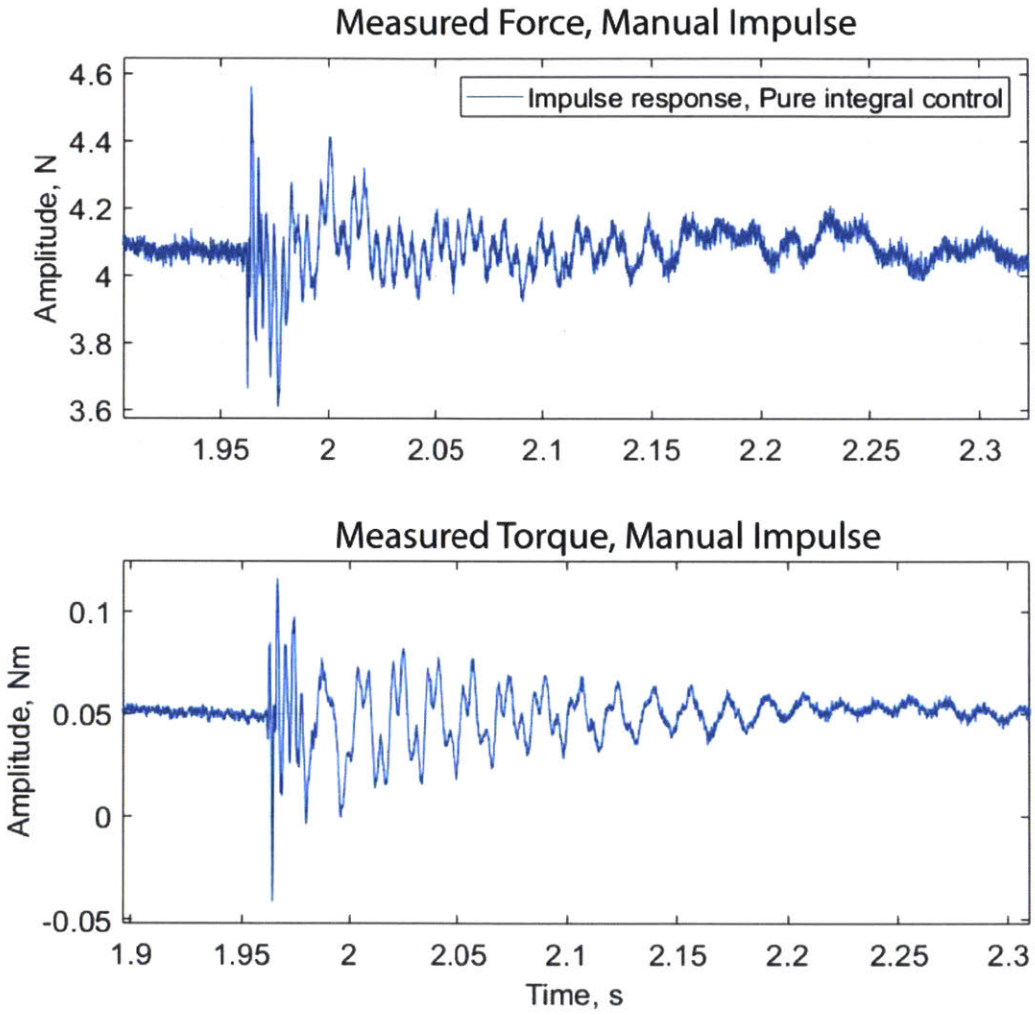

Figure 4-9: *Disturbance rejection of a manual impulse to the closed-loop system under pure integral control.* An impulse of approximately the same magnitude was induced using the same method as in 4-8. The initial transient is considerably lower in amplitude and noticeably rejects high frequency content more quickly; however, the 60Hz mode is not well controlled and persists in the system response beyond 200ms.

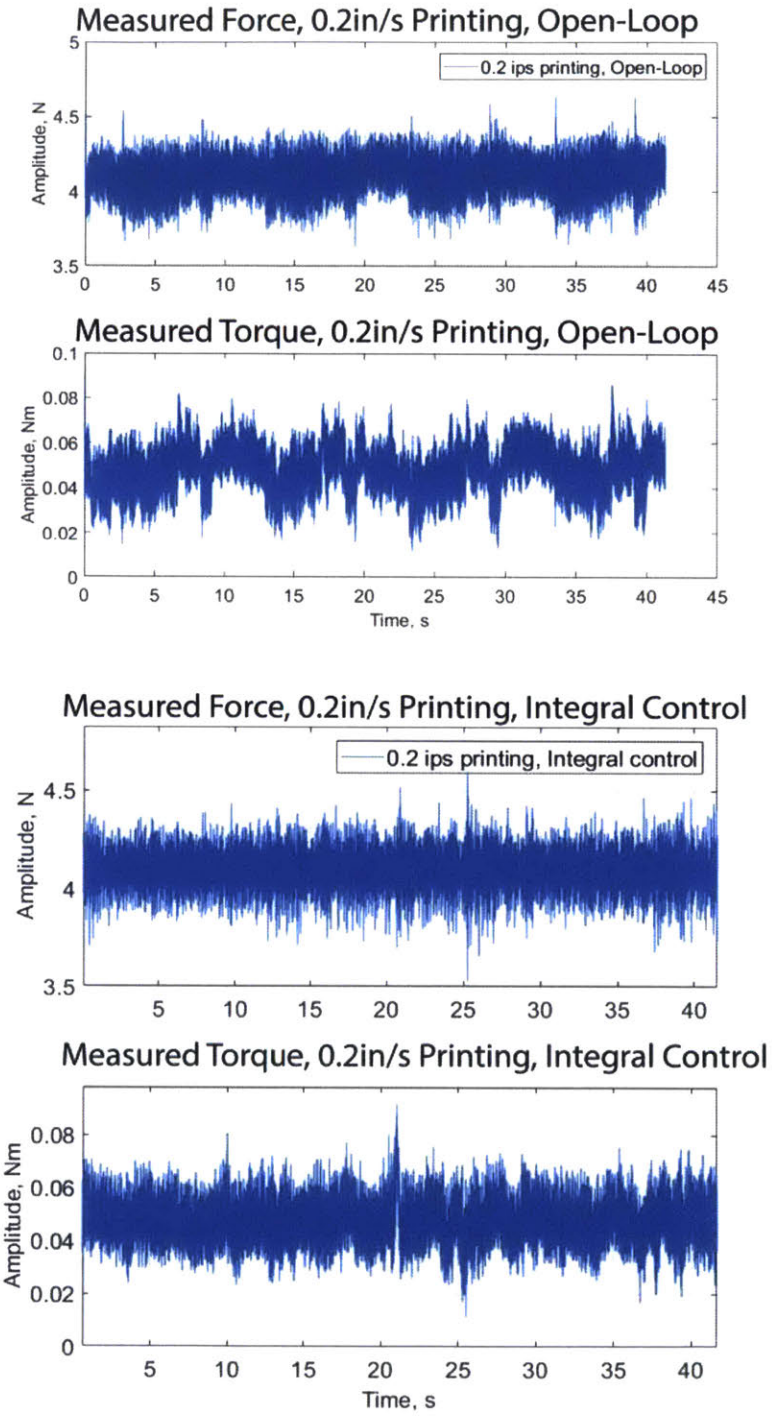

Figure 4-10: *Output comparison for 0.2 in/s printing speed for open-loop and integral force control.* These graphs show force and torque output response while printing at 0.2 in/s and 30N tension. The pure integral control does a noticeably better job maintaining the setpoint, but the signal is undesirably noisy.

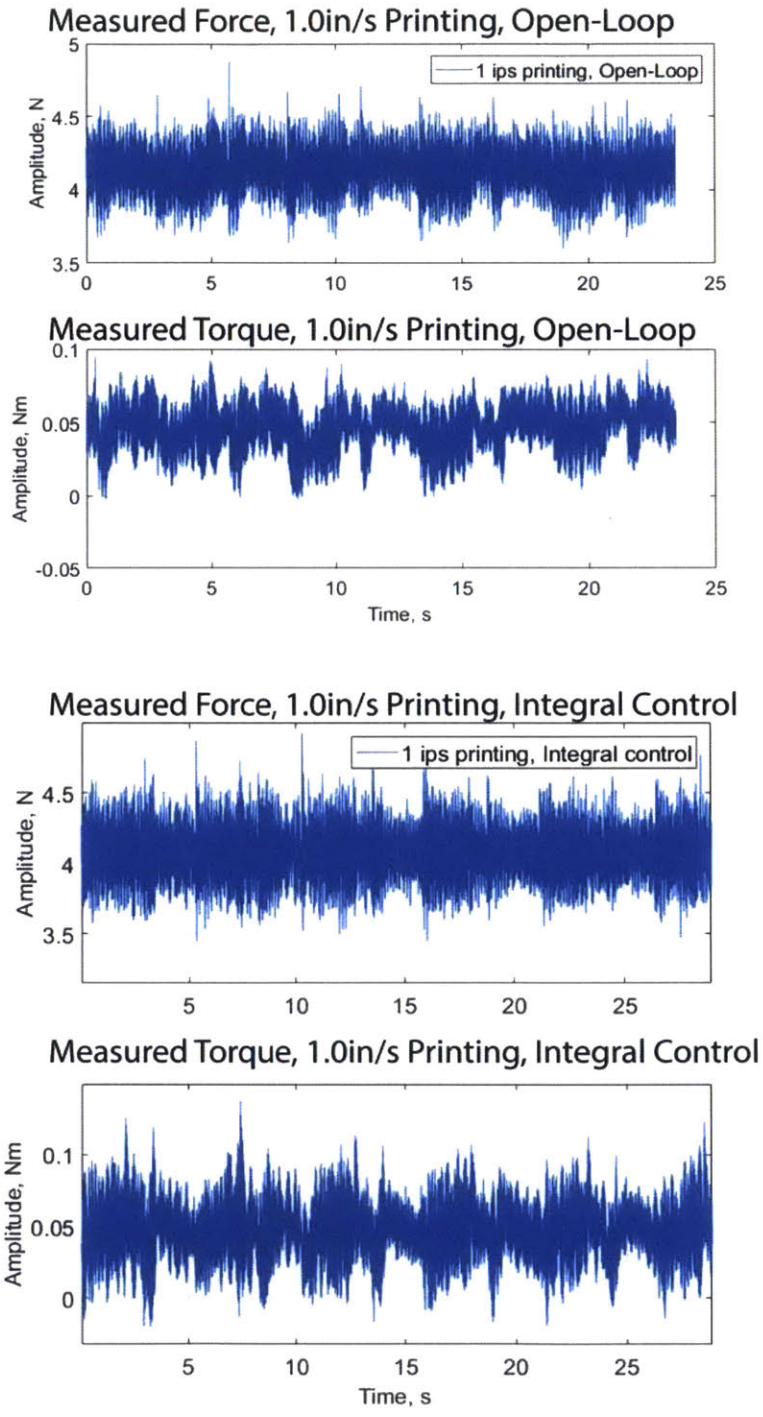

Figure 4-11: *Output comparison for 1.0 in/s printing speed for open-loop and integral force control.* For printing at 1.0 in/s and 30N tension, similar results to the 0.2 in/s case are observed.

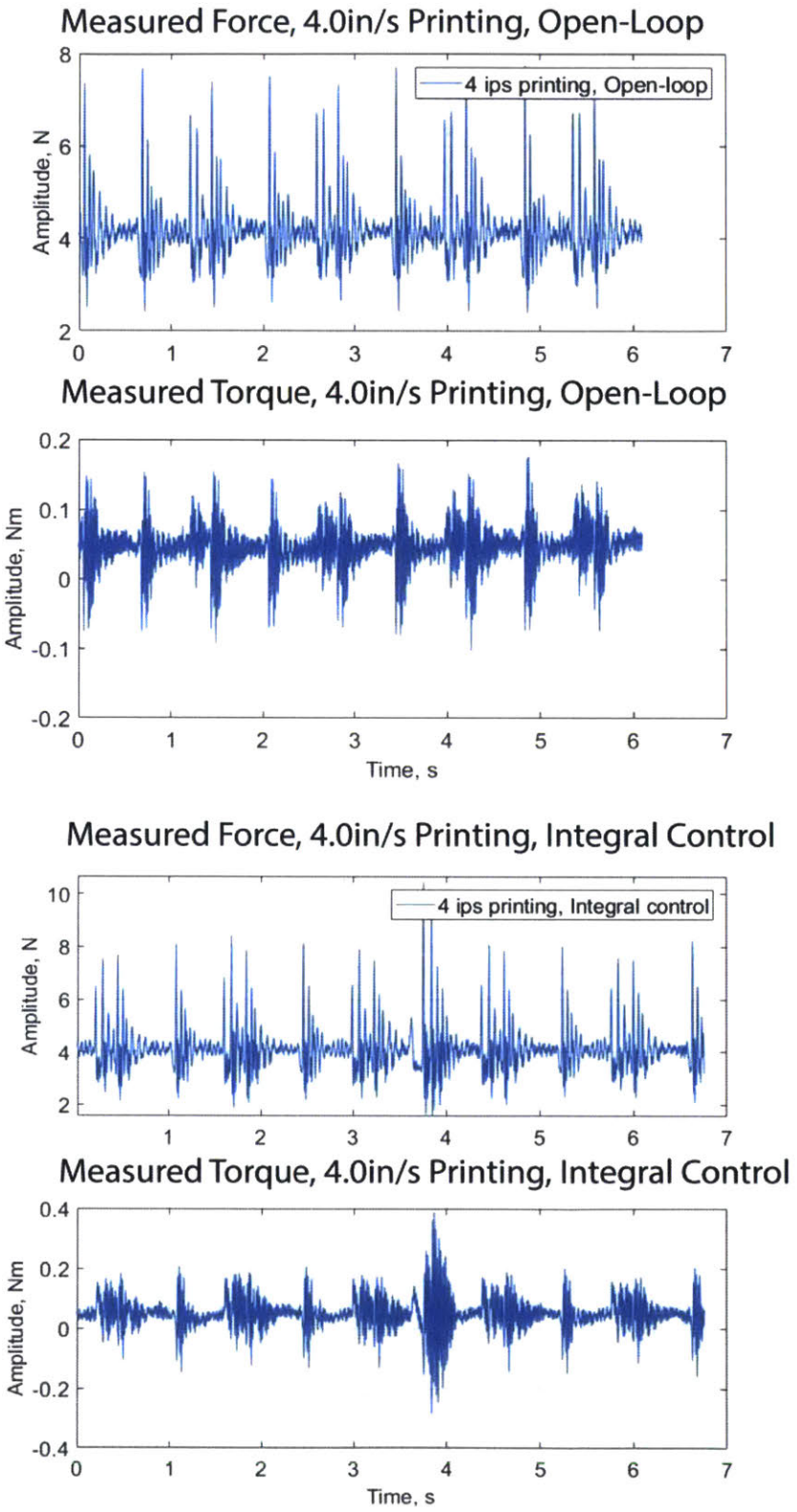

Figure 4-12: *Output comparison for 4.0 in/s printing speed for open-loop and integral force control.* The controller appears to be no better than the open-loop system in rejecting disturbances at the 4 in/s printing speed; likelhy the increased printing vibration at higher printing speeds is off too large a magnitude for this controller to effectively reject.

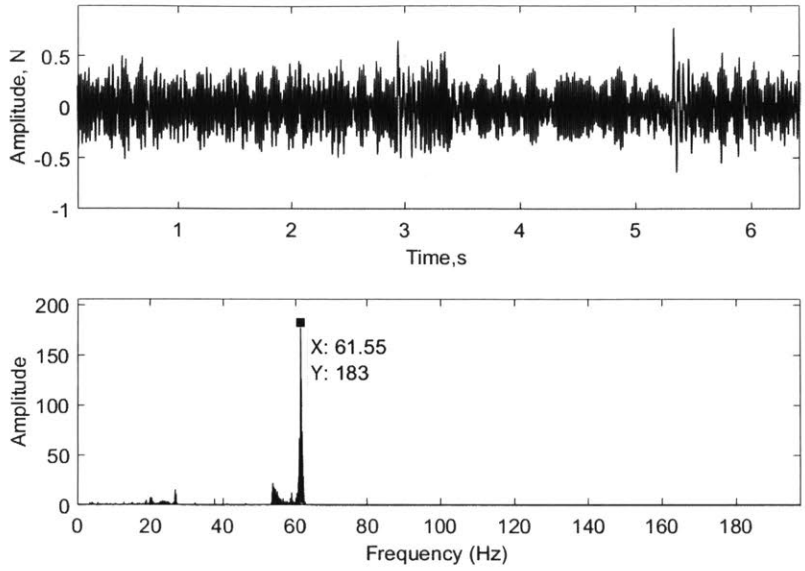

Figure 4-13: *Frequency content of printing force output under integral control.* The mean value of the force output has been substracted to accentuate dynamic variation. The frequency content of the measured output shows a clear peak at 60Hz.

ble model is not sufficient to capture the system dynamics. Though the low frequency behavior is well-controlled, with low steady-state error and rejection of low-frequency disturbances like the "cogging" of the web drive motors, the high frequency behavior is clearly not as expected. Checking the frequency content, a peak at 60Hz is clearly visible, as in 4-13; either this frequency is poking above crossover, or the disturbance sensitivity for this frequency range is not sufficiently low.

The conclusion from these experiments was that SISO loop shaping techniques alone were inadequate to deal with the undesirable base system response (which was not fully modeled under the SISO assumption), and that pole-placement techniques for the coupled system model needed to be explored. However, the pure integral controller's low steady-state error and elimination of rotational bias was sufficient for printing experiments that were not sensitive to high-frequency force fluctuations and actually produced improved prints over the open-loop system for the nominal experimental stamp, so the design still had significant utility to other researchers.

4.3 Control of Coupled System

The control of the 12th order full system offers a significantly more complex challenge than the control of the separable systems. Again, the control objectives are the same: enable the system to reject disturbances and to achieve minimal steady state error.

To achieve this approach, a hybrid controller was selected: a multi-input, multi-output full state feedback controller, augmented with states allowing for integral control. The stated goal of the pole placement component was to smooth the resonances at 60Hz and 180Hz in order to remove them from the system response as much as possible, but otherwise to exert minimal changes to the system. The augmented states, representing the integral of the error, could then be used to achieve zero steady state error, and effectively increased low-frequency loop gain as well.

In both cases, only two states (x_1 and x_2) and the two outputs ($F = F_1 + F_2$ and $T = -lF_1 + lF_2$) are directly measured. Additionally, position states x_1 and x_2 are subject to an unknown offset on machine startup, due to the fact that repeatably calibrating these inputs to the sub-micron level was not possible within the design constraints inherent to the existing printhead. (This meant that not only were the initial conditions of x_1 and x_2 unknown, the "home" position of x_1 and x_2 corresponding to some stamp nominal compression δ could not be determined to the micron level without knowing the stamp's precise stiffness.) If physically x_1 and x_2 start at some nonzero displacement (even if the controller sees their position as zero), a nonzero disturbance torque and force is imparted to the system; fortunately, if the initial offsets are not excessive, an integral controller will be able to compensate these initial offsets.

But, given that only two states could be directly measured for this 12th order system, that meant that ten other states needed to be computed or estimated. To accomplish this a full order observer was implemented. Though a partial order observer with the two measurable states could also have been implemented, the estimation of these states was deemed superior to the measurement for control purposes, as a large initial offset could cause system instability, and filtering could be applied via the

observer's dynamics. Both a fast, "ideal" pole-placed observer and a robust Kalman optimal observer were developed.

The controller and observer designs were completed in discrete time after the initial pole location selection. The poles were selected to have a particular frequency and damping, the s-plane value corresponding to those characteristics was computed, and the s-plane locations were mapped to z-plane locations using a zero-order-hold (forward rectangular) mapping. From this point, design was undertaken completely in discrete time, using a sample rate of 4kHz.

4.3.1 Pole Placement with Augmented States

Pole placement, or full-state feedback is a well-known technique for controlling multi-input, multi-output systems. Given a system described by the state space representation

$$\dot{x} = Ax + Bu \tag{4.13}$$

$$y = Cx + Du, \tag{4.14}$$

typically one selects a matrix of gains K, and sets the control law to be $u = -Kx$. This changes the closed-loop dynamics to be $\dot{x} = (A - BK)x$.

However, this structure does not allow for a nonzero reference value for the output to be selected; to include a nonzero reference r dictating the desired value of the output y, one may select a control law of the form $u = r - Kx$. Closing the loop with this control law changes the system dynamics to be:

$$\begin{aligned} \dot{x} &= (A - BK)x + Br \\ y &= (C - DK)x + Dr \end{aligned} \tag{4.15}$$

In both cases, the effect is to move the poles from the eigenvalues of A to be

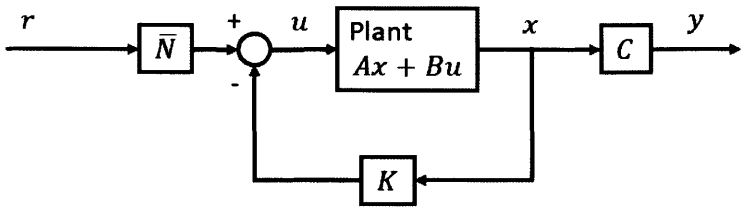

Figure 4-14: *Block diagram for a full-state feedback system with a reference command.* When a reference is introduced to the state feedback system, it should be multiplied by a weighting function $\bar{N} = N_u + KN_x$, where N_u is the proportionality constant relating the reference to the steady state, and N_x is the proportionality constant giving the state x_r associated with reference r. [15]

the eigenvalues of $A - BK$, allowing the open-loop poles to be arbitrarily adjusted. [15, 60]

For the printhead system, a design goal was undertaken to minimize control effort (and stay within the bounds set by the uncontrollability of the system, per the next section) by limiting the function of the full-state feedback controller to imparting additional damping to the resonant modes.

On top of the full-state feedback, an integral controller was applied. The goal here was to allow for zero steady-state error, and to shape the overall transfer function to boost DC gain and further taper higher frequency dynamics. The technique used was the augmented state controller, in which two additional states were added to the controller that represented the integral of output error.

These two additional states, q_1 and q_2, were defined by

$$\dot{q}_i = y_i - r_i; \tag{4.16}$$

i.e., $q_i = \int e_i(\tau)d\tau$. Then, a term may be added to the control law that takes into account this integral of error:

$$u = -Kx - K_i q = -\begin{bmatrix} K \\ K_i \end{bmatrix} \begin{bmatrix} x // x_a \end{bmatrix} = -K_a x_a, \tag{4.17}$$

making the augmented system state space representation

$$\dot{x}_a = (A_a - B_a K_a)x_a + B_r r$$
$$y = C_a x_a + Du, \tag{4.18}$$

where B_r is the input matrix for the reference r. [60]

For the printhead system, this state space representation took the form

$$\begin{bmatrix} \dot{x} \\ \dot{q} \end{bmatrix} = \begin{bmatrix} A & 0 & 0 \\ \vdots & \vdots & \vdots \\ C & 0 & 0 \\ \vdots & 0 & 0 \end{bmatrix} \begin{bmatrix} x \\ q \end{bmatrix} + \begin{bmatrix} B & \cdots \\ 0 & 0 \\ 0 & 0 \end{bmatrix} u + \begin{bmatrix} 0 & 0 \\ \vdots & \vdots \\ -1 & 0 \\ 0 & -1 \end{bmatrix} r$$
$$y = \begin{bmatrix} C & 0 & 0 \\ \vdots & 0 & 0 \end{bmatrix} \begin{bmatrix} x \\ q \end{bmatrix} + 0 \tag{4.19}$$

A is 12x12, B 12x2, and C 2x12. This makes the augmented state x_a 14x1, and the augmented matrices A_a 14x14, B_a 14x2, C_a 2x14, and B_r 14x2.

Additionally, feedforward of the reference was added to introduce a low-frequency zero. This would help isolate the activity of the integrator to reducing steady-state error and reduce its detriment to phase at higher frequencies. The feedforward gain is chosen to be $\bar{N} = N_u + KN_x$, where $N_x r = x_r = x_{ss}$ and $N_u r = u_{ss}$. This places a zero at $z_I = 1 - \frac{K_I}{N}$, where K_I is the integrator gain.

By the separation principle, it is possible to choose values for K_a separately from the observer design, without either choice influencing the other. (The combined controller-estimator system with have the combined poles of both the closed-loop system and the estimator, but they are separable and may be designed independently.) [15]

The pole locations in the left half-plane for $A - BK$ were selected to be 20, 30, 55, 60, 180, and 180Hz, with a damping of $\zeta = 1$ for each. These frequencies were chosen to increase the frequencies of the slow poles as much as possible, while leaving

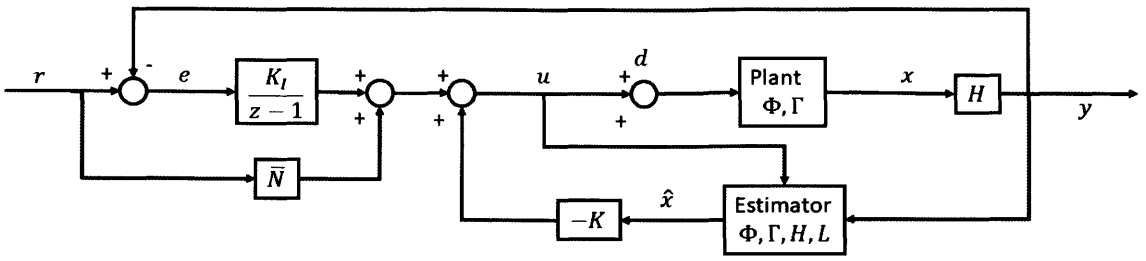

Figure 4-15: *Block diagram for MIMO system, controller, and estimator.* Shown is the block diagram for the discrete time implementation of the full-state feedback controller with augmented state integral control, reference feedforward, and full-state feedback generated from an estimator. [15]

the frequencies of the fast poles minimally affected. These selections were converted to discrete time with a sampling rate of 4kHz, and the Matlab `place()` command used to compute the K matrix. The resulting closed-loop design is shown in 4-16.

The integral function of the augmented states can be conceptually considered a wrapper around the closed-loop pole placement design. Figure 4-19 shows how adding the augmented states with the integral gain matrix $K_i = I$ adds clear integrator behavior to the pole-placed system, with rolloff starting at a low frequency. (Note that this is not a true integrator and is instead implemented as a low-frequency pole when the feedforward is taken into account; this improves the system stability and the flexibility in applying the integrator.) Figure 4-20 shows that low controller effort is required to follow a step command.

Overall, this design was deemed the best possible, due to limitations discussed in the next section. It was expected that the system would meet the goal of less than 2% steady state error on the command, but that the system would reject disturbances poorly, especially in frequencies corresponding to the transmission zeros.

Limitations on Control Design

The design for this controller was undertaken with knowledge that there would be two critical limitations: first, that the system was subject to transmission zeros, which could not be modified with full-state feedback; and second, that most of the

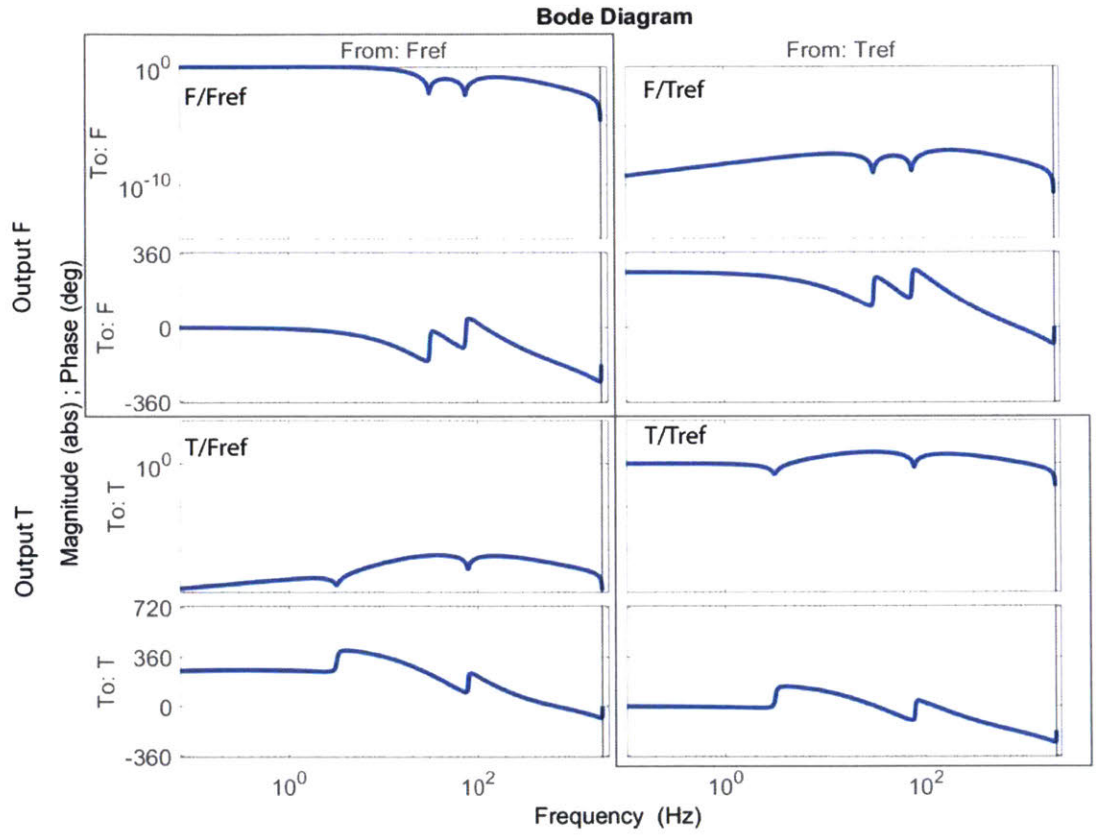

Figure 4-16: *Closed-loop response for the pole-placement design with feedforward, without augmented integrator states.* The "normal" terms F/F_{ref} and T/T_{ref} are boxed, and the "cross-terms" F/T_{ref} and T/F_{ref} unboxed. Note that there is generally good following in the 1-100Hz range, but the zeros mar the response in at 3Hz, 30Hz, and 75Hz. Note also that the cross terms have magnitudes 5-10 orders of magnitude below the normal terms.

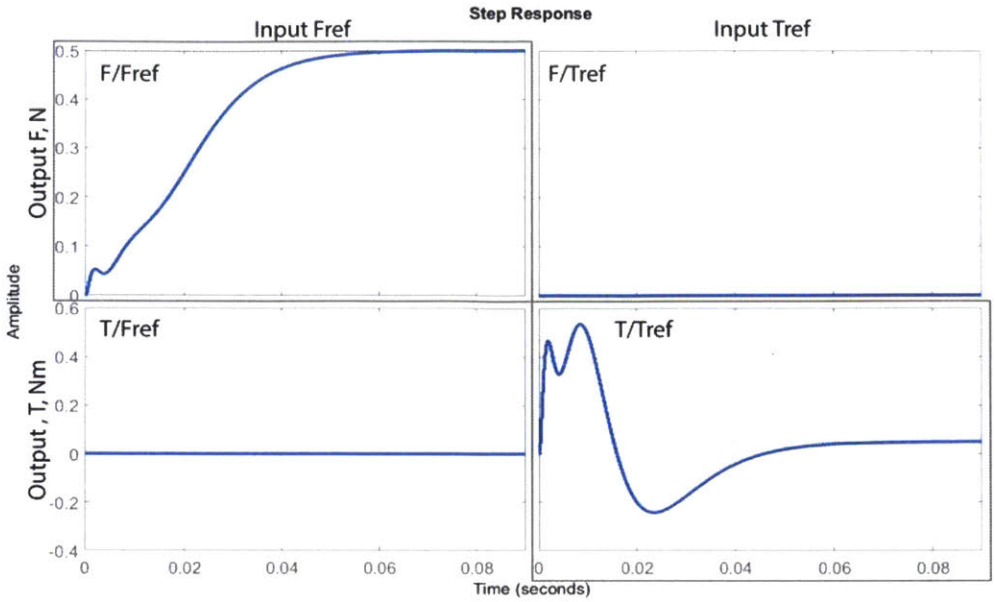

Figure 4-17: *Step response for a 0.5N input into F and a 0.05Nm input into T.* The cross terms are satisfactorily decoupled, but the torsional response in particular is strongly affected by its low-frequency zero. Both normal outputs settle to their command values, but any errors in the model would prevent this.

modes of the system were uncontrollable, and also could not be modified with full-state feedback. However, to demonstrate the maximum capabilities of the system as-designed, the full controller development exercise was still undertaken.

The first limitation was that the poorly damped zeros, which appeared in the desired bandwidth range of 1-100Hz, could not be modified by full-stated feedback. Zeros in a multi-input, multi-output system may be defined as a the generalized frequencies z_0 at which the system has a nonzero input $u(t) = u_0 e^{z_0 t}$ but exactly zero output, i.e. $y(t) = 0$, and can be found by solving the generalized eigenvalue problem

$$\begin{bmatrix} -(z_0 - A) & B \\ C & D \end{bmatrix} \begin{bmatrix} x_0 \\ u_0 \end{bmatrix} = 0 \tag{4.20}$$

(More simply, open-loop zeros will appear in the numerator of the transfer functions that express F/F_1, F/F_2, T/F_1, and T/F_2, when computed using the expression $G(s) = C(sI - A)^{-1}B + D$.) [61, 62]

Upon closing the loop, the system state space representation is given by 4.15; if

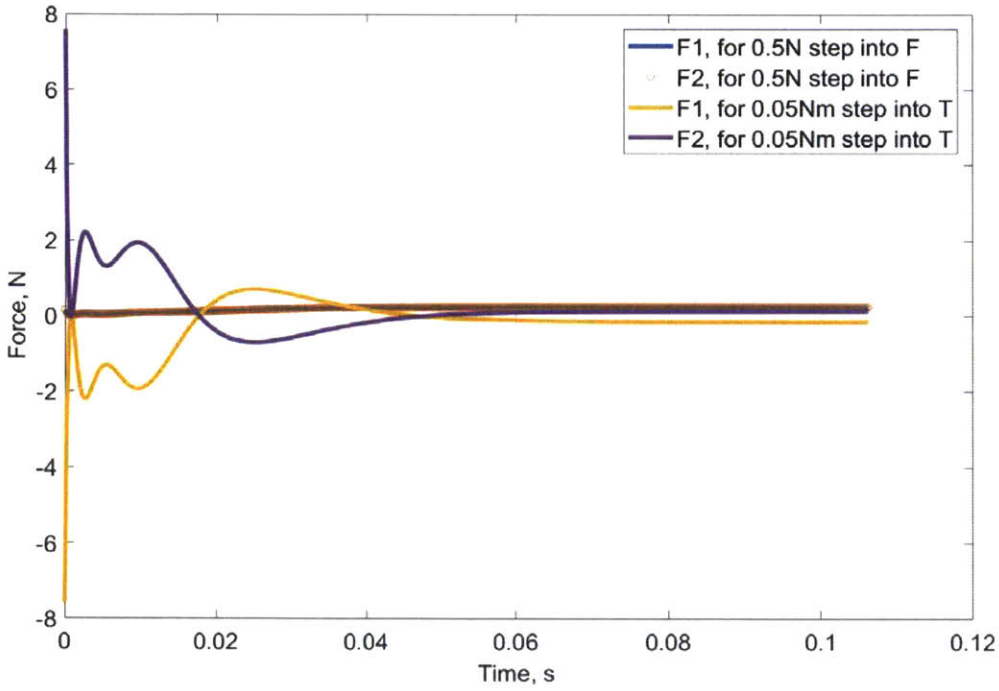

Figure 4-18: *Simulated controller effort for integral control.* Controller effort resulting from an input of 0.5N into F and an input of 0.05Nm into T. 8N is well within the capabilities of the voice coils.

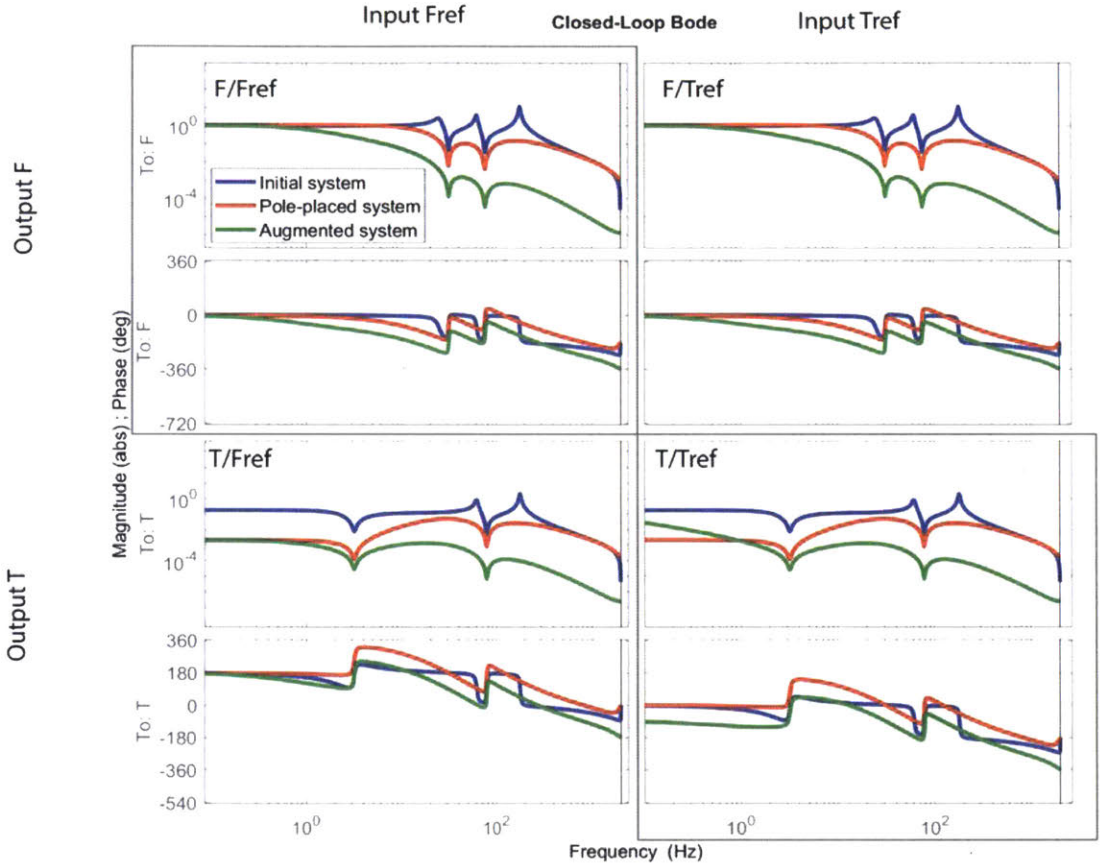

Figure 4-19: *A comparison of the integral state-augmented system, the pole-placed system, and the open-loop system design performance.* Note that these plots are shown without the feedforward component, $\bar{N}r$ (as indicated in Figure 4-15); the nonzero initial phase in T/F_{ref} stems from the sign choice for T. Augmented integral gains K_i are both chosen to be 1. Strong rolloff in the green curve is visible versus the red curve, indicating the effect of the integrator.

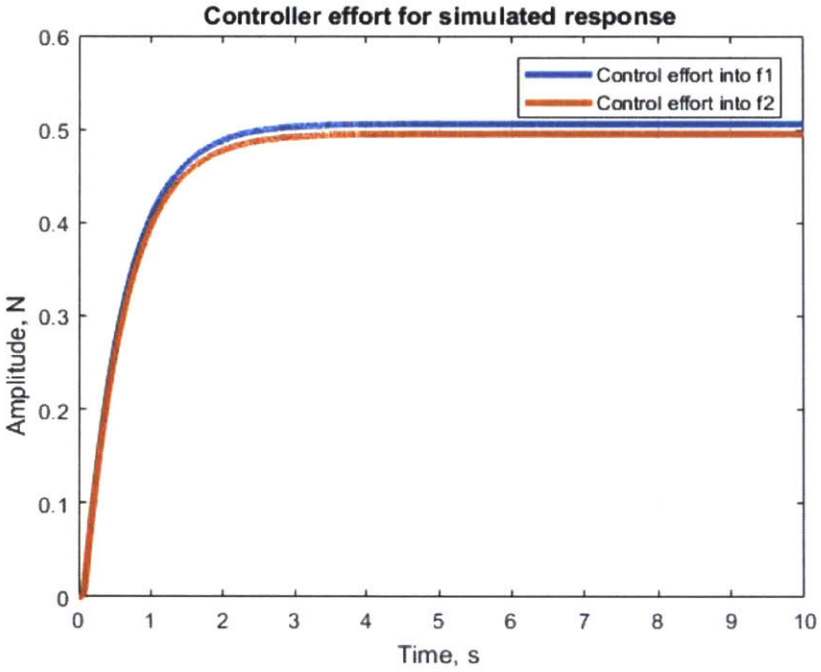

Figure 4-20: *Controller effort in response to a unit step command into F for the augmented system.* The effort exerted by the actuators in response to a unit step is much reduced in the augmented system as compared to the integral control system, but the rise time is also longer.

z_0 is again the frequency of a closed loop zero, then the transmission zeros for the closed-loop system will be given by

$$\begin{bmatrix} -(z_0 I - (A - BK)) & B \\ C - DK & D \end{bmatrix} \begin{bmatrix} x_0 \\ r_0 + Kx_0 \end{bmatrix} = 0, \tag{4.21}$$

which, upon solving, gives equivalent values for z_0 as 4.20. [18] The consequence of this is that zeros cannot be modified by state feedback; and, as visible in 3-20 and 3-24, poorly damped zeros appear at approximately 1.5Hz, 30Hz, and 90Hz among the four transfer function pairings. This means that the closed-loop system will not follow frequency commands around those points, and that disturbances occuring around those frequencies will also be poorly rejected. However, it does not rule out the possibility of achieving acceptable performance if the disturbances in these frequency bands are small, especially since for the experimental stamp, which had a constant pattern, the reference was set to be a constant.

A similar consequence arises from the fact that the system is not controllable. Controllability may be determined by evaluating the expression

$$\text{rank}(C_{trb}) = \text{rank}\left(\begin{bmatrix} B & AB & A^2B & \ldots & A^{n-1}B \end{bmatrix}\right). \tag{4.22}$$

If $\text{rank}(C_{trb}) = n$ for A being n by n in dimension, i.e. C is of full rank, then the system is controllable. [15] If a system is controllable, then the input is capable of affecting each mode, and arbitrary placement of poles can be achieved through full-state feedback.

For the 12th order printhead model, the system would be controllable if $\text{rank}(C_{trb}) = 12$. The actual rank of the controllability matrix is 6. The consequences of this are that $12 - 6 = 6$ poles cannot be arbitrarily moved, even by full-state feedback.

However, this system is inherently stable; except for the mode at 60Hz (the mode associated with the bushing o-rings), modes appearing between 1-100Hz are well-damped; and fortunately, the mode at 60Hz is controllable, so that even if it cannot be arbitrarily placed, it can be damped and reduced or eliminated from the system

response. The uncontrollability imparts undesirable constraints on the control design, but does not render it impossible.

Sensitivity Analysis

The design was also analyzed for its sensitivity to noise in order to predict its potential capability for disturbance rejection. From the "gang of six" transfer functions describing sensitivity, the closed-loop output response to process disturbances is given by

$$S = \frac{1}{1 + PC}, \tag{4.23}$$

where P is the plant and C the controller. [63] Where this value is low is where the output is not sensitive to disturbances (i.e., disturbances are well rejected); where it is high, those frequencies will appear in the output. Typically a high loop gain results in a low sensitivity and vice versa; that is, in frequency ranges where the magnitude of the sensitivity is large, the closed-loop output will be less able to attenuate. Sensitivity is shown in Figure 4-21. Noticeably, the transmission zeros, which appear as points of low magnitude in the loop gain, appear as peaks rising above unity in the sensitivity plot. The controller can do little to reject disturbances in those frequencies (as expected). Over a frequency band ranging from 1-30Hz, noise should be attenuated by about 3dB. Additionally, cross-coupling between the outputs and the inputs is well-removed by the controller, attenuated by many orders of magnitude.

Another measure of sensitivity is the complementary sensitivity, given by

$$S_c = \frac{PC}{1 + PC} \tag{4.24}$$

This is a measure of the sensitivity of the closed-loop to variations in the model, which are expected in this application due to variations in the stamp's properties. [63] Qualitatively, complementary output sensitivity could be considered the difference between an expected plant output and the actual plant output—i.e., how much the actual plant differing from the plant expected by the controller will affect the closed-loop output. Figure 4-22 shows the complementary sensitivity. Both outputs are

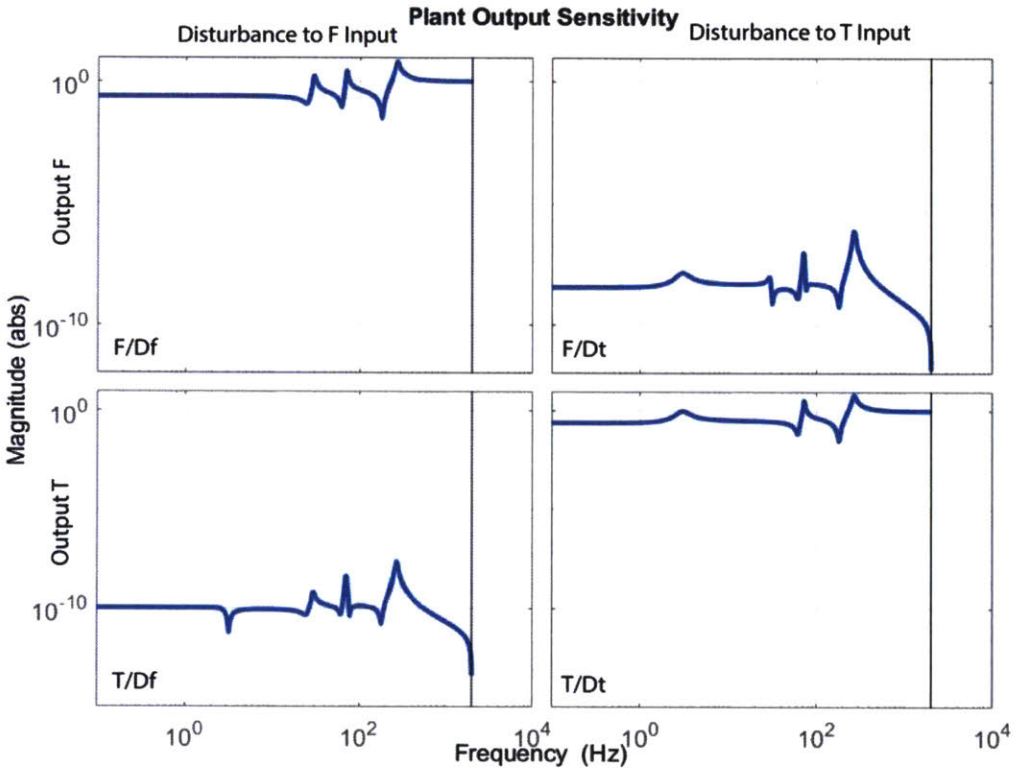

Figure 4-21: *Sensitivity for the plant with pole-placement controller.* The effects of the observer and the augmented integrator states are not shown here. Sensitivity can be considered a measure of the magnitude of a process disturbance (D_f or D_t) appearing in the closed-loop output. Though the sensitivity of the cross-terms to disturbances is low, the sensitivity of F/F_{ref} crosses unity at about 30Hz, and the sensitivity of T/T_{ref} at about 3Hz and again at about 70Hz.

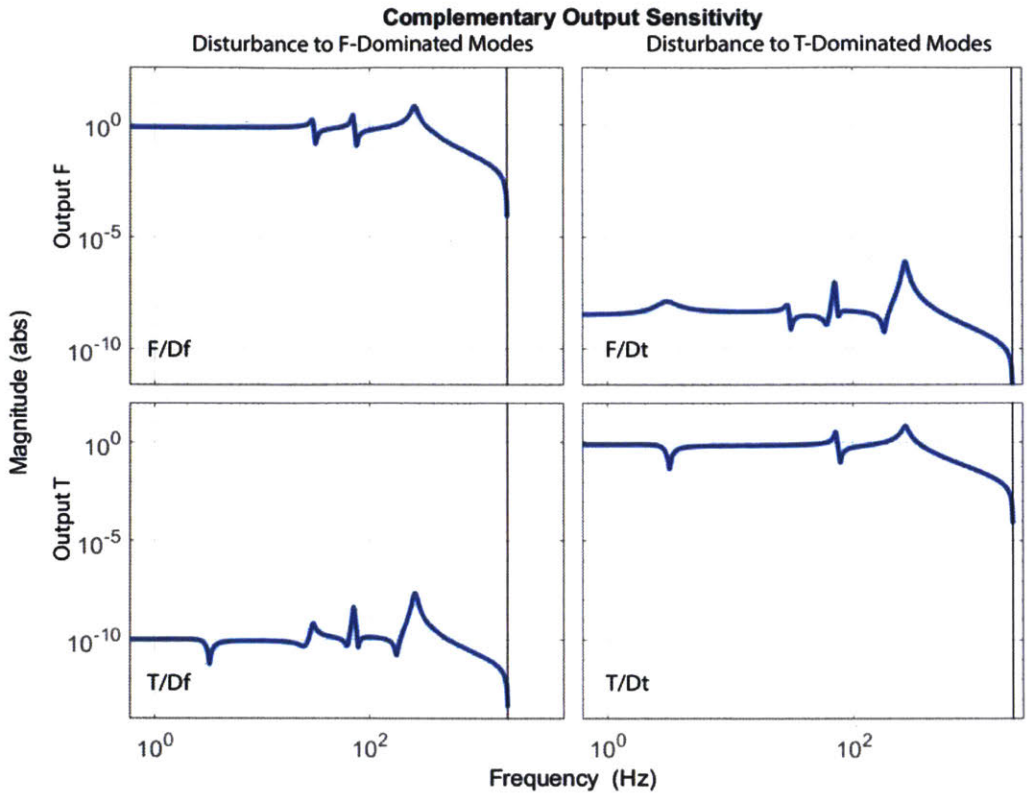

Figure 4-22: *Complementary output sensitivity for the plant and pole-placement controller.* The effects of the observer and the augmented integrator states are not shown here. Functionally, the "Disturbance to F-Dominated Modes" input group shows how the closed-loop outputs respond to differences in the F output between the expected and actual. In this measure of sensitivity, the F/D_f output is most sensitive to plant variations, which indicates that small changes in stamp stiffness k_{sy}, for example, may have a notable effect.

clearly sensitive to the lower frequency antiresonances at 30Hz and 70Hz, but the F output is notably more sensitive to model variation. The 30Hz peak depends on the stamp's translational stiffness properties and will vary, so this sensitivity is undesirable.

Clearly, severe limitations on what a controller with only these inputs and outputs can accomplish exist. From this initial design analysis, it was expected that reasonable performance in the 1-100Hz bandwidth cold not be achieved, but that satisfactory performance in the 1-10Hz bandwidth may still be accessible.

4.3.2 Closed-loop Observer Design

Because full-state feedback was to be implemented, an observer was needed. It was desirable to make this observer closed-loop in order to accommodate expected variations in the stamp properties, inherent damping of the system, and mounting errors of the stamp.

As previously stated, a partial-order observer could have been implemented, as the states x_1 and x_2 are measured; however, due to the potentially large inherent offsets in these states creating undesirable initial conditions, they were estimated instead.

Two design approaches were explored for the observer. The first was to follow the rules of thumb to design an estimator with poles 3 - 10 times faster than the system poles using pole placement on the error dynamics. [15] The second was to utilize a Kalman filter to design an optimal estimator.

The first design proved to be difficult to implement. The printhead system is unobservable; the rank of the observability matrix $[C\ CA\ CA^2\ ...\ CA^{n-1}]^T$ is 6 instead of the full 12. (The augmented integrator states did not need to be estimated because they are computed directly from the output.) Because the placement of the observer poles depends on the observability matrix in an analogous way to how the controller poles depend on the controllability matrix, the observer poles cannot be arbitrarily placed for this system. [15]

However, they may still be placed within some bounds. The goal is to choose a matrix of gains L that controls the dynamics of the error system $\dot{\tilde{x}} = (A - LC)\tilde{x}$ (where $\tilde{x} = x - \hat{x}$, and $\hat{x}$ is the estimated state) in a satisfactory manner; that is, that converges these error dynamics to zero sufficiently fast. [15]

To make the observer successful, it was desirable to make all of the poles at least three times faster than the fastest pole pair; this would have put the slowest observer poles at approximately 540Hz. However, this was not possible due to the unobservable nature of the system; instead, the slowest observer pole that was mathematically limited to approximately 150Hz, putting it in the same range as the fastest system pole.

The consequences of this are that the observer will unintentionally filter behavior based on its slowest pole; by the rule of thumb, then, the observer will not correctly estimate behavior in the 180Hz frequency, but should be able to capture behavior at 60Hz and below. The 180Hz behavior would not be correctly reproduced by the estimator, and the overall effect would be to reduce closed-loop controller gain for that frequency, reducing the controller's ability there.

The aggressive pole locations of this observer (shown in 4-24), in an attempt to maximize the speed of the error convergence, made it very sensitive to errors in the model; slight changes in the frequency or damping of the model peaks could push an observer pole into the right half-plane and cause the system to go unstable. Since the physical system does exhibit some uncertainty in these values, the robustness of the manually placed observer was very poor.

An observer based on the steady-state Kalman filter was also developed. Optimal estimation techniques are attractive for higher-order systems like this one, as the design parameters can be reduced to a few values describing a cost function, instead of requiring the designer to manually select each of many individual parameters. For this system, the steady-state Kalman filter was employed, as steady-state measurements of both process noise and measurement noise could be derived from experiment. With a white noise model assumed, measurements placed the sensor noise RMS magnitude at 0.01, and the sensor noise magnitude was adjusted from its estimate in order to control the behavior of the Kalman estimator; a value of 0.001 was selected for each channel. Cross-variance coupling between the two was assumed not to be present.

With these design parameters, the steady-state Kalman gains could be computed; Franklin details its computation, but it will not be reproduced here. [15] the resulting error dynamics are shown in Figure 4-25.

The Kalman-optimized filter is notably slower than the manually designed filter, and relatively little effort has been expended to increase the speed of the poles. This is in part because real-world noise values are used to design the filter, and in part because of the limits unobservabilty places on the system. For example, even if the steady-state Kalman sensor noise input is artificially scaled down by six orders of

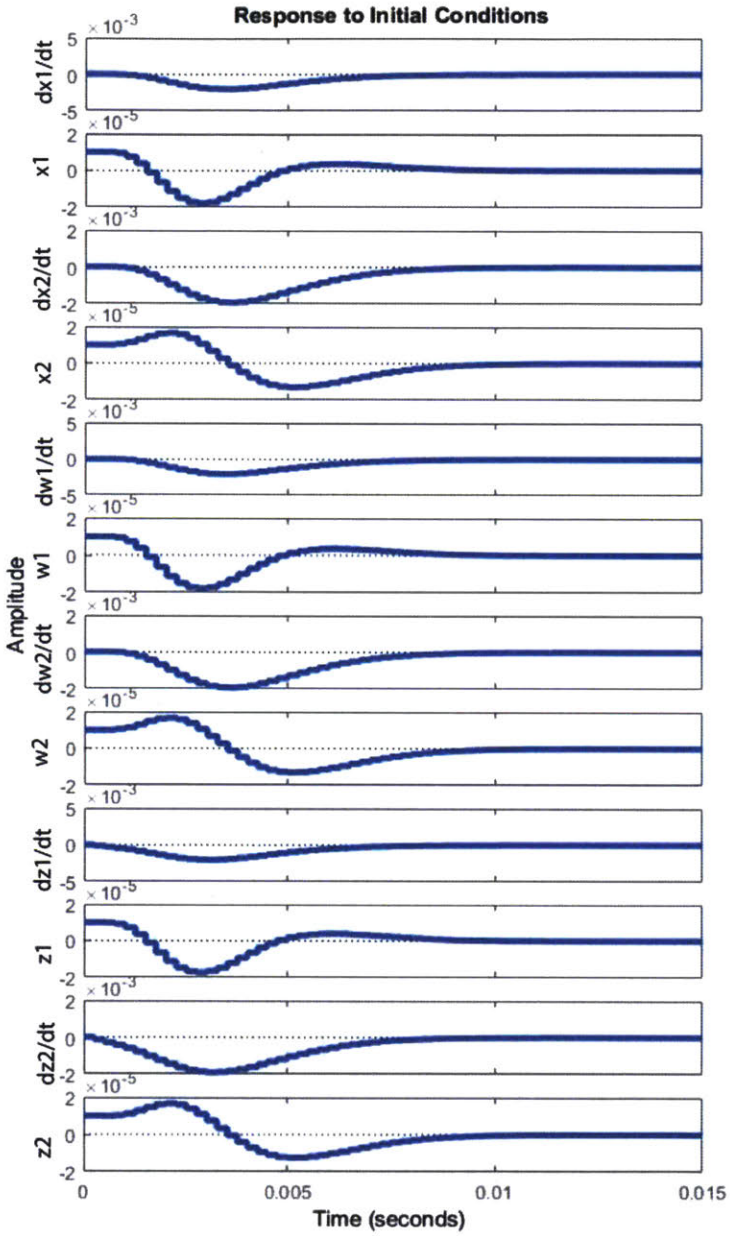

Figure 4-23: *Manually designed observer error dynamics initial condition response.* The manual pole-placed observer design rejected initial conditions errors within 10ms for all states (states correspond to the labeled displacements in Figure 3-15). The poles selected for this design were all real poles with frequencies 180-191 Hz, but due to the unobservability of the system, they could not be placed at those exact locations. The Matlab `place()` command optimized their placement within constraints.

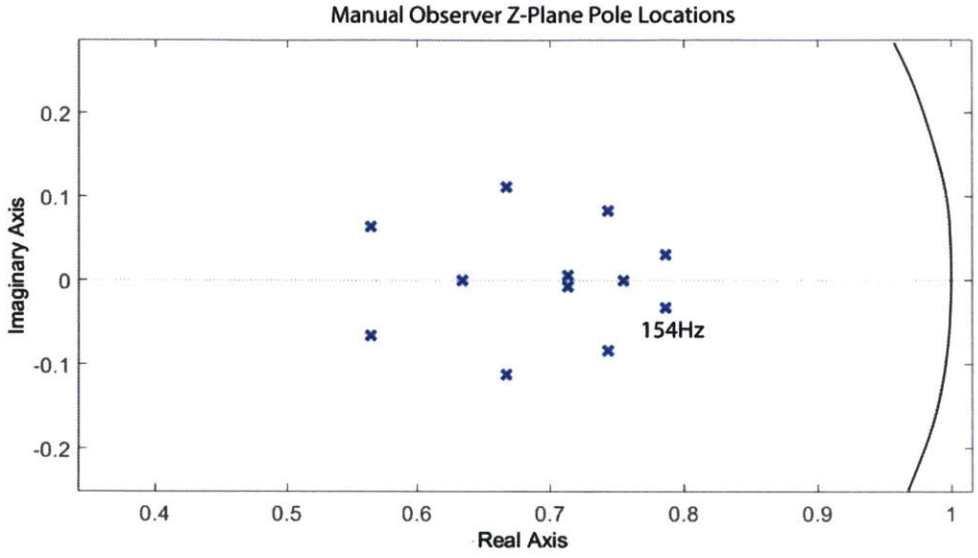

Figure 4-24: *Z-plane plot of manually placed observer poles.* These are the actual pole locations corresponding to the error dynamics in Figure 4-23. Note that they do not fall at the exact values of the design; the slowest pole actually falls at 154Hz.

magnitude, the slow system poles at approximately 2Hz are only increased to 3.2Hz, as shown in 4-27. (This occurs for the same fundamental reason that unobservability prevents arbitrary manual placement of the observer poles; that is, unobservability constrains the solution region for the expression defining the estimator gains, and thus the estimator pole locations. In the case of the Kalman filter, the steady-state gains L_∞ are given by the expression $L_\infty = M_\infty H^T \left(H M_\infty H^T + R_v\right)^{-1}$, where M_∞ is the covariance of the estimate error, R_v is a matrix derived from expected measurement noise, and H is the system's state space output matrix; in an unobservable system, this expression is not guaranteed to be invertible, constraining the values of L_∞. [15])

This causes the effect of greater filtering on the system and very robust stability, but also again degrades the controller's ability to reject disturbances exciting high-frequency modes. As upcoming sections will detail, the robustness of the heavily-filtering Kalman estimator was necessary in order to implement a stable controller in the face of physical system variation.

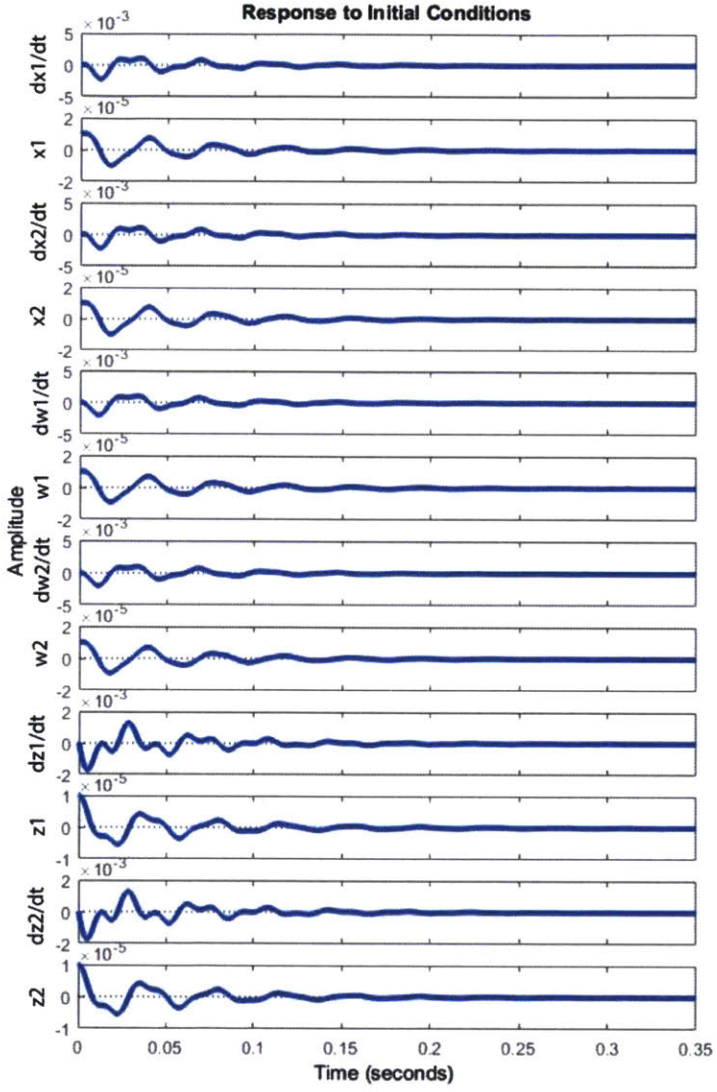

Figure 4-25: *Kalman-optimized observer error dynamics initial condition response.* The Kalman-optimal error dynamics converge in about 100ms, as opposed to the 10ms of the manually placed observer. States correspond to the displacements labeled in 3-15.

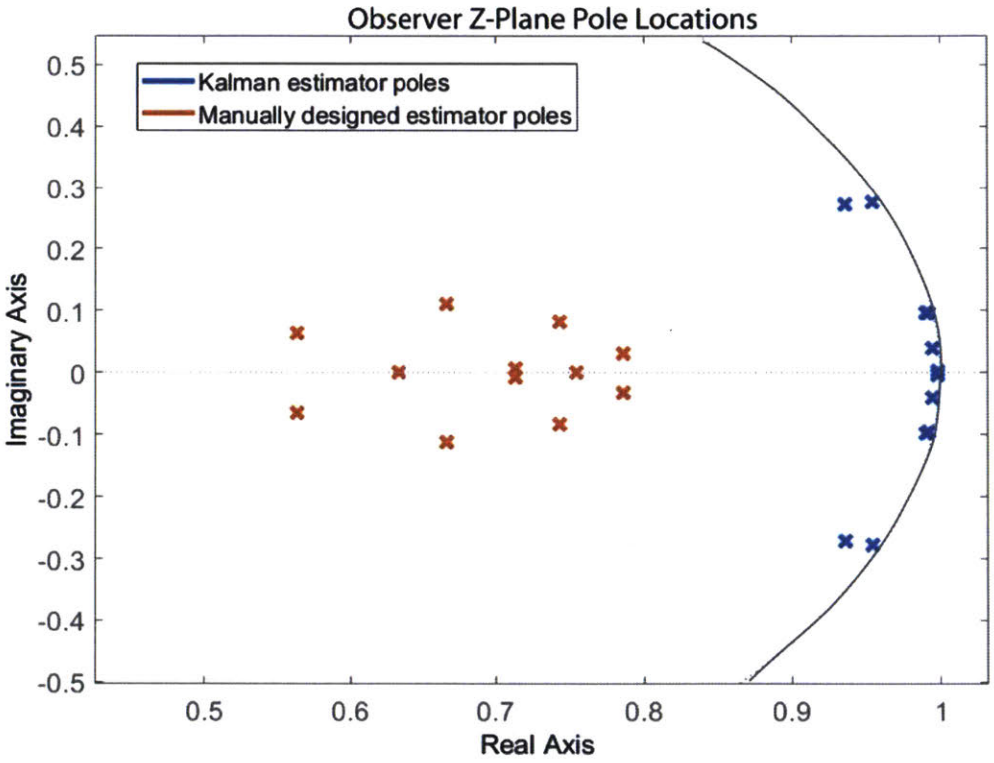

Figure 4-26: *Comparison of Kalman-optimized and manually selected poles.* The Kalman-optimized poles are much slower than the manual placement design. While the fastest Kalman poles are around 180Hz, the slowest is less than 10Hz.

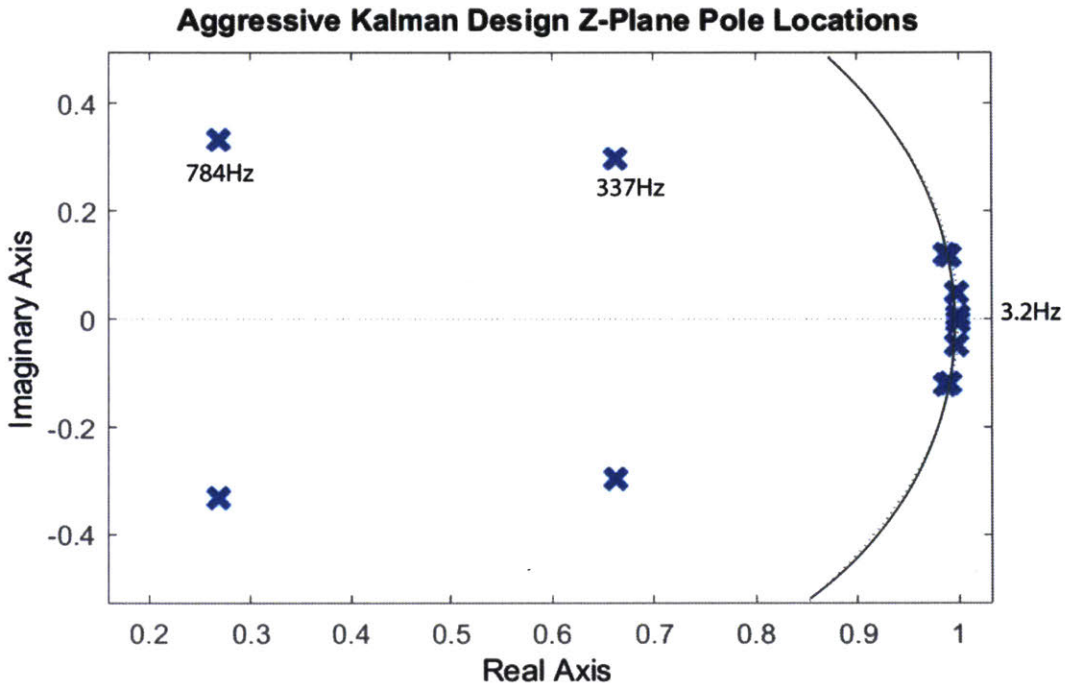

Figure 4-27: *Kalman-optimized filter with artificially manipulated noise inputs.* Even if the noise inputs for the Kalman filter are aggressively changed (by 6 orders of magnitude), only two pairs of poles are noticeably increased in frequency; the other four pairs cannot be arbitrarily moved because of the limitations of unobservability.

4.3.3 Simulated Results

The separation principle established that the controller and estimator could be designed separately, and that the entire system poles would be a combination of the two. Because the Kalman poles and the controller poles overlapped in frequency bands, the behavior would be a complex combination of the two. (When the observer is significantly faster than the controller, its poles can be ignored as high-frequency dynamics.)

A discrete-time simulation was constructed to investigate the disturbance rejection capabilities and overall stability of the combined estimator-controller system. Saturation limits were also incorporated into this simulation because of their potential effect on stability. Figures 4-28, 4-29, 4-30, 4-31, and 4-32 show the simulated behavior of the system under various conditions and discuss observations.

Overall, this controller and observer design do not accomplish all control objectives. The controller is robust to model variation and does produces behavior with zero steady-state error, but has very poor disturbance rejection ability. However, this is the maximum performance that can be obtained given the physical limitations of this system.

4.3.4 Implementation

Design for this system was done in discrete time, so there was no loss in mapping continuous time to a lower discrete time sampling rate.

Initially, efforts were made to implement the observer on the FPGA target. This seemed like an ideal situation because a much faster sampling rate could be used, approximating the observer as continuous and "perfect." However, the 12th order observer required a number of matrix operations, even after accounting for matrix sparsity that could reduce operations. The FPGA target did not natively support two-dimensional arrays, which made computation difficult to implement; further, the large dynamic range of the variables involved required large datatypes (64-bit fixed point numbers, e.g.) to accommodate them, further eating up FPGA resources and

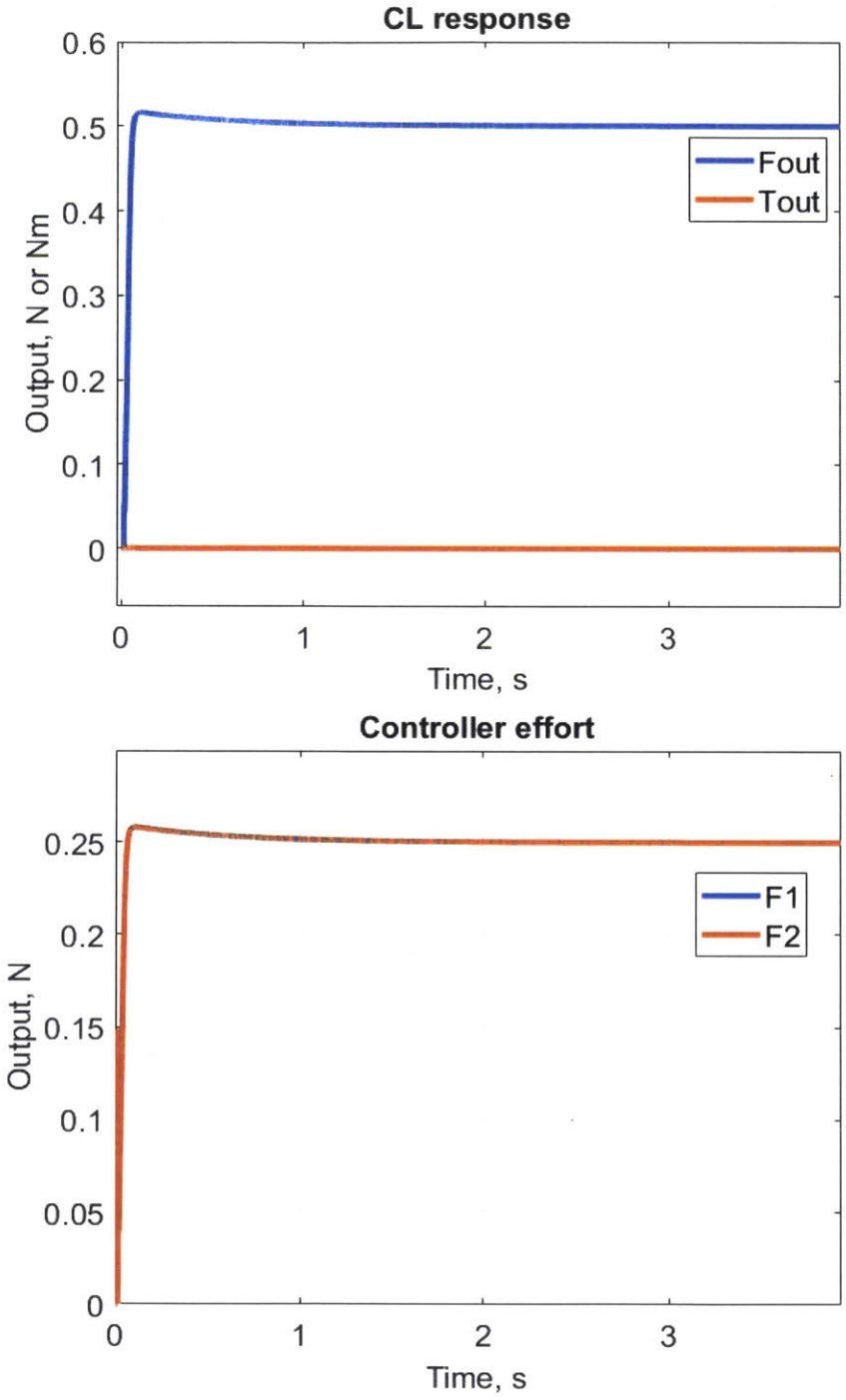

Figure 4-28: *Simulated output and controller effort step response for augmented state-feedback system with Kalman estimator.* Simulated response for a noise-free 0.5N step into F, and a static 0Nm command into T. Stead state error is quickly removed, and no cross-behavior in T is observed. The controller effort is also well-controlled.

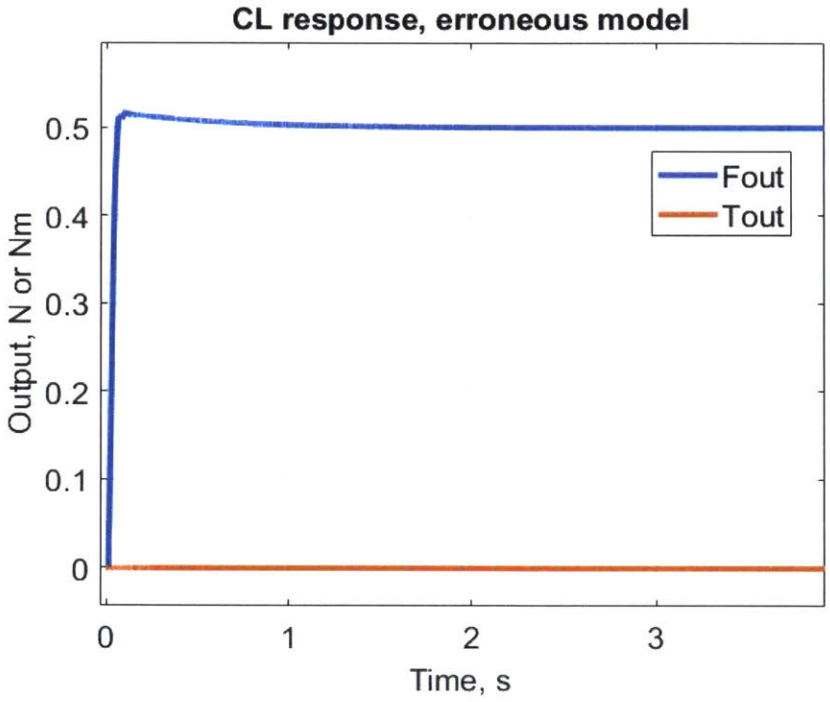

Figure 4-29: *Simulated output and controller effort step response for erroneous plant under augmented state-feedback control with Kalman estimator.* The same controller and observer as in Figure 4-28 are used, but the plant has been modified such that its stiffness parameters are increased by 10%. The results are still robust and settle to the correct value. The system will remain stable and eventually converge to the correct steady-state value with up to 20% error on the stiffness values.

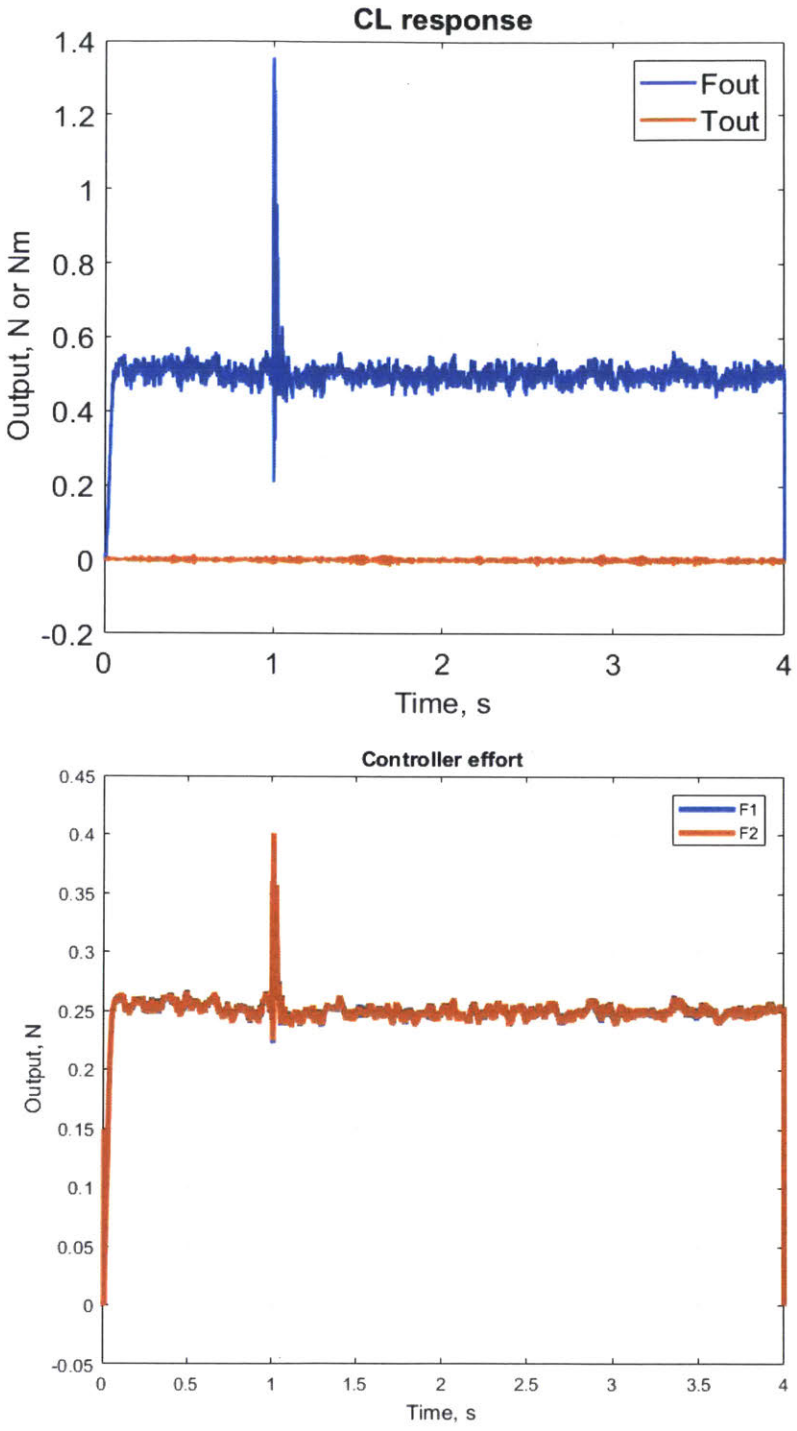

Figure 4-30: *Simulated output and controller effort for a noisy step input to the augmented state-feedback system with Kalman estimator.* A white noise signal filtered above 250Hz with an amplitude of 0.01, and an impulse signal into of magnitude 1.0 at $t = 1$, are injected as process noise on the 0.5N step command. (The impulse is only injected into the force input, not the torque input.) Poor noise rejection is clearly visible, but the impulse stably settles within 50ms.

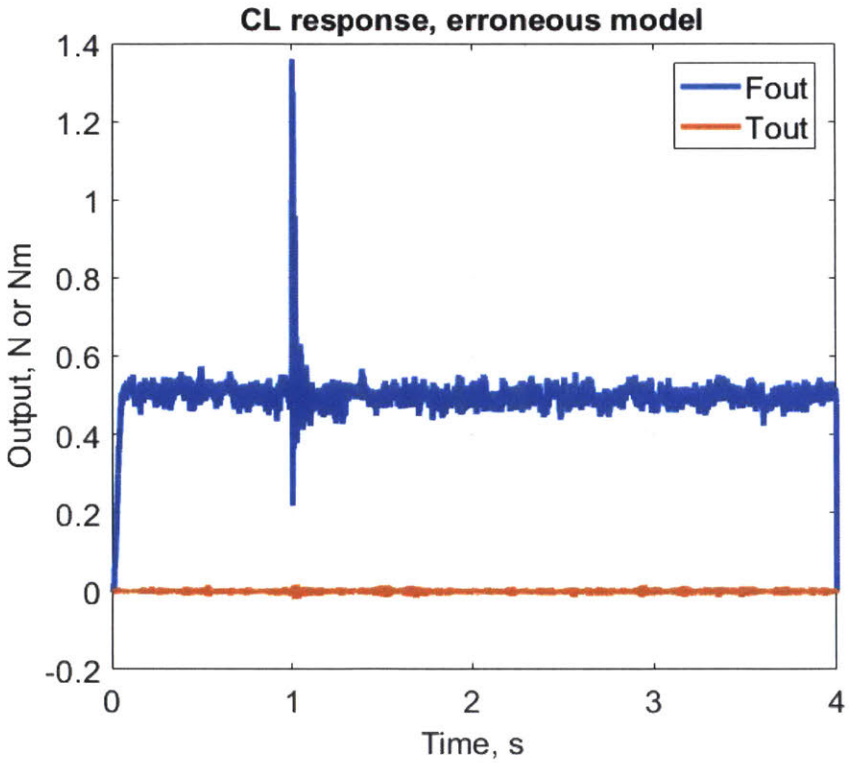

Figure 4-31: *Simulated output and controller effort for erroneous plant under a noisy step input to the augmented state-feedback system with Kalman estimator.* The same combination of filtered white noise and an impulse are applied to the erroneous plant used in 4-29. Again, the output settles within 50ms of the disturbance, but the noise is poorly rejected.

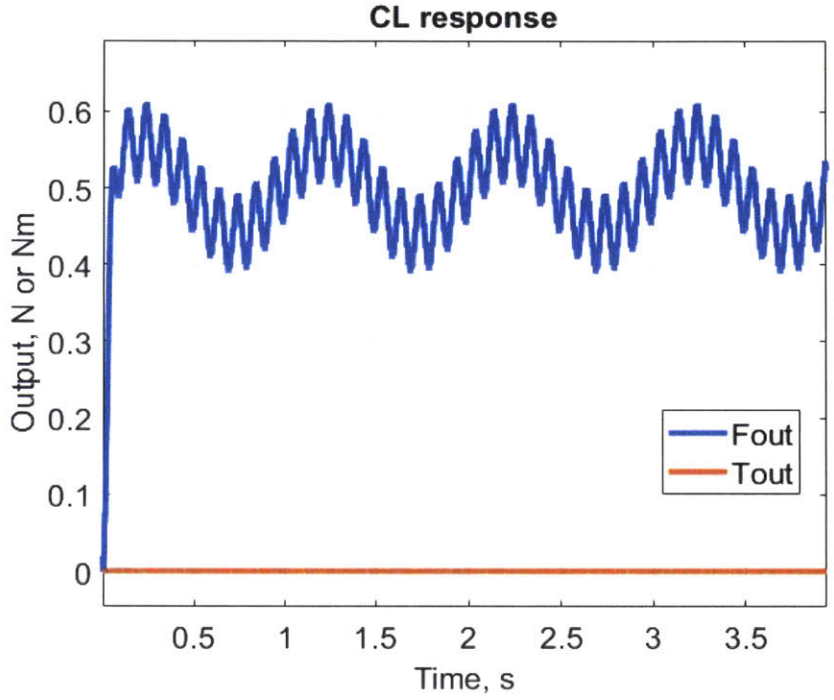

Figure 4-32: *Simulated output and controller effort for sine-overlaid step input to the augmented state-feedback system with Kalman estimator.* Injected on the 0.5N step command into F are a 1Hz, 10Hz, and 100Hz sine wave process noise, each with a 0.01 amplitude. The 1Hz frequency is amplified to about 0.1N in magnitude; the 10Hz frequency is amplified to about 0.05N in magnitude; and the 100Hz frequency is attenuated (not visible at this zoom level). This indicates that the system is able to reject disturbances at higher frequencies, but not lower frequencies.

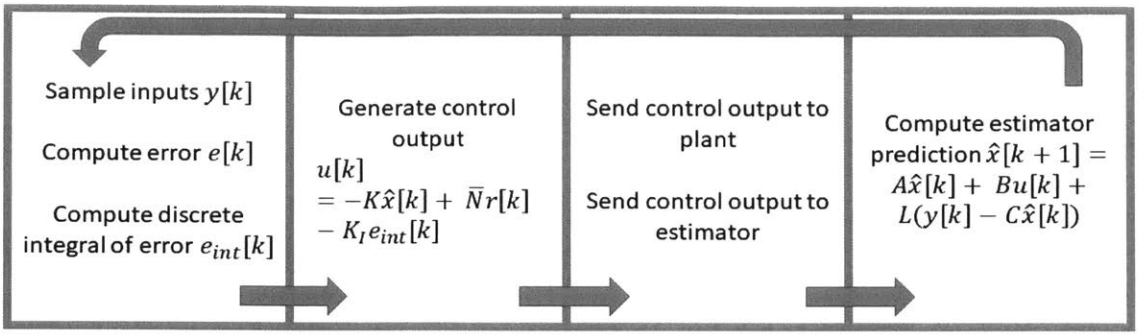

Figure 4-33: *Discrete-time control dataflow schematic.* This loop operates on the LabVIEW real-time controller at a 4kHz rate. Updating the steps in the proper order for the selected formulation of control law and estimator is critical to stability.

reducing numerical precision.

Eventually, with the move to the robust but slow Kalman optimal design, the choice was made to implement the observer in step with the controller on the real-time target. The real-time controller loop operated at 4kHz, and supported both two-dimensional arrays and floating point numbers, greatly increasing the accuracy and speed of the observer computation. Order of computation was important, and the general sequence of operations was: (1) sample outputs from hardware; (2) compute output signal $u[k]$ using measured outputs $y[k]$ and estimated states $\hat{x}[k-1]$; (3) send control outputs to the system and to the observer; (4) compute current observer outputs $\hat{x}[k]$. A diagram showing this flow is shown in 4-33.

4.3.5 Experimental Results

The same experiments conducted for the pure integral control system were also conducted for the closed-loop system with the observer; namely,

1. Contact measurement of manually rolling the undriven imaging system over a piece of tape placed under the stamp, to simulate a disturbance in sample thickness or assembly;

2. Contact measurement and on-machine meeasurement of disturbance rejection to manual disturbances created by imparting impulses with hand tools;

3. Contact measurement of step response, sent as a command to the actuators;

4. And on-machine printing at speeds of 0.2, 0.5, 1, and 4 in/s. Printing was conducted without ink onto a PET substrate due to the scarcity of the necessary gold substrate.

To reiterate, all of the tests were conducted with a reference of $F = 4$ and $T = 0$, and the printing tests were conducted under open loop web tension of 30N. Results from these tests are shown in Figures 4-36, 4-37, 4-38, and 4-39.

Under contact measurement (shown in 4-34), little difference was observed between the performance of the open-loop system and the MIMO control system; contact measurements suggest that the MIMO controller may have been able to better reject the step disturbance posed by the tape edge (in that it maintains contact closer to the tape edge), but quantifying this measurement under the limitations of the contact imaging system (rough manual roll positioning, noisy images, small capture area) is difficult.

Quantitatively, the performance of the augmented state controller was marginally better than that of the pure integral controller. At the 1 in/s printing speed, for example, the RMS noise was reduced from about 0.15 N or 0.014 Nm for the open-loop case to about 0.12 N or 0.012 Nm for the closed-loop augmented state controller. The steady-state error was also slightly reduced from the pure integral case, falling below 2% error for force, and approximately the same (0.05 Nm mean value) for torque.

However, these marginal benefits came at the cost of a great deal of effort and implementation complexity. For only a few percentage points of improvement on the stated control objectives, the controller went from a simple one-line control law to a complex system with 26 poles and numerous coupled dynamics.

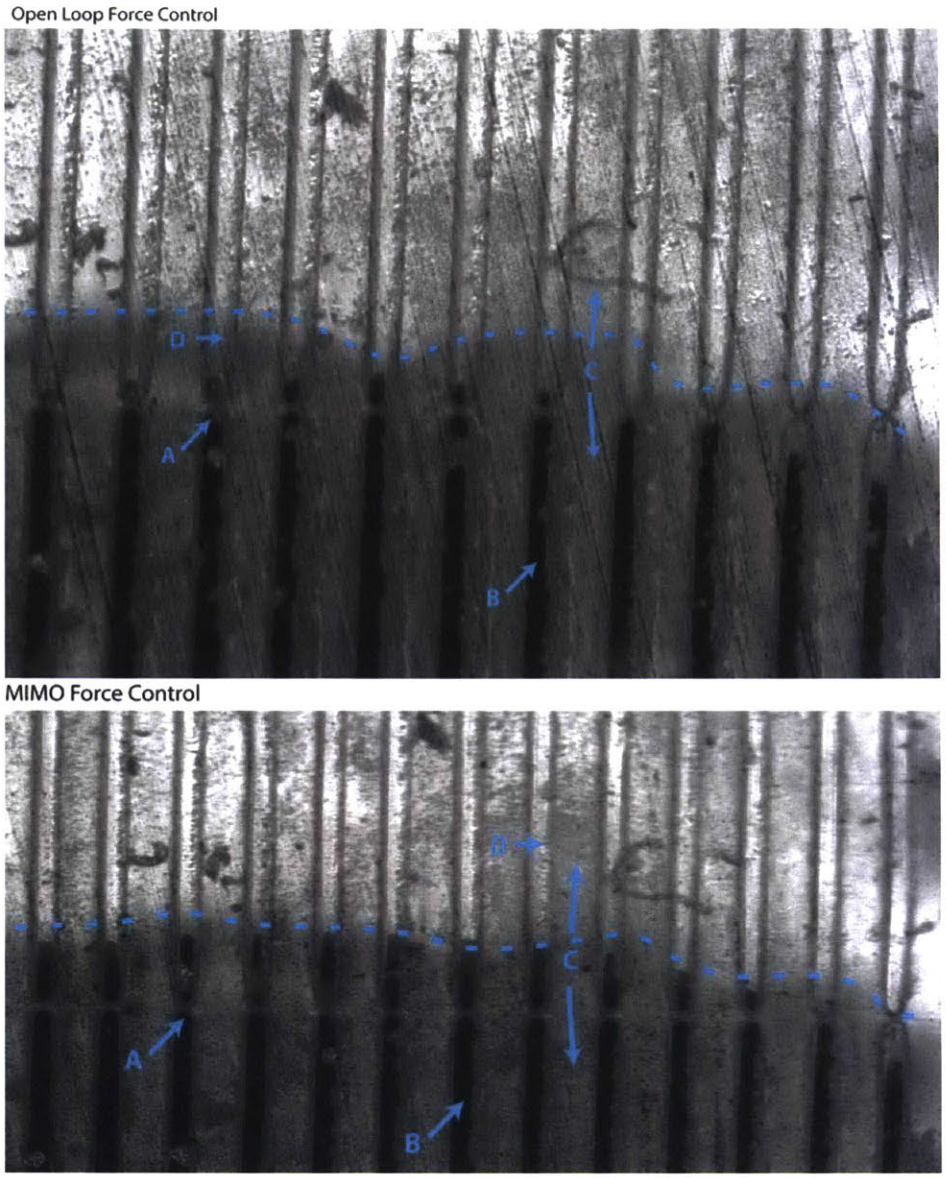

Figure 4-34: *Contact imaging measurements of the open-loop and MIMO-controlled systems.* Both images have been enhanced for clarity. As in 4-7, the top image was acquired using open-loop force control, and the bottom image acquired under augmented state feedback control. The edge of the strip of tape is demarcated with a dotted line. (A) indicates a gap in the continuous line features occurring at 0 degrees rotation; (B) indicates the dark region in which contact is occurring; the light regions in (C) and (D) respectively are the stamp roof and a stamp feature, neither of which are in contact with the glass roll. Qualitatively, the MIMO system appears to be able to ensure contact occurs right at the edge of the tape, which the open-loop and integral control systems (see 4-7) do not.

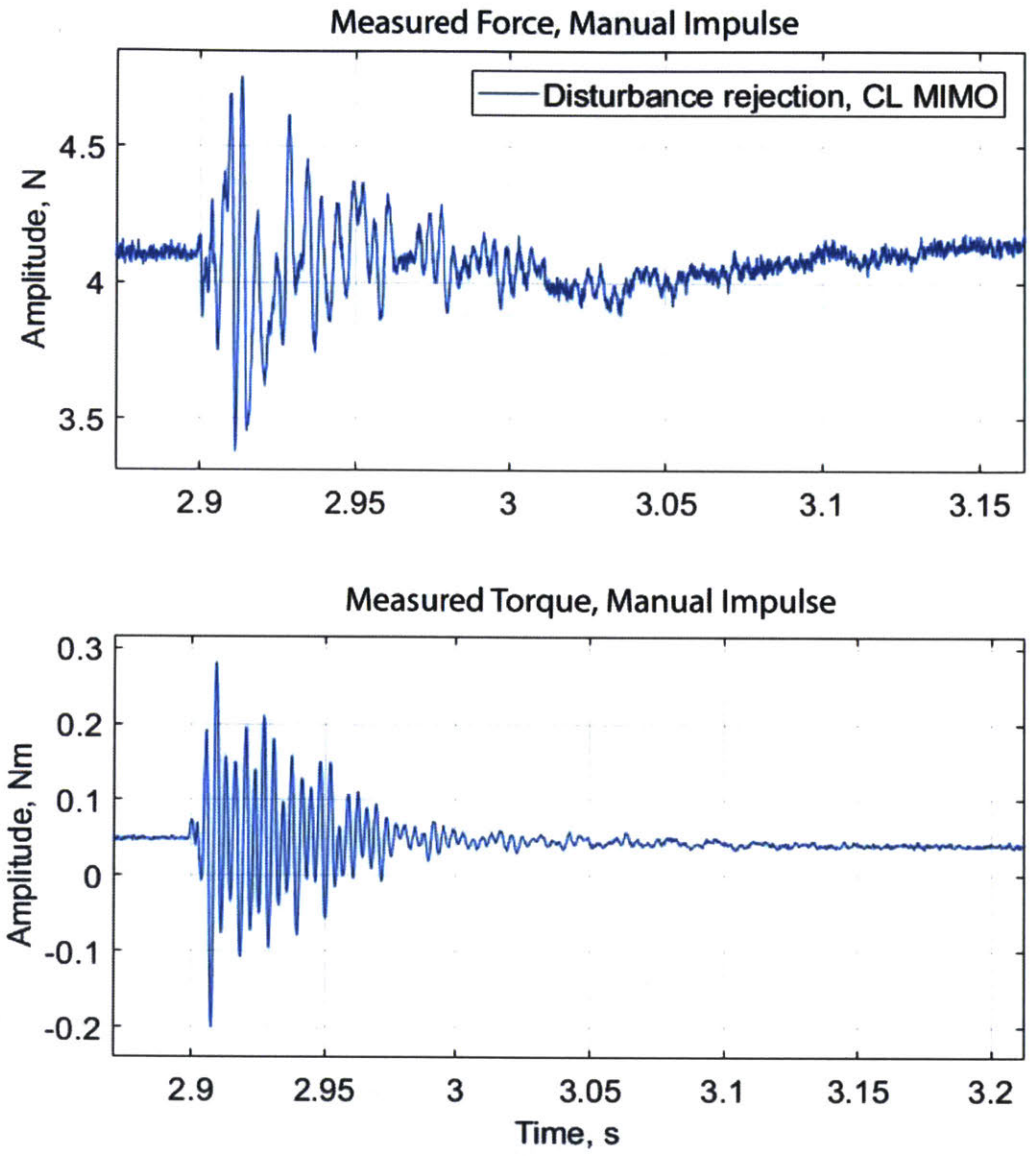

Figure 4-35: *Disturbance rejection of a manual impulse to the closed-loop system.* Attenuation is marginally better than the pure integral system and the open-loop system, as shown in 4-9 and 4-8. A manual disturbance applied with a hand tool just beside the stamp is attenuated with about 80ms, and the lingering 60Hz ringing apparent in the integral output is not visible here.

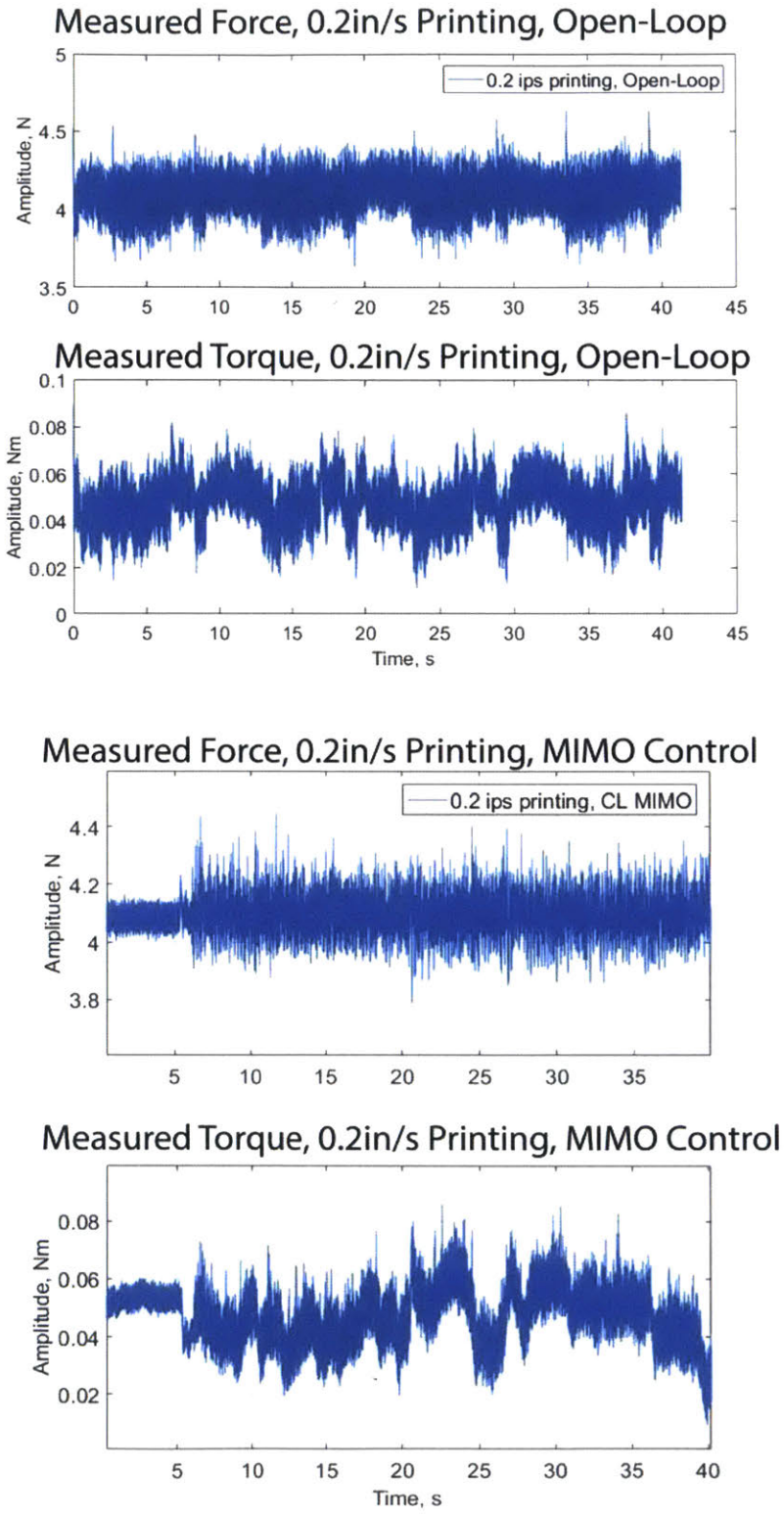

Figure 4-36: *Output comparison for 0.2 in/s printing speed for open-loop and MIMO force control.* The closed-loop full order observer MIMO system does not achieve observably superior performance to the pure integral controller.

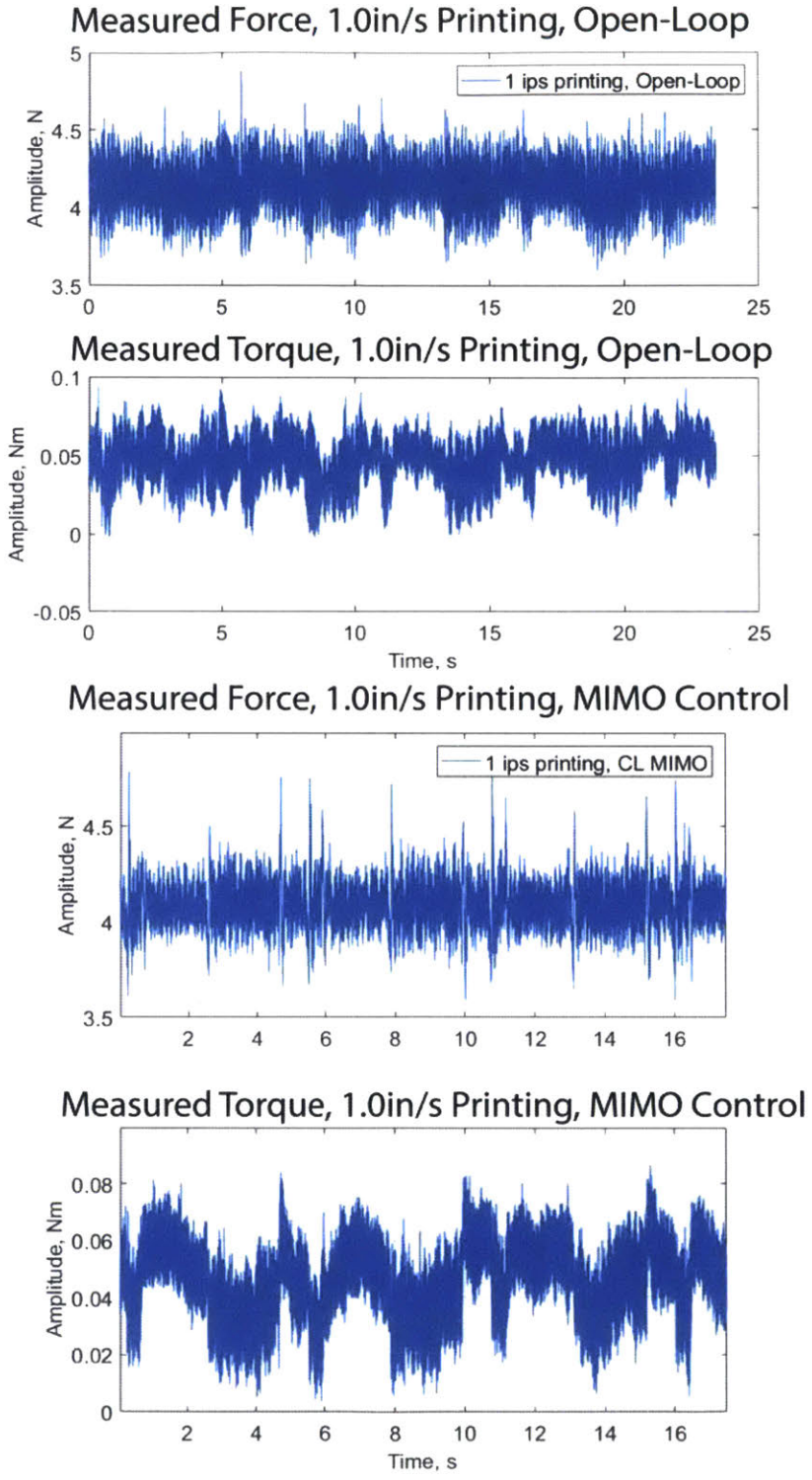

Figure 4-37: *Output comparison for 1.0 in/s printing speed for open-loop and MIMO force control.* As in the 0.2 in/s case, at 1 in/s, the augmented state controller with observer does not meet control target goals.

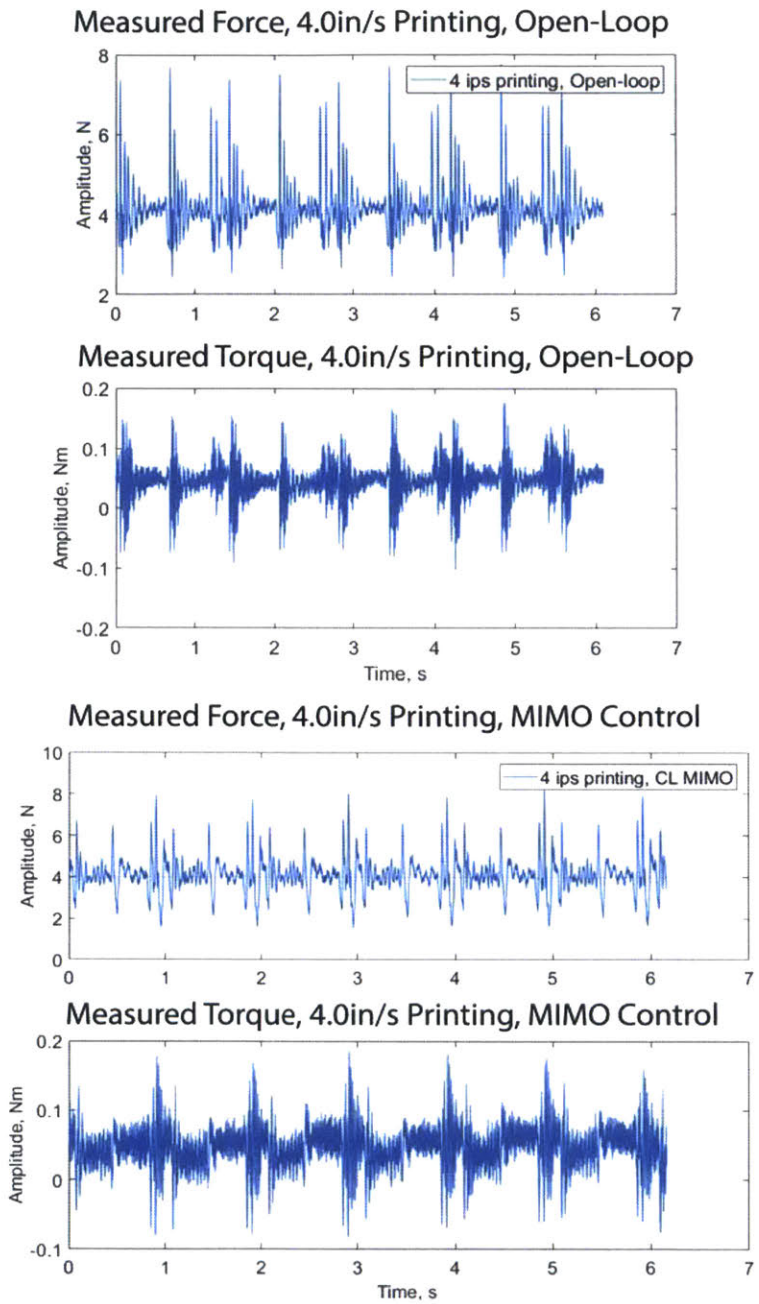

Figure 4-38: *Output comparison for 4.0 in/s printing speed for open-loop and MIMO force control.* At 4 in/s printing speed, the closed-loop system is clearly attenuating some of the high-frequency disturbances, but its performance still falls short of achieving the stated control objectives.

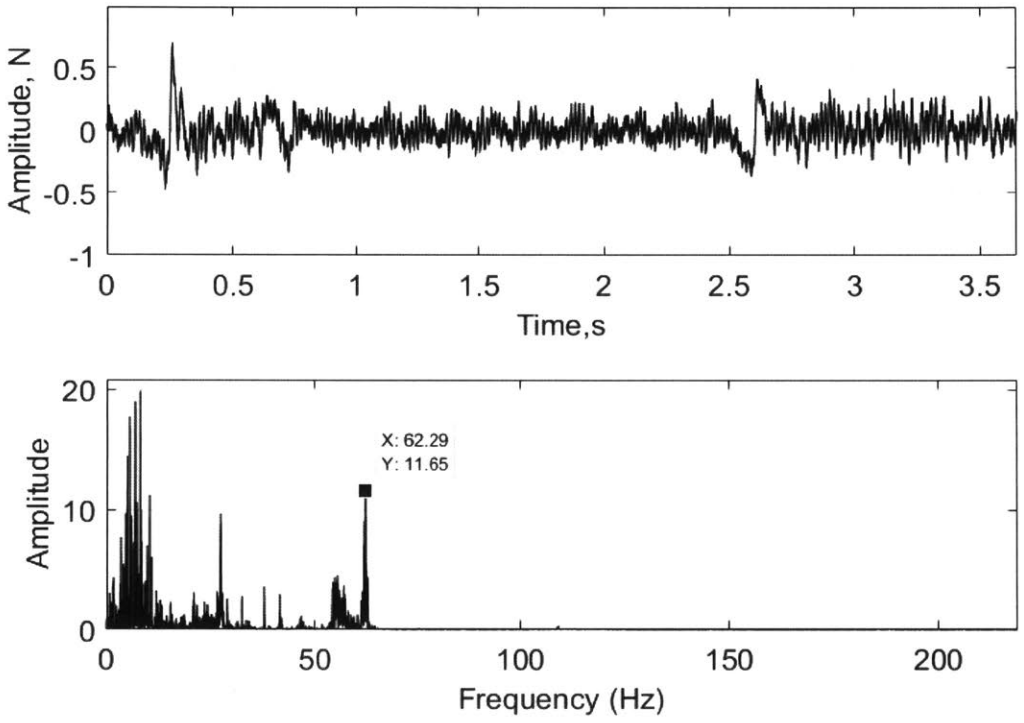

Figure 4-39: *Frequency content of closed-loop force under MIMO control during printing.* The mean value has been removed from the force output to accentuate dynamic frequencies. The frequency content of the output of the augmented state controller shows the same peak at 60Hz as that of the pure integral controller (see 4-13), its magnitude is greatly attenuated.

4.4 Discussion

Overall, the results of the augmented state controller plus full-order optimal closed loop observer are disheartening. Even with the powerful tools afforded by the MIMO controller design, improved performance over the simple integral controller, or even the open-loop plant, could not be demonstrated.

The key impediment to achieving the control objectives is in the configuration of the system itself. Having many sets of stacked compliances but only two inputs results in many uncontrollable modes, meaning that even a sophisticated pole-placement controller cannot remedy undesirable modes that fall into the desired closed-loop system bandwidth. Additionally, the observer itself could not accurately reproduce dynamics for the controller to reject, as its bandwidth was also severely limited by the unobservability of the system.

As detailed above in the section regarding the Kalman filter design, the controller's limited ability to modify the system response stems from the boundaries on the mathematical solutions to the equations that produce the controller or estimator gains. In the case of the Kalman filter, it was the cases in which the steady-state gains L_∞ were constrained by an uninvertible right hand side in the equation $L_\infty = M_\infty H^T \left(HM_\infty H^T + R_v\right)^{-1}$.

For the placement of the controller poles, the desired discrete time characteristic equation for a selected set of poles is given by $z^n + \alpha_1 z^{n-1} + ... + \alpha_n$; the controller gains resulting in this exact set of poles may be found by solving the equation

$$|zI - \Phi + \Gamma K| = z^n + \alpha_1 z^{n-1} + ... + \alpha_n, \tag{4.25}$$

where Φ is the discrete-time state space A-matrix, Γ the B-matrix, and K the set of gains. Exactly analogously for the placement of the observer poles using the observer gain matrix L_p, with characteristic coefficients β_i, the relationship is

$$z^n + \beta_1 z^{n-1} + ... + \beta_n = |zI - \Phi + L_p H|, \tag{4.26}$$

where H is the discrete-time state space C-matrix. [15]

In both of these cases, when the controllability or observability matrix is not full rank, there will be sets of α_n and β_n for which no K or L_p may be selected that will solve these equations; that is, the control designer has lost the ability to arbitrarily select the controller and estimator pole locations. However, there are still many potential choices for α_n and K, and for β_n and L_p, that may still achieve a particular control performance goal; but the control designer's ability has been circumscribed from arbitrary adjustment within actuator capability to a limited set of permissible gains.

Recall that the goal of the MIMO controller was to be able to flatten or damp the undesirable higher-frequency modes appearing between 1 and 100Hz using pole placement, and then to use an augmented state controller with integrator states to further boost low-frequency gain. Though a satisfactory set of gains K that added damping without changing frequency could be selected, sets of gains that, for example, signficantly increased the frequency of the 2Hz mode did not exist. The integrator "wrapper" around the pole-placement controller did offer an additional tool to the designer, but it was limited to boosting steady-state gain and rolling off high-frequency noise; it had no effect on modifying the dynamics in the desired bandwidth or on the transmission zeros.

It was particularly detrimental that L_p could not be chosen arbitrarily for the state estimator, enforcing unwanted filtering on the states and reducing the controller's ability to detect and reject changes in the outputs. Though the controller and the observer may be designed separately, the combined system will have the poles of both. [15] When the high-performance "fast" observer was implemented, small variations in the system model would induce instability, so the Kalman observer was used experimentally. But, when the slower but robust Kalman filter was utilized, the combined system's response was now dominated by the Kalman poles, which were approximately the same as those of the open-loop system—i.e. with slow poles all the way down to 2.6Hz. Examining figure 4-25, it is clear that the states converge on the timescale of 0.1s, which estimates the dominant poles at no faster

than about 40Hz. (The "fast" observer states converged about 10 times faster.)

The net effect is that the state estimate going to the controller is filtered by these slow poles, and that frequencies significantly above the Kalman poles will not be passed to the controller–effectively limiting the speed of the closed loop system's response to the slow observer poles. This can of course be used to effectively remove noise from an otherwise unusable signal, but in this case, it is hiding physical signals that the controller should be removing. In the end, only the augmented states, which are directly computed from the inputs, directly see disturbances in the outputs; and so the disturbance rejection is coming chiefly from this integral capability.

Another side effect of the stacked compliances is the presence of a number of transmission zeros. Even assuming that the observer and controller gains could be selected as desired, the poorly damped transmission zeros cause large magnitude peaks in the sensitivity function, indicating that the system would be sensitive to disturbances in those frequency ranges. (Figure 4-39 shows some indication of this, with a strong frequency component associated with the locations where sensitivity peaks are high in the output sensitivity.) Additionally, the upper bound to the potential bandwidth of the system is set by the 2Hz mode of the rotational component, cutting the design goal of 100Hz bandwidth down to a maximum possible bandwidth of approximately 1Hz.

Overall, then, this control design was unsuccessful in meeting the stated control objectives. This was because of physical limitations inherent in the system's response (uncontrollability, unobservability, and transmission zeros occuring within the target bandwidth), which derive from its physical properties (stacked compliances), and can only be solved with physical modification of the printhead.

If an active, feedback-controlled printhead system capable of managing printing forces down to level suitable for nanoscale features is to be developed, it must be designed for control from the beginning, with thought into how its mechanical features will influence its dynamic performance. The next chapter will present design principles and an improved design enabling high-performance printing control.

Chapter 5

Design for Microcontact Printing

5.1 Design Principles for Microcontact Printing

As detailed in Chapter 4, the existing printhead imparts significant limitations on control design. If its capabilities are to be extended so that force may be very finely controlled for stamps with features on the order of micrometer or nanometers, then it becomes necessary to iterate on the existing printhead and take on a redesign with the intent of control capability in mind.

This chapter details design rules and lessons learned from work on the existing printhead, and details an improved design that improves control capability immensely. Implementation of this design in hardware is left to future work.

5.1.1 Potential Modifications to the Existing Printhead

The path of least resistance is to first consider what modifications to the existing printhead design could be made in order to improve its dynamic characteristics.

There are numerous ways to frame the limitations of the existing printhead. Two logical ways to are to posit that (1) the system's uncontrollability and unobservability are the problems, or that (2) the frequency and nature of the system's modes are the problem.

Achieving Controllability and Observability with Sensors and Actuators

The system as-built is capable of four independent measurements (displacements x_1 and x_2, and forces F_1 and F_2). To make the system fully observable, the system order must be reduced until these four measurements can measure all of the system modes; or, additional sensors must be added, such as accelerometers or position sensors on each independent mass.

Though this may remedy the unobservability problem, the addition of sensors alone does not address the uncontrollability problem. Even if perfect state information is available, there are modes that the controller cannot compensate, because the actuator inputs are unable to independently affect them. To correct this, additional actuators would need to be installed, increasing the system configuration beyond two inputs to four or more. One could envision actuators mounted across various compliances on the system such as the flexure sensors, but physically packaging them is difficult.

Also, merely adding sensors or actuators to the printhead as designed is equivalent to applying a bandage when surgery is needed, and will greatly increase the complexity of an already complex system. A better strategy, then, would be to physically correct some of the undesirable dynamics of the printhead by physically modifying its components.

System Parameter Modification

The first, simplest effort would be to introduce epoxy into the gap around the print roll air bushings, greatly increasing the upper o-ring stiffness k_{uf} without making any other changes. As shown in Figure 5-1, the net effect of this is to great increase the frequencies of the dynamics related to this compliance.

However, though this stopgap fix could improve the system behavior, it does not make the system anywhere near ideal. Printhead dynamics dominated by the stamp-print roll interaction still appear in the 1-100Hz range; in fact, the undesirable antiresonances dominated by the stamp dynamics have hardly moved, still appearing

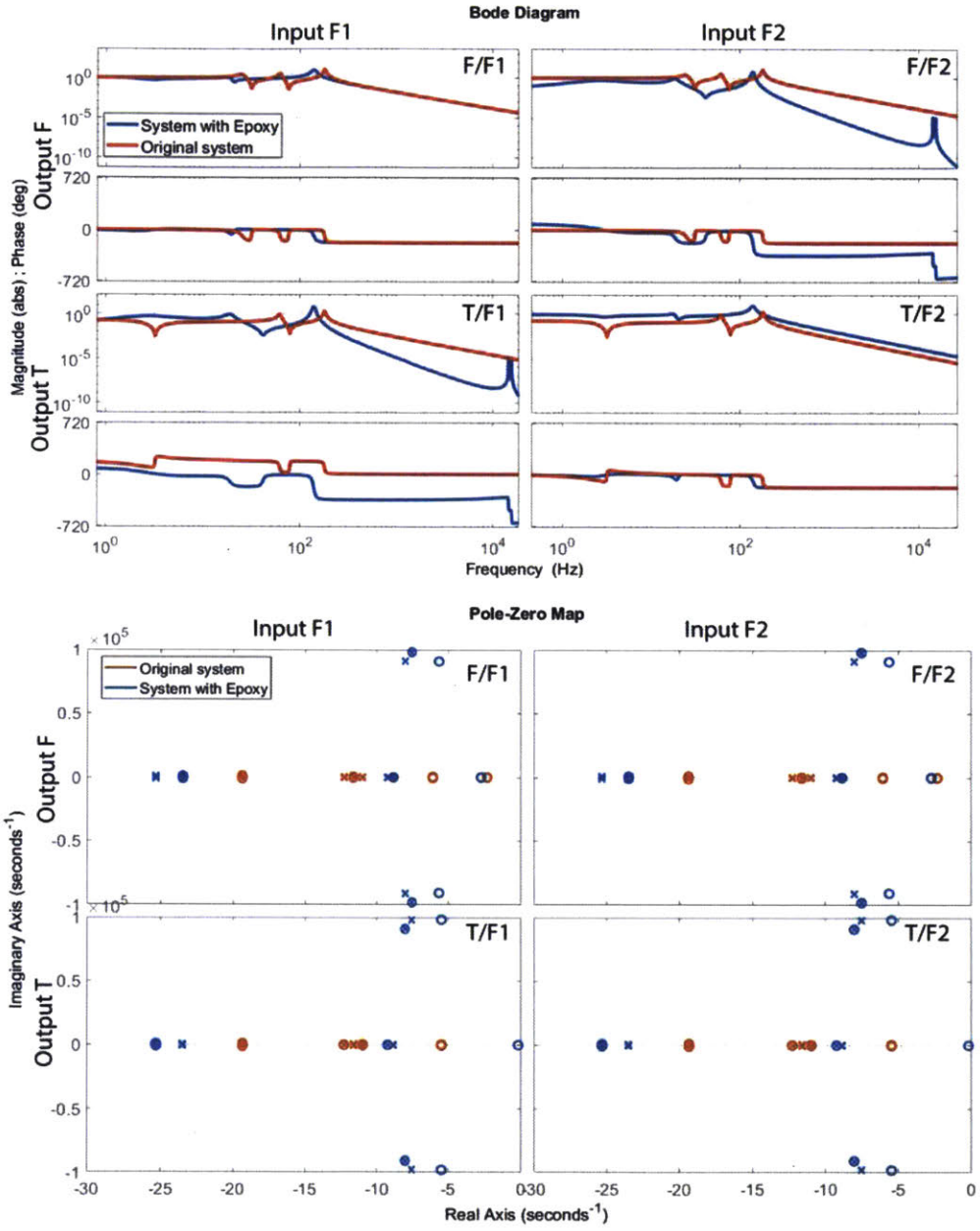

Figure 5-1: *Changes in system behavior resulting from decreasing o-ring compliance.* If stiffness k_{uf} is greatly increased by filling a gap currently occupied by o-rings with epoxy, the 60Hz mode moves up to frequencies greater than 1kHz, and the flexure sensor mode at 180Hz settles at 120Hz.

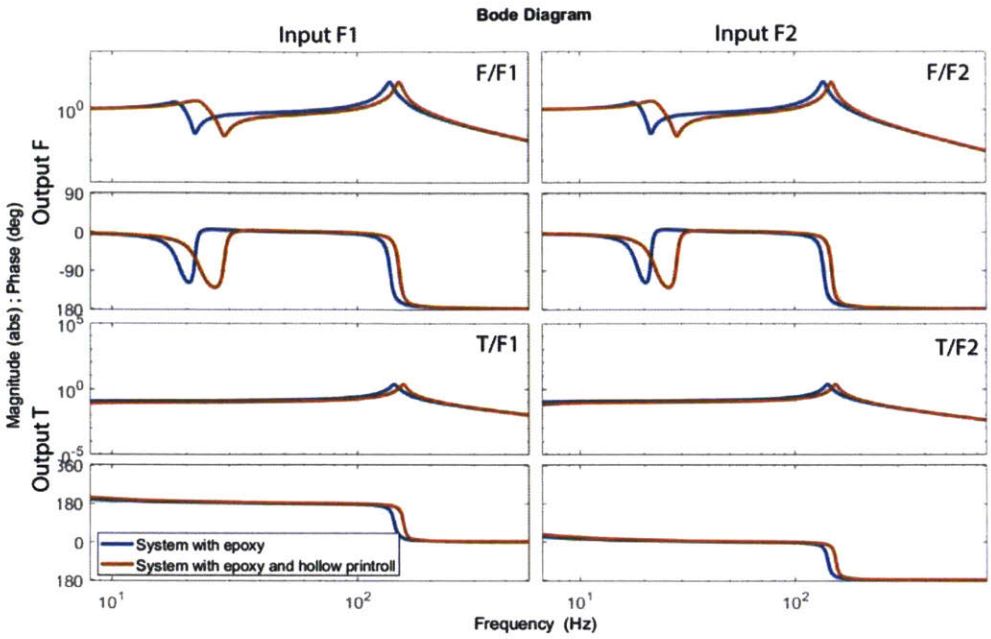

Figure 5-2: *Changes in system behavior resulting from decreasing o-ring compliance and utilizing a lightweight print roll.* Changing the print roll to a tube with walls 1mm creates only a minor improvement, more noticable in the stamp-dominated dynamics, which move up about 10Hz.

below 50Hz.

To further drive up the inherent frequencies of the printhead system, a switch from the solid steel print roll, weighting some 7kg, to a hollow tubular roll weighing about 2kg, could be undertaken. But because the other components in the system are still massive—the print roll bushings alone weigh 0.5kg each, and the pillow blocks another 2kg each—this reduction does not significantly improve the system response, as shown in Figure 5-2. (Furthermore, axially constraining a hollow tube with such narrow walls may require additional thrust bearing complexity that renders weight savings from the hollow tube moot.)

Finally, if the flexure sensor stiffness k_{lf} is also increased by an order of magnitude, only the resonances dominated by the stamp compliances appear in the 1-100Hz range; the first printhead-dominated resonance appears at about 500Hz, as shown in Figure 5-3.

These modifications are only effective if o-ring stiffness k_{uf} and flexure stiffness k_{lf}

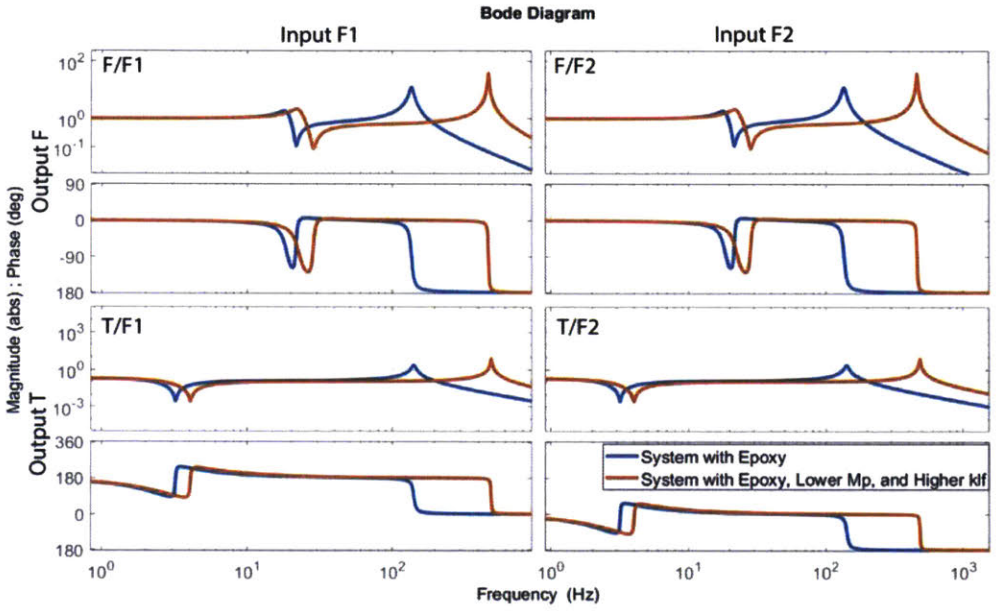

Figure 5-3: *Changes in system behavior resulting from decreasing o-ring compliance, switching to a lightweight print roll, and increasing flexure sensor stiffness.* Decreasing print roll mass M_p by a factor of 3, increasing flexure sensor stiffness k_{lf} by a factor of 10, and effectively removing the compliance of the o-rings can push unwanted resonances out of the 1-100Hz range, but not unwanted antiresonances (which stem from the transmission zeros).

are so rigid that they may be dropped from the model; **and** if there is sufficient damping in the accompanying damping coefficients, b_{uf} and b_{lf}. This is because the zeros appearing at approximately 2.5Hz and 20Hz are both stamp-printroll modes created by stacked compliances. The depth of the antiresonance at these locations depends on the combined damping and frequency of the involved elements. Even if o-ring stiffness k_{uf} and flexure sensor stiffness k_{lf} are extremely high, if they have low damping, deep antiresonances will still be coupled with the low-frequency stamp-dominated compliances, whether included in the designer's model or not. Additionally, if the system order is not dropped, the modified system is still uncontrollable, and the uncontrollable modes and transmission zeros that proved troublesome in Chapter 4 are still present.

A better approach would be to replace many aspects of the current design in order to achieve a number of foundational design principles from the start.

5.1.2 Design Principles

To construct the ideal printhead, there are a number of design principles that should be observed. They fall into two chief categories: design for dynamic control; and design for precision and repeatability. Repeatability does also affect the dynamics of the current system, as, for example, disassembly and reassembly to install a stamp can introduce friction in a voice coil and significantly alter the damping of the system.

The suggested design principles are:

1. *Minimization of mass:* All moving components should be as light as possible and right-sized for the application without loss of function. This means e.g. the print roll must be 2in in diameter, but only where the stamp is mounted; and it need only be wider maximum stamp width that can be fabricated using current equipment (about 2in).

2. *Maximization of stiffness:* All elements should be constructed with maximum stiffness in order to prevent any printhead-derived compliances from falling at

low frequencies. Where stiffnesses may be selected, it is desirable to use knowledge of the mass design to choose a stiffness placing printhead dynamic frequencies above 500Hz, and preferably above 1000Hz.

3. *Avoidance of stacked compliances:* If a compliance falling between the actuator and the stamp is insufficiently stiff and has low damping, it should be included in the model, and will render the system uncontrollable. Any compliances between the actuator and the stamp should be very stiff, and ideally should display a high degree of damping. The control designer will benefit from the largest possible design space if the system is fully controllable and observable.

4. *Avoidance of reliance on stamp properties:* The dynamic properties of the printhead should not be dependent on the variable and potentially undesirable stamp properties. At minimum, damping should not be dependent on the stamp; even if the system response is dependent on stamp compliance, if damping can be fixed at a desirable (large) value, then an agreeable system response can be assured.

5. *Design for repeatable assembly:* No changes in system performance or precision should be incurred by any disassembly necessary to install tooling or access any other basic function of the equipment.

If these design principles are observed, the control problem becomes greatly simplified. Instead of an uncontrollable high-order MIMO system, the separable SISO system model can apply; and the remaining problem in this case is to develop a control law with sufficient performance and robustness for the range of stamp geometries of interest.

5.1.3 Design Concepts

After establishing the five design principles outlined above, the first question became on the potential archetype of the printhead design—i.e., where should sensors, actua-

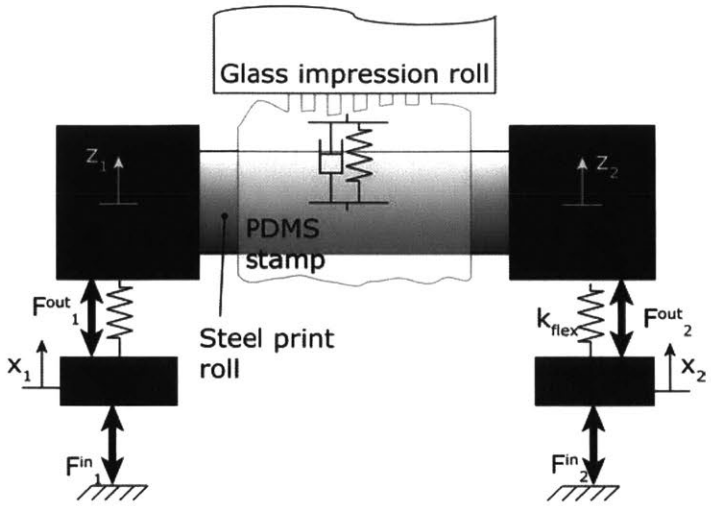

Figure 5-4: *Design Type 1: As-is.* Four design archetypes are considered in this work, and their merits and shortcomings discussed. Design Type 1 is conceptually the same as the existing system in terms of the actuator and sensor locations.

tors, and compliances be located in the system? By making intelligent choices about these, can we solve potential problems early?

One key principle to keep in mind is displacement is inherent in almost all direct force measurement techniques. Typically, force is measured by recording strain or deformation of an element of known stiffness. Additionally, it is necessary to measure the force in the actual load application path in order to accurately determine how much load is being applied to the stamp. This conundrum implies that an effective printhead design is going to introduce a stacked compliance somewhere in the load path, potentially violating principle (3).

Type 1: As-is Design

Consider the current system layout as Type 1, shown in Figure 5-4. In this design, the force sensors are located between the actuators and the stamp. This is ideal in that the force sensors are in the load path between the actuator and ground, and thus accurately measure the force transmitted through each load path. Unfortunately, this violates principle (3), potentially introducing an uncontrollable mode to the system.

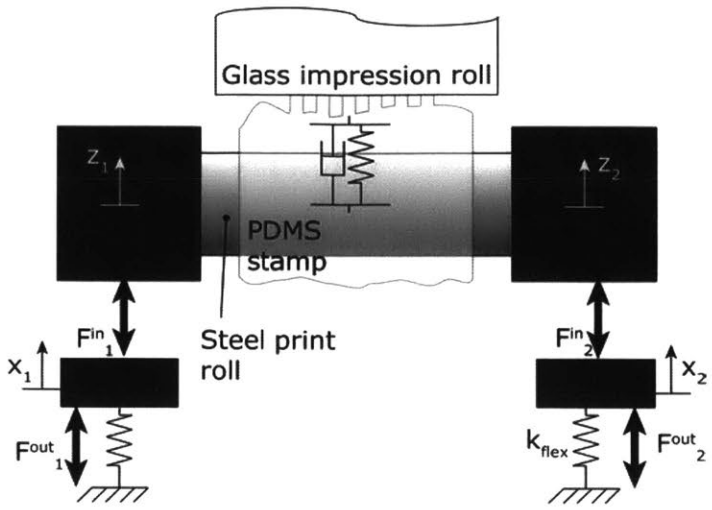

Figure 5-5: *Design Type 2: Sensors Below Actuators.* In Design Type 2, the locations of the actuators and sensors have been swapped. This allows the actuators to act directly on the print roll, but invalidates the sensor measurements, they do not measure the print roll dynamics. Design Type 2 is rejected for this reason.

Type 2: Sensors Below Actuators

A schematic of the Type 2 design is shown in 5-5. In this design, the sensors are still in the structural load path, but have been moved to below the actuators, to be between the actuators and ground. The benefit of this design is that there is no longer a compliance between the actuators and the stamp, removing uncontrollable modes.

However, if the actuators F_{in} are such that they behave as ideal force sources, the sensor k_{flex} actually becomes decoupled from the stamp system, rendering it useless. This could be considered an applicable model for a "floating" voice coil design, where bearing-less, no-contact voice coils are used in conjuction with air bearings, so that no mechanical element exists in parallel to the force sources F_i^{in} (as shown in 5-5.).

If the actuators behave as a force source alongside a compliance (as a piezoactuator might), then the sensors are no longer isolated from the stamp; however, they are now coupled through fairly complex output dynamics, which meets the design criteria but imparts undesirable additional complexity.

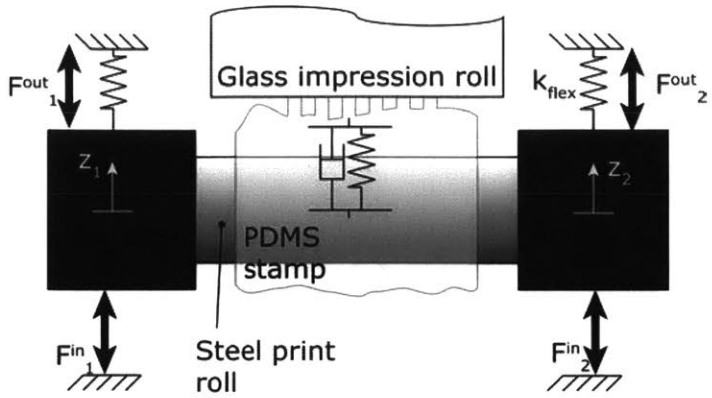

Figure 5-6: *Design Type 3: Sensor Compliance in Parallel with Stamp.* Design Type 3 places the sensors in parallel to the stamp. In this configuration, the load path is now split through the stamp and the sensors, preventing the sensors from measuring load applied to the stamp. Design Type 3 is rejected for this reason.

Type 3: Sensors Parallel Stamp

In Design Type 3, the sensors have been moved to be in parallel with the stamp's compliance, as shown in 5-6. The benefits of this are that there is now no compliance between the stamp and the actuators, observing principle (3).

However, now the load path from the actuators to ground is split between the sensors and the stamp. The sensors will be measuring not the load through the stamp, but some fraction of it that will depend on their relative stiffness to the stamp; and, the load being applied to the stamp will now be some fraction of the actuator command. Given the stamp's inherent variations in stiffness and surface profile, determining the actual force applied to the stamp now becomes a significant problem.

Type 4: Combined Sensors and Actuators

Another potential design, Type 4, is made possible by products available on the market that consist of piezoactuators with integrated elongation sensors. (A notable example of this is the Physik Instrumente (PI) P-601 and P-602 actuators [64, 65].) Though similar to Type 2, only one well-controlled compliance is introduced to the system. By measuring displacement z, either through the actuator's internal sensor or an external displacement sensor, the force applied to the roll by the piezoactuator

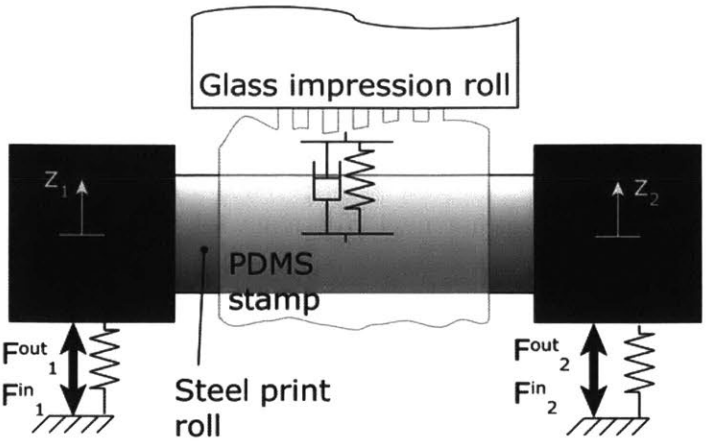

Figure 5-7: *Design Type 4: Combined Sensor and Actuator (Piezoactuator-based).* Design Type 4 is based on compliant piezoactuators that have internal sensing, effectively combining the sensor and compliant actuator. Design Type 4 is a feasible design if a commercial piezoactuator meeting design needs becomes available in the future.

can be accurately measured.

This design is very attractive because it solves many of the dynamic problems associated with the current design. However, piezoactuators present serious physical limitations; notably, they have low capability for force output, and their bandwidth drops significantly when forced to move inertial loads. [66]

The piezoactuator is essentially a mass-spring-damper system, with the piezo-generated force applied to the mass. The dynamic response of this system is inherently an oscillatory second-order system, with natural frequency $\omega_n = \sqrt{k/m}$. Building the actuator into a system such as the printhead applies an additional inertial load, increasing the effective mass of the mass-spring-damper system, and decreasing the resonance frequency.

For the PI actuators, effective mass is given as

$$m_{eff} = \frac{m_{piezo}}{3} + M_{load}, \tag{5.1}$$

where m_{piezo} is the mass inherent in the piezoactuator, and M_{load} is any additional inertial mass attached to and driven by the actuator. The resonant frequency

reduction predicted for this increase in mass is then given by

$$f_{load} = f_{piezo}\sqrt{\frac{m_{piezo}}{m_{eff}}}, \tag{5.2}$$

where f_{piezo} is the inherent natural frequency of the actuator, and f_{load} is the decreased natural frequency. [66]

For the PI P-602 actuator, the product with a 500μm stroke has an unloaded natural frequency of 230Hz. Adding only 500g of inertial load to this actuator drops its resonant frequency to 126Hz; adding 1kg further decreases it to 97Hz. For longer strokes, f_{piezo} is lower; and for greater loads, M_{load} is larger, in both cases rendering the loaded natural frequency even lower. The manufacturer recommends that the natural frequency be the upper bound on the appliation bandwidth, so the actuator bandwidth cannot be realistically above about 100Hz, limiting the printhead system bandwidth to that as well. [65]

Additionally, depending on their use and the particular product, piezoactuators may present nonlinear dynamic control characteristics, which may create additional complexity to the control designer. If future products similar to this actuator but with greater bandwidth and force capability are released to the market, then the Type 4 design will be very attractive. To enable a printhead bandwidth in the 100Hz range, a piezoactuator with a loaded resonance at or above 200Hz should enable the design to be feasible. Alternatively, innovative design resulting in a printhead with ultra-lightweight components could take advantage of products like the PI P-602; it is anticipated that this design would require elimination of some of the air bushings to reduce mass, instead utilizing, for example, flexural bearings.

5.2 Proposed Design

The resulting design is based on Type 1, the as-is design. Notably, this design does **not** remove the stacked compliance problem. (The Type 4 design would solve this problem, but currently there is no product available on the market that can meet the

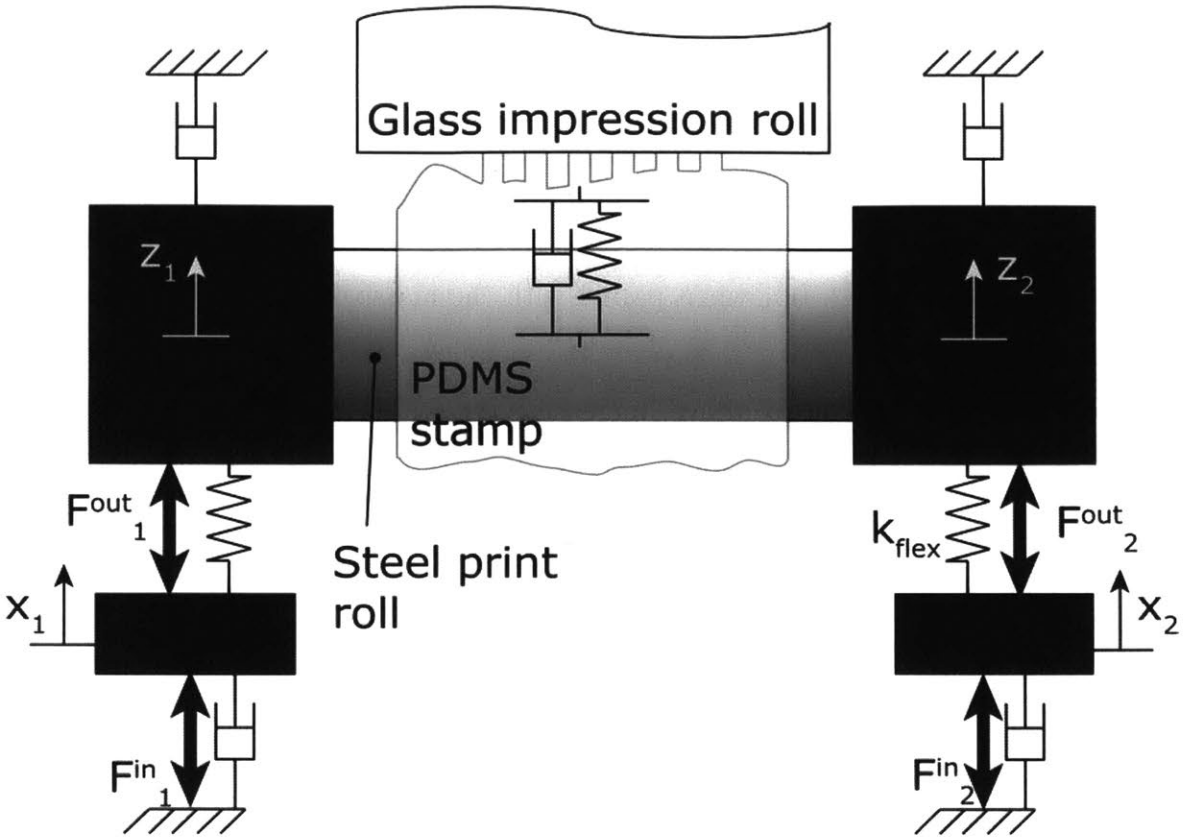

Figure 5-8: *A schematic of the new design for printing, based on Type 1.* Key changes are the addition of damping to the print roll and the elimination of the o-ring compliance.

application needs.) However, this problem can be mitigated with thoughtful design.

A schematic of the improved design is shown in 5-8. Two major changes from the original design are key: first, the removal of the intermediate compliance created by the print roll air bushing o-rings; and second, the addition of damping to the print roll in parallel to the stamp.

The first change is clearly important to observe design principle (3), and prevent uncontrolled modes from occurring within the desired bandwidth. However, the second change is also very important. Adding damping in parallel to the stamp's damping first implements design principle (4), and means that the designer has the ability to smooth the system response at the plant rather than in the controller. (This also means that any modes that appear in the desired bandwidth can be very well damped at the plant, meaning that their response to disturbances will also be very

well damped.)

The violation of design principle (3) is unfortunately unavoidable if a force sensor is to be placed in the load path between the actuator and the stamp. However, it can be mitigated if the sensor is made so stiff as to be essentially rigid compared to the stamp; i.e., such that $x_i \approx z_i$ (as labeled in 5-8). This was the original design intent, as detailed in Chapter 2; but when paired with the massive printhead components, the sensor was insufficiently stiff to push its dynamics above about 160Hz.

Additionally, as discussed above, increasing the stiffness of the sensor, with the intent of dropping it from the model, is only effective if damping can also be added, as an antiresonance will pair with the stamp dynamics regardless of flexure stiffness; but the addition of damping in parallel to the stamp accomplishes this.

A conceptual model of the new design is shown in Figures 5-9, 5-11, and 5-12. This design has focused on fitting and packaging of the necessary conceptual components in order to estimate their mass and size, but has neglected many details such as fasteners. Some additional design effort to produce a hardware demonstration of this concept is expected, though many elements may be reused from the existing printhead; additional off-the-shelf components beyond the original design are listed in a table below. The design elements annotated in the figures are as follows:

1. *Passive voice coil damper.* To add damping in parallel to the stamp, it is desirable to find a method that is both non-contact and tunable. An attractive solution is to use a voice coil with an undersized permanent magnet core. The undersized core is necessary to create a gap between coil and core in order to accommodate the angular motion of the printhead. For the voice coil unit shown, which has an outer diameter of 1 in, a diametrical gap of 0.125in will accommodate a printhead angle of 9 degrees. The voice coil may then be wired directly to a resistor or potentiometer, creating a passive energy dissipater that may be tuned by the designer by selecting a resistance. Though the larger gap between the coils and core will reduce the effectiveness of the voice coil, using a 10kΩ resistor with a typical voice coil of this size can increase the damping coefficient ζ to be approximately 1 for the stamp-dominated modes.

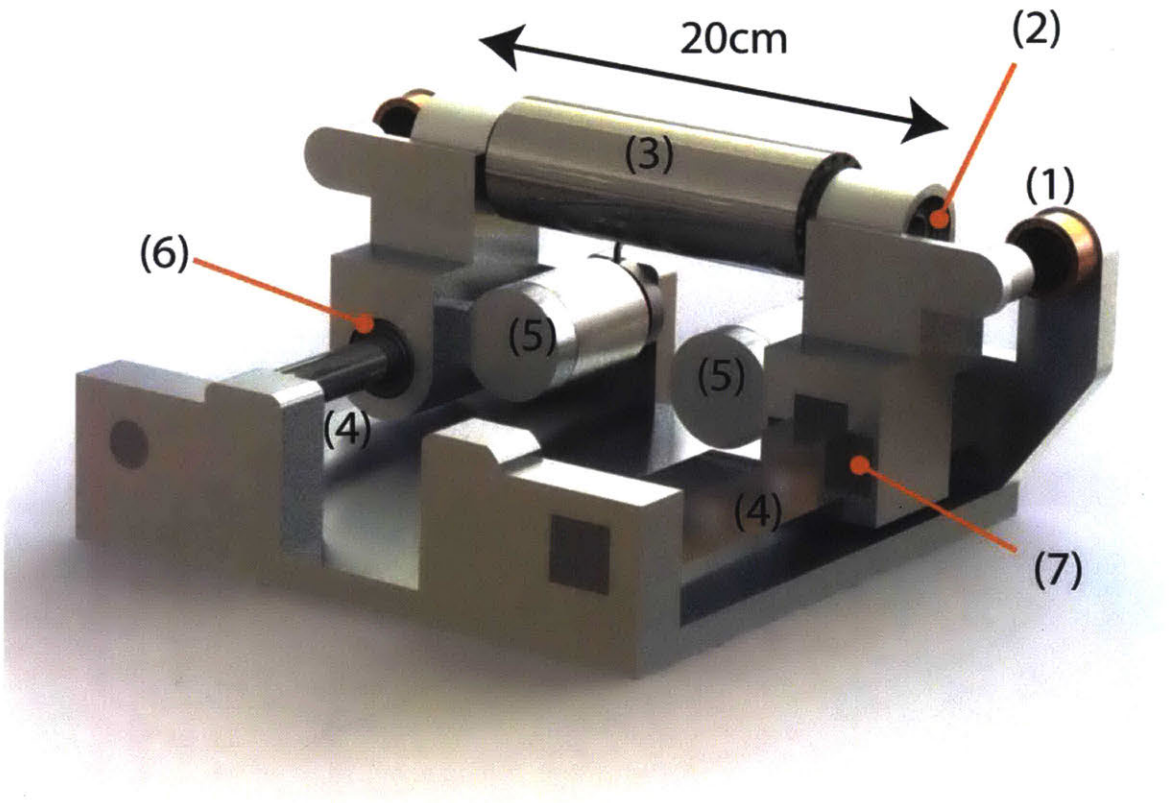

Figure 5-9: *A basic conceptual model of the new design concept, isometric view.* Detailed explanations are given in the corresponding numbered paragraphs in the text. The labeled components shown are (1) passive voice coil damper; (2) flanged air bushing; (3) stepped print roll; (4) combination round and square shafts; (5) voice coil actuators; (6) round shaft air bushing; and (7) square shaft air bushing.

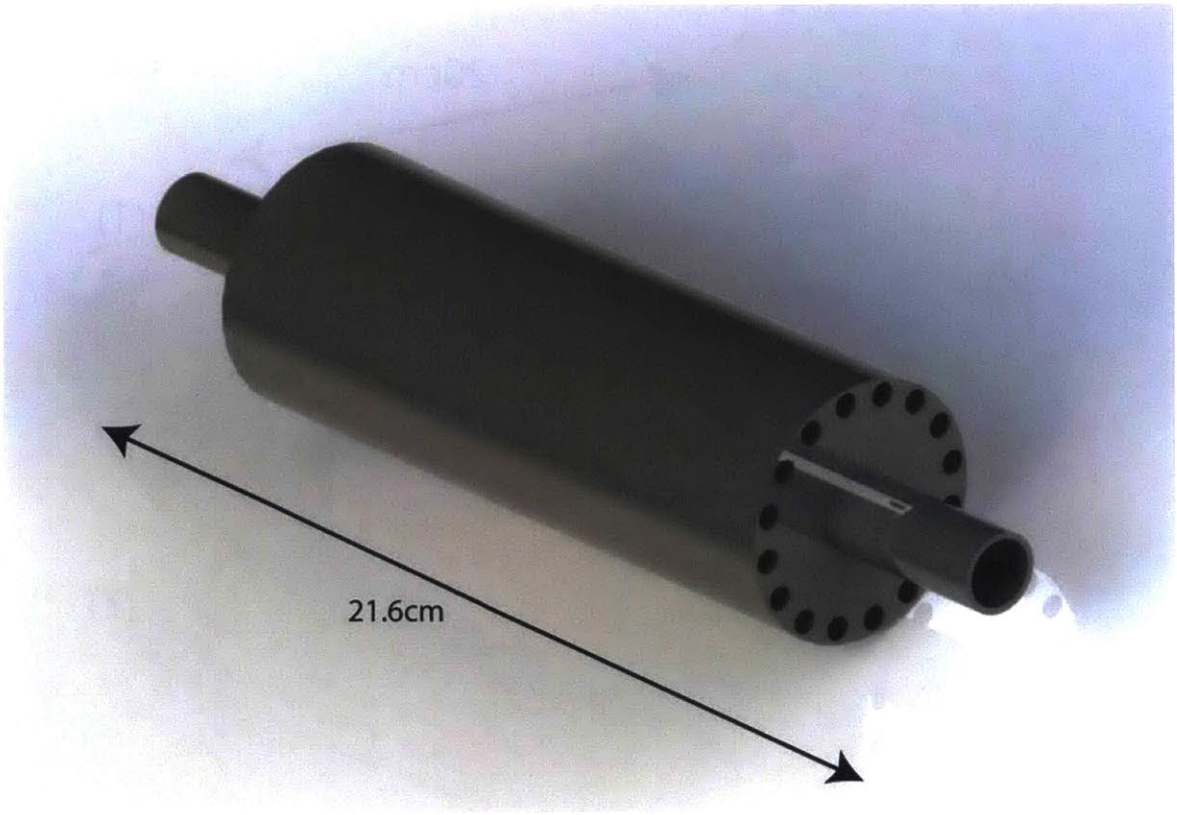

Figure 5-10: *A basic conceptual model of the stepped shaft part for the new design concept.* The hollow shaft, reduced length (21.6cm) as compared to the original design (43cm), and "speed holes" reduce its inertia.

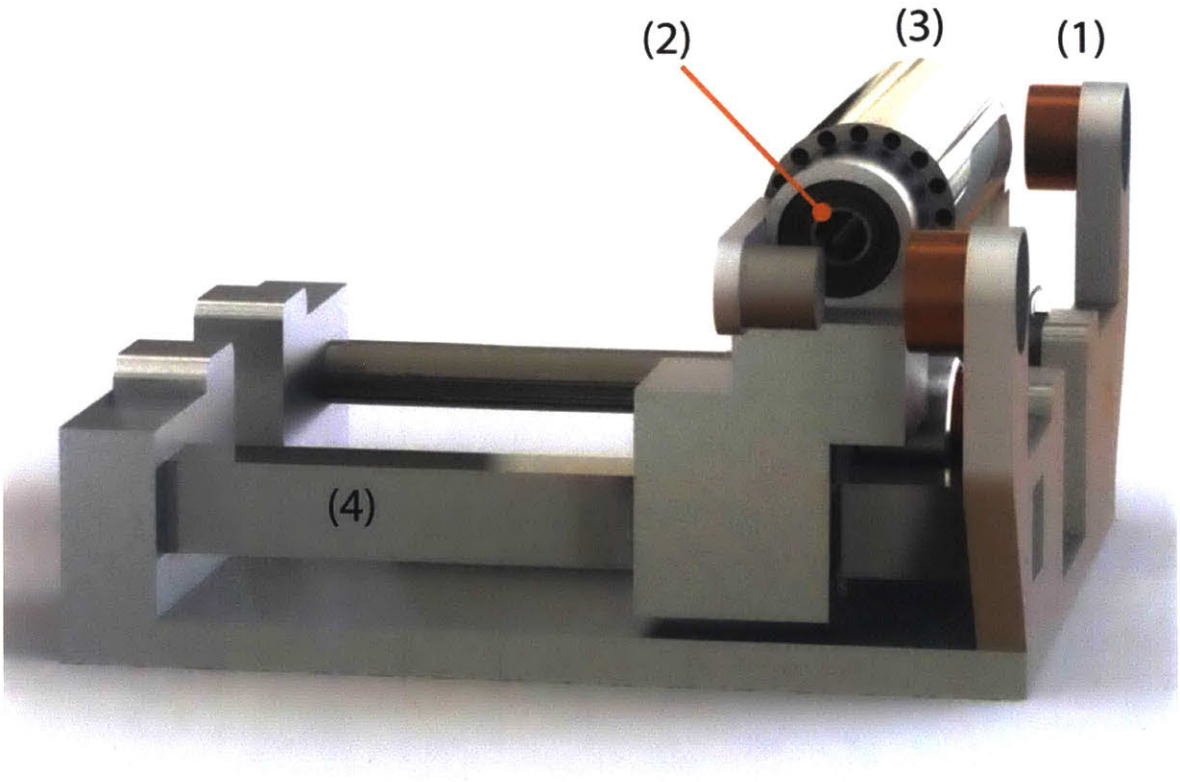

Figure 5-11: *A basic conceptual model of the new design concept, side view.* Detailed explanations are given in the corresponding numbered paragraphs in the text. The labeled components shown are (1) passive voice coil damper; (2) flanged air bushing; (3) stepped print rol; and (4) square shafts.

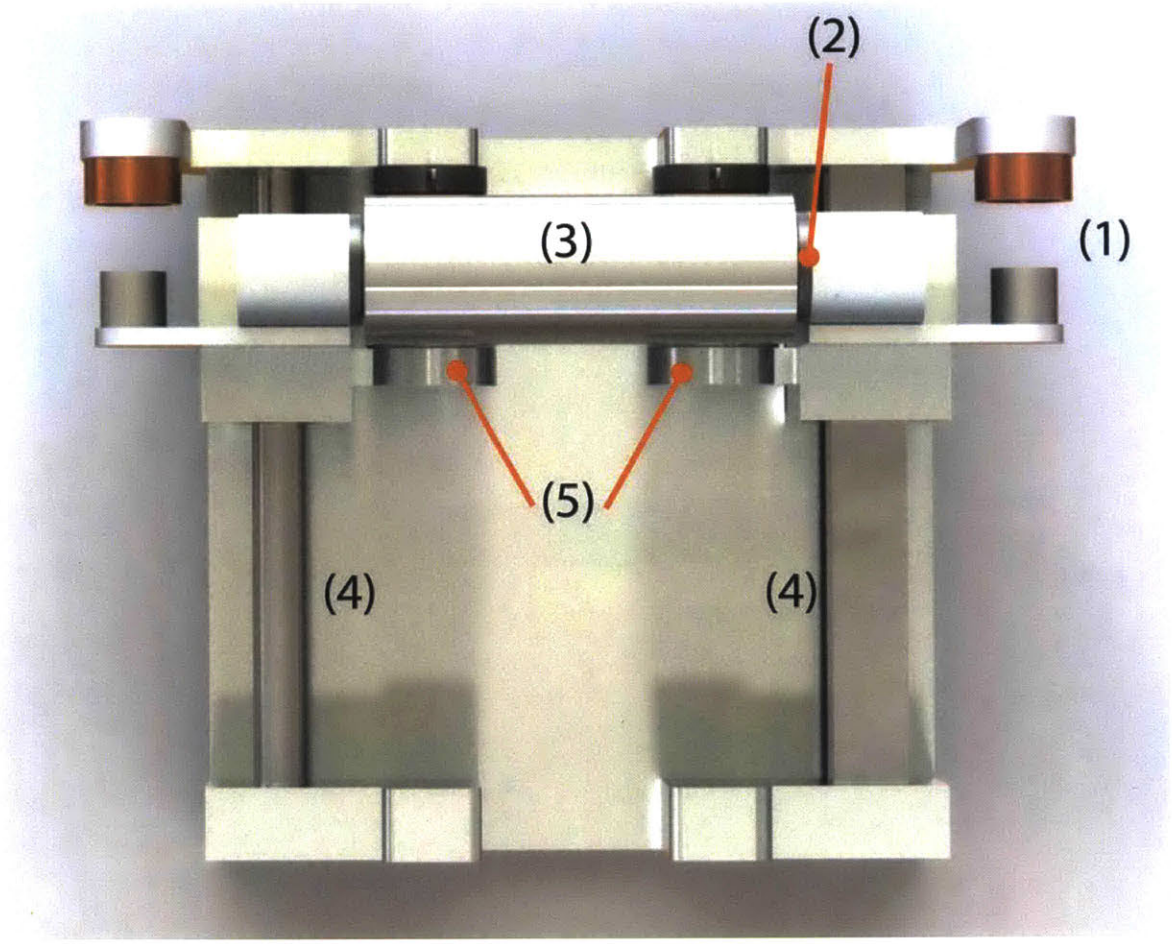

Figure 5-12: *A basic conceptual model of the new design concept, top view.* Detailed explanations are given in the corresponding numbered paragraphs in the text. The labeled components shown are (1) passive voice coil damper; (2) flanged air bushing; (3) stepped print rol; (4) combination round and square shafts; and (5) voice coil actuators.

2. *Flanged air bushing in minimal, kinematic mount.* To reduce the weight and complexity of the print roll assembly, instead of utilizing a bulky, heavy air bushing plus separate thrust bearing, a stepped shaft that abuts two combination air bushings can be used. New Way Air Bearings offers a 5/8in thrust bushing (product C301601) that constrains both radially and in thrust. These bushings can be potted with epoxy in a minimal, custom-made holder that is significantly lighter than the off-the-shelf pillow blocks offered by New Way.

3. *Stepped shaft.* In order to reduce the weight of the system while still accommodating a 2in inner diameter stamp, a stepped shaft with minimum length is ideal.

   In the existing system, the fact that the pillow blocks constraining the print roll overhang the diameter of the print roll means that the print roll must be sufficiently wide to locate these pillow blocks outside the impression roll assembly. If, instead, a stepped shaft with smaller constraints is used, the print roll outer diameter becomes the foremost point, and the length of the print roll can be reduced to the minimum required to accommodate the stamp and ink bath.

   A stepped roll also allows reduction of weight, as the 2in diameter section need only be where the stamp is placed. The roll shown in the concept, as seen in Figure 5-10, is a hollow roll, 8.5in long, with a 5.6in long stamp mounting section in the center. Holes are drilled outside the thrust surface presented to the air bearings to further reduce mass, but the added expense of this operation is not strictly necessary. The 5.6in stamp mounting area accommodates the current machine limitation of a 5in wide substrate, but it could be made narrower to further reduce mass if the stamp length is constrained to 2-3in.

   One key design consideration will be ensuring repeatable assembly between the stepped shaft thrust surfaces and the thrust bearings. The typical air gap range for the thrust bearings is 150-400μin, which means the assembly tolerance should be 300-800μin, which is equivalent to 0.3-0.8 thousandths of an

inch. [67] This may be very difficult to achieve, so it may be desirable to replace one or both of the fixed thrust surfaces of the print roll with adjustable clamped surfaces, based on a shaft collar design, that allows for adjustment after disassembly during the stamp installation process.

4. *Combination round and square rails.* In the current printhead design, the print roll must be removed in order to install or remove a stamp. However, the print roll also serves as the constraint between the two translational rails, which serve as the bearing constraint for the voice coil. A frequent problem is that disassembly and reassembly introduces some errors in this constraint, and can cause the small gap in the voice coils to close and induce friction in part of the voice coil stroke. The unpredictability of this friction significantly changes the system dynamic response and spoils the control designer's efforts.

   To solve this problem, one square and one round shaft are used. As in the current design, clamping of the rails is used to fixture them. During installation of a stamp, the outboard (round shaft) print roll constraint will need to be removed, and the print roll will be removed. However, the inboard (square shaft) side will retain its reference independent of the print roll. When the stepped shaft is reinstalled, it will enforce a constraint on the round side based on the tolerance of the air bushings, rather than on the assembly. (Using two square shafts, however, would mechanically overconstrain the system). The round shaft will then be able to accommodate assembly variations in angle, which will be sufficiently small to prevent the voice coil from closing the coil-core gap.

   Additionally, it is recommended that a ball-in-groove kinematic coupling (not shown in the concept) be used to mate the outboard flanged bushing mount with the translational assembly, so that removal and replacement of this component is highly precise, returning it to exactly the same position. This allows elastic averaging among the air bushings to then re-center the print roll to an assembled position with great precision.

5. *Voice coil actuators.* The same voice coil actuators in the original design suit the new design as well. With plenty of force capability and bandwidth and good empirical open-loop accuracy, they are attractive actuators.

   In this design, because of the reduced width of the printhead, the voice coil actuators could also be moved to the outside of the assembly, and the linear encoder sensors moved to the inside. This would create more room below the print roll for an ink bath.

6. *Round shaft air bushing and stackup.* On the outboard side, a 0.75in round shaft is used. This enables the use of a New Way Air Bushing, which should be potted with epoxy in a custom-made assembly block with minimal material.

   On top of this assembly block is the flexural force sensor. The existing flexural design may be reused, as its stiffness is sufficient (in the lighter conceptual design) to keep its dynamics out of the region of interest. Packaging tweaks to fit the smaller concept may be required, but the flexure blades and strain gauges may be reused.

   Above the flexural force sensor, as in the existing design, should be a slewing flexure. Again, the existing design, reduced in size for packaging, may be reused. The stiffness should be kept significantly less than that of the stamp to prevent the stiffness of the slewing flexures from preventing moment equalization during force control; the current designed stiffness is suitable for the new design. [10]

   The rotational bearing flexure should mate kinematically with the print roll mounting block, preloaded with an easily removable constraint such as thumb- or socket cap screw.

   Also notable is that the stackup is designed to overhang the front edge of the assembly by 0.25in, and the print roll protrudes even further beyond the print roll mounting blocks. This ensures that the printhead has enough range to contact the impression roll even if very thin stamps are utilized.

7. *Square shaft air bushing and stackup.* On the inboard side, a square rail is

used. The square rail necessitates a custom bearing solution, which can be a simple design consisting of a block with pockets to mount four New Way Air Bearings bonded bearings. The bonded bearings are simply flat air bearing elements that may be potted with epoxy in a custom assembly. Highly accurate potting to achieve the design air gaps of 150-400 μin will be necessary; or, some adjustment mechanism to allow for one-time installation and calibration onto the square shaft will be necessary. Once installed, however, this element should not need to be disassembled, and will remain a repeatable reference constraint for the entire assembly.

An identical stackup as used in (6) may be used here as well. The kinematic coupling for the print roll mounting block is not necessary here, but may be incorporated for symmetry and future-proofing.

8. *Base positioning,* not shown in concept. As in the prior design, the base may be positioned using a planar pseudo-kinematic ball contact system installed into the optical breadboard on the machine, and preloaded with a clamp or latch element. The existing components currently installed on the machine can likely be reused with slight modification.

9. *Position sensors,* not shown in concept. The same position sensors, namely Renishaw linear optical encoders, may be used in the new design. Though these are not necessary for control, they offer a useful, clean, and highly accurate measurement. They should be installed in the same location as on the existing design.

Component	Vendor	Product Number
Bonded bearing	New Way Air Bearings	S17023210
Air bushing, 0.75in ID	New Way Air Bearings	S301901
Thrust bushing, 5/8in	New Way Air Bearings	C301601
Voice coil actuator, 0.50in stroke*	H2W Technologies	NCC02-13-008-1R

* The voice coil actuator should be paired with a smaller core to create a larger gap. A cylindrical permanent magnet with an outer diameter 0.125in less than the inner

diameter of the core could be used. This should also be paired with a potentiometer or resistor.

Resulting Dynamic Model

The goal of the redesign process is to achieve a fully controllable and fully observable system with dynamics that no longer appear within the desired bandwidth. Inclusion of the compliance of the force sensor in this design the results in an 8th order system with one uncontrollable mode; if it can be shown that the force sensor does not have a significant effect on dynamics within a range of interest, it may be dropped from the model and the simplified separable system model used instead.

For the eighth-order system including the force sensor compliance, the resulting open-loop frequency response is shown in Figure 5-13. Notably, the increased damping from the passive voice coil damper has improved the system response in the 1-100Hz range tremendously.

As the sensor stiffness increases, its associated resonance is pushed toward 1kHz, but the damping also becomes less effective. No changes in the flexure's stiffness still result in a resonance frequency of about 300Hz, an improvement by a factor of 2 over the original design.

Additionally, it becomes possible to revisit the separable system model, which was determined to be inapplicable for the original printhead design. It is still an approximate model, but as shown in Figure 5-14, it represents the dynamics of the system below 100Hz quite well. Further increasing the stiffness of the flexure sensor, as expected, extends this region in which the SISO model is a good substitute for the MIMO model.

Overall, designing a controller has become a much more tractable task. The separable model captures the relevant dynamics sufficiently that it can be used for design; for both F and T, a PI or lag controller, possibly with additional poles to rolloff above 200Hz, will produce a very satisfactory system response. The loop gain under PI control for the separable system is shown in 5-16.

If the coupled model is necessary, potentially due to the resonance from the flexure

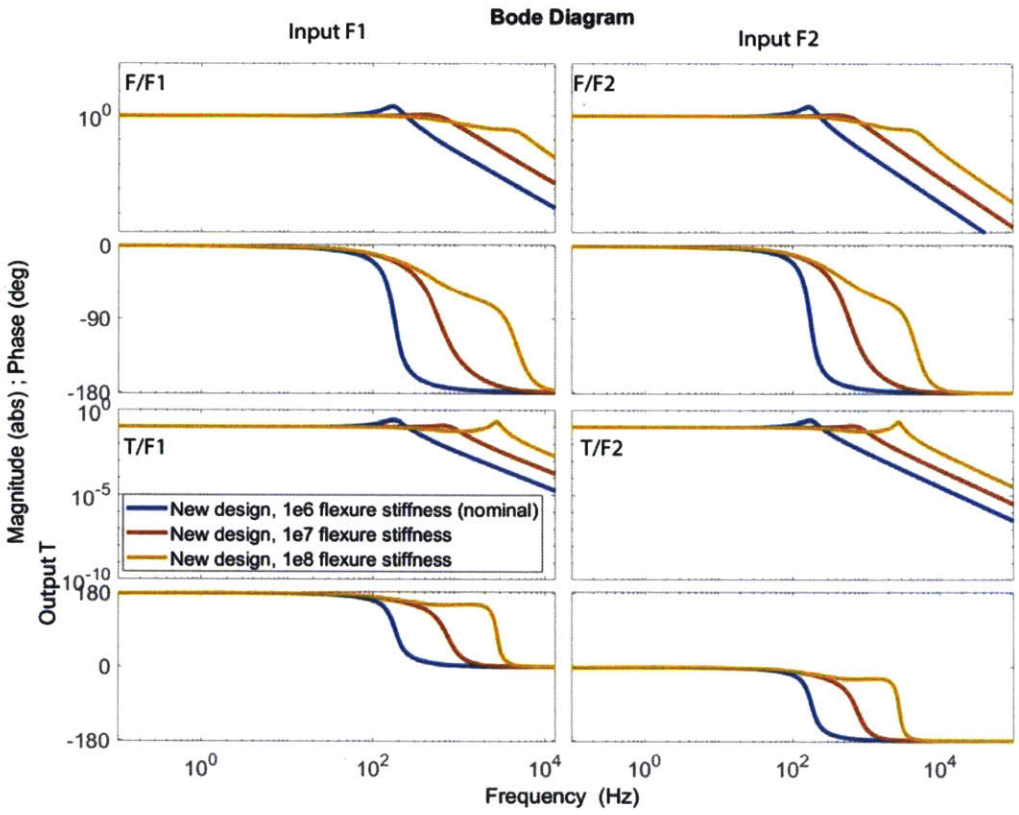

Figure 5-13: *Simulated frequency response for the new design concept, MIMO model.* Frequency response of the new concept for the F/F_i and T/F_i systems; designs using both the same flexure stiffness (1N/μm) and increased flexure stiffness are compared. Though it is kept constant in these plots, increasing the passive damping further reduces the magnitude of the high-frequency peak created by the force sensor flexure compliance.

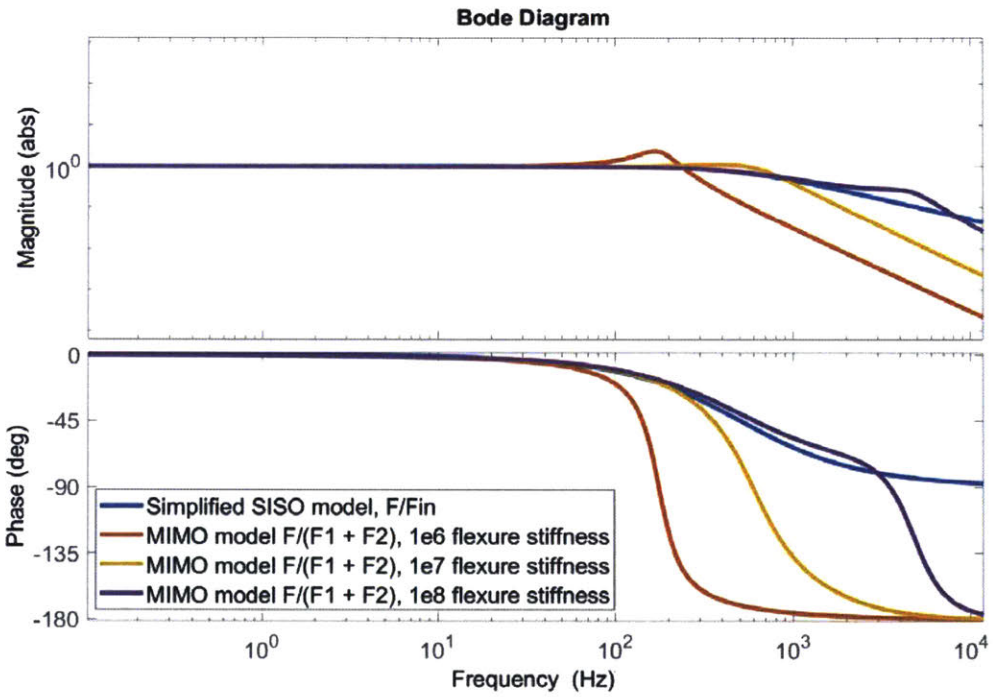

Figure 5-14: *Comparison of simplified SISO model and full MIMO model for new design concept.* The red, yellow, and purple MIMO curves above have been constructed by the expression $F/F_{in} = F/F_1 + F/F_2$, which is true if $F_{in} = F_1 + F_2$, as in the simplified separable model. When the nominal sensor flexure stiffness of 1N/μm is increased to 10N/μm, the SISO response substitutes well for the MIMO response up to 400Hz; at 100N/μm, the SISO response represents the MIMO response up to about 1kHz.

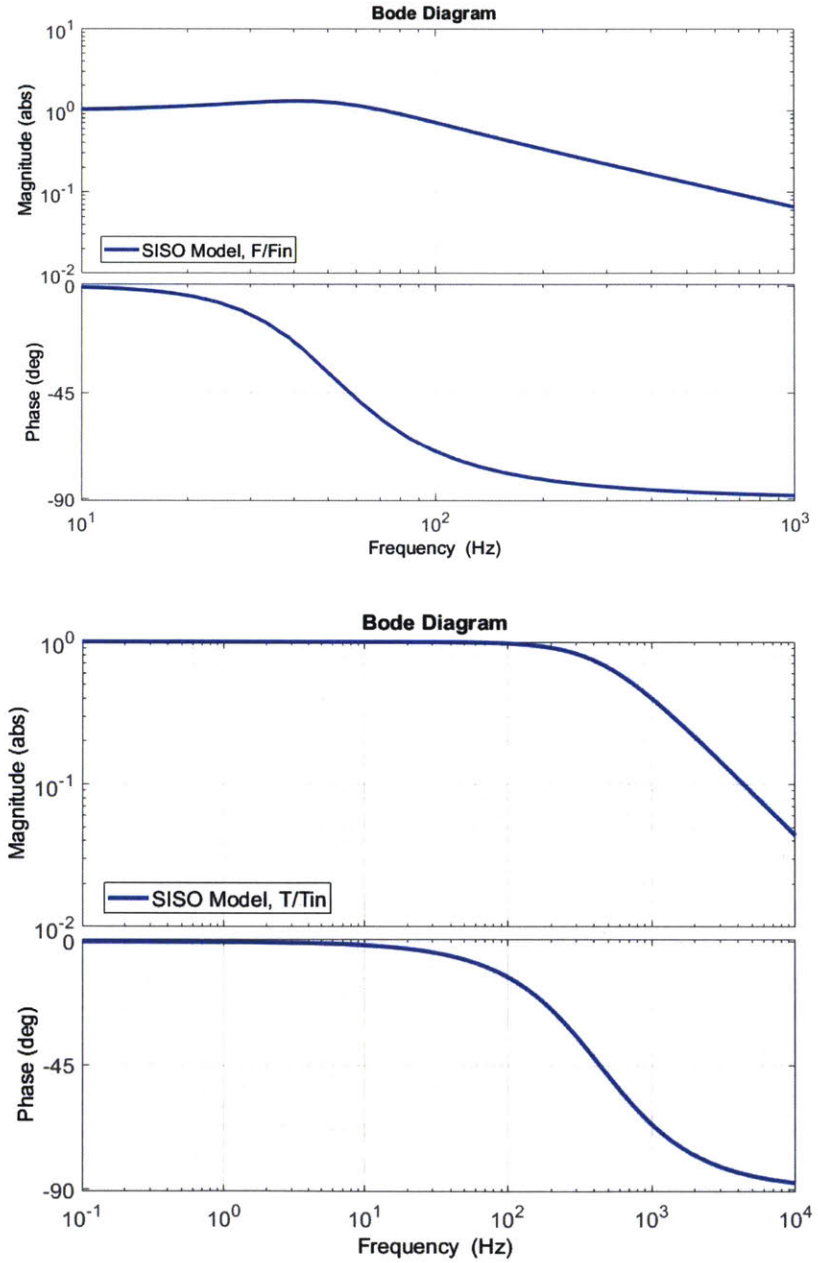

Figure 5-15: *Simulated frequency response for the new design concept, SISO model.* Frequency response for the separable system model for the new design concept. This model is a good representation of the MIMO dynamics below about 100Hz.

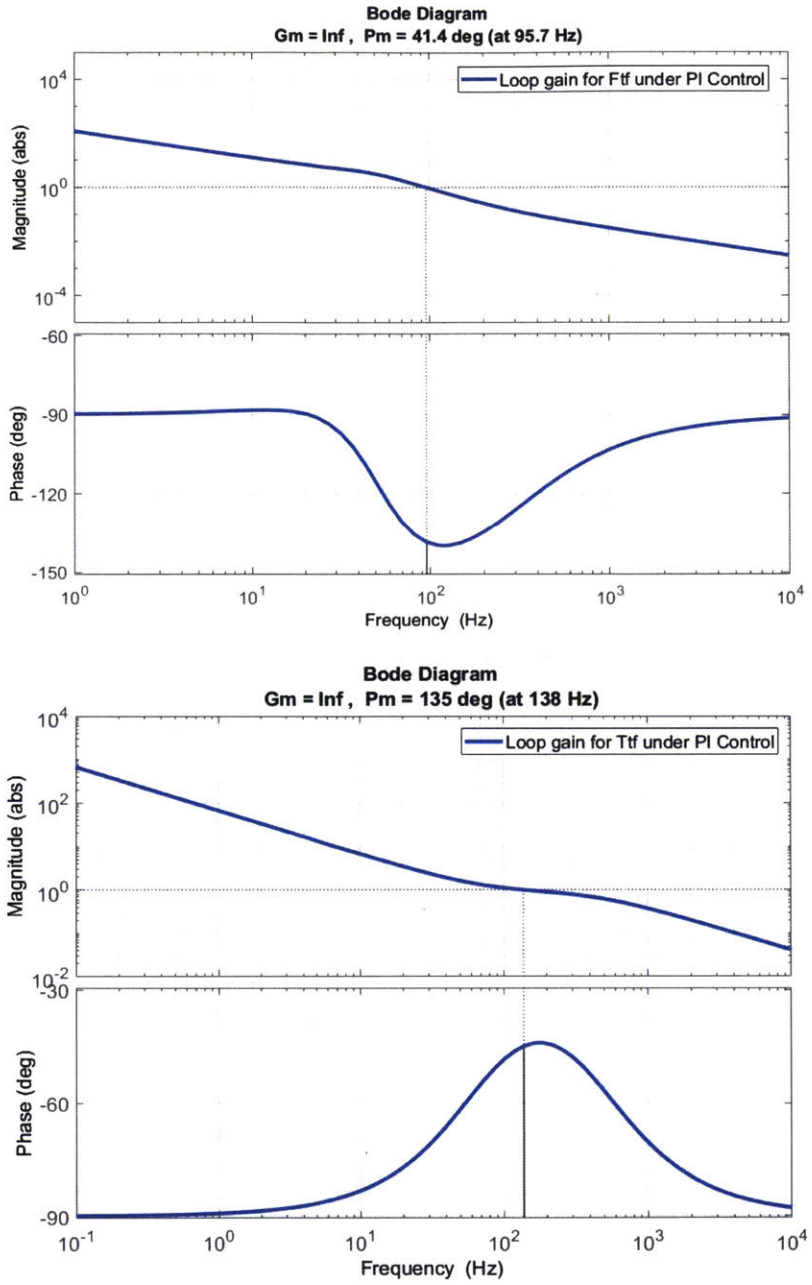

Figure 5-16: *PI control design loop gain for the new design separable systems model.* PI control produces infinite gain at DC (i.e. zero steady-state error) and a very acceptable system response for both the F/F_{in} (top) and T/T_{in} (bottom) systems. In both systems, crossover has been selected to be about 100Hz, but ample phase margin is available to increase the system bandwidth if desired. Compared to the MIMO design for the existing system shown back in 4-19, this system presents a much improved frequency response, with no uncompensatable antiresonances.

sensor appearing in the system response, it should be noted that including the compliance of the flexure in the model does create one uncontrollable mode ($\texttt{rank}(C_{trb}) = 6$, but full rank is 8), which is again associated with the low frequency rotational mode of the print roll. This results in a zero behavior with a potentially large overshoot for commands to the rotational mode. In this case the best course of action would be to increase the damping from the passive voice coils to decrease the magnitude of the resonance. This should lessen the impact of the uncontrollable mode on the coupled system, potentially enabling the separable model to be employed; but excessive damping hampers the system's ability to compensate the rotational degree of freedom, so a balance must be struck.

5.3 Summary

In sum, it is clear that making modifications to the existing system with the purpose of control design in mind can produce a design that offers behavior amenable to high-performance control design. Though eliminating the compliance between the actuator and stamp is not possible if a compliance-based force sensor is to be used, as in a Type 1 design, it can be mitigated by reducing the mass of the printhead components and potentially increasing the stiffness of the sensor. (A Type 4 piezoactuator design circumvents this, but no piezoactuator with sufficient capability is available on the market.)

A key addition to the Type 1 design is the inclusion of passive, designer-selected damping in the form of passive voice coil actuators that dissipate energy into a resistor. This allows for the designer to increase damping to compensate for bad behavior that may be inherent in the system due to the violation of design principle (3).

With the addition of damping and the reduction of size and mass, the printhead's dynamic behavior becomes very agreeable, and the control design becomes simple.

Chapter 6

Conclusion

The work presented in this thesis document is focused on the mechanical and control design of experimental manufacturing equipment used to study the process of microcontact printing. The stated objective at the beginning of this work was to develop and demonstrate precise closed-loop printing control that could maintain high quality, defect-free microcontact printed output for a variety of stamp geometries in the face of various disturbances.

This contribution is novel because though microcontact printing has been successfully demonstrated at a benchtop level in many cases, scale-up to an industrial capacity has not yet been conclusively demonstrated, and a key reason for this is a lack of understanding of the inherent needs of the process combined with a lack of production equipment with the relevant capabilities.

The first step in consideration of the scale-up problem is to understand the advantages and limitations of the microcontact printing process, as discussed in Chapter 3. Though the compliance of the stamp does enable the passive compensation of surface irregularities, it also necessitates the precise control of feature compression in order to avoid inducing printing defects cause by over- or under-pressure. Feature compression could be dictated either by imposing a displacement or a force condition; but, because of the uncertainty and disturbances inherent in displacement due to physical nonidealities of assembly components and tooling, it is shown in Chapter 3 that force control is superior.

Existing experimental hardware was already available, which was originally developed with the goal of controlling microcontact printing through contact imaging. However, as explained in Chapter 2, numerous deficiencies in this equipment were present, including no deterministic hardware or software platform for control; unreliable and difficult contact measurements; limited web handling capabilities; and no force sensing. The first major contribution of this thesis was to correct these deficiencies and overhaul numerous aspects of the existing equipment in order to bring it to a suitable state for control experimentation. This included installing a new computational system based on a real-time and FPGA controller; rewriting the software stack to take advantage of these computational platforms; design, installation, and characterization of custom force sensors; and various improvements to web handling control and sensing.

The next step undertaken was to build on the improved experimental platform in order to develop a closed-loop force control algorithm that was capable of achieving high performance. The general idea was that with sufficient precision of force control, smaller and more sensitive stamp features and arbitrary stamp geometries could be used in printing without loss of output quality. An initial simple model of the printhead system was developed, but control results were not satisfactory, and it was determined that the model did not accurately represent the system.

The next contribution was the construction and application of tools to identify the printhead system properties, including frequency response measurement tools and processing scripts. These tools revealed that the simple system model was inadequate, and that the printhead had a number of undesirable dynamic characteristics: notably, that it had a number of uncontrollable modes and poorly-damped complex transmission zeros, which appeared in the desired minimum bandwidth range of 1-10Hz.

Even so, both a simple PI-based and a sophisticated augmented full state feedback with estimation control design were able to improve some aspects of the system response. However, the improvement of the sophisticated controller over the PI controller was not significant, and high-performance control designs were typically unstable in the face of plant variability. Also, both controllers failed to meet the stated

control objectives, and were deemed unsuitable for both the nominal experimental stamp and for potential arbitrarily sensitive stamps.

Based on the understanding of the needs of the microcontact printing process, as presented in Chapter 3, and the control design results, as presented in Chapter 4, a design with desirable dynamic characteristics is presented in Chapter 5. This design focuses on mitigating two key problems: the presence of uncontrollable modes within the desired bandwidth, and the complete dependence of some system parameters on uncontrolled and unsatisfactory stamp properties. A number of design concepts are explored, but an iteration on the original design is selected as optimal. The resulting concept's dynamic performance is extrapolated, and found to be much more amenable to control design than the original printhead.

Overall, the contributions of this thesis work are summarized as follows:

- A study of the physics of the microcontact printing process to understand its requirements and limitations;
- Development of a deterministic control platform based on real-time and FPGA computational targets;
- Development of a software stack for this platform that also incorporates control of the entire system, facilitating other researchers' tangential efforts;
- Upgrades and improvements to the sensing and control of the web handling system;
- Design, installation, and characterization of force sensors with custom packaging;
- Construction and implementation of system frequency response measurement tools;
- Development of multiple system models with increasing levels of complexity;
- Experimental confirmation of the analytical system model;

- Simple and complex control design for the analytical system model;
- Experimental implementation of both simple and complex control designs, and analysis of the experimental results;
- A discussion of the fundamental shortcomings of the existing printhead equipment, and a listing of the design principles that need be observed to improve these shortcomings;
- And a conceptual mechanical and control design demonstrating the success resulting from implementing these design principles.

Future Work

It is hoped that future research will be able to physically implement the printhead design described in Chapter 5, and to verify that a simple control design can produce ideal results. Some detailed design work such as fastener selection, flexure repackaging, and component mounting remains to be completed, but component selection, approximate component design and packaging, and system layout have all been established as contributions in this thesis.

Other additional work concerns the web handling system. Though web handling has a non-negligible effect on the printing output, its parameters in the printing process are only open-loop controlled, and various nonidealities in the system cause both speed and tension to be subject to steady-state errors and dynamic fluctuations. Improved hardware, a study of the web dynamics, and implementation of a closed-loop web controller using the sensors installed as a part of this work would be all be worthy exercises. Improved web control is also necessary for any online optical imaging efforts, as these will depend on having the web move at a well-controlled speed in order to acquire and process meaningful images.

Finally, the demonstration of successful, high-quality closed loop printing over a long time period remains incomplete. This is due to a number of factors that require iteration, including the limitations of the ink bath; limited quantities of the needed gold-coated substrate; poor web control; inadequate printing force control;

and difficulties in making large-area measurements of microscale patterns to judge quality. A quantity of work has gone into each of these aspects, but bringing them all together into a machine capable of industrial reliability and quantity remains a task for future researchers.

Appendix A

Table of Major Hardware Components

A.1 Printhead and Impression Components

Component	Manufacturer	Part Number
Magnetic encoder ring	RLS	MR075E-060-A-048-B-00
Ring encoder readhead	RLS	LM15-IB-1D0-C-B-10-A-00
Voice coil actuators (2)	H2W Tech	
Linear encoders (2)	Renishaw	
Print roll radial bearings (2)	New Way	2.00in ID air bushing S305001
Print roll axial bearings (2)	New Way	50mm Flat Round S105001
Print roll translation bearings (4)	New Way	1.00in ID air bushing S302501
Impression roll radial bearings (6)	New Way	30mm x 60mm concave L-profile, 3in radius
Impression roll axial bearings (2)	New Way	40mm Flat Round S104001

A.2 Web Handling Components

Component	Manufacturer	Part Number
Web drive motors (2)	SureServo	SVL-204
Web drive rollers (2)	Double E Co.	CLEV12-TBA
Tension measuring idler rolls (2)	FMS	RMGZ900
Tension control unit	FMS	CMGZ309

A.3 Major Electronic Components

Component	Manufacturer	Part Number
Web drive motor controllers (2)	SureServo	SVA-2040
Print roll voice coil amplifiers (2)	H2W Tech	LCAM 5/15
Real-time computation platform	National Instruments	cRIO-9030
Analog input module	National Instruments	NI-9215
Analog output module	National Instruments	NI-9263
Digital I/O module	National Instruments	NI-9401
Digital relays	Terminator	T1K-16 series

Appendix B

Matlab Code Containing Model

```
%Roll length
l = 0.1778;

%Lower flexure properties
klf1 = 9.7e5;
klf2 = 9.7e5;
blf1 = 10;
blf2 = 10;

%Upper compliance properties
kuf1 = 280e4;
kuf2 = 280e4;
buf1 = 10;
buf2 = 10;

%Mass properties
Mp = 6.9113+0.480*2;
Jp = 0.1251+2*0.480*l2̂;
Mu = 1.78-0.480+0.210;
Mvc = 1.99-0.210;
```

```
%Stamp properties
ksy = 2e5;
bsy = 60;
kst = 60;
bst = 0.1;

%Rotational flexure
kt = 40;

%Voice coil/external damping
bvc1 = 100;
bvc2 = 100;

%% For manual adjustment
kuf1 = .08*kuf1;
kuf2 = .08*kuf2;
ksy = 2.3*ksy;


%% Create a state space model from these terms
%Define terms for compactness of A.
Jcon = 2*l/Jp;
aa = (Jcon)*(-l*buf1); %wd1
bb = (Jcon)*(-l*kuf1); %w1
cc = (Jcon)*(l*buf2); %wd2
dd = (Jcon)*(l*kuf2); %w2
ee = (Jcon)*(l*buf1+bst/2/l); %zd1
ff = (Jcon)*(l*kuf1+kst/2/l+kt/2/l); %z1
gg = (Jcon)*(-l*buf2-bst/2/l); %zd2
```

```
hh = (Jcon)*(-l*kuf2-kst/2/l-kt/2/l); %z2

Mcon = 2/Mp;
ii = Mcon*(buf1); %wd1
jj = Mcon*(kuf1); %w1
kk = Mcon*(buf2); %wd2
ll = Mcon*(kuf2); %w2
mm = Mcon*(-bsy/2-buf1); %zd1
nn = Mcon*(-ksy/2-kuf1); %z1
oo = Mcon*(-bsy/2-buf2); %zd2
pp = Mcon*(-ksy/2-kuf2); %z2

%state [x1 xd1 x2 xd2 w1 wd1 w2 wd2 z1 zd1 z2 zd2] -> 12 states
A = [ (-bvc1-blf1)/Mvc -klf1/Mvc 0 0 blf1/Mvc klf1/Mvc 0 0 0 0 0 0;
1 0 0 0 0 0 0 0 0 0 0 0;
0 0 (-bvc2-blf2)/Mvc -klf2/Mvc 0 0 blf2/Mvc klf2/Mvc 0 0 0 0;
0 0 1 0 0 0 0 0 0 0 0 0;
blf1/Mu klf1/Mu 0 0 (-blf1-buf1)/Mu (-klf1-kuf1)/Mu 0 0 buf1/Mu kuf1/Mu
0 0;
0 0 0 0 1 0 0 0 0 0 0 0;
0 0 blf2/Mu klf2/Mu 0 0 (-blf2-buf2)/Mu (-klf2-kuf2)/Mu 0 0 buf2/Mu kuf2/Mu;
0 0 0 0 0 0 1 0 0 0 0 0;
0 0 0 0 .5*(ii-aa) .5*(jj-bb) .5*(kk-cc) .5*(ll-dd) .5*(mm-ee) .5*(nn-ff)
.5*(oo-gg) .5*(pp-hh);
0 0 0 0 0 0 0 0 1 0 0 0;
0 0 0 0 .5*(ii+aa) .5*(jj+bb) .5*(kk+cc) .5*(ll+dd) .5*(mm+ee) .5*(nn+ff)
.5*(oo+gg) .5*(pp+hh);
0 0 0 0 0 0 0 0 0 0 1 0];

B = [1/Mvc 0;
```

```
0 0;
0 1/Mvc;
0 0;
zeros(8,2)];

%% Define outputs
%state [xd1 x1 xd2 x2 wd1 w1 wd2 w2 zd1 z1 zd2 z2] -> 12 states
%As measured
C1 = [0 klf1 0 klf2 0 -klf1 0 -klf2 0 0 0 0;
0 -l*klf1 0 l*klf2 0 l*klf1 0 -l*klf2 0 0 0 0];

%Actual force on printhead
C2 = -[0 0 0 0 0 -kuf1 0 -kuf2 0 kuf1 0 kuf2;
0 0 0 0 0 l*kuf1 0 -l*kuf2 0 -l*kuf1 0 l*kuf2];

%Displacements x1 and x2 in um
C3 = [0 1e6 zeros(1,10);
0 0 0 1e6 zeros(1,8)];

%Forces F1out and F2out
C4 = [0 klf1 0 0 0 -klf1 0 0 0 0 0 0;
0 0 0 klf2 0 0 0 -klf2 0 0 0 0];

D = zeros(2,2);

%% Define systems
system1 = ss(A,B,C1,D);
system2 = ss(A,B,C2,D);
system3 = ss(A,B,C3,D);
system4 = ss(A,B,C4,D);
```

```
%% Check bode

%% For system4
figure(1); clf; bode(system4); grid on;

%% For system1
figure(2); clf; bode(system1); grid on;

%% For system3
figure(3); clf; bode(system3); grid on;
```

Appendix C

Matlab Code Generating CL Gains

```
%Use this script to compute all the necessary matrices for DT state %augmented
control.
   %% Grab system sys = system1;
   %Jump immediately into dt representation dt = 1/4000; dtsys = c2d(system1,dt);
   %Match naming convention in FPE text phi = dtsys.A; gam = dtsys.B; H
= dtsys.C;
   %% Compute CL gains, Kc
   %Choose poles in CT j = sqrt(-1);
   w_poles = [20 30 55 60 180 190]*2*pi; z_poles = [1 1 1 1 1 1]; real_poles
= -[]*2*pi;
   %% Construct DT matrices of pole and zero complex locations poles = [real_poles];
for m=1:length(w_poles) poles = [poles (-w_poles(m)*z_poles(m) + j*w_poles(m)*sqrt(1-
(-w_poles(m)*z_poles(m) - j*w_poles(m)*sqrt(1-z_poles(m)^2))]; end
   des_poles = poles; des_poles_dt = pole(c2d(zpk([],des_poles,1),dt));
   %% If you want butterworth poles...  realbutter = -[60 65 70 75]*2*pi;
realbutter = pole(c2d(zpk([],realbutter,1),dt)); [z,p,k] = butter(8,100/2000);
des_poles_butter = [realbutter; pole(zpk(z,p,k,1/4000))];
   %% Place DT poles Kcl = place(phi, gam, des_poles_dt)
   %% Compute state command matrix N NxNu = [phi-eye(length(phi)) gam; H
zeros(size(H,1))]^-1*[zeros(length(phi),size(H,1)); eye(size(H,1))]; Nx =
```

```
NxNu(1:12,:); Nu = NxNu(13:14,:); Nbar_cl = Nu + Kcl*Nx;
   %% Examine controller performance without integrator states CLsys = ss(phi-gam*Kc
gam*Nbar_cl, H, dtsys.D, dt,'InputName','fref','tref','OutputName','Fout','Tout');
figure(1); clf; bode(CLsys); grid on;
   step_opts = stepDataOptions('StepAmplitude',[0.5 0.05]); figure(2); clf;
step(CLsys,step_opts); grid on;
   %% Controller effort [ysim, tsim, xtraj] = step(CLsys,step_opts); xtraj_f1
= xtraj(:,:,1)'; xtraj_f2 = xtraj(:,:,2)'; usim1 = -Kcl*xtraj_f1; usim2
= -Kcl*xtraj_f2; figure(3); clf; plot(tsim, [usim1', usim2']); grid on;
   %% Process noise sensitivity loops = loopsens(dtsys,Kcl/dtsys.C); figure(7);
clf; bodemag(loops.To); grid on;
   ct_CLsys = d2c(CLsys); figure(5); clf; pzmap(CLsys);
```

Appendix D

Matlab Code Generating Observer Gains

```
% Compute steady state Kalman gains
   % [KEST,L,P] = kalman(SYS,QN,RN,NN)
   Ts = 1/4000; dt_sys = c2d(system1,Ts); gam = dt_sys.B;
   %Process noise.  Qn = [0.001 0; 0 0.001];
   %Rn is measurement or sensor noise vv' Rn = [0.01 0; 0 0.01];
   %Nn is the cross-variance wv'.  This is probably zero is the input process
%noise has no relation or correlation to the sensor noise.  Nn = [0 0; 0
0];
   [kest, L_kal, P_kal] = kalman(dt_sys, Qn, Rn, Nn); [kestd,L_kal_d,P_d,M_d,Z_d]
= kalmd(system1,Qn,Rn,Ts)
   %% Examine error dynamics dt_obs_errordyn = ss(dt_sys.A - L_kal_d*dt_sys.C,
zeros(12,2), eye(12), zeros(12,2), Ts); figure(1); pzmap(dt_obs_errordyn)
   %figure(1); clf; initial(dt_obs_errordyn, 10e-6*ones(12,1));
```

Appendix E

Matlab Code Simulating Whole System

```
%% Simulate CL system with integrators
   %% Set systems dt = 1/4000; dtsys = c2d(system1,dt); phi = dtsys.A; gam
= dtsys.B; H = dtsys.C;
   wrongsys = c2d(system1_wrong, dt); phi_wrong = wrongsys.A; gam_wrong =
wrongsys.B; H_wrong = wrongsys.C;
   %% Set controller parameters Lp = L_kal_d; Kcl = Kcl; Nbar = Nbar_cl;
   %Set KI KI_f = 1; KI_t = 1; KI = [KI_f 0; 0 KI_t];
   %% Generate reference vector fref = 0.5*[zeros(1,50) ones(1, 15950)];
%fref = zeros(1,5000); %tref = 0.1*downsample(fref_sweptsine,10)'*0.5; %fref
= 0.5*chirp([0:9999]*dt, 1, 9999*dt, 500); tref = zeros(1,length(fref));
   %Filter reference to see if avoiding excitation of HF is helpful [khzb,
khza] = butter(6,0.10,'low'); r = [fref; tref];
   %% Pre-generate vectors of disturbance noise sampled/filtered at 2kHz
wnoise = [rand(2,length(r))-0.5]; wnoise = [filter(khzb, khza, wnoise(1,:));
filter(khzb, khza, wnoise(2,:))]; wnoise = 0.01*[1/rms(wnoise(1,:))  0;
0 1/rms(wnoise(2,:))]*wnoise;
   wimpulse = [zeros(1,4000) ones(1,10) zeros(1,length(fref)-4010)]*0.5;
wstep = [zeros(1,500) ones(1,length(fref)-500)]*0.01; wsine1 = [sin(1*2*pi*[0:length
```

```
wsine10 = [sin(10*2*pi*[0:length(r)-1]*(dt))]*0.01; wsine100 = [sin(100*2*pi*[0:leng
   wdist = wnoise + [wimpulse+wsine; wimpulse+wsine+zeros(1,length(r))];
wdist = [wsine1+wsine10+wsine100; wsine1+wsine10+wsine100];
   %% Setup xtraj = zeros(12,length(r)); xtraj_wrong = xtraj; xtrajobs =
xtraj; xtrajobs_wrong = xtraj;
   u = [0; 0]; eint_k = [0; 0]; eint_k_wrong = eint_k;
   utraj = zeros(2,length(r)); utraj_wrong = utraj;
   ytraj = utraj; ytraj_wrong = utraj;
   tvec = [0:length(r)-1]*dt; %% Manually simulate for i=2:length(r)-1 %Sample
output for this cycle ytraj_wrong(:,i) = H_wrong*xtraj_wrong(:,i); ytraj(:,i)
= H*xtraj(:,i);
   %Compute integral based on current y-meas eint_k = (eint_k + dt*(-r(:,i)
+ ytraj(:,i))); %For erroneous model...  eint_k_wrong = eint_k_wrong + dt*(-r(:,i)
+ ytraj_wrong(:,i));
   %Compute current values u = -Kcl*xtrajobs(:,i) + -KI*eint_k + Nbar*r(:,i);
satlimit = 15; for m=1:2 if u(m)>satlimit u(m) = satlimit; elseif u(m)<-satlimit
u(m) = -satlimit; end end utraj(:,i) = u;
   u_wrong = -Kcl*xtrajobs_wrong(:,i) + -KI*eint_k_wrong + Nbar*r(:,i); for
m=1:2 if u_wrong(m)>satlimit u_wrong(m) = satlimit; elseif u_wrong(m)<-satlimit
u_wrong(m) = -satlimit; end end utraj_wrong(:,i) = u_wrong;
   %Compute update for next cycle based on u %Physical system response:
xtraj(:,i+1) = phi*xtraj(:,i) + gam*u + gam*wdist(:,i); xtraj_wrong(:,i+1)
= phi_wrong*xtraj_wrong(:,i) + gam_wrong*u_wrong + gam_wrong*wdist(:,i);
   %Observer prediction xtrajobs(:,i+1) = phi*xtrajobs(:,i) + Lp*(ytraj(:,i)
- H*xtrajobs(:,i)) + gam*u; xtrajobs_wrong(:,i+1) = phi*xtrajobs_wrong(:,i)
+ Lp*(ytraj_wrong(:,i) - H*xtrajobs_wrong(:,i)) + gam*u_wrong;
   end
   %% How'd we do?  figure(4); clf; plot(tvec, ytraj); grid on; %axis([0
.6 -0.1 0.8]); xlabel('Time, s'); ylabel('Output, N or Nm'); legend('Fout','Tout');
title('CL response');
```

```
%Controller effort figure(5); clf; plot(tvec,utraj); grid on; %axis([0
.6 0 0.4]); xlabel('Time, s'); ylabel('Output, N'); legend('F1','F2'); title('Contrc
effort');
% figure(6); clf; plot(tvec, xtraj([2,4],:)*1e6); % grid on; % xlabel('Time,
s'); ylabel('Position, um'); % legend('x1','x2'); % title('Position');
figure(7); clf; plot(tvec, ytraj_wrong); grid on; %axis([0 .6 -0.1 0.8]);
xlabel('Time, s'); ylabel('Output, N or Nm'); legend('Fout','Tout'); title('CL
response, erroneous model');
%Controller effort % figure(8); clf; plot(tvec,utraj_wrong); % grid on;
%axis([0 .6 0 0.4]); % xlabel('Time, s'); ylabel('Output, N'); % legend('F1','F2');
% title('Controller effort, erroneous model');
% figure(9); clf; plot(tvec, xtraj_wrong([2,4],:)*1e6); % grid on; %
xlabel('Time, s'); ylabel('Position, um'); % legend('x1','x2'); % title('Position,
erroneous model');
```

Bibliography

[1] J. Snyder, "A Chip Is Born: Inside a State-of-the-Art Clean Room."

[2] Y. Nuevo and S. Ylonen, *Bit Bang: Rays to the Future.* Helsinki University Print, 2009.

[3] "Microcontact printing," July 2017. Page Version ID: 791594427.

[4] C. Vericat, M. E. Vela, G. Benitez, P. Carro, and R. C. Salvarezza, "Self-assembled monolayers of thiols and dithiols on gold: new challenges for a well-known system," *Chemical Society Reviews*, vol. 39, no. 5, p. 1805, 2010.

[5] J. E. Petrzelka and D. E. Hardt, "Laser direct write system for fabricating seamless roll-to-roll lithography tools," p. 861205, Mar. 2013.

[6] G. Grau, J. Cen, H. Kang, R. Kitsomboonloha, W. J. Scheideler, and V. Subramanian, "Gravure-printed electronics: recent progress in tooling development, understanding of printing physics, and realization of printed devices," *Flexible and Printed Electronics*, vol. 1, no. 2, p. 023002, 2016.

[7] H. Kipphan, *Handbook of Print Media: Technologies and Production Methods.* Springer Science & Business Media, July 2001. Google-Books-ID: VrdqBRgSKasC.

[8] M. Hale, *Manufacturing conductive patterns on polymeric substrates: development of a microcontact printing process.* PhD thesis, Massachusetts Institute of Technology, 2013.

[9] J. E. Petrzelka, *Contact region fidelity, sensitivity, and control in roll-based soft lithography.* PhD thesis, Massachusetts Institute of Technology, 2012.

[10] A. Libert, *Precision Control of Cylindrical Stamp Contact in a Continuous Roll-to-Roll Microcontact Printing Machine.* PhD thesis, Massachusetts Institute of Technology, 2014.

[11] Automation Direct, "SureServo AC Servo Systems User Manual, Second Edition, Revision B," Aug. 2011.

[12] Automation Direct, "SureServo AC Servo System Configuration," Oct. 2015.

[13] C. Merian, *Development of an Inking System for Continuous Roll-to-Roll Microcontact Printing of Hexadecanethiol (HDT) on Gold-coated PET Substrate.* MS, Massachusetts Institute of Technology, June 2016.

[14] "Resonance frequency of multilayer actuator stacks."

[15] G. F. Franklin, J. D. Powell, and M. L. Workman, *Digital control of dynamic systems.* Menlo Park, Calif.: Addison-Wesley, 3. ed., [nachdr.] ed., 2002. OCLC: 249361424.

[16] S. Kalpakjian, *Manufacturing engineering and technology.* New York: Prentice Hall, 6th ed ed., 2010.

[17] R. Castellano, "The Switch To ASML's EUV Lithography Will Impact The Entire Semiconductor Supply Chain," Mar. 2017.

[18] "The State of Flexible and Printed Electronics."

[19] D. Corning, *Electronics Sylgard 184 Silicone Elastomer.* 2013.

[20] D. B. Wolfe, J. C. Love, and G. M. Whitesides, "Nanostructures Replicated by Polymer Molding," *Dekker Encyclopedia of Nanoscience and Nanotechnology*, pp. 2657–2666, 2004.

[21] Y. Xia and G. M. Whitesides, "Soft Lithography," *Annual Review of Materials Science*, vol. 28, no. 1, pp. 153–184, 1998.

[22] P. Ascoli, *Fabrication and Qualification of Arbitrarily Patterned Seamless Tooling for Continuous Roll-to-Roll Microcontact Printing.* MS, Massachusetts Institute of Technology, Cambridge, MA, June 2017.

[23] A. Stagnaro, *Design and Development of a Roll-to-Roll Machine for Continuous High-Speed Microcontact Printing.* Master's of Engineering, Massachusetts Institute of Technology, 2008.

[24] J. C. Love, L. A. Estroff, J. K. Kriebel, R. G. Nuzzo, and G. M. Whitesides, "Self-Assembled Monolayers of Thiolates on Metals as a Form of Nanotechnology," *Chemical Reviews*, vol. 105, pp. 1103–1170, Apr. 2005.

[25] X. Zhou, H. Xu, N. Zhao, S.-c. Chen, and H. K. Sar, "A FLEXURE-BASED ROLL-TO-ROLL MACHINE FOR FABRICATING FLEXIBLE PHOTONIC DEVICES," in *ASPE 2015 Annual Meeting*, (Austin, Texas, USA), 2015.

[26] "AZ 9200 Photoresist: Product Data Sheet," July 1997.

[27] L. F. Nietner, *A Direct-Write Thick-Film Lithography Process for Multi-Parameter Control of Tooling in Continuous Roll-to-Roll Microcontact Printing.* PhD thesis, Massachusetts Institute of Technology, 2014.

[28] S. T. Nill, *Integrated Hardware , Software , and Sensor Design for Control of a Scalable Continuous Microcontact Printing Process by.* Master's, Massachusetts Institute of Technology, 2014.

[29] F. E. Hizir, *Phase-Field Modeling of Liquids Splitting Between Separating Surfaces and its Application to High-Resolution Roll-Based Printing Technologiess.* PhD, Massachusetts Institute of Technology, June 2016.

[30] C. Merian, X. Du, D. Hardt, and H. AlQahtani, "Roll-to-Roll Microcontact Printing of Flexible Aluminum Substrates Using Octadecylphosphonic Acid (ODPA)," p. V014T11A016, ASME, Nov. 2015.

[31] H. Hannebauer, T. Dullweber, T. Falcon, and R. Brendel, "Fineline Printing Options for High Efficiencies and Low Ag Paste Consumption," *Energy Procedia*, vol. 38, pp. 725–731, Jan. 2013.

[32] M. Joyce, S. G. Avuthu, S. Emamian, A. Eshkeiti, M. Atashbar, P. D. Fleming III, and T. Donato, "Contribution of Flexo Process Variables to Fine Line Ag Electrode Performance," *International Journal of Engineering Reseearch & Technology*, vol. 3, pp. 1645–1656, Aug. 2014.

[33] J.-U. Park, M. Hardy, S. J. Kang, K. Barton, K. Adair, D. k. Mukhopadhyay, C. Y. Lee, M. S. Strano, A. G. Alleyne, J. G. Georgiadis, P. M. Ferreira, and J. A. Rogers, "High-resolution electrohydrodynamic jetprinting," *Nature Materials*, vol. 6, pp. 782–789, Aug. 2007.

[34] T. Sekitani, Y. Noguchi, U. Zschieschang, H. Klauk, and T. Someya, "Organic transistors manufactured using inkjet technology with subfemtoliter accuracy," *Proceedings of the National Academy of Sciences*, vol. 105, pp. 4976–4980, Apr. 2008.

[35] "Center for Hierarchical Manufacturing | an NSF Nanoscale Science and Engineering Center."

[36] "Roll-to-Roll Fabrication and Processing Facility | Institute for Applied Life Sciences."

[37] S. Khandavalli and J. P. Rothstein, "Ink transfer of non-Newtonian fluids from an idealized gravure cell: The effect of shear and extensional deformation," *Journal of Non-Newtonian Fluid Mechanics*, vol. 243, pp. 16–26, May 2017.

[38] J. A. Lee, J. P. Rothstein, and M. Pasquali, "Computational study of viscoelastic effects on liquid transfer during gravure printing," *Journal of Non-Newtonian Fluid Mechanics*, vol. 199, pp. 1–11, Sept. 2013.

[39] A. Goel, S. Laxminarayanan, and Y. Xia, *Understanding and Developing Capabilities for Large Area and Continuous Micro Contact Printing.* PhD thesis, Massachusetts Institute of Technology, Sept. 2007.

[40] K. Khanna, *Analysis of the Capabilities of Continuous High-Speed Microcontact Printing.* Master's of Engineering, Massachusetts Institute of Technology, Aug. 2008.

[41] X. Zhou, H. Xu, J. Cheng, N. Zhao, and S.-C. Chen, "Flexure-based Roll-to-roll Platform: A Practical Solution for Realizing Large-area Microcontact Printing," *Scientific Reports*, vol. 5, no. October 2014, p. 10402, 2015.

[42] FMS Force Measuring Systems AG, "Operating Manual CMGZ309 version 2.10," July 2012.

[43] New Way Air Bearings, "Air Bearing Application and Design Guide, Revision E," Jan. 2006.

[44] "6.777j/2.751j Material Property Database."

[45] "Application Note 078: Strain Gauge Measurement - A Tutorial," Aug. 1998.

[46] M. Instruments, "Backed Half-and Full Bridge Strain Gages."

[47] N. Instruments, "NI 9215 Datasheet," Mar. 2016.

[48] "FPGA Fundamentals - National Instruments."

[49] K. Johnson, *Contact Mechanics.* Cambridge, UK: Cambridge University Press, 1985.

[50] R. H. Bentall and K. L. Johnson, "An elastic strip in plane rolling contact," *International Journal of Mechanical Sciences*, vol. 10, pp. 637–663, Aug. 1968.

[51] P. Meijers, "The contact problem of a rigid cylinder on an elastic layer," *Applied Scientific Research*, vol. 18, pp. 353–383, Jan. 1968.

[52] "Transfer function estimation - MATLAB tfest."

[53] "Solve nonlinear least-squares (nonlinear data-fitting) problems - MATLAB lsqnonlin."

[54] "Estimate state-space model using time or frequency domain data - MATLAB ssest."

[55] "Prediction error estimate for linear and nonlinear model - MATLAB pem."

[56] L. Ljung, *System identification: theory for the user.* Prentice Hall information and system sciences series, Upper Saddle River, NJ: Prentice Hall PTR, 2nd ed ed., 1999.

[57] "Linear grey-box model estimation - MATLAB greyest."

[58] K. S. Narendra and A. M. Annaswamy, *Stable adaptive systems.* Mineola, N.Y: Dover Publications, 2005.

[59] D. W. Limoge, *Reduced-Order Modeling and Adaptive Observer Design for Lithium-Ion Battery Cells.* PhD, Massachusetts Institute of Technology, June 2017.

[60] "Control Tutorials for MATLAB and Simulink - Introduction: State-Space Methods for Controller Design."

[61] "Transformation: Transfer Function State Space."

[62] "16.30/31 Feedback Control Systems: Topic 8," Oct. 2010.

[63] K. Astrom, "Chapter 5: Feedback Fundamentals," in *Control System Design: Lecture Notes for ME 155A*, California Institute of Technology, 2002.

[64] P. I. P. GmbH, "P-601 PiezoMove Flexure-Guided Linear Actuator."

[65] P. I. P. GmbH, "P-602 PiezoMove High-Stiffness Linear Piezo Actuator."

[66] P. I. P. G. . C. KG, "Dynamic Operation."

[67] "5/8" Thrust Bushing."